A Study on Nonlinear Dynamics of Agricultural Tractor for Prevention of Overturning Accidents

2021.3

Department of Food and Energy Systems Science,
Graduate School of Bio-Applications and Systems Engineering,
Tokyo University of Agriculture and Technology

Masahisa Watanabe（渡辺将央）

A thesis submitted in conformity with the

requirements for the degree of

Doctor of Philosophy in

Agricultural and Environmental Engineering

Advisor: Prof. Dr. Kenshi Sakai

Committee: Prof. Dr. Koki Toyota

Prof. Dr. Masafumi Yohda

Prof. Dr. Tojo Seishu

Prof. Dr. Hirotaka Saito

Prof. Dr. Hiroshi Mouri

Abstract

The present study is an extensive investigation into the nonlinear dynamics of the agricultural tractor in order to prevent accidents which involve tractors overturning. Globally, accidents involving overturned tractors are a serious problem in agriculture. Not only do they threaten the lives and wellbeing of farmers, but these accidents can be a major obstruction for farm automation.

In Japan, small tractors are used in harsh operating environments which can include uneven farm roads, steep passage slopes, and narrow inclined side paths. In these potentially dangerous terrain conditions, frequent nonlinearity of the agricultural tractor occurs via vertical jumping and lateral sliding. Violent vibrations can occur in tractor operations and the wheels of a tractor will sometimes leave the ground. Furthermore, even if a wheel does not lose contact with the ground, vertical forces can be reduced low enough to cause lateral sliding, resulting in steering instability during operations. In addition to the abovementioned phenomena, the combination of jumping and sliding cause the power hop phenomenon, which is a major dynamic instability of agricultural tractors when engaged in towing operations on dry soil. Nonlinear dynamics of the agricultural tractor are thus crucial for determining their dynamic behaviors so that overturning accidents can be prevented.

This study investigates the nonlinear dynamics of an agricultural tractor through dynamic modeling and driving simulation. First, the nonlinear dynamic modeling of tractor dynamics is conducted to elucidate the tractor overturning mechanism. Jumping or bouncing tractor dynamics are modeled as a nonlinear impact on the basis of bouncing ball dynamics. Using the developed bouncing tractor model, the impact dynamics of the tractor are intensively investigated in numerical parametric investigations. The numerical

results reveal that nonlinear characteristics and parameter sensitivity can lead to overturing accidents. The steering instability of the agricultural tractor is then numerically investigated by developing a lateral sliding model of an agricultural tractor based on the friction circle; i.e., adopting classic Coulomb friction theory. The bouncing tractor model and bicycle model are coupled in lateral sliding modeling. The parametric investigation results obtained in the numerical experiments strongly demonstrate that bouncing and sliding on specific terrain result in steering instability and are a major cause of overturning accidents. The power hop is a major dynamics instability of an agricultural tractor during towing operations on dry soil. A novel power hop model is developed by coupling three nonlinear elements, namely bouncing, sliding, and free play in the joint between the tractor and implement. The developed model reveals the occurrence process of power hop in transitional and steady-state dynamics. In addition to the establishment of the abovementioned nonlinear dynamic tractor models, a tractor driving simulator with a motion system is developed in this study. Road profile analysis is first conducted to generate the road surface in the tractor driving simulator. In road profile modeling, the power spectrum density and coherence function are combined to generate a random road surface. A tractor driving simulator with a motion system is then developed using CarSim® DS, MATLAB®/Simulink®, a Logitech® G27, and a motion system offered by Solution Inc. Using the developed tractor driving simulator with a motion system, numerical experiments are carried out to identify scenarios of tractor overturning.

Acknowledgement

The current work was supported and inspired by many people over the last five years at the Graduate School of Bio-Applications and Systems Engineering, Tokyo University of Agriculture and Technology. I first express my sincere gratitude to my principal supervisor Professor Dr. Kenshi Sakai for his continuous encouragement, suggestions, and patient guidance. I also equally thank my co-advisers Professor Dr. Koki Toyota, Professor Dr. Yohda Hirohumi, Professor Dr. Seishu Tojo, Professor Dr. Hirotaka Saito, and Professor Dr. Hiroshi Mouri for their support and valuable suggestions.

I thank Professor Dr. Tohru Ikeguchi at the Tokyo University of Science for his kind support and suggestions during my research visit at his laboratory. I thank Professor Dr. Sakae Shibisawa at the Tokyo University of Agriculture and Technology for his insightful suggestions relating to my research.

I specially acknowledge Professor Dr. Heinz Bernhardt at the School of Life Science, Technical University of Munich, Germany for his kind support and guidance during my intensive research internship at the university. I express my appreciation to Professor Dr. Shrinivasa K. Upadhyaya, Professor Dr. Ken Giles, Professor Dr. Fadi Fathallah, and Professor Dr. Bryan Jenkins at the Biological and Agricultural Engineering Department, University of California, Davis, the United States for their kind support and guidance during my research workshop at UC Davis. I express my appreciation to Professor Awadesh Prasad at the Department of Physics & Astrophysics, Delhi University, India for his valuable suggestion and kind support for my research.

I thank Dr. Yusuke Kikuchi at NEC Corporation for kind support during my research internship at NEC Corporation. I also thanks Dr. Eiji Murayama and Dr. Kuniharu Arai

at Neorium Technology, Co., Ltd. for kind support during my engineering internship at Nerioum Technology, Co., Ltd. I thank Ryo Hosoda, Kimitaka Suzuki, and Dr. Yasuo Aoki at Solution, Inc for their kind support in developing the motion system for the tractor driving simulator.

I thank Kenshi Sakai's laboratory members at the Tokyo University of Agriculture and Technology, Dr. Sviridova Nina, Oto Kiriyama, and Akira Ishibashi, and others. I especially thank Dr. Masayuki Nitta for his kind support during my visit to the Technical University of Munich. I also thank Josef Bauerdick, Maximiliam Treibar, and Matthias Stettmer at the Technical University of Munich for their kind support during my visit. I thank Dr. Scott Strobel, Dr. Tyler Barzee, Wayland Singh, Alexander Olenskyj, and Irving Rabasa at UC Davis for their kind support and suggestions during our research workshop at UC Davis.

I give special thanks to my loving parents, brother, and sister for their kind support during my doctoral study. I also pay tribute to my beloved grandmother (1935–2017) for her support.

I would also like to thank the Japan Society for the Promotion of Science (JSPS) for their financial support of my doctoral study through the Leading Graduate School Program Fellowship and Research Fellowship DC2. My research was supported by JSPS Grants-in-Aid (15H04572 and 19H00959) and a JSPS Grant-in-Aid for JSPS Research Fellow (19J11183). I thank the Japanese Society of Agricultural Machinery and Food Engineers for their financial support in the form of international conference participation support at the American Society of Agricultural and Biological Engineers Annual International Meeting 2019, Boston, MA, USA.

Table of contents

Abstract 3

Acknowledgement 5

Table of contents 7

List of figures 12

List of tables 22

Nomenclature and Abbreviations 23

Manuscripts for publication and conference presentation based on the thesis 26

1. Introduction 29

1.1. Research background 29

1.2. Research objective 31

1.3. Literature review 33

1.3.1. General remarks 33

1.3.2. Tire forces 35

1.3.3. Road profile 42

1.3.4. Dynamic models of agricultural tractors 45

1.3.5. Patterns of tractor overturning 52

1.3.6. Summary 58

2 Impact dynamics of bouncing tractor model 61

2.1. Introduction 61

2.2. Mathematical model 62

2.2.1. Motion equations of tractor with two degrees of freedom 62

2.2.2. Modelling of bouncing process 64
2.3. Numerical experiments 69
2.3.1. Frequency response analysis 71
2.3.2. Bifurcation diagram 74
2.3.3. Numerical experiments of the tractor running along passage slope 80
2.3.4. Comparison between large and small tractor 86
2.4. Control method for a bouncing tractor model 89
2.4.1. Proportional control 89
2.4.2. Delayed feedback control 92
2.5. Summary 95
3. Steering instability induced by bouncing and sliding 97
3.1. Introduction 97
3.2. Mathematical model 98
3.2.1. Bouncing tractor model 98
3.2.2. Bicycle model 100
3.2.3. Coupling of bouncing and bicycle model 101
3.3. Numerical experiments 103
3.3.1. Turning test 105
3.3.2. Operation on steep passage slope 110
3.4. Summary 113
4. Power hop model 115
4.1. Introduction 115
4.2. Modelling of power hop 117
4.2.1. Bouncing modelling 119

4.2.2. Stick–slip modelling 120
4.2.3. Free-play modelling 121
4.3. Numerical experiments 122
4.3.1. Occurrence process of power hop 123
4.3.2. Drawbar pull conditions 129
4.3.3. Soil conditions 131
4.3.4. Tire conditions 133
4.3.5. Power hop for a 2WD tractor 135
4.3.6. Bifurcation diagram of the power hop dynamics 136
4.4. Summary 140
5. Road profile generation for a tractor driving simulator 142
5.1. Introduction 142
5.2. Analysis of the surveyed road profile 143
5.2.1. Power spectrum density analysis 145
5.2.2. Coherence analysis 146
5.3. Algorithms for generating the road profile 148
5.3.1. Fourier Transform surrogate method 148
5.3.2. Autoregressive model 149
5.4. Generation of the road profile 151
5.4.1. Road profile generation for a single wheel path 151
5.4.2. Road profile generation for two-wheel paths 152
5.4.3. Gap elimination using a one-sided Hanning window 155
5.5. Summary 156
6. Development of a tractor driving simulator 158

6.1. Introduction 158

6.2. Configuration of the tractor driving simulator 160

6.2.1. Powertrain system 162

6.2.2. Steering system 166

6.2.3. Brake system 166

6.2.4. Suspension and axle system 167

6.3. Validation test of configurations of the tractor driving simulator 168

6.3.1. Gear shift operation test 168

6.3.2. Minimum radius turning test 169

6.3.3. Validation of the suspension system 171

6.4. Development of a motion system for a tractor driving simulator 173

6.4.1. Outline of the tractor driving simulator with a motion system 173

6.4.2. Simulink model of the developed system 176

6.4.3. Developed tractor driving simulator with a motion system 177

6.5. Summary 177

7. Numerical experiments conducted using the developed tractor driving simulator 179

7.1. Introduction 179

7.2. Field-experiment validation of the tractor driving simulator 179

7.2.1. Experimental instruments 180

7.2.2. Bump test validation 181

7.2.3. Double-lane-change test validation 187

7.3. Nonlinear dynamics in the tractor driving simulator 192

7.3.1. Bouncing in the tractor driving simulator 192

7.3.2. Power hop in the tractor driving simulator 195

7.4. Reproducing overturning scenarios using the developed tractor driving simulator 197

7.4.1. Overturning accident on a steep passage slope 197

7.4.2. Overturning accident on a steep slope in rain 201

7.5. Summary 203

8. Conclusion 204

8.1. Perspective 204

8.2. Summary 205

8.3. Further investigations 207

References 209

A. Appendix: Results of tractor field experiments 220

A.1 Bump test results 220

A.2 Frequency analysis of the tire lug 225

List of figures

Figure 1.1 Fatalities in agriculture, construction, all industries, and traffic accidents (Graph is made from fatality report from Ministry of Agriculture, Forestry and Fisheries, Ministry of Health, Labour and Welfare, National Police Agency).29

Figure 1.2 Breakdown of fatal farm accidents in 2017. 30

Figure 1.3 Schematic diagram of three mutually perpendicular forces acting on tire. 35

Figure 1.4 Models of tire characteristics: (a) Kelvin-Voigt model (linear spring and damper in parallel); (b) Maxwell model (linear spring and damper in series). 36

Figure 1.5 Schematic diagram of friction circle concept: (a) static friction state; (b) dynamic friction state (Watanabe & Sakai, 2020). 39

Figure 1.6 Power spectrum density standardized by International Organization for Standardization. 44

Figure 1.7 Liner tractor model with seven degrees of freedom and rear-mounted implement (Collins, 1991). 48

Figure 1.8 Nonlinear bouncing tractor model (Sakai, 1999) 50

Figure 2.1Schematic diagram of the two-dimensional tractor model. 63

Figure 2.2 Schematic diagram of bouncing tractor; (a) Both wheels remain on ground, (b) Front wheel departs from the ground and rear wheel remains on ground (Wheelie state), (c) Front wheel remains on ground and rear wheel departs from the ground, (d) Both wheels depart from the ground (Jump state). 65

Figure 2.3 Flow chart for the numerical implementation of the bouncing. 69

Figure 2.4 Frequency response curve of the linear conventional model (blue line) and the nonlinear bouncing model (red line) 72

Figure 2.5 Fourier spectrum for 2.3, 2.9, 4.4, and 6.8 Hz input oscillating frequency. 73

Figure 2.6 The results of the numerical experiment for the forcing frequency 2.2 Hz; (a) Time series of the vertical acceleration of C.G.; (b) Fourier spectrum of the vertical acceleration of C.G.; (c) Trajectory in phase space; (d) Poincaré section. 75

Figure 2.7 The results of the numerical experiment for the forcing frequency 2.5 Hz; (a) Time series of the vertical acceleration of C.G.; (b) Fourier spectrum of the vertical acceleration of C.G.; (c) Trajectory in phase space; (d) Poincaré section. 76

Figure 2.8 The results of the numerical experiment for the forcing frequency 3.5 Hz; (a) Time series of the vertical acceleration of C.G.; (b) Fourier spectrum of the vertical acceleration of C.G.; (c) Trajectory in phase space; (d) Poincaré section. 77

Figure 2.9 The results of the numerical experiment for the forcing frequency 4.8 Hz; (a) Time series of the vertical acceleration of C.G.; (b) Fourier spectrum of the vertical acceleration of C.G.; (c) Trajectory in phase space; (d) Poincaré section. 78

Figure 2.10 The results of the numerical experiment for the forcing frequency 6.6 Hz; (a) Time series of the vertical acceleration of C.G.; (b) Fourier spectrum of the vertical acceleration of C.G.; (c) Trajectory in phase space; (d) Poincaré section. 79

Figure 2.11 Bifurcation diagram of the vertical displacement concerning to the forcing frequency f_t. 80

Figure 2.12 (a) Schematic diagram of the accident topography based on the real case of tractor overturning accidents on the passage slope collected in the Japanese Association of Rural Medicine survey ("Case study of farm accidents", 2013), (b) Cross section of passage slope. 81

Figure 2.13 Numerical results of the tractor running on passage slope when the travel velocity is considered as a control parameter. The blue line is the result of the linear conventional model while the red line is the results of the nonlinear bouncing model. 82

Figure 2.14 Time series of the vertical load on front axle f_1 [kN], the vertical load on rear axle f_2 [kN], and the vertical acceleration of C.G. Az [g]. (a) Results at 3.4 m s^{-1}; Top; Vertical load on front axle f_1, Medium; Vertical load on rear axle f_2, Bottom; Vertical acceleration of C.G. A_z. 84

Figure 2.15 Numerical results of the tractor running on passage slope when the angle of passage slope is taken as control parameter. The blue line is the result of the linear conventional model while the red line is the results of the nonlinear bouncing model. 85

Figure 2.16 Simulation results for (a) the small-sized tractor (travel velocity 4.020 m/s) and (b) the large-sized tractor (travel velocity 2.355 m/s). (1) Front-tire dynamic load; (2) rear-tire dynamic load; (3) front-tire relative displacement; (4) rear-tire relative displacement; (5) vertical acceleration at the center of gravity (CG). 88

Figure 2.17 Numerical results of the bump test, with red and blue lines respectively showing results obtained with and without control: (a) vertical force acting on the front wheel; (b) vertical force acting on the rear wheel. 91

Figure 2.18 Numerical results of the bump test when P-control was implemented: (a) driving force; (b) travel velocity. 92
Figure 2.19 Schematic diagram of the delayed feedback control algorithm. 93
Figure 2.20 Numerical results of DF-control: (top) vertical motion z [m]; (middle) force input in the vertical equation; (bottom) torque input in the pitch equation. 94
Figure 2.21 Numerical results of DF-control. Blue and red lines respectively show the uncontrolled and controlled vertical accelerations. 95
Figure 3.1 Developed mathematical model (a) Bouncing tractor model with two degrees of freedom: vertical motion z and pitch motion γ; (b) Bicycle model with two degrees of freedom: yaw rate r and slip angle β. 99
Figure 3.2 Schematic diagram of friction circle: (a) static friction without slippage; (b) dynamic friction with slippage 102
Figure 3.3 Turning trajectories of tractor in turning test; solid line and dashed line indicate stable and unstable steering, respectively; trajectory A (μ_s=0.6 and d_0=0.00 m) represents desired turning without steering instability; trajectory B (μ_s=0.6 and d_0=0.05 m) represents turning with steering instability; trajectory C (μ_s=0.4, d_0=0.05 m) represents turning failure. 106
Figure 3.4 Numerical results of Trajectory A and C in numerical turning test experiment; solid line and dashed line indicate Trajectory A and C results, respectively. Top: vertical load on front wheel f_1. Middle: grip margin of front wheel ε_1. Bottom: Cornering force on front wheel Y_1. 107
Figure 3.5 Maximum lateral difference from the desired trajectory L_{max} for different travel velocities V, friction coefficients μ_s, bump length l_b, and turning radius ρ;

white blank areas represent that L_{max} could not be defined owing to the failure of the tractor to turn; (a) d_0 = 0.00 m, l_b = 0.5 m, and ρ= 3.5 m; (b) d_0 = 0.05 m, l_b = 0.5 m, and ρ= 3.5 m; (c) d_0 = 0.00 m, V = 3.0 m s^{-1}, and μ_s = 0.6; (d) d_0 = 0.05 m, V = 3.0 m s^{-1}, and μ_s = 0.6. 109

Figure 3.6 Tractor trajectories with different travel velocity and friction coefficient; solid line and dashed line indicate stable and unstable steering, respectively; Trajectory A under V=1.5 m s^{-1} and μ_s=0.8; Trajectory B under V=3.0 m s^{-1} and μ_s=0.8; Trajectory C under V=1.5 m s^{-1} and μ_s=0.4; Trajectory D under V=3.0 m s^{-1} and μ_s=0.4. 111

Figure 3.7 Numerical results for Trajectories B and D in numerical experiments for operation on passage slope. Top: vertical load on front wheel f_1. Middle: grip margin of front wheel ε_1. Bottom: cornering force on front wheel Y_1.....112

Figure 4.1 Schematic diagram of tractor power hop with three degrees of freedom, i.e., vertical, longitudinal, and pitch motion. 118

Figure 4.2 Transitional behaviour of power-hop dynamics; Top: Draft load P [kN]: Middle: Tractive force acting on the front wheel $F_{d,1}$ [kN] and static friction limitation of the front tyres $\mu f_{v,1}$; Bottom: Tractive force acting on the front tyres $F_{d,2}$ [kN] and static friction limitation of the front tyres $\mu f_{v,2}$. 124

Figure 4.3 Enlargement for the points T_1 and T_2. Top: The tractive force acting on the front tyres $F_{d,1}$; Bottom: The tractive force acting on rear tyres $F_{d,2}$..... 125

Figure 4.4 Tractor motions excited by power hop instability. Top: Longitudinal motion x [m]; Middle: Pitch motion γ [rad]; Bottom: Vertical motion z [m]. 126

Figure 4.5 Steady-state behaviour of the power hop dynamics; Top: Draft load P [kN]: Middle: Tractive force acting on the front tyres $F_{d,1}$ [kN] and static friction

limitation of the front tyres $\mu f_{v,1}$ [kN] as a red line; Bottom: Tractive force acting on the front tyres $F_{d,2}$ [kN] and static friction limitation of the front tyres $\mu f_{v,2}$ [kN] as a red line. 127

Figure 4.6 The flow chart of the obtained power hop occurrence mechanism 128

Figure 4.7 Maximum vertical acceleration of the tractor centre of gravity A_z when varying P_0 from 3 to 10 kN and d from 0 to 0.025 m. 129

Figure 4.8 Time series of the vertical acceleration of the tractor centre of gravity A_z longitudinal acceleration of the tractor centre of gravity A_x, and draft load P for an original draft load P_0 of 9 kN and joint clearance of 0.005 m. 130

Figure 4.9 Maximum vertical acceleration of the tractor centre of gravity A_z for μ varying from 0.3 to 0.65 and R_μ from 0.1 to 0.8. 132

Figure 4.10 Maximum vertical acceleration of the tractor centre of gravity A_z for $k_{v,1}$ varying from 150,000 N m^{-1} to 650,000 N m^{-1} and $k_{v,2}$ and $k_{l,2}$ varying from 150,000 N m^{-1} to 650,000 N m^{-1} 134

Figure 4.11 Maximum vertical acceleration of the tractor centre of gravity A_z for μ varying from 0.3 to 0.9 and P_0 from 0 to 30 kN. 136

Figure 4.12 Bifurcation diagram of the power hop model plotting the vertical motion z against the original draft load P_0. 137

Figure 4.13 Phase space spanned by vertical motion z, vertical velocity $\dot{z}$, and pitch γ : (a) P_0 = 5.5 kN; (b) P_0 = 7.0 kN; (c) P_0 = 11.0 kN; (d) P_0 = 13.0 kN. 138

Figure 4.14 Fourier spectrum of the vertical acceleration of the tractor centre of gravity A_z. Top: Limit cycle at P_0 = 5.5 kN; Middle: Torus at P_0 = 7.0 kN; Bottom: Chaos at P_0 = 11.0 kN. 139

Figure 5.1 (a) Real road data from surveying and (b) the surveying method..... 144

Figure 5.2 PSDs of real road data. 146
Figure 5.3 Coherence of surveyed data and the mean coherence. 147
Figure 5.4 (a) AR road, (b) surrogate road, and (c) PSDs of the AR road and surrogate road. 152
Figure 5.5 (a) Right surrogate road, (b) left surrogate road, and (c) difference between right and left surrogate roads. 153
Figure 5.6 (a) Coherence of 100 pairs of the surrogate road and (b) mean coherence of 100 pairs of the surrogate road and coherence of the real road..... 155
Figure 5.7 (a) Road before removing the discontinuous part, (b) one-sided Hanning window, and (c) road after removing the discontinuous part. 156
Figure 6.1 CarSim® sprung mass screen for setting the tractor dimensions, mass, and moment of inertia. 162
Figure 6.2 Schematic diagram of power flow in the CarSim® powertrain system from engine to wheel. 163
Figure 6.3 Engine characteristics of a small agricultural tractor (JISB8018, 1989). 163
Figure 6.4 4WD and RWD powertrain systems in CarSim ®. 165
Figure 6.5 Gear transmission ratios for the RWD tractor; first, second, third, fourth, fifth, and sixth speeds correspond to 0.05, 0.5, 1.0. 2.0, 3.0, and 4.0 m s^{-1} respectively. 165
Figure 6.6 Screen for setting the brake systems in CarSim®. 167
Figure 6.7 Axle and suspension system setting. 168
Figure 6.8 Numerical results of the gear shift test: (top) travel velocity of the tractor [km h^{-1}]; (middle) engine speed [rpm]; (bottom) gear position [–]. 169

Figure 6.9 Numerical result of the minimum radius turning test with left-braking: (top) steering wheel angle and front road wheel angle [deg]; (middle) front left and right cornering forces [kN]; (bottom) rear left and right cornering forces [kN]. 170
Figure 6.10 Road surface having a 0.035-m bump used in validation of the suspension system. 172
Figure 6.11 Difference between the tractor body position and rear axial position. 173
Figure 6.12 Schematic diagram of the configuration of the developed tractor driving simulator. 175
Figure 6.13 Simulink® model used in the tractor driving simulator. 176
Figure 6.14 Developed tractor driving simulator with a motion system setup..... 177
Figure 7.1 Three-axis acceleration transducer (KYOWA AS-10TB). 180
Figure 7.2 Schematic diagram of the measurement system. 181
Figure 7.3 Schematic diagram of bump tests. 182
Figure 7.4 Experimental results of a bump test (fourth gear, N = 1). 183
Figure 7.5 Vertical acceleration of the bump excitation vibration in each test..... 184
Figure 7.6 Fourier spectrum of vertical acceleration in each test. 185
Figure 7.7 Time series and Fourier spectrum of vertical acceleration in the fourth gear, N = 3 experiment. 186
Figure 7.8 Comparison of the MATLAB® bouncing tractor model, CarSim® tractor model, and experimental results (fourth gear, N = 3). 187
Figure 7.9 Schematic diagram of the proposed double-lane-change test for agricultural tractors. 188
Figure 7.10 Raw data and 0.5-Hz lowpass filter data of lateral acceleration (fourth

gear, N = 3). 189
Figure 7.11 Lateral acceleration in double-lane-change tests. 190
Figure 7.12 Comparison of the lateral acceleration among the MATLAB® bicycle model, CarSim® tractor model, and experiment (fourth gear, N = 3). 191
Figure 7.13 Time series of vertical loads acting on the wheels. Blue and red lines show the front and rear vertical loads, respectively..... 193
Figure 7.14 (Left) Time series of the vertical acceleration A_z and (right) Fourier spectrum of the vertical displacement. 193
Figure 7.15 Numerical trajectory in the phase plane of the vertical displacement and velocity..... 194
Figure 7.16 Maximum vertical acceleration of the tractor in each numerical simulation. 196
Figure 7.17 Numerical results (slope inclination of 10 degrees): (top) time series of the vertical acceleration; (middle) longitudinal acceleration; (bottom) vertical loads acting on the front and rear wheels. 197
Figure 7.18 Numerical simulation results of the accident on the passage slope. .. 198
Figure 7.19 (Top) Front axial load [kN] and (bottom) front cornering force [kN]. 199
Figure 7.20 Overturning process of the tractor on a passage slope. 200
Figure 7.21 Motion system behavior during the tractor overturing simulation..... 201
Figure 7.22 Numerical simulation results of the accident on a steep slope..... 202
Figure 7.23 Process of the tractor overturning on a steep slope. 203
Figure A.1 Vertical acceleration of engine vibrations. 221
Figure A.2 Fourier spectrum of vertical acceleration during engine vibrations. ... 222

Figure A.3 Time series of vertical acceleration during engine vibrations. 223

Figure A.4 Fourier spectrum of vertical acceleration during lug vibrations. 224

Figure A.5 Frequency of tire lug vibration vs travel velocity of the tractor. 225

List of tables

Table 1.1 Main development of dynamic tractor models. 51

Table 1.2 Summary of developed stability indicators. 57

Table 2.1 Parameter specification of the tractor for the numerical experiments (Bukta, Sakai, Sasao & Shibusawa, 2002). 70

Table 2.2 Specification of the small-sized tractor and the large-sized tractor used in the simulations. 87

Table 3.1 Parameter specification of tractor considered in numerical experiments (Bukta, Sakai, Sasao, Shibusawa, 2002; Umeda & Honami, 1975; Sakai & Terao, 1987). 104

Table 4.1 Parameter specifications of the tractor considered in numerical experiments (Collins, 1991, Flaugh, 2011). 121

Table 5.1 AR coefficients of respective roads 150

Table 6.1 Specifications for a small tractor designed to operate in a paddy field . 160

Table 7.1 Average travel velocity of the agricultural tractor for each gear position 182

Table A.1 Average travel velocity and frequency band in the experiment 225

Nomenclature and Abbreviations

Symbols	Meaning of symbols
A_z	Vertical acceleration of centre of gravity [g]
$C_{p,1}$	Cornering power of front wheel [N deg $^{-1}$]
$C_{p,2}$	Cornering power of front wheel [N deg $^{-1}$]
D_1	Distance between front wheel and road surface [m]
D_2	Distance between rear wheel and road surface [m]
$F_{d,1}$	Tractive force on front wheel [kN]
$F_{d,2}$	Tractive force on rear wheel [kN]
H_0	Slope height [m]
I_{yy}	Pitch moment of inertia [kg m^2]
I_{zz}	Yaw moment of inertia [kg m^2]
L_{max}	Lateral difference from the desired trajectory [m]
M	Mass of tractor [kg]
M_1	Set of mode of front wheel [-]
M_2	Set of mode of rear wheel [-]
M_I	Mass of implement [kg]
M_T	Mass of tractor [kg]
P	Draft load [kN]
P_0	Original draft load [kN]
R_μ	Ratio of coefficients of static and dynamic friction [–]
T	Simulation time [s]
T_i	Longitudinal force [kN]
T_δ	Duration of steering for turning [s]
WB	Wheel base of tractor [m]
Y_1	Cornering force on the front wheel [kN]
Y_2	Cornering force on the rear wheel [kN]
$Y_{max,i}$	Maximum cornering force [kN]
c_1	Damping coefficient of front wheel [N s m^{-1}]
c_2	Damping coefficient of rear wheel [N s m^{-1}]
$c_{l,2}$	Longitudinal damping coefficient of rear wheel [N s m^{-1}]
$c_{v,1}$	Vertical damping coefficient of front wheel [N s m^{-1}]
$c_{v,2}$	Vertical damping coefficient of rear wheel [N s m^{-1}]
d	Joint clearance [m]

d_0	Road amplitude of sinusoidal function or bump [m]
d_1	Front road surface [m]
d_2	Rear road surface [m]
f_1	Vertical load on front axle [kN]
f_2	Vertical load on rear axle [kN]
f_{in}	Forcing frequency [Hz]
$f_{l,2}$	Longitudinal load on rear wheel [kN]
f_{sd}	Secondary frequency in the Fourier spectrum [Hz]
$f_{v,1}$	Vertical load on front wheel [kN]
$f_{v,2}$	Vertical load on rear wheel [kN]
g	Gravitational acceleration [g]
h_{CG}	Height of centre of gravity from ground [m]
h_o	Distance of centre of gravity to drawbar [m]
k_1	Stiffness of front wheel [N m^{-1}]
k_2	Stiffness of rear wheel [N m^{-1}]
$k_{l,2}$	Longitudinal stiffness of rear wheel [kN m^{-1}]
$k_{v,1}$	Vertical stiffness of front wheel [kN m^{-1}]
$k_{v,2}$	Vertical stiffness of rear wheel [kN m^{-1}]
l_1	Distance between centre of gravity of tractor body and front wheel [m]
l_2	Distance between centre of gravity of tractor body and rear wheel [m]
l_3	Distance between centre of gravity of tractor body and centre of gravity of implement [m]
l_b	Bump length [m]
l_s	Slope length [m]
t	Time [s]
x	Longitudinal motion [m]
z	Vertical motion [m]
z_1	Vertical motion of front wheel [m]
z_2	Vertical motion of rear wheel [m]
μ	Static friction coefficient [–]
β	Slip angle of tractor [rad]
β_1	Slip angle of front wheel [rad]
β_2	Slip angle of rear wheel [rad]

γ	Pitch motion [rad]
δ	Steering angle of the wheel [rad]
ε_i	Grip margin [-]
θ	Angle of passage slope [degree]
μ_d	Dynamic friction coefficient [-]
$\mu_{r,i}$	Motion resistance coefficient [–]

Abbreviations	
C.G.	Centre of gravity
ROPS	Roll Over Protective Structure

Manuscripts for publication and conference presentation based on the thesis

Journal publications

渡辺将央, 酒井憲司,”トラクタドライブシミュレータに用いる路面生成アルゴリズム,” 農業食料工学会誌, 農業食料工学会, vol.79, no.2 , pp.149-157, 2017 年 3 月.

Masahisa Watanabe, Kenshi Sakai, "Impact dynamics model for a nonlinear bouncing tractor during inclined passage", Biosystems Engineering, 2019, Volume 182, pp84-94.

Masahisa Watanabe, Kenshi Sakai, "Numerical analysis of steering instability in an agricultural tractor induced by bouncing and sliding", Biosystems Engineering, 2020, Volume 192, pp108-116.

Masahisa Watanabe, Kenshi Sakai, “Novel power hop model of an agricultural tractor coupling bouncing, stick–slip, and free-play dynamics”, Biosystems Engineering, 2021, Volume 204, pp156-169.

Masahisa Watanabe, Kenshi Sakai, “Tractor dynamic modeling and stability analysis: A critical review and future perspective”, Biosystems Engineering, (under review).

Masahisa Watanabe, Kenshi Sakai, “Development of a tractor driving simulator for a virtual test drive to identify overturning scenario”, Biosystems Engineering (in submission).

Conference presentations

Masahisa Watanabe, Kenshi Sakai, "Development of a Nonlinear Tractor Model using in Constructing a Tractor Driving Simulator", American Society of Agricultural and Biological Engineers, Machinery Systems(MS), 307 Machinery Systems POSTER Session, Paper No.1700374, Spoken, Washington USA, July 16-19, 2017.

Masahisa Watanabe, Josef Bauerdick, Kenshi Sakai, Heinz Bernhardt, "Comparison of jumping process between small-sized and large-sized tractors", 38. Gesellschaft für Informatik in der Land-, Forst,- und ernährungswirtshaft-Jahrestagung, Feburary 26-27, 2018, Christian-Albrechts-Universität zu Kiel.

Masahisa Watanabe, Kenshi Sakai, “NONLINEAR DYNAMICS OF THREE-DIMENSIONAL TRACTOR MODEL INCORPORATING BOUNCING PHENOMENON”, The 9th International Symposium on Machinery and Mechatronics for Agricultural and Biosystems Engineering, Jeju, Korea, May, 28-30, 2018.

Masahisa Watanabe, Kenshi Sakai,“Numerical Analysis of Tractor Accidents using Driving Simulator for Autonomous Driving Tractor”, The 3rd International Conference on Mechatronics Systems and Control Engineering, Nice, France, February 26-28, 2019.

Masahisa Watanabe, Kenshi Sakai (2019, July). Development of Tractor Bicycle Model with Ride Vibration. In 2019 ASABE Annual International Meeting (p. 1). American Society of Agricultural and Biological Engineers.

Masahisa Watanabe, Kenshi Sakai (2019, Sep.), "Investigation by Driving Simulation of Tractor Overturning Accidents Caused by Steering Instability", 13th CIGR VI Technical Symposium, Sapporo, Japan, September 3-6, 2019.

Masahisa Watanabe, Kenshi Sakai, "Stick Slip Vibration in Tractor Dynamics ",

NOLTA 2019, Kuala Lumpar, Malaysia, December, 2-6, 2019.

Masahisa Watanabe, Kenshi Sakai, (2020). Nonlinear Dynamics of a Bouncing Tractor in a Tractor Driving Simulator. In 2020 ASABE Annual International Virtual Meeting (p. 1). American Society of Agricultural and Biological Engineers.

1. Introduction

1.1. Research background

Accidents and injuries related to farm machinery are a globally important issue regarding farm safety and automation in agriculture. Fatal or deadly farm accidents are a serious safety problem. In the United States, 417 farmers and farm workers died from work-related injuries in 2016 (CDC Agricultural safety, 2018) while in Japan, 312 fatal farm accidents occurred in the same year ("Reports on fatal farm accidents," 2018).

Figure 1.1 shows fatalities in agriculture, construction, all industries, and traffic accidents from 1971 to 2017 (fatality report by MAFF, MHLW, NPA) in Japan. In the graph, the number of fatalities in 1971 is taken as 100%.

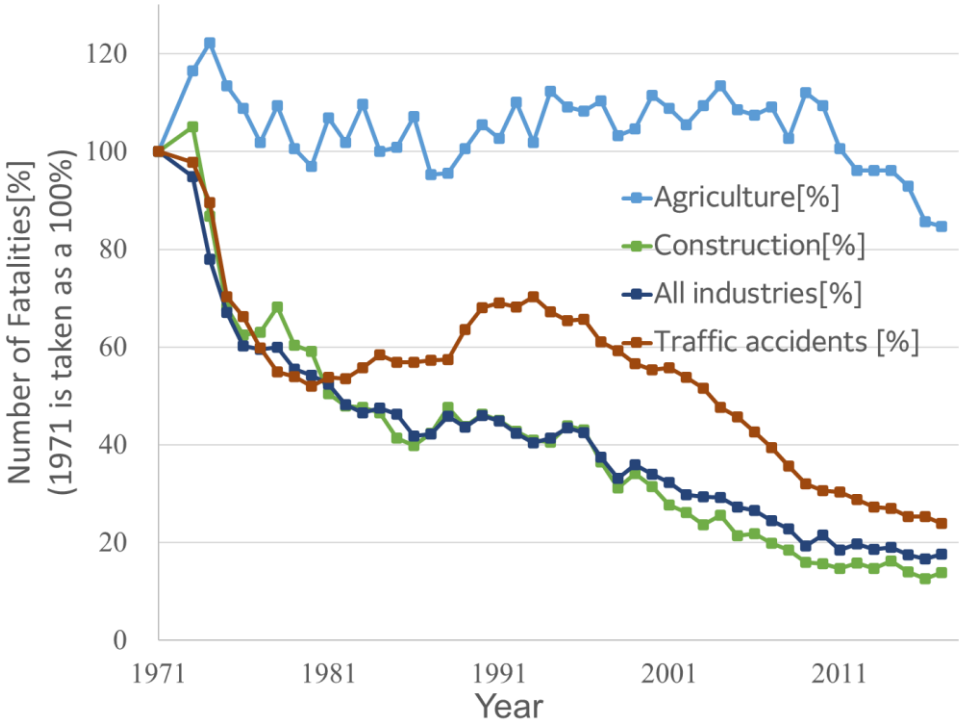

Figure 1.1 Fatalities in agriculture, construction, all industries, and traffic accidents (Graph is made from fatality report from Ministry of Agriculture, Forestry and

Fisheries, Ministry of Health, Labour and Welfare, National Police Agency).

Fatalities in agriculture have remained high for nearly half a century. Meanwhile, fatalities in construction, all industries, and traffic accidents have decreased considerably. Compared with other industries, the measure of farm safety is poor and needs improvement.

Among global fatal farm accidents, the overturning of a tractor is the leading cause of death for farmers (Abubakar, Ahmad, & Akande, 2010). Figure 1.2 shows a breakdown of fatal farm accidents in 2017 in Japan.

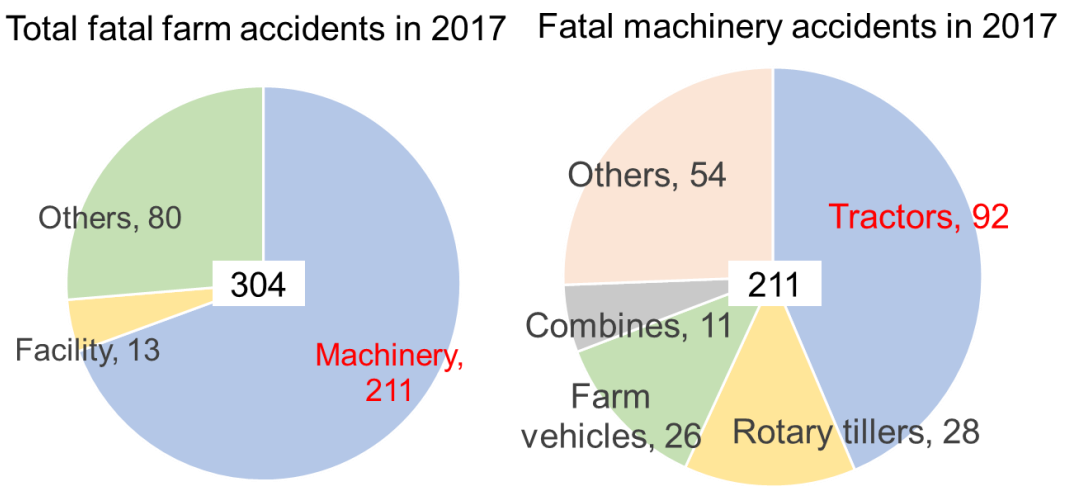

Figure 1.2 Breakdown of fatal farm accidents in 2017.

In Japan, there were 304 fatal farm accidents in 2017. Among them, there were 211 fatal machinery accidents, including 56 tractor overturning accidents (Report on fatal farm accidents, 2019). Tractor overturning not only threatens the lives and wellbeing of farmers, but is also a major obstruction to farm automation. It is therefore important to prevent tractor overturning accidents in pursuing farm safety and automation.

Many efforts have been made to address tractor overturning; e.g., passive safety

protection and active safety prevention. Passive safety protection helps operators stay alive and avoid injury whereas active safety prevention helps operators avoid the accident itself (Making Europe's roads safer for everyone, 2001). The protective rollover structure has been developed and investigated as a typical passive safety protection measure for many years to reduce injury to operators (Chisholm, 1979; Guzzomi, Rondelli, Guarnieri, Molari, Molari, 2009; Langley, Clarke, Marshall, Cryer, Alsop, 1997; Reynolds & Groves, 2000). Moreover, research on active safety protection has mainly focused on tractor dynamics (Raney, Liljedahl, Cohen, 1961; Matthews & Talamo, 1965; Stayner, Collins, Lines, 1984; Crolla, Horton, Stayner, 1990; Collins, 1991; Ahmed & Goupillon, 1997; Gunston, Rebelle, Griffin, 2004; Previati, Gobbi, Mastinu, 2007; Sun et al., 2018;) and the development of overturning evaluation indicators (Yisa, Terao, Noguchi, Kubota, 1998; Ahmadi, 2011; Li, Mitsuoka, Inoue, Okayasu, Hirai, 2015; Li et al., 2016). In addition to the abovementioned studies, active steering control, which is widely used for automobiles, has been applied to tractor dynamics to prevent overturning (Qin et al., 2019).

1.2. Research objective

As mentioned above, many safety studies have been conducted and various safety technologies have been developed to reduce the number of fatalities involving agricultural tractors. These investigations, mainly conducted in Europe and the United States, assumed a large tractor specialized for relatively flat upland fields. In contrast, farm operations in Japan are carried out using smaller tractors that are specifically designed for paddy fields in harsh terrain environments, where there are rough farm roads, slippery fields, steep passage slopes, and narrow inclined side paths. In these potentially

dangerous environments, violent vibrations often lead to serious accidents. In recent years, this has led to Japanese studies of accident topography (Aoyagi et al., 2016; Matsui et al., 2017), tractor lateral stability (Li et al., 2016), and the development of an algorithm that generates the road surface (Watanabe & Sakai, 2017). Excessive and violent vibrations frequently result in vertical jumping or bouncing and lateral sliding. These nonlinear phenomena are a source of abnormal behaviors of a tractor, such as excessive vibration and steering instability, and can lead to fatal overturning accidents. In addition to tractor overturning, the power hop phenomenon can result from these nonlinearities. Power hop is a well-known dynamic instability of a tractor during towing operations and reduces operational performance. Nonlinear dynamics are therefore an essential factor for determining dynamic tractor behaviors.

The present paper investigates the nonlinear dynamics of an agricultural tractor mainly adopting numerical analysis and driving simulation. The present research is divided into two main parts, namely the nonlinear modeling of typical tractor instability (Chapters 2, 3, and 4) and the development of a driving simulator for agricultural tractors (Chapters 5, 6, and 7). The paper is structured as follows. In Chapter 2, tractor jumping or bouncing is modeled as a nonlinear impact oscillation using bouncing-ball dynamics and parametric investigations are conducted to demonstrate nonlinear characteristics. In Chapter 3, the steering instability of a tractor is numerically investigated by modeling lateral sliding based on friction circle theory. In Chapter 4, a novel power hop model is developed by coupling three nonlinear elements, namely bouncing, a stick and slip process, and free play in the implement. Parametric investigations are conducted to validate the developed model. In Chapter 5, algorithms for generating the road profile are developed for a tractor driving simulator. In the algorithm development, the power spectrum density (PSD),

coherence function, and autoregressive (AR) model are used to represent typical characteristics of a farm road surface. In Chapter 6, a tractor driving simulator with a motion system is developed using CarSim®, MATLAB®/Simulink, and a shaking table offered by Solution Inc (Tokyo, Japan). Characteristic mechanisms of an agricultural tractor, such as the throttle lever and left and right brakes, are developed in simulator hardware and implemented on the MATLAB®/Simulink® platform. In Chapter 7, numerical experiments are conducted using the developed tractor driving simulator. The developed tractor driving simulator is applied to identify overturning scenarios. Numerical experiments are conducted using real accident cases surveyed by the Japanese government.

1.3.Literature review

1.3.1. General remarks

Tractors are multitasking vehicles with specialized engineering, and are important as farming equipment for ploughing and tilling. Tractor operations are conducted over different terrain and operating conditions, and the tractor dynamics and stability drastically vary under different operating conditions. When the tractor operates in a harsh environment, such as rough farm roads, steep passage slopes, and narrow inclined side paths, the dynamic and static stability of the tractor dramatically deteriorates and tractor rollover may occur when the tractor instability becomes severe. Tractor overturning reduces the work efficiency and safety of farm operations, and is not only a safety issue but can also be a major obstacle to autonomous tractor driving. Therefore, the tractor dynamics and stability in various environments have been extensively investigated to improve the operational performance and safety in agricultural operations.

Much effort has been put into formulating the tractor dynamics and evaluating the tractor stability. Mathematical modelling is the first step toward understanding and controlling the tractor dynamics and predicting and preventing fatal accidents. Thus far, many mathematical models of the tractor's dynamic behaviour with different degrees of freedom have been proposed for time domain simulations. Particularly, tractor dynamic modelling research has significantly advanced after computer simulation was introduced in the 1960s. To date, several stability indicators have been developed based on mathematical tractor models. Using the developed indicators, the dynamic and static tractor stability has been evaluated to predict abnormal behaviour such as overturning and side slipping. In addition to the mathematical modelling of tractors, the terrain environment or road profile has also been measured and modelled to clarify the tractor's dynamic behaviour.

Literature reviews on tractor dynamic modelling and stability analyses have already been published by several studies in the 1980s and 1990s (Kim & Rehkugler, 1987; Yisa & Terao, 1995; Prasad, Tewari, & Yadav, 1995). However, a critical review of recent of technological advancements and methods applied to tractor investigation has not yet been conducted. This paper reviews recent literature related to tractor dynamics and stability and discusses future research directions. The rest of this literature review is structured as follows. First, the tire forces are described and discussed as a major source of tractor dynamics. Then, road profile modelling and analysis are reviewed. In Section 1.3.4 various tractor dynamic models are reviewed in chronological order. In Section 1.3.5, various types of overturning and stability indicators are discussed. The last section presents the concluding remarks and discusses future research directions.

1.3.2. Tire forces

This section discusses the tire forces exerted on an agricultural tractor. The tire forces are external forces acting on the tire, and have substantial impact on the tractor's dynamics and stability. In each tire, the tire forces are generally divided into three mutually perpendicular forces, namely, the vertical, lateral, and longitudinal forces. Figure 1.3 shows the schematic diagram of the forces acting on the tire.

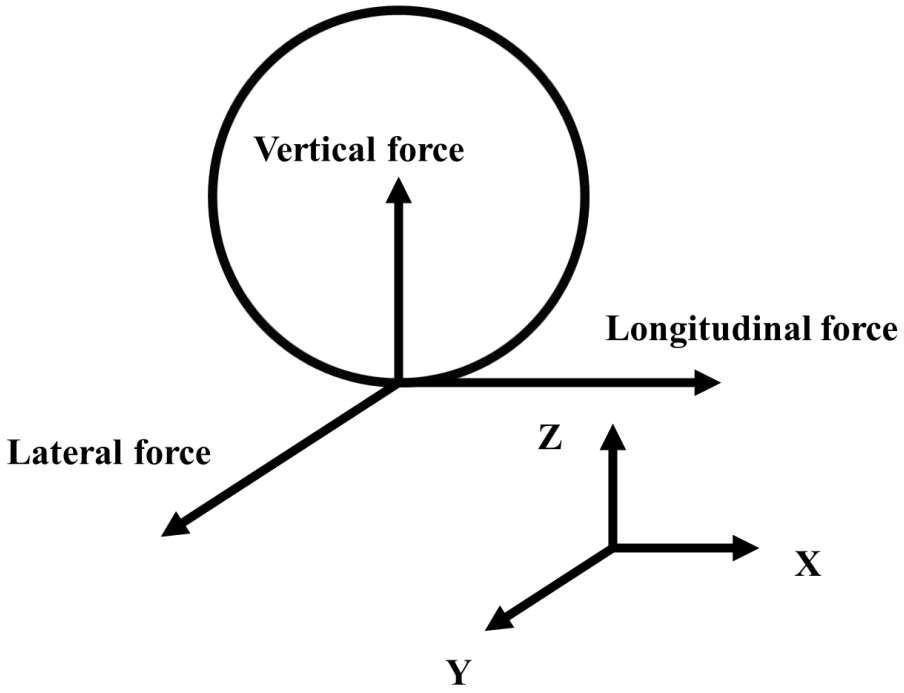

Figure 1.3 Schematic diagram of three mutually perpendicular forces acting on tire.

The longitudinal, lateral, and vertical forces act along the X, Y, and Z coordinate, respectively. As shown in Figure 1, the X-axis indicates the forward traveling direction, the Y-axis is transverse to the tire, and the Z-axis is perpendicular to the tire-ground contact point. The tire deflection in each direction is a major source of tire forces, which are produced by operator handling, drawbar pull, and road surface excitations.

The tire characteristics have been investigated to formulate the tire forces. The agricultural tire has generally been represented by three mutually perpendicular Kelvin-

Voigt units jointed in the vertical, lateral, and longitudinal directions. The Kelvin-Voigt model is a mathematical description of the tire's viscoelasticity and comprises a linear spring and damper in parallel as shown in Figure 1.4a. The Kelvin-Voigt description of tire viscoelasticity has been accepted and employed as a standard tractor tire model by many studies (Raney, Liljedahl, & Cohen, 1961; Stayner, Collins, & Lines, 1984). However, Crolla, Horton, and Stayner (1990) have demonstrated that a linear spring and damper in series, which is known as the Maxwell model, can improve the tire modelling accuracy in the longitudinal and lateral directions. The schematic diagram of the Maxwell model is shown in Figure 1.4b. Although the above-mentioned linear tire model satisfactorily represents the tractor behaviour, the nonlinear tire characteristics should be implemented in large deflection situations, which has not been extensively investigated.

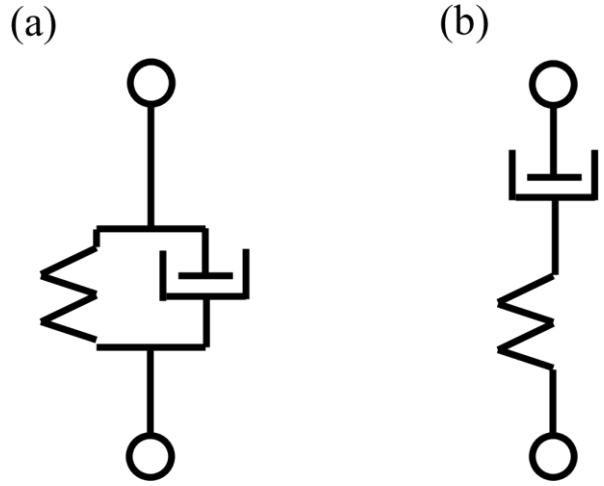

Figure 1.4 Models of tire characteristics: (a) Kelvin-Voigt model (linear spring and damper in parallel); (b) Maxwell model (linear spring and damper in series).

In addition to the modelling of tire characteristics, the tire-ground contact model should also be investigated to represent the tractor dynamics. Traditionally, the tire-

ground interaction has been modelled by point contact. The tire contacts a single point and the ground reaction force is applied to the tire through this point. The single-point contact model has been accepted as the standard model and can adequately represent the tractor dynamics, although some modifications have been made by various studies in agricultural tractor dynamics. The rigid tread band model was employed by Ahmed and Gouplion (1997). Homori, Sakai, Sasao, and Sibusawa (2003) modified the footprint tire model employed in general vehicle dynamics (Captain, Boghani, & Wormley, 1979) to better predict the tractor vibration.

Although many studies have investigated the agricultural tractor tire (Nguyen, Matsuo, Koumoto, & Inaba, 2009a, 2009b; Nguyen & Inaba, 2011; Šmerda & Čupera, 2010), its characteristics have not yet been fully elucidated and further investigation is needed. In the following subsections, the Kelvin-Voigt and single-point-contact tire models are reviewed as standard tire modelling approaches.

Vertical force

The vertical (or radial, normal) tire force is a tire force acting perpendicularly to the ground surface. This force is a major factor contributing to ride vibration and dynamic tractor behaviour. The vertical tire force is generally determined by the vertical tire deflection and deflection rate. The general formula for the vertical force is expressed as follows:

$$f_v = -k_v X - c_v \dot{X}. \tag{1.1}$$

Assuming that the road surface is not deformable, the tire deflection X and deflection

rate $\dot{X}$ can be calculated as follows:

$$X = x - d \tag{1.2}$$

$$\dot{X} = \dot{x} - \dot{d} \tag{1.3}$$

where x and d is vertical displacement of the wheel and the road surface input respectively. According to the above equations, the vertical force is caused by road surface excitations and determined by the vertical tire stiffness and damping coefficient. The identification of the tire stiffness and damping coefficient is difficult and thus presents a challenge to the modelling of the vertical force. These parameters are affected by the inflation pressure, tire type (for example, bias or radial tire), tractor's travel velocity, and tread conditions. Although substantial effort has been put into identifying the tire stiffness and tire damping coefficient (Taylor, Bashford, & Schrock, 2000), the existing modelling and identification approaches are not sufficient and a discrepancy between the model and the experimental results still exists.

Lateral force

The lateral or transverse force is a tire force acting perpendicularly to the traveling direction of the tire. The lateral forces are essential for deciding the handling behaviour of the vehicle. The lateral force generally depends on the vertical force, slip angle, tire inflation pressure, road surface, and camber angle. The tractive and the braking forces also contribute to the variation of the lateral force when the wheel is powered. Many studies have attempted to formulate a lateral force model using linear, cubic, and exponential functions. The linear expression of the lateral force is the most common

among the developed formulations.

$$Y = \mathrm{C_l} f_v = \mathrm{k}\beta f_v = \mathrm{C}_p \beta \tag{1.4}$$

where Y is the lateral force, $\mathrm{C_l}$ is the lateral force coefficient, k is constant, and β is the slip angle of the tire. If f_v is constant, k f_v is also constant and equal to the cornering coefficient $\mathrm{C_p}$. In this case, the lateral force or cornering force is linearly proportional to the slip angle of the tire. Identifying the lateral force coefficient and cornering power coefficient is as difficult as identifying the tire stiffness and damping coefficient (Umeda & Honami, 1975). When the vertical force and longitudinal force are present, the maximum lateral force is limited by the friction circle (Gillespie, 1992; Pacejka, 2005). The friction circle or ellipse is represented by the following inequality:

$$\sqrt{Y^2 + T^2} \leq \mu_s f_v. \tag{1.5}$$

The schematic diagram of the friction circle concept is shown in Figure 1.5.

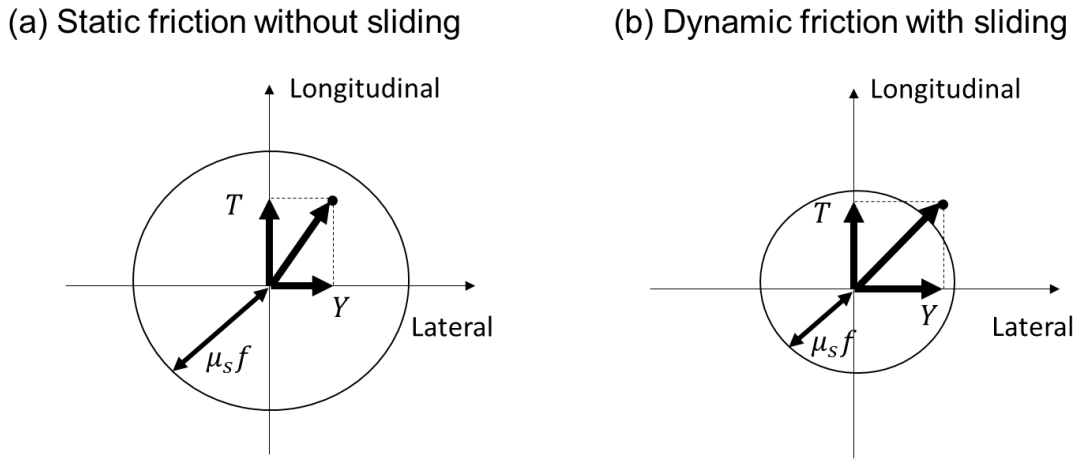

Figure 1.5 Schematic diagram of friction circle concept: (a) static friction state; (b)

dynamic friction state (Watanabe & Sakai, 2020).

Based on this inequality, the maximum cornering force under a certain vertical force and longitudinal force is expressed as follows:

$$Y_{\max} = \sqrt{\mu_s^2 f_v^2 - T^2}. \quad (1.6)$$

If the above inequality (6) is violated as shown in Figure 3b, lateral sliding will occur and may result in abnormal tractor behaviour (Watanabe & Sakai, 2020).

Longitudinal force

The longitudinal or circumferential force is a tire force acting parallel to the tractor's travelling direction. The longitudinal force plays a significant role in driving and towing performance. The longitudinal force is generally divided into the resistance force, tractive force, and braking force. Resistance forces act against the forward movement of the tractor. The main source of resistance is motion or rolling resistance and grade resistance caused by sloping terrain. The motion resistance or rolling resistance is a major resistance force during tractor operation. The motion resistance force R_m is calculated as follows:

$$R_m = \mu_m f_v, \quad (1.7)$$

where μ_m is the motion resistance coefficient, and f_v is a vertical force acting on the wheel. As expressed by Equation (1.7), the motion resistance force is linearly proportional to the vertical force on the wheel. The motion resistance coefficient varies under variable axial

loading, wheel slippage, and soil conditions.

Grade resistance is a resistance force exerted while the tractor runs on the slope. The grade resistance force R_g is calculated as follows:

$$R_g = \frac{l}{WB} f_v \sin\theta, \tag{1.8}$$

where l is the distance from the centre of gravity to the wheels, WB is the wheelbase of the tractor, and θ is the slope inclination angle.

The tractive force is a primary factor for drawbar pull, and is expressed as follows:

$$T = \mu_T f_v, \tag{1.9}$$

where μ_T is the coefficient of traction, and T is the traction force.

The coefficient of traction is calculated as follows (Wismer & Luth, 1974):

$$\mu_T = A(1 - e^{-Bs}), \tag{1.10}$$

where A is the maximum obtainable value of the coefficient, B is the determinant of the curve shape, and s is the travel reduction calculated as follows:

$$s = \frac{r\omega - V}{r\omega}, \tag{1.11}$$

where V is the travel velocity, r is the effective rolling radius of the tire, and ω is the

angular velocity.

1.3.3. Road profile

In this section, the road profile and roughness, which are major contributors to the tractor dynamics, are discussed. Agricultural tractors are exposed to excessive vibrations, which are caused by the road roughness or profile and result in equipment damages and dynamic disturbances. Unfavourable road conditions are a major contributor to the decrease of operational performance and increase of overturning risk. Indicators for the assessment of road roughness, such as the International Roughness Index (IRI; Sayers, 1990, 1995) and Power Spectrum Density (PSD; Andren, 2006), have been developed; PSD is used as the road roughness standard by the International Organization for Standardization (ISO; ISO 8608, 1995). The theoretical relationship between the PSD and the IRI of road roughness has been investigated by Sun (2001).

Agricultural tractors are generally operated off-road, such as on farm fields and roads. Therefore, road profile reconstruction is an important technique in tractor dynamics research. The measurement of the terrain environment has been extensively investigated to clarify the vehicle's dynamic disturbances caused by road profile excitations. Recently, road profile acquisition has become easier owing to the rapid advance of laser measurement technology such as LiDAR. Thus, accurate and high-resolution road profile data are available at high-speed and low-cost compared with previous measurement methods. By using recent road data, more precise and accurate road profile modelling can be achieved. Much effort has been put into modelling and generating the road profile as a vertical disturbance for vehicle dynamics simulation. The technique used for road profile modelling and analysis is presented in the following subsections.

Power spectrum density

In studies on vehicle dynamics, road profile analysis typically considers the PSD, which is used to investigate the signal characteristics in the frequency domain. The PSD is generally defined as follows:

$$P(f) = \int_{-\infty}^{\infty} C(\tau) e^{-j2\pi f\tau} df. \tag{1.12}$$

where $P(f)$ is the PSD and $C(\tau)$ is an autocorrelation function. Here, the PSD is defined as a Fourier transform of the autocorrelation function. This definition is also known as the Wiener–Khinchin theorem.

The road roughness has been standardized by ISO and its PSD is defined as follows (Ohmiya, 1990):

$$P(f) = P(f_0)\left(\frac{f}{f_0}\right)^{-W}, \tag{1.13}$$

where f_0=1/2π[c/m], W=2[-], f is the spatial frequency [c/m], and $P(f_0)$ [10^{-6}m^{2}c/m] is the PSD when f is f_0. In this ISO model, the PSD for high roughness is expressed as red or random walk noise. In the ISO standard, the road roughness is divided into Class A–H depending on the value of $P(f_0)$. Class A is the least rough surface and Class H is the roughest surface. Class A, Class D, and Class E correspond to highway road, unpaved road, and bad unpaved road, respectively (Yamakawa, 1976). Figure 4 shows the PSD standard of ISO as a log-log plot.

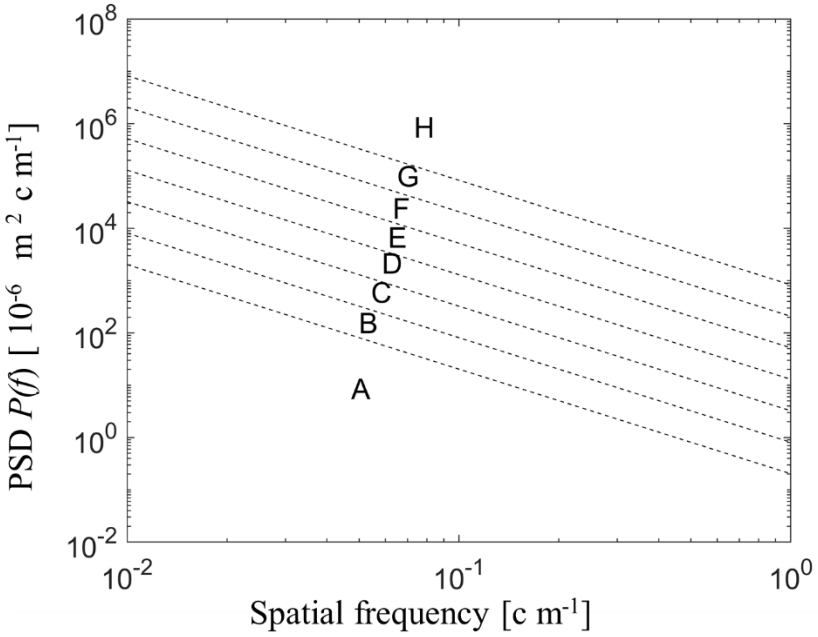

Figure 1.6 Power spectrum density standardized by International Organization for Standardization.

Recently, based on PSD analysis, random road profiles have been reconstructed using the wavelet transform (Hesami & McManus, 2010), Fourier transform surrogate, and autoregressive modelling (Watanabe & Sakai, 2017). Li et al. (2016) used a random road profile to assess the sensitivity of tractor parameters.

Coherence function

The road profile of a single wheel path can be modelled based only on PSD analysis. In the field, however, the left and right track are not identical. Thus, the road profiles of the two (left and right) wheel paths must be constructed based on the combination of the PSD and coherence function (Liu, Wang, Shan, & He, 2015). This subsection presents the modelling of the road profiles on the left and right wheel paths based on the coherence function.

Generally, the coherence function is used to investigate the correlation between two signals in the frequency domain, and is defined as follows:

$$r^2(f) = \frac{|P_{xy}(f)|^2}{P_{xx}(f)P_{yy}(f)}, \tag{1.14}$$

where $P_{xx}(f)$ is the PSD of $x(t)$, $P_{yy}(f)$ is the PSD of $y(t)$, and $P_{xy}(f)$ is the cross spectrum density between $x(t)$ and $y(t)$. The range of the coherence function is $0 \leqq r^2(f) \leqq 1$ and the correlation between the signals is proportional to the coherence function.

Based on the coherence function, the isotropic model (Usui, Tani, Shirai, & Horiguchi, 1990), filtered Poisson model (Xiang & Nakagiri, 1986), and exponential parametric model (Bogsjö, 2008) have been developed to reconstruct the left-right statistical relationship. Watanabe and Sakai (2017) combined the PSD with coherence analysis to generate a terrain environment that could be used in tractor driving simulations.

1.3.4. Dynamic models of agricultural tractors

In this section, the techniques and methods related to the dynamic modelling of agricultural tractors are discussed. Numerical simulation conducted using digital computers is one of the most effective approaches for elucidating the tractor dynamics and stability. Many tractor dynamic models have been developed for time-domain simulations. These models are particularly beneficial for predicting the tractor's dynamic responses to external disturbances and designing control algorithms to avoid overturning accidents. Parametric investigation using mathematical models is easier compared with physical experiments using actual tractors. Many conventional tractor models with various degrees of freedom have been developed. In tractor modelling, the tractor body

is considered to be rigid in three-dimensional space and generally has six degrees of freedom for translational and rotational motion, that is, longitudinal (X), lateral (Y), vertical (Z), pitch (γ), roll (α), and yaw (φ) motion.

General assumptions in dynamic tractor modelling

In the development of dynamic tractor models, several assumptions are made to simplify the complexity of actual tractor behaviour. The typical assumptions made in conventional linear modelling are listed below (Raney, Liljedahl, Cohen, 1961; Kim & Rehkugler, 1987; Yisa & Terao, 1995).

1) The tire is modelled as a Kelvin-Voigt unit, which is a linear spring and damper connected in parallel.
2) The tire maintains contact with the ground
3) The tire has single-point contact with the ground
4) The tractor body, frame, and axle are rigid bodies.
5) The tractor is symmetrical to a plane perpendicular to the rear axle that passes through the rear axle's midpoint.
6) The road surface is not deformable
7) Aerodynamics are ignored owing to the low operational speed

Most published studies on tractor model development have assumed the above conditions, which are highly idealized. For example, the tire characteristics can be nonlinear instead of linear, as in the case of the spring and damper. Additionally, soft soil can be deformable and the tire-ground interaction can be more complicated than single-point contact. To

extend the dynamic model by accounting for various ground-wheel interactions, several studies have not assumed the above-mentioned conditions.

Development of dynamic agricultural tractor models

In this section, the development of dynamic tractor models is extensively reviewed mostly in chronological order, from pioneering work to modern studies on tractor dynamics and stability. Several early tractor dynamic modelling studies using very simple tractor models were published in the 1960s. One of the earliest attempts to develop a dynamic model was made by Raney, Liljedahl, and Cohen (1961). The developed model was derived based on the Newtonian method and has three degrees of freedom: vertical, pitch, and roll motion. In their paper, the developed model was numerically solved using an analogue computer and the design parameters were evaluated. Matthews and Talamo (1965) developed a dynamic model with two degrees of freedom, that is, vertical and pitch motion, and applied it to ride vibration analysis. Goering and Buchle (1967) dealt with a large-amplitude problem to predict backward overturning. A tractor model with three degrees of freedom, that is, vertical, longitudinal, and pitch motion was developed by Shibata and Sakai (1979). In their study, the effect of the rear-mounted rotary tiller on the tractor dynamics was numerically investigated through computer simulations.

Subsequently, the above-mentioned simple models were extended to more complicated dynamic models with more degrees of freedoms based on the Lagrangian method, including lateral, yaw, and front axle motion. Pershing and Yoerger (1969) and Smith and Yoerger (1975) proposed dynamic models for the tractor transient response and variation in forward motion, respectively. Stayner, Collins, and Lines (1984) developed a tractor model with seven degrees of freedom, and Collins (1991) extended this model by

adding a rear-mounted implement to investigate the influence of loads in the tractor linkage on the tractor dynamics. Figure 1.7 shows Collins's model as a culmination of the linear tractor modelling in the 20th century.

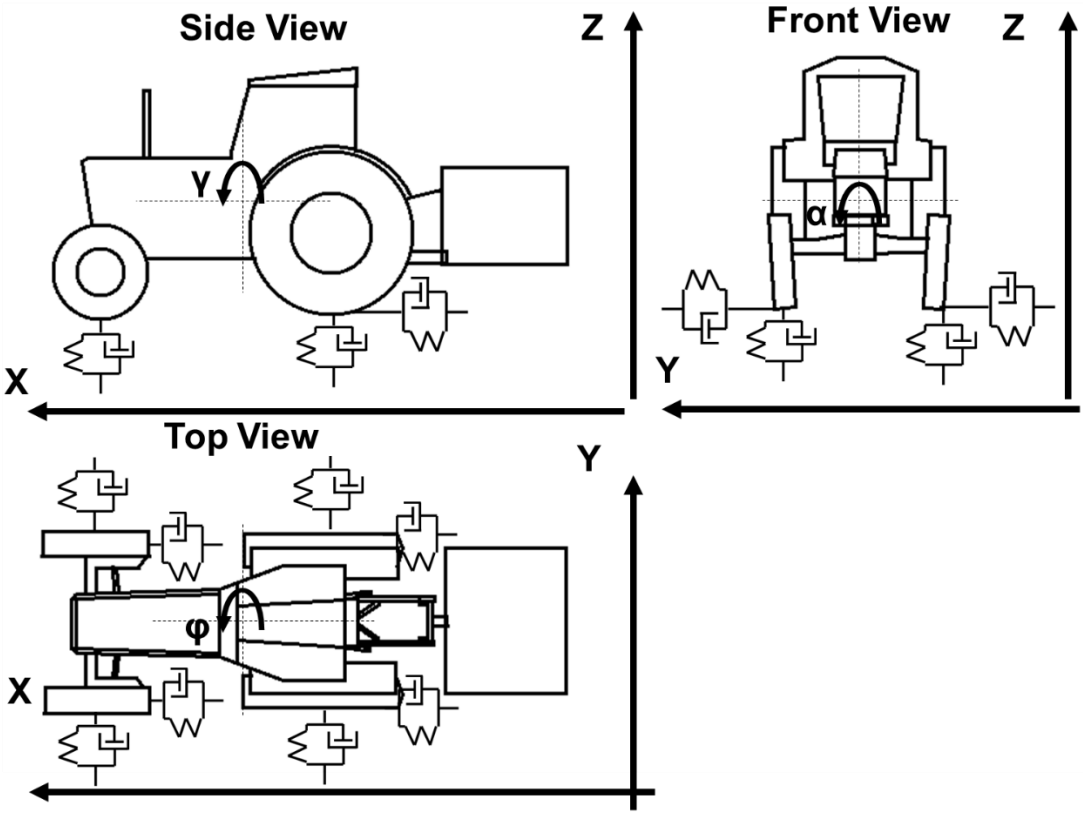

Figure 1.7 Liner tractor model with seven degrees of freedom and rear-mounted implement (Collins, 1991).

Since the 1980s, larger and higher-speed tractors have emerged to improve the operational efficiency, and there is growing demand for the suppression of excessive vibrations in these tractors. Therefore, tractor suspension systems that are capable of attenuating excessive vibrations have been extensively investigated in the field of dynamic tractor modelling (Claar, Sheth, Buchele, & Marley, 1982). Hanson (1995, 1996, 2002) conducted extensive studies on cab and full axial suspension systems to improve

the vibration damping capacity.

Excessive vibrations cause nonlinearities in the tractor dynamics, such as collision, jumping, and sliding. These nonlinearities do not necessarily satisfy all of the general assumptions discussed above. Thus, many nonlinear tractor models have been developed to more accurately describe the tractor behaviour. The earliest studies on nonlinear tractor dynamics investigated the impact dynamics in the vibratory subsoiler (Sakai & Aihara, 1994, 1999) and rear-mounted implement (Bukta, Sakai, Sasao, & Shibusawa, 1998). The jumping or bouncing tractor is also a source of impact dynamics and has been investigated by several studies (Sakai, 1999; Sakai, Sasao, Shibusawa, & Bukta, 2000; Garciano, Sakai, & Torisu, 2005). The stick slip vibrations caused by tire-soil interaction have been modelled to formulate the power hop dynamics (Sakai, Sasao, & Shibusawa, 1999; Volfson & Estrin, 1983; Volfson, 1999). Figure 1.8 shows Sakai's bouncing tractor model as a typical nonlinear tractor modelling.

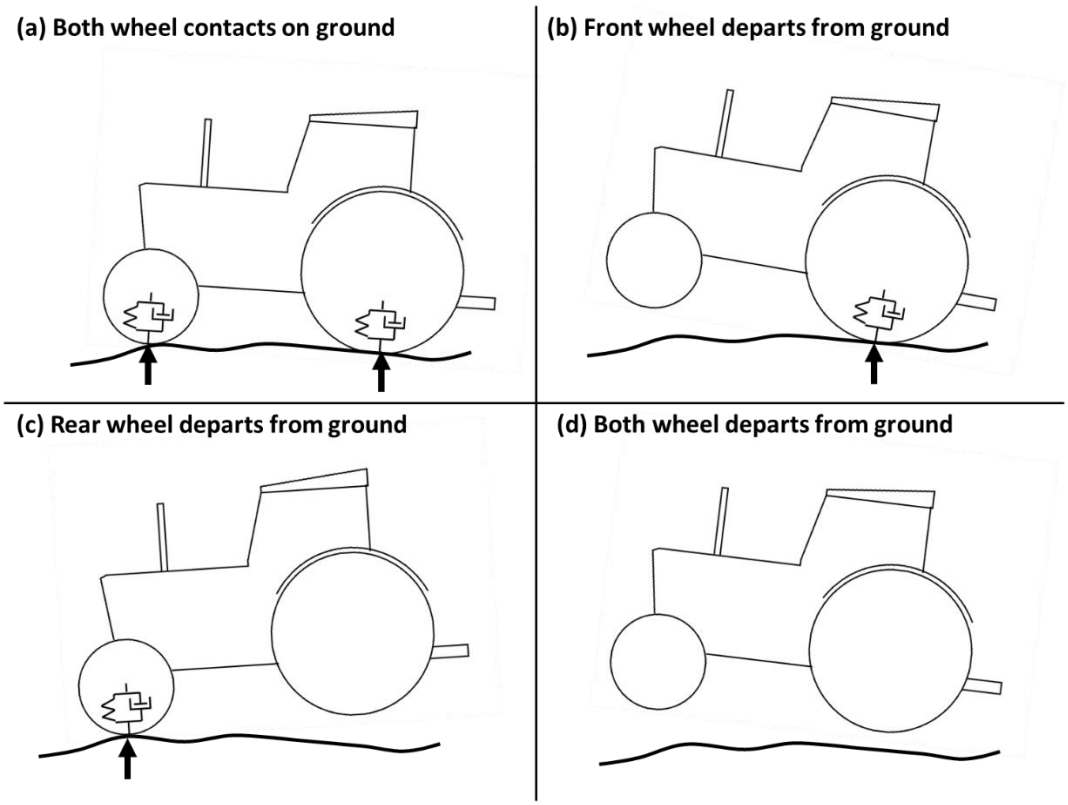

Figure 1.8 Nonlinear bouncing tractor model (Sakai, 1999)

As described above, many tractor dynamic models had been developed up to the end of the 20th century, including simple and complex models and nonlinear models. Recently, increased attention on farm safety has led to dynamic tractor modelling for the prevention of fatal farm accidents such as overturning and rollover. Li, Mitsuoka, Inoue, Okayasu, and Hirai (2015) developed a 3D tractor model and stability indicator for Phase I overturning. Aoyagi et al. (2017) conducted numerical simulations by considering surveyed topography where actual overturning accidents had previously occurred. Watanabe and Sakai (2019, 2020a) conducted numerical simulations by considering a nonlinear model on a steep passage slope, and demonstrated the manner in which nonlinearities can cause overturning accidents. Sun, Nakashima, Shimizu, Miyasaka, and Ohdoi (2019) used a physics engine to predict tractor overturning and compared

numerical and experimental results. In addition to the analysis of tractor overturning behaviour, prevention methods have also been developed. By conducting numerical simulations, Previati, Gobbi, and Mastinu (2014) demonstrated that front-axle suspension can suppress the occurrence of rollover. The active steering control technique, which is widely used in automotive engineering, has been used to prevent overturning accidents (Qin et al., 2019).

In addition to the above-mentioned ride vibration models, lateral dynamic models have also been developed to describe the tractor's turning behaviour and tractor-trailer combinations. A simple bicycle model is generally used for automatic guidance (Zhang & Qiu, 2004), while more detained four-wheel-drive and four-wheel-steering models have been developed to evaluate the tractor's turning performance (Itoh, Oida, Yamazaki, 1999). Karkee and Steward (2010a, 2010b, 2011) developed and validated a tractor and single-axle towed implement model for accurate automatic guidance. A nonlinear tractor-trailer model, which includes longitudinal and yaw dynamics, has been developed for tractor automation (Kayacan, Kayacan, Ramon, & Saeys, 2014).

Table 1.1 summarizes the main development of tractor dynamic models over several decades.

Table 1.1 Main development of dynamic tractor models.

Reference	Degrees of freedom	Model description
Raney Liljedahl, and Cohen (1961)	3	Model for response to disturbance excitation.
Matthews and Talamo (1965)	2	Model for operator ride comfort.
Simith and Yoerger (1975)	7	Model for transient response and variation in forwarding motion caused by periodic

		drawbar pull
Shitaba and Sakai (1979)	3	Model for small tractor equipped with rotary tiller.
Claar, Sheth, Buchele, Marley (1982)	-	Model for tractor chassis suspension system using Integrated Mechanics Programing (IMP)
Stayner, Collins, and Lines (1984)	8	Model for tractor ride vibrations considering longitudinal, lateral, and vertical direction.
Collins (1991)	8	Extended model of Stayner et al. (1984) incorporating implement.
Sakai (1999)	2	Nonlinear model considering jumping effects when wheel of tractor lose contact with ground.
Hanson (2002)	7	Model for tractor axial suspension systems.
Zhang and Qiu (2004)	2	Bicycle model for path search algorithm in tractor automatic navigation.
Li, Mitsuoka, Inoue, Okayasu, Hirai (2015)	5	Model for response to sloping embankment to assess Phase I overturning.
Qin et al. (2019)	3	Model for developing active steering control to avoid overturing.

1.3.5. Patterns of tractor overturning

When tractor stability is lost owing to harsh terrain or inappropriate handling, tractor overturning may occur and result in fatal accidents. Tractor overturning has been a major cause of farming-related deaths since the beginning of mechanized agriculture.

Theoretically, tractor overturning behaviour can be divided into sideways, forward, and rearward overturning. Forward overturning is theoretically possible but practically very rare and has not received much attention by previous studies. However, sideways overturning and rearward overturning are major causes of fatal farming accidents and have been extensively investigated. In this section, two types of tractor overturning,

namely, sideways and rearward overturning, are reviewed and the development of overturning models and stability indicators is discussed.

Sideways overturning

Sideways overturning or lateral rollover is the tractor overturning accident that most commonly results in fatal farming accidents. Many studies have been conducted to clarify the mechanics of sideways overturning, which typically involves two processes. Initially, the tractor tips or tilts sideways about the axis connecting the pivoted hinge point of the front axle and the ground-contact point of the rear wheel. Next, the entire tractor starts to rotate about the axis of the ground-contact point of the front and rear wheels when the front axle reaches the rotation stop (Smith, Perumpral, & Liljedahl, 1974). Sideways overturning generally comprises two phases, that is, Phase I and Phase II overturning. Initially, the rear wheel of the tractor on the uphill loses contact with the ground. This phenomenon is called Phase I overturning. During Phase II overturning, the front and rear wheels lose contact with the ground simultaneously (Nguyen, Harada, Takimoto, & Shimomoto, 2020).

The earliest tractor overturning modelling studies were conducted in the 1970s (Smith, Perumpral, & Liljedahl, 1974; Larson, Smith, & Liljedahl, 1976; Davis & Rehkugler, 1974a). The developed handling and sideway overturning models can simulate and predict the actual overturning behaviour on sloping terrain. Chisholm (1979a, 1979b) developed a dynamic mathematical model to simulate overturning on a downward slope, and validated the developed model by conducting field experiments. Rehkugler (1980) developed a four-wheel drive, formulated a steer tractor model, and conducted an overturning simulation on sloping embankments. Yisa, Terao, Noguchi, and Kubota

(1998) developed a dynamic overturning model for tractor-implement combinations and identified the stability regions to design appropriate operational parameters. Recently, mathematical models for Phase I overturning were developed by Baker & Guzzomi (2013) and Guzzomi (2012). Franceschetti, Lenain, and Rondelli (2014) compared the results obtained by the lateral overturning model to those obtained by an actual overturning experiment.

Rearward overturning

Although rearward or backward overturning is relatively rare compared with sideways overturning, much effort has been put into preventing rearward overturning because it has a high fatality rate. Goering and Buchle (1967) conducted one of the first studies for predicting rearward overturning and developed a dynamic model. The common assumption in rearward overturning modelling is that the tractor rotates only about the axis passing through the tractor's centre of gravity (Mitchell, Zachariah, & Liljedahl, 1972). However, Smith and Liljedahl (1972) have reported that the rearward overturning process also comprises two stages, similarly to sideways overturning. Initially, all wheels of the tractor maintain contact with the ground. In this initial stage, tilting occurs about the axis passing through the tractor's centre of gravity. Subsequently, the front wheel of the tractor leaves the ground and the tractor frame rotates about the rear wheel axle. The second stage of overturning is an actual overturning process. The influence of the drawbar position on the rearward overturning stability has been investigated by Smith (1984).

Tractor stability indicators

In addition to the classification of tractor overturning processes, stability criteria or indicators for tractor overturning have been developed by many studies to evaluate the tractor stability during farming operations. These indicators can be used to predict tractor overturning and improve tractor stability.

Generally, tractor stability can be classified into dynamic and static stability. Static stability mainly depends on the tractor position, such as the pitch, roll, and yaw angle, and tractor dimensions, such as the centre of gravity, wheelbase, and track width. Static stability indicators can be used to assess the tractor behaviour when the tractor is stationary or performs steady-state operations. However, dynamic stability indicators can assess the tractor stability in more realistic operational scenarios, such as road traveling and ploughing, compared with static indicators. Dynamic stability indicators are mainly based on dynamic factors, such as the tractor's travel velocity, pitch rate, roll rate, and yaw rate.

The lateral stability or sideways overturning stability can be assessed by considering the roll angle and rate, while the longitudinal stability or rearward overturning stability can be assessed by the pitch angle and rate. The typical static stability indicators for sideways and rearward overturning are described below (Liu & Ayers, 1998, 1999).

$$\mathrm{SI}_{\mathrm{static}} = \left(1 - \frac{U}{U_{cr}}\right) * 100, \tag{1.15}$$

where SI_{static}, U, and U_{cr} are the static stability indicator for sideways and rearward overturning, state variable (roll or pitch angle), and critical state variable, respectively. Typically, the dynamic indicator considers the angular rate as follows:

$$\mathrm{SI}_{\mathrm{dynamic}} = \left(1 - \frac{U}{U_{cr}}\right)\left(1 - \left(\frac{\dot{U}}{\dot{U}_{cr}}\right)^2\right) * 100, \tag{1.16}$$

Liu and Koc (2013) modified the above-mentioned dynamic indicators with consideration to a combination of sideways and rearward stability, as follows:

$$\mathrm{SI}_{\mathrm{dynamic}} = \left(1 - \sqrt{\left(\frac{\phi}{\phi_{cr}}\right)^2 + \left(\frac{\theta}{\theta_{cr}}\right)^2}\right)\left(1 - \sqrt{\left(\frac{\dot{\phi}}{\dot{\phi}_{cr}}\right)^4 + \left(\frac{\dot{\theta}}{\dot{\theta}_{cr}}\right)^4}\right) * 100, \tag{1.17}$$

where φ, θ, φ_{cr}, and θ_{cr} are the roll, pitch, critical roll, and critical pitch, respectively. In the above-mentioned indicator, a value of 100% indicates the highest stability while a value of 0% indicates the lowest stability. Ahmadi (2011) developed a stability indicator for overturning and skid with consideration to the friction coefficient. These stability indicators have been applied to automatic controls and robotic tractors to monitor the tractor's operational stability (Mashadi & Nasrolahi, 2009; Vidoni, Bietresato, Gasparetto, & Mazzetto, 2015).

The above-mentioned stability indicators are based on the vehicle position and rate. Recently, dynamic stability indicators based on the wheel forces have been developed by several studies. Li, Mitsuoka, Inoue, Okayasu, and Hirai (2015) have developed new stability indicators based on the wheel forces, as follows:

$$i_o = \frac{F_{z,i}}{F_{s,i}}, \tag{1.18}$$

$$i_s = 1 - \frac{F_{\frac{f}{r}}}{F_{\frac{f}{limit}}}, \tag{1.19}$$

where i_o and i_s are stability indicators for Phase I overturning and lateral skidding, respectively; $F_{z,i}$, $F_{s,i}$, $F_{f/r}$, and $F_{f/limit}$ are the dynamic vertical force on the wheel during operation, static vertical force on the wheel, lateral friction force acting on the rear tire, and maximum static friction force acting on the rear tire, respectively. Watanabe and Sakai (2020) applied the following grip margin concept, which is typically used in automotive dynamics:

$$\varepsilon_i = 1 - \frac{\sqrt{T_i^2 + Y_i^2}}{\mu_s f_i}, \tag{1.20}$$

where ε_i, T_i, Y_i, and f_i are the grip margin on the wheel, traction force on the wheel, cornering force on the wheel, and vertical force on the wheel, respectively. According to the above-mentioned studies, the wheel-force-based indicators can also be used to evaluate the tractor stability. The above-mentioned stability indicators are summarized in Table 1.2.

Table 1.2 Summary of developed stability indicators.

Reference	Equation	Indicator description
Liu and Ayers (1998, 1999)	$\mathrm{SI}_{\mathrm{static}} = \left(1 - \frac{U}{U_{cr}}\right) * 100$	Indicator for static stability. U can be roll or pitch for sideways or rearward overturning respectively.
Liu and Ayers (1998, 1999)	$\mathrm{SI}_{\mathrm{dynamic}} = \left(1 - \frac{U}{U_{cr}}\right)\left(1 - \left(\frac{\dot{U}}{\dot{U}_{cr}}\right)^2\right) * 100$	Indicator for dynamic stability. U can be roll or pitch for sideways or rearward overturning

		respectively.
Liu and Koc (2013)	$\mathrm{SI}_{\mathrm{dynamic}} = \left(1 - \sqrt{\left(\frac{\phi}{\phi_{cr}}\right)^2 + \left(\frac{\theta}{\theta_{cr}}\right)^2}\right)\left(1 - \sqrt{\left(\frac{\dot{\phi}}{\dot{\phi}_{cr}}\right)^4 + \left(\frac{\dot{\theta}}{\dot{\theta}_{cr}}\right)^4}\right) * 100$	Indicator for dynamic stability. Sideways and rearward overturing can be assessed simultaneously.
Li, Mitsuoka, Inoue, Okayasu, Hirai (2015)	$i_o = \frac{F_{z,i}}{F_{s,i}}$	Indicator for dynamic overturing stability based on vertical wheel force.
Li, Mitsuoka, Inoue, Okayasu, Hirai (2015)	$i_s = 1 - \frac{F_{\frac{f}{r}}}{F_{\frac{f}{limit}}}$	Indicator for dynamic skidding based on friction force.
Watanabe and Sakai (2020)	$\varepsilon_{\mathrm{i}} = 1 - \frac{\sqrt{T_i^2 + Y_i^2}}{\mu_s f_i}$	Indicator for dynamic steering stability based on friction circle theory.

1.3.6. Summary

Tractor dynamics and stability have been investigated for more than 50 years. Throughout the history of relevant research, theoretical tractor dynamic models and stability indicators have been developed and validated by field experiments or scale models (Yisa & Terao, 1999; Davis & Rehkugler, 1974). These research contributions have influenced tractor design and development, and improved the operational efficiency and safety of tractor operations. The developed mathematical models are useful for autonomous tractor driving and the prevention of overturning accidents. The directions of future research on tractor dynamics and stability are outlined below.

Although massive validation experiments pertinent to tractor models have been carried out, more precise and comprehensive measurements of the model parameters are necessary in future investigations. Parameter measurements have been conducted with

regard to the tire characteristics and ground-wheel interactions. However, the data obtained thus far are not adequate for accurately modelling the dynamic behaviour of tractors. With regard to the tire characteristics, the measurement of the lateral and longitudinal stiffness is relatively inferior compared with the measurement of vertical stiffness. The lateral dynamics, such as the cornering characteristics, must also be investigated to prevent accidents and develop autonomous driving for tractors. In addition to the tractor specifications, off-road profile surveying and analysis are needed to identify the topographies of overturning accidents.

Based on the above-mentioned contributions, many passive safety measures, such as the rollover protective structure (ROPS), have been developed to protect the tractor operator during overturning and reduce operator injuries caused by accidents (Reynolds & Groves, 2000; Guzzomi, Rondelli, Guarnieri, Molari, & Molari, 2009; Khorsandi, Ayers, & Truster, 2017; Ayers, Khorsandi, Wang, & Araujo, 2018). However, passive safety measures cannot prevent overturning or rollover; therefore, active safety measures must be developed by future studies. Active safety technology has mainly been developed in the automotive industry, such as the Anti-lock Brake System (ABS), Traction Control System (TCS), and Electronic Stability Control (ESC). In tractor engineering, active steering control has been numerically investigated as the initial stage of active safety control (Qin et al, 2019). In automotive engineering, many of the above-mentioned electronic controls have been developed by virtual test driving using driving simulators. Hence, a driving simulator is a good platform for safety and autonomous driving studies. Although several simulators have recently been developed (Karimi, Mann, & Ehsani, 2008; Lleras et al., 2016; Gonzalez et al., 2017; Han et al., 2019; Watanabe & Sakai, 2019b), the investigation and development of tractor driving simulators in the field of

tractor engineering is still in the early stage. By using a tractor driving simulator, studies can identify overturning scenarios and develop control methods to avoid severe accidents. Furthermore, tractor driving simulators will benefit the practical implementation of robot tractors in farm fields (Noguchi, Reid, Zhang, Will, & Ishii, 1998; Takai, Barawid, Ishii, & Noguchi, 2010; Yang & Noguchi, 2012; Zhang & Noguchi, 2017). The development of tractor driving simulators and active control technology are possible future directions for research on tractor dynamics and stability as well as the development of autonomous tractor driving.

2 Impact dynamics of bouncing tractor model

2.1. Introduction

In Japan, small tractors specially developed for paddy fields are used in the harsh environments, such as rough farm roads, steep passage slopes, and narrow inclined side paths. These terrain environments can lead to excessive oscillations and sudden sideslips. The violent vibrations of a tractor can lead to separation of the wheels from the supporting ground. If the front wheel loses the contact with the ground, then the steering system cannot perform properly. Furthermore, if the rear wheel loses the contact with the ground, then the lack of the lateral resistant force of the wheel can cause a sudden sideslip of the tractor. This jumping and hopping phenomenon is called “bouncing.” Bouncing is a typical nonlinear impact dynamics, which is equivalent to bouncing ball (Holmes, 1982; Moon & Shaw, 1983; Luck & Mehta, 1993; Luo & Han., 1996; Gilet, Vandewalle & Dorbolo, 2009; Hubert, Ludewig, Dorbolo & Vandewalle, 2014) and can cause excessive vibration, sideslip and decline of steering performance which can lead to overturning. In Japan, bouncing tractor has been studied in terms of nonlinear dynamics and chaos theory (Sakai, 1999; Sakai, Sasao, Shibusawa, & Bukta, 2000; Garciano, Torisu, Takeda & Sakai, 2002; Garciano, Sakai & Torisu, 2005; Watanabe, Bauerdick, Sakai & Bernhardt, 2018). These studies mainly investigated the theoretical aspects of a nonlinear bouncing tractor using Lyapunov exponent, Poincaré section and a bifurcation diagram. However, the nonlinear dynamics of a bouncing tractor in a practical situation have not been investigated to explain one of the possible cause of tractor overturning.

Many tractor overturnings occur on the steep inclined surfaces or slopes that connect a paddy field to a farm road. Although the maximum allowable slope angle of a passage

slope permitted by the Japanese government in a land consolidation project is 18°, it has been reported (Kimura, Chino, Arita & Seto, 1991) that there are passage slopes with slopes > 18°. When a tractor traverses these steep passage slopes, bouncing can become serious because the vertical load on axle become zero.

The objective of the present chapter was to analyse the impact dynamics model of the nonlinear bouncing tractor on a steep passage slope using numerical simulation. The paper is structured as follows: First, the model of the bouncing tractor is presented basically following Sakai's model (1999). However, some modification of the model are necessary to implement the numerical process of bouncing. This technical detail is presented in the Appendix. Next, a frequency response analysis and numerical experiments of the tractor running on passage slope were conducted. Discontinuous response, which is typical characteristics of nonlinear dynamics was observed both in the frequency response and numerical experiments.

2.2. Mathematical model

2.2.1. Motion equations of tractor with two degrees of freedom

Figure 2.1 shows the schematic diagram of the two-dimensional tractor model.

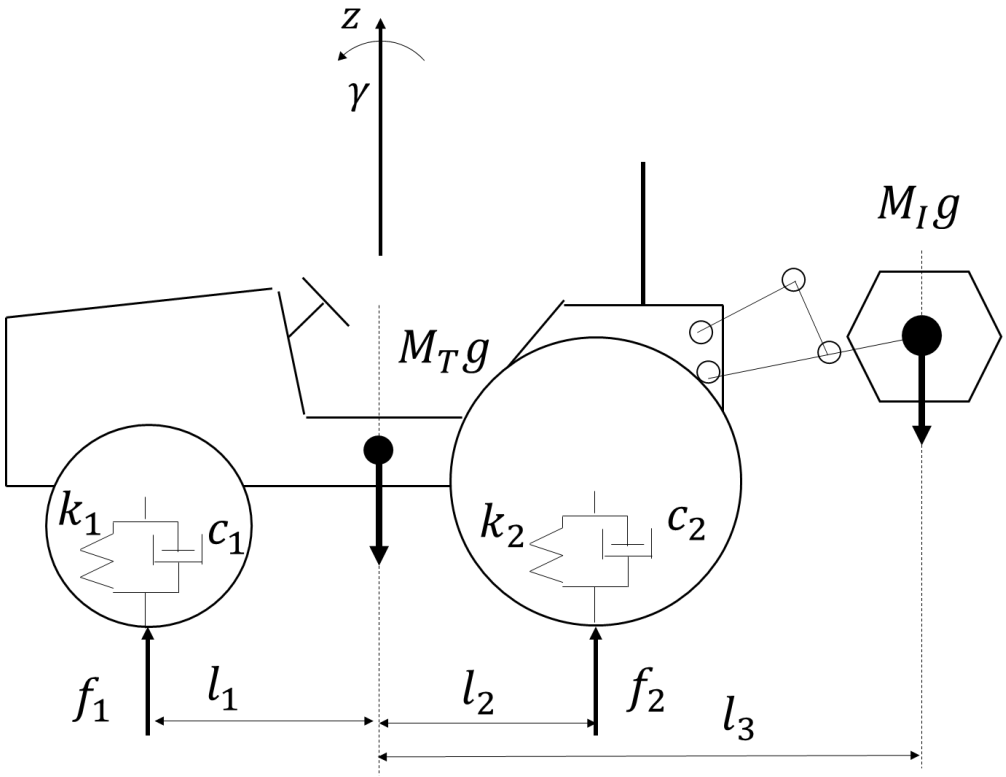

Figure 2.1Schematic diagram of the two-dimensional tractor model.

The model has two degrees of freedom, that is, vertical motion *z* and pitch motion γ, and is equipped with an implement. The wheel characteristics are represented by Kelvin–Voigt units as a linear spring and damper in parallel. The following equations of motion (Homori, Sakai, Sasao & Shibusawa, 2003) are derived by applying the force balance analysis to the tractor model:

$$(M_T + M_I)\ddot{z} = f_1 + f_2 - (M_T + M_I)g \tag{2.1}$$

$$\left(I_{yy} + l_3^2 M_I\right)\ddot{\gamma} = l_2 f_2 - l_1 f_1, \tag{2.2}$$

where a dot indicates differentiation with respect to time *t*, M_T is the mass of the tractor body, M_I is the mass of the implement, l_1 is the distance between the centre of gravity

(C.G.) of the tractor and the front wheel, l_2 is the distance between C.G. of the tractor and the rear wheel, l_3 is the distance between C.G. of the tractor and the implement, I_{yy} is the pitch axis moment of inertia, f_1 is the vertical load on front axle, f_2 is the vertical load on rear axle, and g is gravitational acceleration. The dynamic loads, f_1 and f_2, are described as follows:

$$f_1 = -k_1(z_1 - d_1) - c_1(\dot{z}_1 - \dot{d}_1) \tag{2.3}$$

$$f_2 = -k_2(z_2 - d_2) - c_2(\dot{z}_2 - \dot{d}_2), \tag{2.4}$$

where k_1 and k_2 are the stiffness of the front and rear wheels, respectively, c_1 and c_2 are the damping coefficients of the front and rear wheels, respectively, z_1 is the displacement of the front wheel, z_2 is the displacement of the rear wheel, d_1 is the front road elevation, and d_2 is the rear road elevation. The displacements of the wheels are described as follows:

$$z_1 = z + (l_1 - l_3 \frac{M_I}{M_T + M_I})\gamma \tag{2.5}$$

$$z_2 = z - (l_1 - l_3 \frac{M_I}{M_T + M_I})\gamma, \tag{2.6}$$

2.2.2. Modelling of bouncing process

The vertical loads on axles can become small and reduce to zero over the rough road and a steep passage slope. In that case, the wheel departs from the ground. If the front wheel departs from the ground, the tractor becomes in a “wheelie” state. If the front and rear wheel depart simultaneously from the ground, the tractor is in a “jump “state. Figure 2.2 is a schematic diagram of a bouncing tractor.

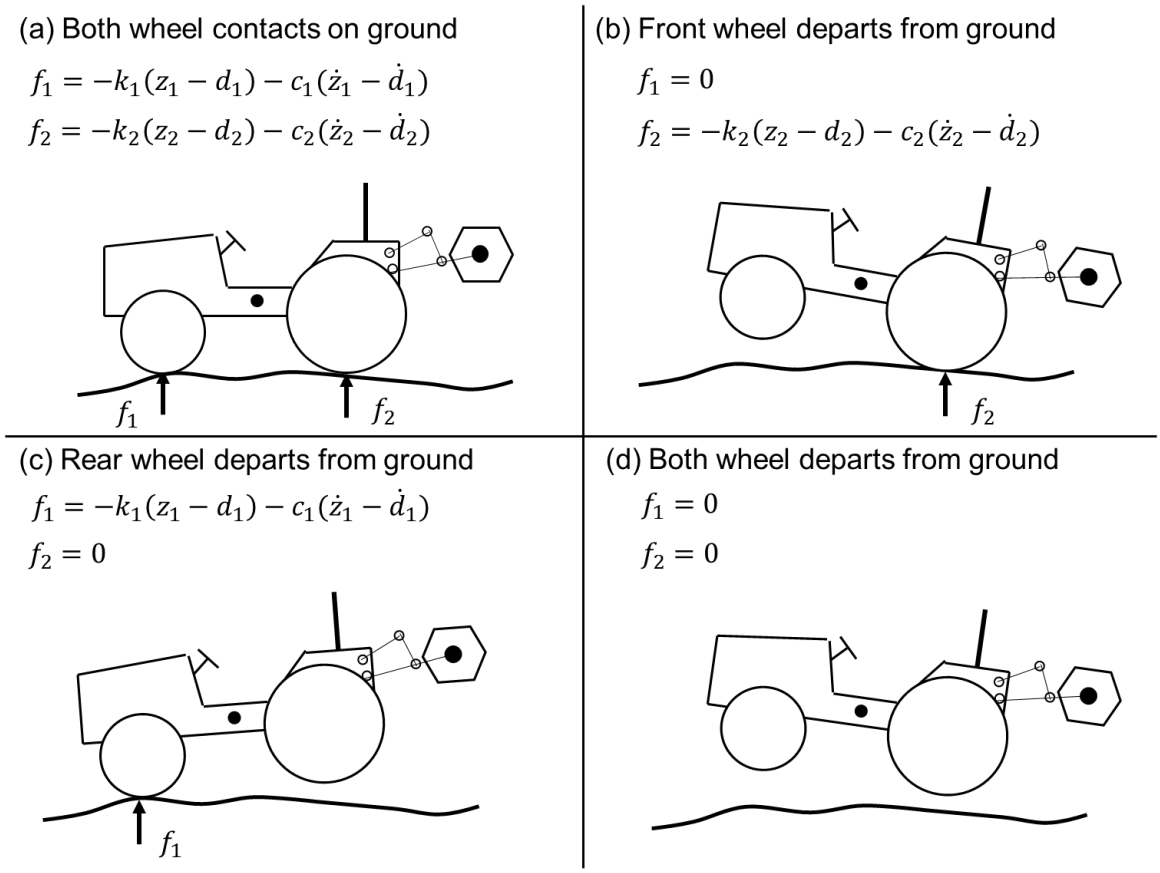

Figure 2.2 Schematic diagram of bouncing tractor; (a) Both wheels remain on ground, (b) Front wheel departs from the ground and rear wheel remains on ground (Wheelie state), (c) Front wheel remains on ground and rear wheel departs from the ground, (d) Both wheels depart from the ground (Jump state).

A bouncing tractor is an example of typical nonlinear dynamics and is equivalent to "bouncing ball" dynamics. Using conventional calculation formulas for vertical loads on axles given by Eqs. (2.3) and (2.4) in this type of situation become negative, which is physically an unrealistic value. In a real situation, the vertical loads on axles should be held at zero when wheels depart from the ground. Sakai (1999) proposed the new definition of vertical loads based on a "bouncing ball" model as follows:

$$f_1(t) =$$

$$\begin{cases} -k_1(z_1 - d_1) - c_1(\dot{z}_1 - \dot{d}_1), & \text{when front wheel is in contact with the ground} \\ 0, & \text{when front wheel departs from the ground} \end{cases} \quad (2.7)$$

$$f_2(t) =$$

$$\begin{cases} -k_2(z_2 - d_2) - c_2(\dot{z}_2 - \dot{d}_2), & \text{when rear wheel is in contact with the ground} \\ 0, & \text{when rear wheel departs from the ground} \end{cases} \quad (2.8)$$

The vertical load on the axle is equal to $-k_i(z_i - d_i) - c_i(\dot{z}_i - \dot{d}_i)$ when the wheel is in contact with the ground. By contrast, when the wheel departs from the ground the vertical load on the axle is set to zero. This switching expression is a piecewise linear model which is inherently nonlinear and beneficial for representing the essential aspects of the bouncing tractor dynamics. In the numerical implementation of this bouncing process into various tyre-road interactions in farm land, it is necessary to consider an intermediate state between contact with and departing from the ground. To expand the bouncing model to higher degree of freedom for developing tractor driving simulators, this improvement becomes not trivial. The technical detail of numerical implementation for bouncing is described in the following.

The detailed implementation of the numerical process of the bouncing tractor used in the paper is presented. In addition to the contact and departure state of the wheel, an intermediate state should be considered to implement the numerical calculation of bouncing although the previous study by Sakai (1999) did not mention it explicitly. Therefore, a modified bouncing model which includes intermediate state is presented in this appendix. In the bouncing model, each wheel has three modes: Mode 1: contact, Mode 2: intermediate, and Mode 3: departure. In the following discussions and the figures, suffix i, where i = 1 and 2, refers to the front and rear wheels, respectively. M_i is the set

of modes of each wheel, M_i = 1, 2, and 3 refers to Mode 1, Mode 2, and Mode 3, respectively. In each mode, the vertical load on axle, f_i , and the distance between the wheel and ground, D_i, is defined differently, as follows:

Mode 1 is the contact mode with the ground. In Mode 1, the wheel is in contact with the ground and f_i can be exerted on the ground. Thus, f_i is positive, and D_i is fixed as zero, as follows:

$$f_i(t) = -k_i(z_i - d_i) - c_i(\dot{z}_i - \dot{d}_i) \tag{2.9}$$

$$D_i(t) = 0. \tag{2.10}$$

When f_i becomes zero, force cannot be exerted on the ground and the mode of the wheel changes from Mode 1 to 2.

Mode 2 is the intermediate mode between contact and departure. In Mode 2, the wheel is still in contact with the ground while f_i becomes zero. Thus, f_i and D_i are both fixed as zero as follows:

$$f_i(t) = 0 \tag{2.11}$$

$$D_i(t) = 0. \tag{2.12}$$

When the vertical displacement of the wheel, z_i, become larger than the road elevation. d_i ($z_i > d_i$), the wheel departs from the ground and the mode of the wheel changes from Mode 2 to 3. In addition to this progressive transition, there is another retrogressive transition in Mode 2. When vertical velocity of the wheel, $\dot{z}_i$, becomes smaller than velocity of the road elevation, $\dot{d}_i$ ($\dot{z}_i < \dot{d}_i$), f_i can be exerted on the ground and the mode

of the wheel returns to Mode 1 from Mode 2.

Mode 3 is the departure mode. In Mode 3, the wheel departs from the ground. Thus, f_i is fixed at zero and D_i is defined as follows:

$$f_i(t) = 0 \tag{2.13}$$

$$D_i(t) = z_i - d_i. \tag{2.14}$$

When D_i becomes zero, the wheel collides with the ground and mode of the wheel changes from Mode 3 to 1. The above process is summarised in the flow chart in Fig. 2.3.

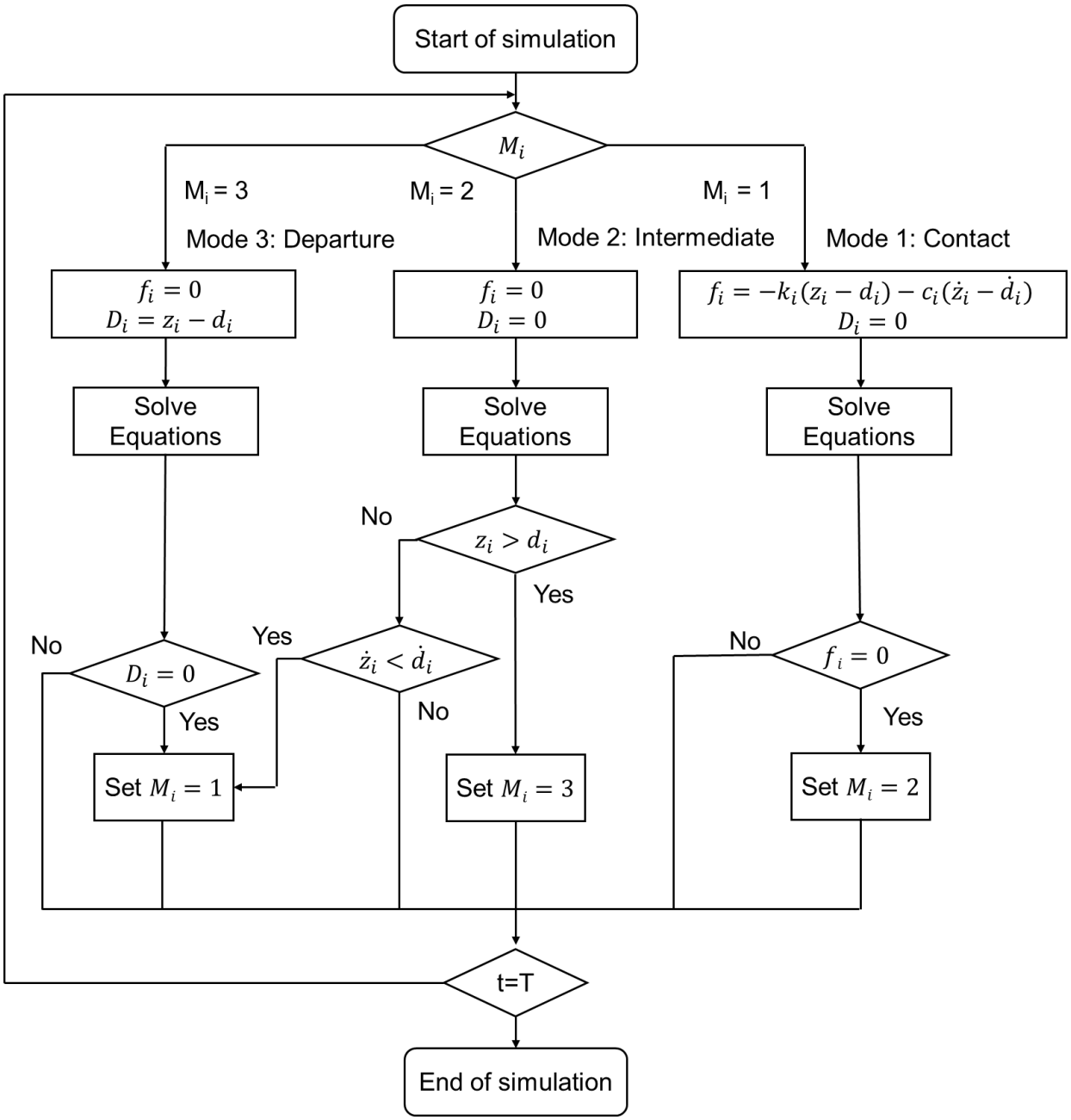

Figure 2.3 Flow chart for the numerical implementation of the bouncing.

2.3. Numerical experiments

In this section, frequency response and parametric study of the tractor running over a passage slope were investigated to discover inherent nonlinearity in bouncing tractor model. The developed model in section 2.2 was used in numerical experiments to describe

the bouncing process. A fourth-order Runge-Kutta method was used to solve the equations of motion. The parameter specification for the tractor is presented in Table 2.1. These parameters specification were measured by one of the authors (Bukta, Sakai, Sasao & Shibusawa, 2002).

Table 2.1 Parameter specification of the tractor for the numerical experiments (Bukta, Sakai, Sasao & Shibusawa, 2002).

Parameters	Symbol	Value	Unit
Stiffness of front wheel	k_1	200	kN m^{-1}
Stiffness of rear wheel	k_2	260	kN m^{-1}
Damping coefficient of front wheel	c_1	5500	N s m^{-1}
Damping coefficient of rear wheel	c_2	6690	N s m^{-1}
Mass of tractor body	M_T	988	kg
Mass of implement	M_I	184	kg
Pitch moment of inertia	I_{yy}	700	kg m^{-2}
Distance between centre of gravity of the tractor body and front wheel	l_1	0.68	m
Distance between centre of gravity of the tractor body and rear wheel	l_2	0.70	m
Wheelbase of the tractor	WB	1.38	m
Distance between centre of gravity of the tractor body and the centre of gravity of implement	l_3	1.24	m
Engine power	-	11.2	kW

First, a frequency response analysis was conducted to investigate basic characteristics of the nonlinear bouncing model. Next, numerical experiments of the tractor and running along passage slopes were conducted.

2.3.1. Frequency response analysis

The frequency response analysis is generally used to analyse dynamic systems. In this study, frequency response was obtained by inputting a sinusoidal function into the linear conventional model and nonlinear bouncing model and plotting the vertical acceleration of the C.G. versus the forcing frequency. The following sinusoidal functions are used to obtain frequency response:

$$d_1 = d_0 \sin(2\pi f_{in} t) \tag{2.15}$$

$$d_2 = d_0 \sin\left(2\pi f_{in}\left(t - \frac{l_1+l_2}{V}\right)\right), \tag{2.16}$$

where d_0 is road amplitude and f_{in} is forcing frequency. Road amplitude d_0 was set to 0.025 m. Figure 2.4 shows the frequency response curve of the linear conventional model and the nonlinear bouncing model.

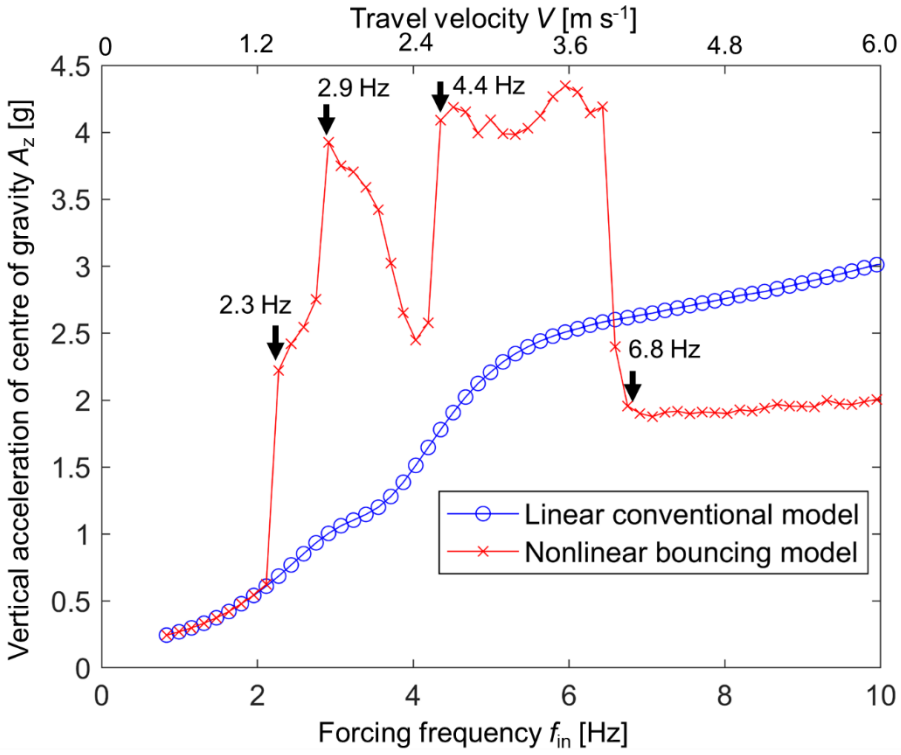

Figure 2.4 Frequency response curve of the linear conventional model (blue line) and the nonlinear bouncing model (red line).

The abscissa is forcing frequency and travel velocity and the ordinate is a vertical acceleration of C.G., A_z. The nonlinear response curve agrees with the linear response curve until 2.1 Hz point. Nonlinearity arises and the qualitative characteristics of the frequency response are totally different for the linear conventional model and the nonlinear bouncing model as the forcing frequency increases. The nonlinear response curve is discontinuous at 2.3 Hz, 2.9 Hz, 4.4 Hz and 6.8 Hz point while the linear response curve is continuous. This discontinuous response is generally observed in nonlinear dynamics.

In order to show the detail of the nonlinearity, Figure 2.5a, b, c, and d shows the Fourier spectrum of the time series of the vertical acceleration of C.G. at 2.3 Hz, 2.9 Hz,

4.4 Hz, and 6.8 Hz points respectively.

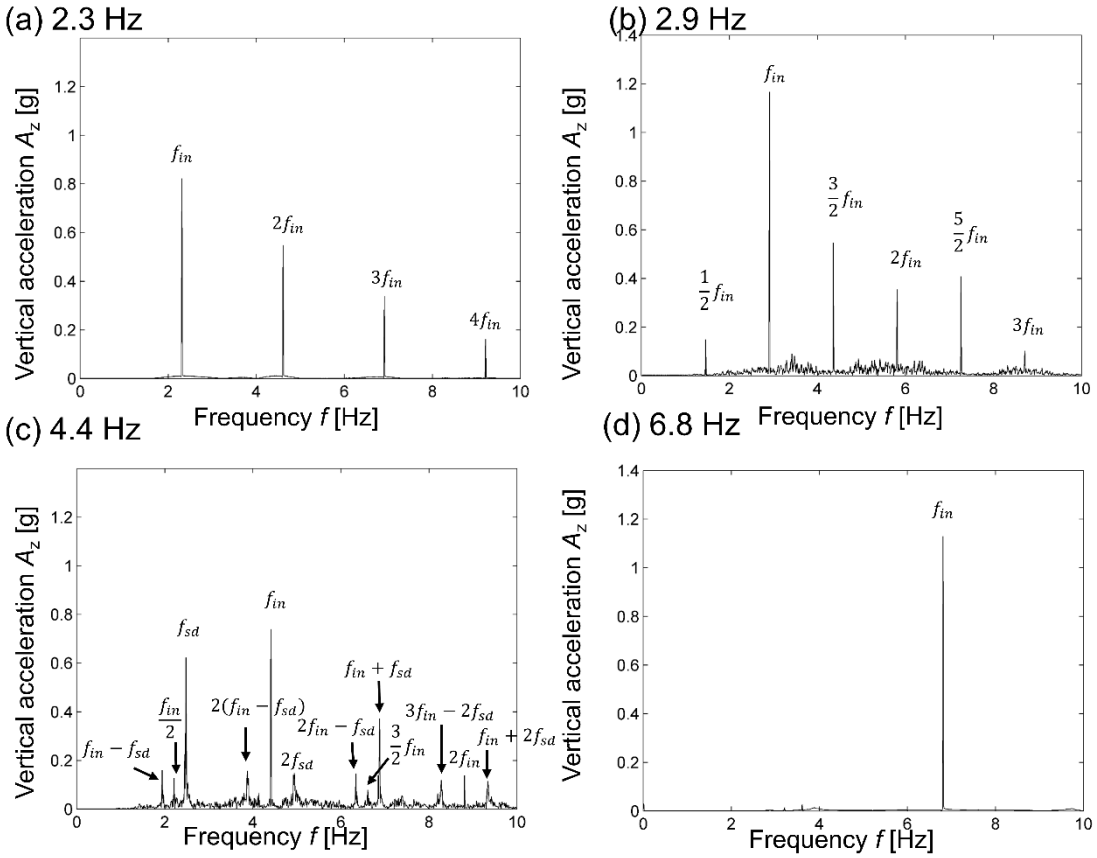

Figure 2.5 Fourier spectrum for 2.3, 2.9, 4.4, and 6.8 Hz input oscillating frequency.

In Fig. 2.5a, super harmonics, that is $2f_{\mathrm{in}} = 4.6\ \mathrm{Hz}$, $3f_{\mathrm{in}} = 6.9\ \mathrm{Hz}$, $4f_{\mathrm{in}} = 9.2\ \mathrm{Hz}$, appear as well as forcing frequency $f_{\mathrm{in}} = 2.3\ \mathrm{Hz}$ In Fig. 2.5b, super-harmonics, that is $2f_{\mathrm{in}} = 5.8\ \mathrm{Hz}$ and $3f_{\mathrm{in}} = 8.7\ \mathrm{Hz}$, subharmonics, $\frac{1}{2}f_{\mathrm{in}} = 1.45\ \mathrm{Hz}$, and ultra-subharmonics, $\frac{3}{2}f_{\mathrm{in}} = 4.35\ \mathrm{Hz}$ and $\frac{5}{2}f_{\mathrm{in}} = 7.25\ \mathrm{Hz}$ appear as well as $f_{\mathrm{in}} = 2.9\ \mathrm{Hz}$. In Fig. 2.5c, the secondary frequency $f_{\mathrm{sd}} = 2.5\ \mathrm{Hz}$ appears as well as $f_{\mathrm{in}} = 4.4\ \mathrm{Hz}$. Addition to the secondary frequency and the forcing frequency, the super-harmonics $2f_{\mathrm{in}} = 8.8\ \mathrm{Hz}$ and $2f_{\mathrm{sd}} = 5.0\ \mathrm{Hz}$, the subharmonics of the forcing frequency $\frac{1}{2}f_{\mathrm{in}} =$

2.2 Hz and the ultra-subharmonics of the forcing frequency $\frac{3}{2}f_{\mathrm{in}} = 6.6$ Hz, and the linear coupling $f_{\mathrm{in}} - f_{\mathrm{sd}} = 1.9\mathrm{Hz}$, $f_{\mathrm{in}} + f_{\mathrm{sd}} = 6.9\mathrm{Hz}$, $2(f_{\mathrm{in}} - f_{\mathrm{sd}}) = 3.8\mathrm{Hz}$, $2f_{\mathrm{in}} - f_{\mathrm{sd}} = 6.3\mathrm{Hz}$, $3f_{\mathrm{in}} - 2f_{\mathrm{sd}} = 8.3\mathrm{Hz}$, and $f_{\mathrm{in}} + 2f_{\mathrm{sd}} = 9.4\mathrm{Hz}$ all appear in the spectrum. This nonlinear response, which does not appear in the linear dynamic system, causes the nonlinear resonance in the frequency response curve.

2.3.2. Bifurcation diagram

In nonlinear dynamics, the qualitative structure of dynamics, for example the stability of the periodic orbit, can change as control parameters are varied (Strogatz, 2014). This qualitative change is called bifurcation. In the present study, the forcing frequency is used as a control parameter and is varied. Figures 2.6–2.10 show the results of the numerical experiments for 2.2 Hz, 2.5 Hz, 3.5 Hz, 4.8 Hz, and 6.6 Hz, respectively.

Figures 2.6–2.10a, b, c, and d show the time series of the vertical acceleration of the C.G., Fourier spectrum of the vertical acceleration of the C.G., phase space, and Poincaré section (or Poincaré map), respectively. The coordinates of the phase plane are the vertical displacement z, vertical velocity v_z, and pitch angle γ. The Poincaré section is typically used to investigate the structure of the trajectory in phase space. The Poincaré section is derived by stroboscopically measuring the point in phase space (Moon, 1987); that is, the point of the trajectory is plotted in the fundamental period of the time series, or the forcing frequency. Thus, one point in the Poincaré section corresponds with one periodic orbit.

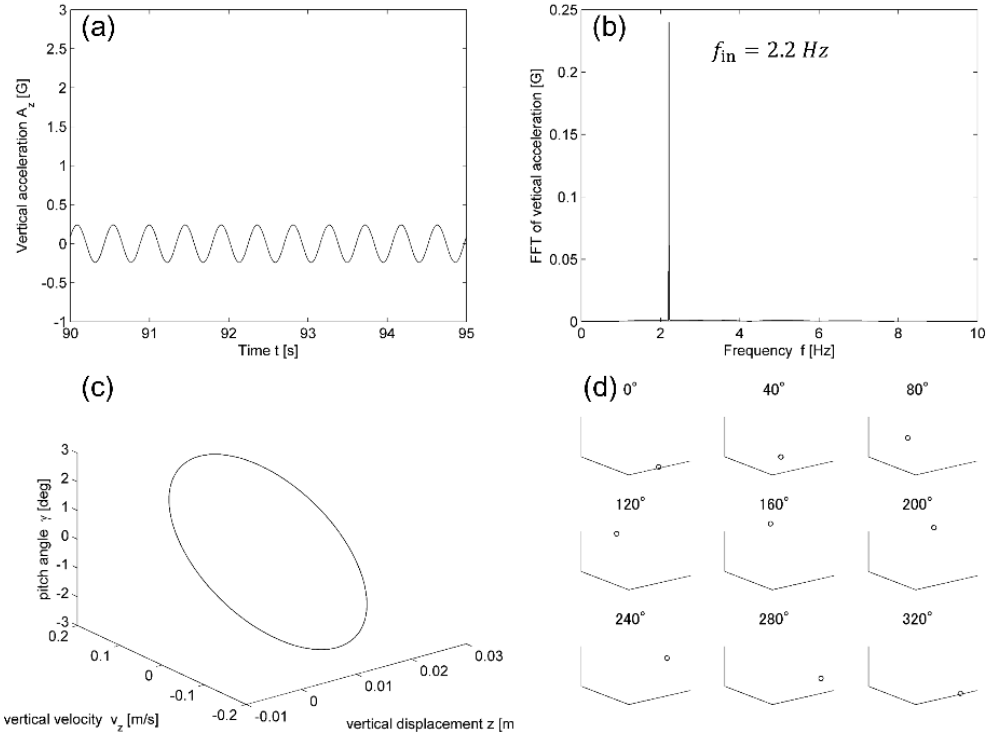

Figure 2.6 The results of the numerical experiment for the forcing frequency 2.2 Hz; (a) Time series of the vertical acceleration of C.G.; (b) Fourier spectrum of the vertical acceleration of C.G.; (c) Trajectory in phase space; (d) Poincaré section.

Figure 2.6 shows the results of the numerical experiment for forcing frequency 2.2 Hz. The vertical acceleration is perfectly sinusoidal in Figure 2.6a. One line spectrum f_{I}, that is, the forcing frequency, is observed in Figure 2.6b. The trajectory in phase space is a limit cycle in Figure 2.6c. One point is observed in Figure 2.6d. The above evidence strongly indicates that a linear periodic vibration occurs at the 2.0 Hz point without the bouncing process.

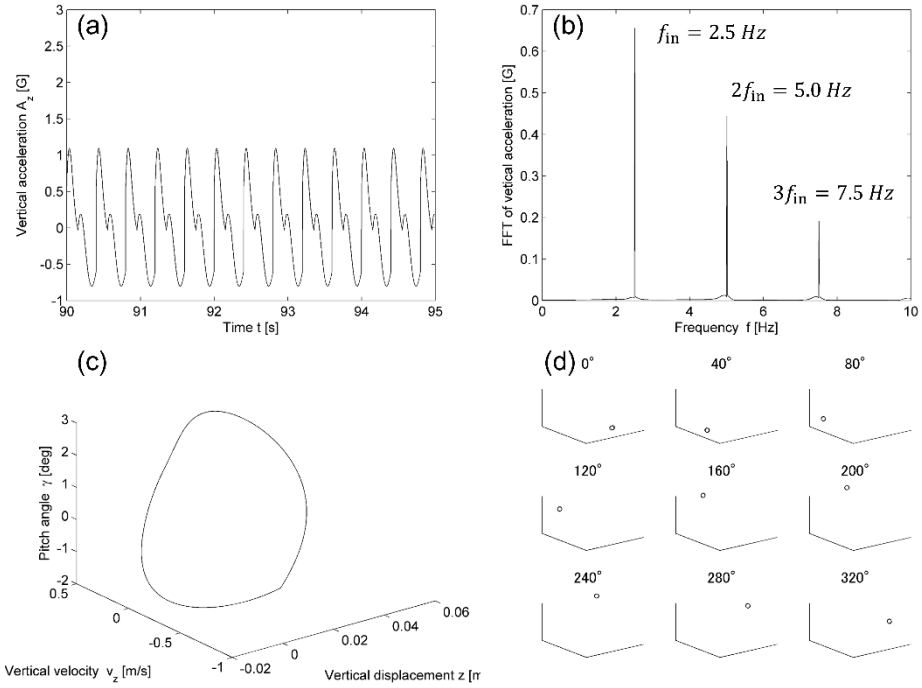

Figure 2.7 The results of the numerical experiment for the forcing frequency 2.5 Hz; (a) Time series of the vertical acceleration of C.G.; (b) Fourier spectrum of the vertical acceleration of C.G.; (c) Trajectory in phase space; (d) Poincaré section.

Figure 2.7 shows the results of the numerical experiment for forcing frequency 2.5 Hz. The time series of the vertical acceleration is not sinusoidal in Figure 2.7a. The super-harmonics $2f_1$ and $3f_1$ are observed in addition to the forcing frequency f_1 in Figure 2.7b. The trajectory in phase space is a skewed limit cycle in Figure 2.7c. One point is observed in Figure 2.7d. The above evidence strongly indicates that nonlinear periodic vibrations occur at the 2.5 Hz point.

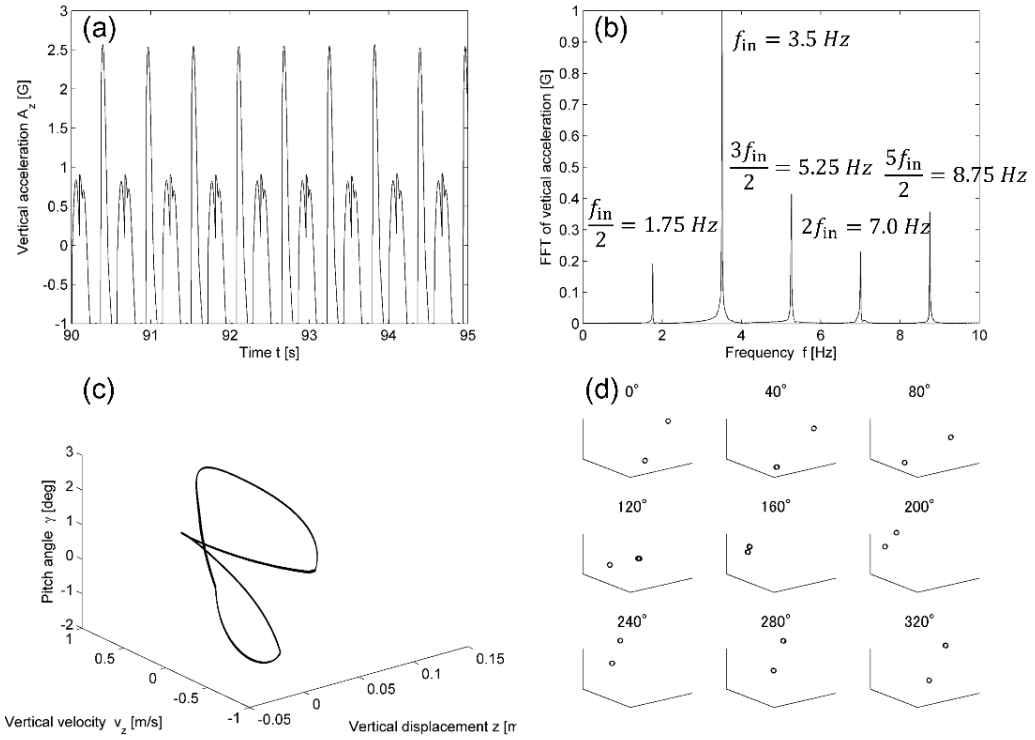

Figure 2.8 The results of the numerical experiment for the forcing frequency 3.5 Hz; (a) Time series of the vertical acceleration of C.G.; (b) Fourier spectrum of the vertical acceleration of C.G.; (c) Trajectory in phase space; (d) Poincaré section.

Figure 2.8 shows the results of the numerical experiment for forcing frequency 3.5 Hz. The time series of the vertical acceleration is a period that doubles in Figure 2.8a. The minimum of the vertical acceleration is -1 g, which suggests the freefall of the tractor. In addition to forcing frequency f_1, super-harmonic $2f_1$, subharmonic $f_1/2$, and ultra-subharmonics $3f_1/2$ and $5f_1/2$ are observed in Figure 2.8b. The trajectory in phase space demonstrates the period doubling structure shown in Figure 2.8c. There are two points in Figure 2.8d. The above evidence strongly indicates that period doubling vibrations occur at the 3.5 Hz point with the freefall of the tractor.

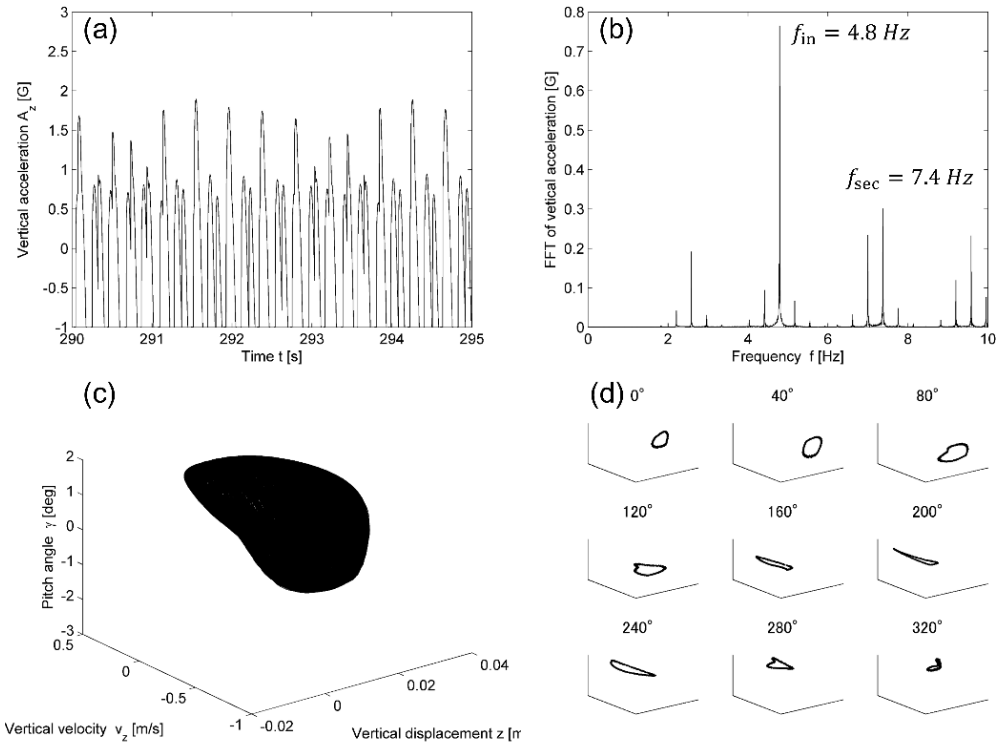

Figure 2.9 The results of the numerical experiment for the forcing frequency 4.8 Hz; (a) Time series of the vertical acceleration of C.G.; (b) Fourier spectrum of the vertical acceleration of C.G.; (c) Trajectory in phase space; (d) Poincaré section.

Figure 2.9 shows the results of the numerical experiment for forcing frequency 4.8 Hz. The time series of the vertical acceleration is aperiodic in Figure 2.9a. Many peaks are observed in Figure 2.9b. The ratio between forcing frequency f_1 and secondary frequency f_2 is irrational number. The Poincaré section of the trajectory in phase space is a closed orbit in Figure 2.9d. The above evidence strongly indicates that quasi-periodic vibrations occur at the 4.8 Hz point.

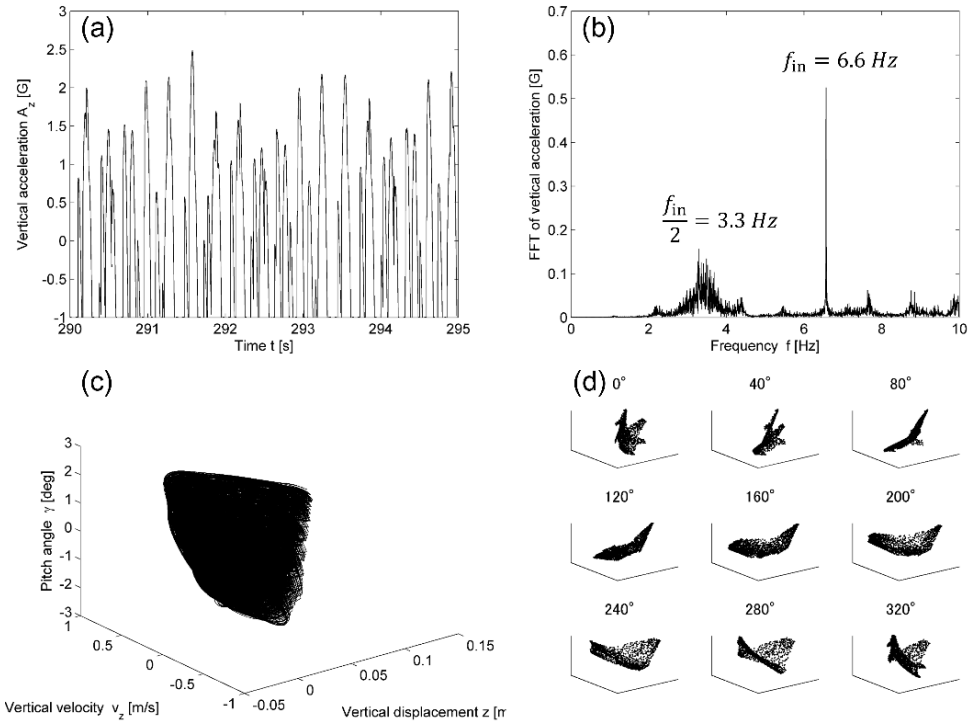

Figure 2.10 The results of the numerical experiment for the forcing frequency 6.6 Hz; (a) Time series of the vertical acceleration of C.G.; (b) Fourier spectrum of the vertical acceleration of C.G.; (c) Trajectory in phase space; (d) Poincaré section.

Figure 2.10 shows the results of the numerical experiment for forcing frequency 6.6 Hz. The time series of the vertical acceleration appears to be random in Figure 2.10a. In addition to forcing frequency f_1, subharmonic $f_1/2$ is observed in Figure 2.10b. Moreover, broad noise is observed in the Fourier spectrum, which indicates that this vibration is chaotic. The trajectory in phase space is called the strange attractor, and the Poincaré section shows the structure of the stretching and folding of the trajectory. The above evidence strongly indicates that chaotic vibrations occur at the 6.6 Hz point.

Clear bifurcation is observed as the forcing frequency is varied. The bifurcation diagram is a widely used technique to visualize the structure of the bifurcation of dynamics. In this study, the bifurcation diagram is obtained by plotting the Poincaré points

of the vertical displacement with regard to the forcing frequency. Figure 2.11 shows the bifurcation diagram of the bouncing model.

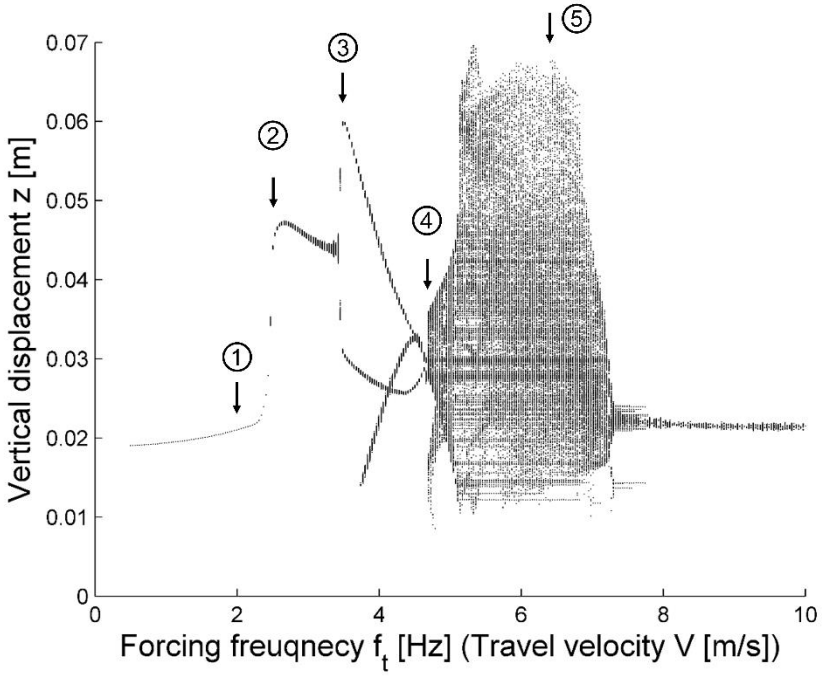

Figure 2.11 Bifurcation diagram of the vertical displacement concerning to the forcing frequency f_t.

Arrows 1 (2.2 Hz), 2 (2.5 Hz), 3 (3.5 Hz), 4 (4.8 Hz), and 5 (6.6 Hz) correspond to Figures 2.6–2.10, respectively. According to the bifurcation diagram, the dynamics of the bouncing model changes from linear periodic, nonlinear periodic, period doubling, and quasi-periodic to chaotic vibrations. These results strongly indicate that there is a clear bifurcation concerning the forcing frequency.

2.3.3. Numerical experiments of the tractor running along passage slope

The Japanese Association of Rural Medicine surveys and collects cases of fatal farm

accidents that occurred in Japan ("Case study of farm accidents", 2013). According to the survey, tractor overturning on steep passage slope is typical of accidents occurring in Japan.

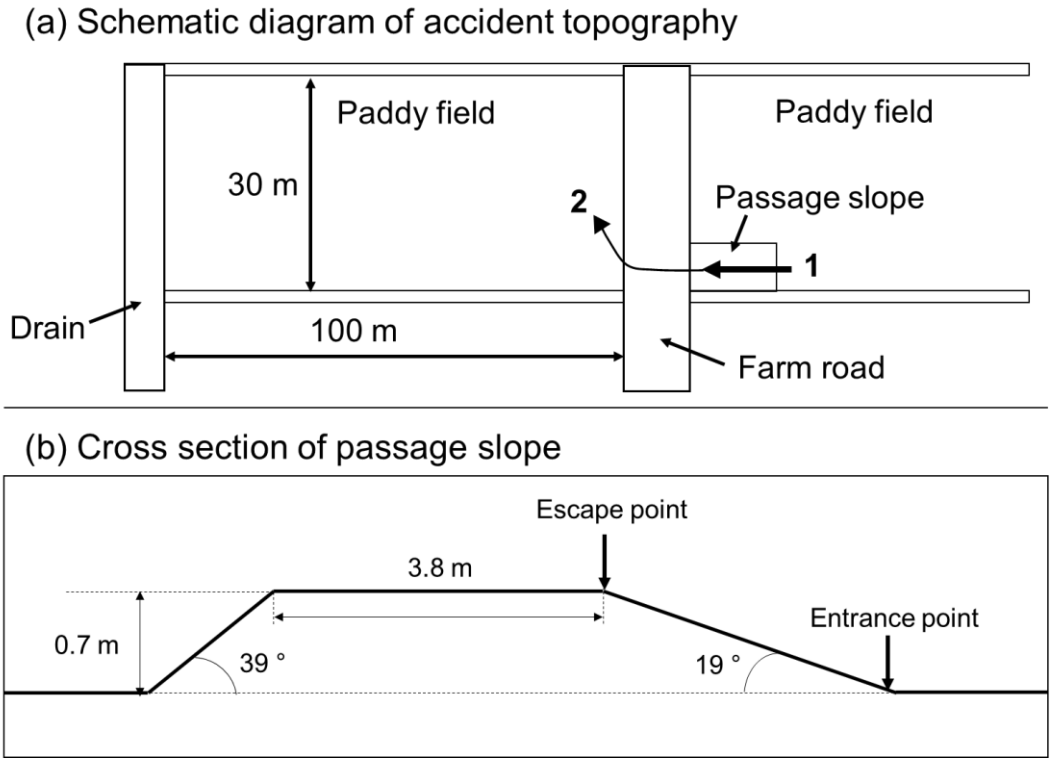

Figure 2.12 (a) Schematic diagram of the accident topography based on the real case of tractor overturning accidents on the passage slope collected in the Japanese Association of Rural Medicine survey ("Case study of farm accidents", 2013), (b) Cross section of passage slope.

Figure 2.12a shows one of the cases of tractor overturning on passage slope. A cross section of the passage slope is also presented in Fig. 2.12b. The angle of the passage slope is 19°, the height of the road is 0.7 m and the width of the road is 3.8 m. This angle slightly exceeds the Japanese regulation slope for a passage of 18°. From the side 1, the tractor moves onto the passage slope from the paddy field to the farm road usually with a constant travel velocity. The gear of the tractor is set to 3rd gear (i.e. high-speed condition). Then,

the operator attempted to turn right onto the farm road. However, during that operation, occasionally the front or rear axial loads became zero or low enough to lose the steering and/or cause sideslip. Thus, the tractor loses its stability on the farm road to fall as it moves to side 2. This accident case implies that "bouncing" can be one of the possible causes of a fatal tractor overturning. In the numerical experiments, simulation of the tractor running on passage slope based on the above accident case was conducted. Travel velocity of the tractor V and angle of the passage slope θ are taken as control parameters of the numerical experiments. In each simulation, the tractor runs on the passage slope of θ ° with the travel velocity of V m s^{-1}.

First, travel velocity of the tractor is taken as a control parameter and varied from 0.5 m s^{-1} to 4.0 m s^{-1}. Figure 2.13 shows the maximum value of vertical acceleration of C.G., A_z in each numerical simulation.

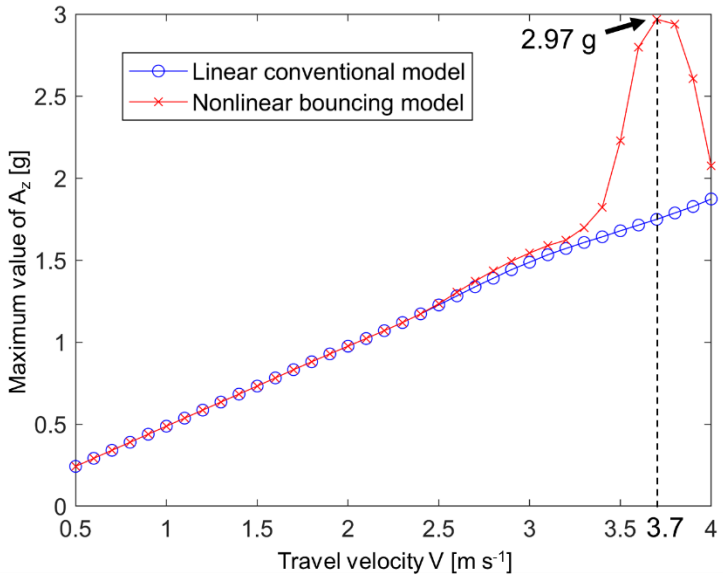

Figure 2.13 Numerical results of the tractor running on passage slope when the travel velocity is considered as a control parameter. The blue line is the result of the linear conventional model while the red line is the results of the nonlinear bouncing model.

The abscissa is the travel velocity V m s^{-1} and the ordinate is the maximum value of the vertical acceleration of C.G. in each simulation. The blue line shows the result of the linear conventional model and the red line shows the result of the nonlinear bouncing model. The maximum value of A_z is linearly proportional to the travel velocity in the linear conventional model. Nonlinear model agreed with linear model until the travel velocity 2.5 m s^{-1}. However, the difference appears between linear and nonlinear as the travel velocity V increases and discontinuous response appear at 3.5 m s^{-1} the same as the frequency response curve. At the 3.7 m s^{-1}point, the maximum value of the vertical acceleration of C.G. A_z is 2.97 g in the nonlinear bouncing model while 1.74 g in the linear bouncing model.

In order to see details of the discontinuous response of the nonlinear bouncing model, Figure 2.14a and b shows the time series of the vertical load on axles and vertical acceleration of 3.4 m s^{-1} and 3.7 m s^{-1} respectively.

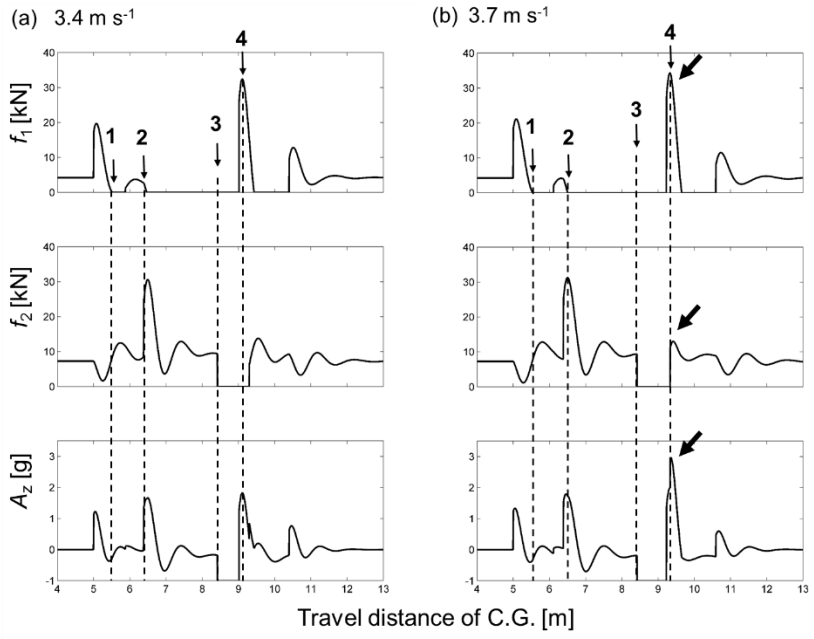

Figure 2.14 Time series of the vertical load on front axle f_1 [kN], the vertical load on rear axle f_2 [kN], and the vertical acceleration of C.G. Az [g]. (a) Results at 3.4 m s^{-1}; Top; Vertical load on front axle f_1, Medium; Vertical load on rear axle f_2, Bottom; Vertical acceleration of C.G. A_z.

In Figure 2.14a (3.4 m s^{-1}), the vertical load on front axle f_1 becomes zero and the front wheel leave the ground at point 1 after the front wheel move on the slope. After the rear wheel move on the slope at point 2, the front wheel departs from the ground and the tractor become wheelie state. The vertical load on rear axle f_2 becomes zero and the rear wheel departs from the ground when the rear wheel escapes from the ground at point 3. At point 4, the front wheel collides with the ground when the rear wheel is in the air. Then, the maximum value of the A_z 1.82 g occur.

In Figure 2.14b (3.7 m s^{-1}), the process from point 1 to 3 is almost same as in Fig. 2.14a (3.4 m s^{-1}). However, the large acceleration of 2.97 g occur at point 4 in the results of 3.7 m s^{-1}. At point 4 in Fig. 2.14b, the front and the rear wheels impact with the ground simultaneously. This produces a large acceleration in the result of 3.7 m s^{-1}.

Above results indicate that the nonlinear bouncing model is sensitive for the change of the control parameter, which is the travel velocity. This parameter sensitivity is typical characteristics of nonlinear dynamics. To further show parameter sensitivity of the nonlinear bouncing model, the angle of the passage slope is taken as a control parameter and the numerical experiments were conducted. The angle is varied from 5 to 20 °. The travel velocity of the tractor is fixed to 3.7 m s^{-1}. The numerical results are shown in Figure 2.15.

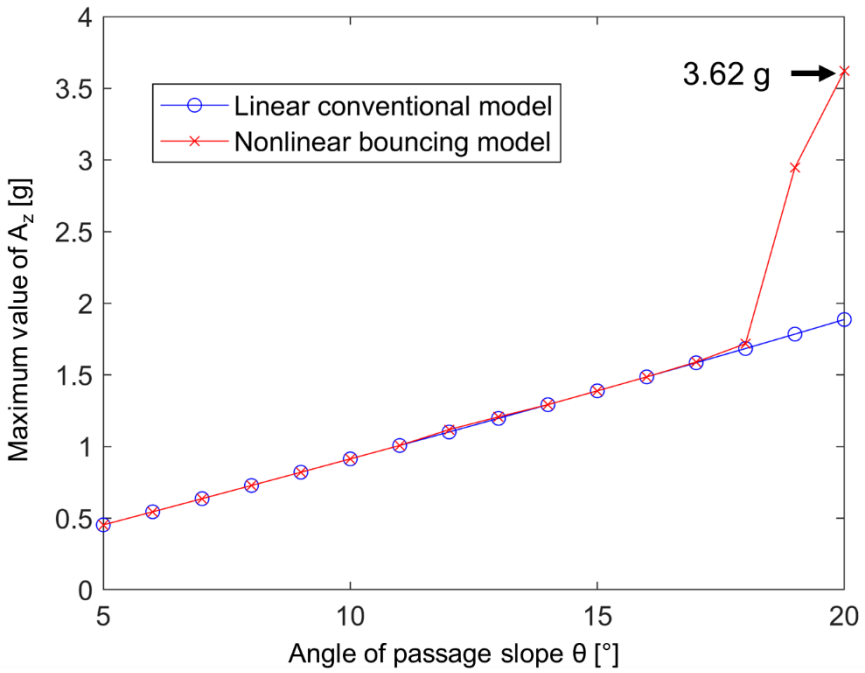

Figure 2.15 Numerical results of the tractor running on passage slope when the angle of passage slope is taken as control parameter. The blue line is the result of the linear conventional model while the red line is the results of the nonlinear bouncing model.

The abscissa is the angle of the passage slope in each simulation and the ordinate is the maximum value of the vertical acceleration of C.G. in each simulation. Blue line shows the result of the linear conventional model and red line shows the result of the nonlinear bouncing model. The maximum value of A_z is linearly proportional to the slope angle in the linear conventional model. On the other hand, the discontinuous response is obtained in the nonlinear bouncing model similar to the frequency response curve and the numerical experiments of the travel velocity. The discontinuity appears in the nonlinear response when the slope angle is 19 and 20°. This indicates that the Japanese normative is reasonable with respect of the maximum allowed slope angle of 18° under the conditions investigated in this study.

The results of the numerical experiments indicate that the nonlinear bouncing model

has strong parameter sensitivity which causes the discontinuous response. This characteristic can lead to the sudden unpredictable phenomenon, such as violent vibration and sideslip and be one of the possible causes of overturning accidents.

In addition to the present study, more advanced works including, analysis of a nonlinear three-dimensional bouncing tractor model with roll motion and steering and development of control method to suppress violent vibration caused by bouncing, are necessary in order to achieve a substantial reduction in fatal accidents caused by tractor overturning.

2.3.4. Comparison between large and small tractor

In 2016, employees in agriculture are 1922.0 and 940.1 thousand in Japan and Germany respectively. In 2014, there were 350 fatal farm accidents in Japan (Report on fatal farm accident that happened in 2014, 2017) and 166 in Germany (Die Sozialversicherung für Landwirtschaft, Forsten und Gartenbau: Tödliche Arbeits- und Wegeunfälle, 2017). In Japan, nearly half of all fatal farm accidents involve agricultural vehicles, such as tractors and trucks. Tractor-related accidents are a severe safety issue for agriculture. In Germany, fatal tractor-related accidents were massively reduced by overrunning brackets and safety cabins. Due to this safety appliance which was mandatory introduced in West Germany in 1970, deadly accidents in this country decreased from more than 150 in 1970 to less than 50 in 1977 (Söhne & Walter, 2013). However, mechanisms of tractor overturning accidents have not yet been clarified. Thus, it is an urgent issue to clarify mechanisms of tractor-related accidents in order to prevent them. Tractors have been shown to jump under certain conditions. Jumping has been investigated in small-sized tractors (approximately 1000 kg) designed for paddy field use

in Japan (Sakai, 1999). Garciano, Sakai, and Torisu (2005) conducted an experimental investigation using medium-sized tractors (approximately 4000 kg). It is controversial as to whether the jumping process could cause a fatal accident with large-sized tractors (approximately 7000 kg) such as those used in Germany. It is important to investigate effects of tractor size on jumping. For the present study conducted numerical simulations for two different sized tractors: a small-sized tractor typical of those used in Japan, and a large-sized tractor typical of those used in Germany. Aims of the present subsection are to investigate how jumping process occur on different sized tractors.

Numerical simulations were conducted for the small-sized tractor and the large-sized tractor. The input road is a sinusoidal function, the amplitude of the road was set to 0.05 m and the wavelength of the road was set to the half of the wheel base in both simulations. Travel velocity was 4.020 m/s (14.4 km/h) for the small-sized tractor and 2.355 m/s (8.48 km/h) for the large-sized tractor. Table 2.2 shows the specifications of both tractors.

Table 2.2 Specification of the small-sized tractor and the large-sized tractor used in the simulations.

Parameters	Small-sized (Japanese)	Large-sized (German)
Mass of tractor	1000 kg	7600 kg
Pitch axis inertia of moment	700 kg m^2	6473 kg m^2
Roll axis inertia of moment	240 kgm^2	2829 kg m^2
Wheel base	1.340 m	2.770 m
Tread	1.035 m	1.940 m

Figure 2.16 shows simulation results for the front- and rear-tire dynamic load, front- and rear-tire relative displacement, and vertical acceleration at the center of gravity (CG). As

shown in Figure 2,16a, the front and rear vertical dynamic load become zero; thus, the front and rear tires of the small-sized tractor leave the ground at certain points. The maximum vertical acceleration at the CG is 5.34 g. The minimum vertical acceleration is −1 g, indicating that the tractor is in freefall at that point. Jumping can cause very severe vibration occur in the small-sized tractor. As shown in Figure 2.16b, the front dynamic load becomes zero whereas the rear dynamic load does not. Thus, only the front tire jumps from the ground in the large-sized tractor. This causes a reduction in steering performance and can lead to accidents. The results show that large-sized tractors jump as well as small-sized tractors for a road amplitude less than 0.05 m. Nonlinearity arising from jumping is omnipresent in tractor dynamics. Jumping may cause safety issues for both small-sized and large-sized tractors.

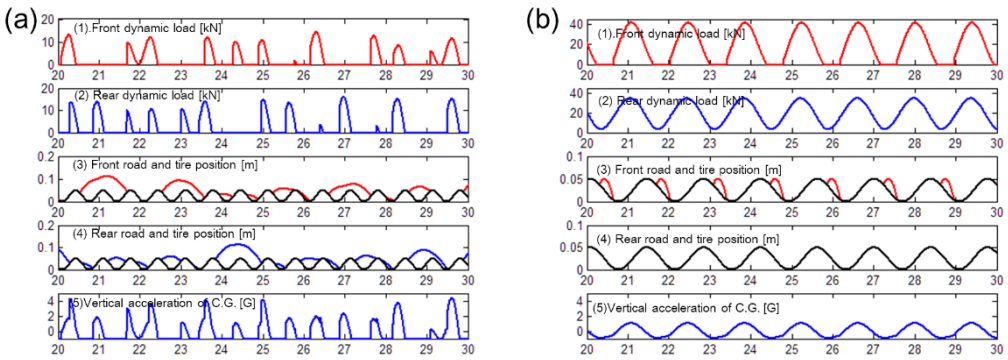

Figure 2.16 Simulation results for (a) the small-sized tractor (travel velocity 4.020 m/s) and (b) the large-sized tractor (travel velocity 2.355 m/s). (1) Front-tire dynamic load; (2) rear-tire dynamic load; (3) front-tire relative displacement; (4) rear-tire relative displacement; (5) vertical acceleration at the center of gravity (CG).

The effects of tractor size on jumping phenomenon were investigated in the present study. Simulations of a small-sized tractor and a large-sized tractor were conducted. Both large-

sized and small-sized tractors were found to jump at certain travel velocities. The results indicate that the jumping is a safety issue for both small-sized and large-sized tractors. Therefore, modeling jumping and nonlinear analysis are important for both small-sized tractors and large-sized tractors.

2.4. Control method for a bouncing tractor model

Active control algorithms are essential to prevent an overturing accident resulting from the nonlinearity of a bouncing tractor. This sub-section develops a control method for avoiding tractor overturning accidents. Driving force control is the most promising way to control the dynamic behavior of a tractor (Aoyagi & Matsui, 2019). In this section, two driving force control approaches, namely proportional control (P-control) and delayed feedback control (DF-control), are developed.

2.4.1. Proportional control

Proportional control is developed to prevent declines in axial loads. As described above, declines in axial loads may lead to overturning accidents. It is thus important to suppress declines in axial loads. Driving force control is adopted to suppress the decline. In the following equations, a control term is added to the abovementioned tractor bouncing equations (2.1) and (2.2):

$$(M_T + M_I)\ddot{z} = f_1 + f_2 - (M_T + M_I)g, \tag{2.17}$$

$$\left(I_{yy} + l_3^2 M_I\right)\ddot{\gamma} = l_2 f_2 - l_1 f_1 + F_d h_{CG}, \tag{2.18}$$

where $F_d h_{CG}$ is the control term and F_d is the driving force. Thus, in this control, the

driving force is a main factor of the control of tractor behavior. The driving force is obtained as

$$F_d = \begin{cases} 0, \ \mathrm{F_{s,1}} < f_1 \\ -\mathrm{K_p}(f_1 - \mathrm{F_{s,1}}), \ \mathrm{F_{s,1}} > f_1. \end{cases} \tag{2.19}$$

The driving force is calculated according to the vertical force acting on the wheel because the vertical force acting on the front wheel essentially decides the steering stability. In equation (2.19), if the vertical force acting on the front wheel f_1 is stronger than the static equilibrium value of the vertical force $\mathrm{F_{s,1}}$, the driving force is zero and the velocity of the tractor does not change. If the vertical force acting on the front wheel f_1 is weaker than the static equilibrium value of the vertical force $\mathrm{F_{s,1}}$, the driving force acts on the wheel to slow the tractor. The calculated driving force is proportional to the difference between f_1 and $\mathrm{F_{s,1}}$. The static equilibrium value of the vertical force $\mathrm{F_{s,1}}$ is calculated as

$$\mathrm{F_{s,1}} = (M_T + M_I) * \frac{l_2}{WB}. \tag{2.20}$$

The travel velocity of the tractor is calculated as

$$V = \mathrm{V_0} + \int \frac{F_{d,1}}{M_T + M_I} dt, \tag{2.21}$$

where $\mathrm{V_0}$ is the initial velocity of the tractor.

In the present numerical experiments, the tractor travelled over a bump with a height of 0.025 m and a length of 0.5 m and the passage slope detailed in Figure 2.12. The initial

travel velocity was set to 2.0 m s^{-1} and the P-control gain K_p was tuned in each experiment using the MATLAB lsqnonlin () function. Figure 2.17 shows the numerical results of the bump test.

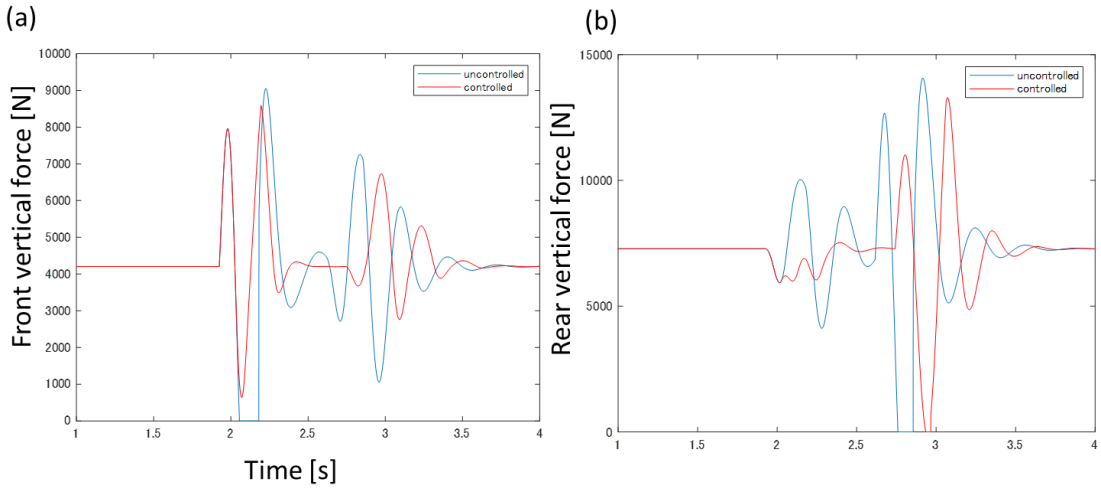

Figure 2.17 Numerical results of the bump test, with red and blue lines respectively showing results obtained with and without control: (a) vertical force acting on the front wheel; (b) vertical force acting on the rear wheel.

When there was no control, the vertical force acting on the front wheel decreased to zero and the front wheel lost contact with the ground. Meanwhile, when P-control was implemented, the front wheel maintained contact with the ground. In the case of the rear wheel, such bouncing was also improved by P-control. Owing to the P-control of the driving force, the declines in vertical forces acting on the front and rear wheels were suppressed. Figure 2.18 shows the driving force and travel velocity when P-control was implemented.

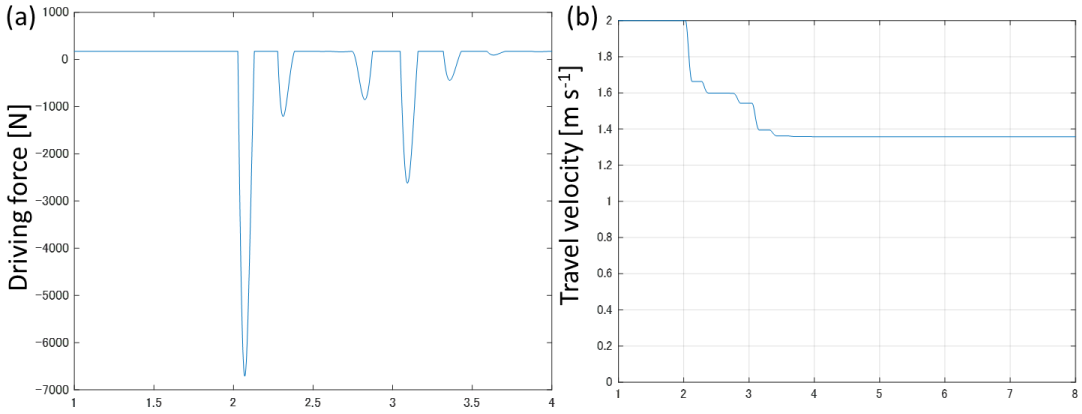

Figure 2.18 Numerical results of the bump test when P-control was implemented: (a) driving force; (b) travel velocity.

The driving force was exerted to slow the tractor when the front vertical force became weaker than the static value. The driving force reduced the travel velocity from 2.0 to 1.4 m s^{-1}. The above numerical results indicate that P-control suppresses the decline of vertical forces and can be used for accident-avoidance control.

2.4.2. Delayed feedback control

This section implements delayed feedback (DF) control to suppress chaotic vibrations. The algorithm of DF-control is generally used to suppress chaotic dynamic behavior (Pyragas, 1992). In the bouncing tractor dynamics, chaotic behavior is also observed under a specific combination of parameters. In this section, the chaotic behavior of the bouncing tractor model is suppressed using the DF-control.

Figure 2.19 is a schematic diagram of the DF-control algorithm.

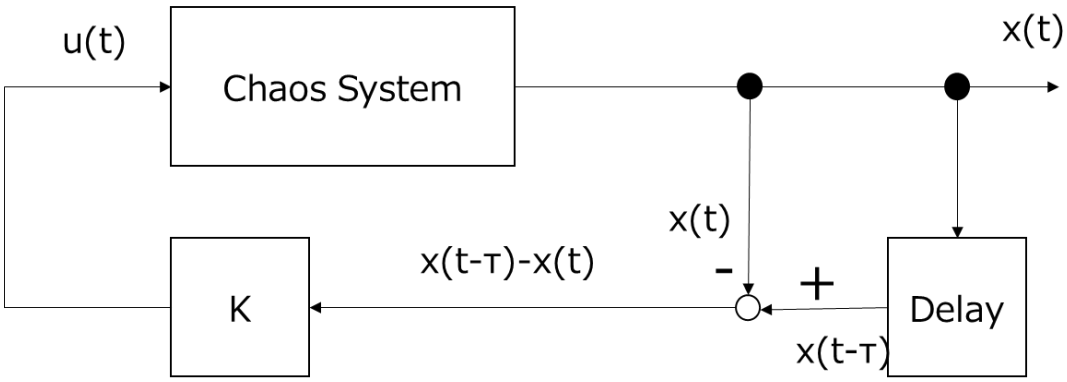

Figure 2.19 Schematic diagram of the delayed feedback control algorithm.

DF control is a chaotic control algorithm and applied to continuous systems. In this control, input is proportional to the difference between x(t) and x(t − τ). τ is the time delay and period of a stable orbit for a chaotic attractor. K is the gain and generally tuned by trial and error. In the present work, we input controls to z and pitch motion simultaneously. K was set to 2000. Figure 2.20 shows the numerical results of applying DF control to the tractor model.

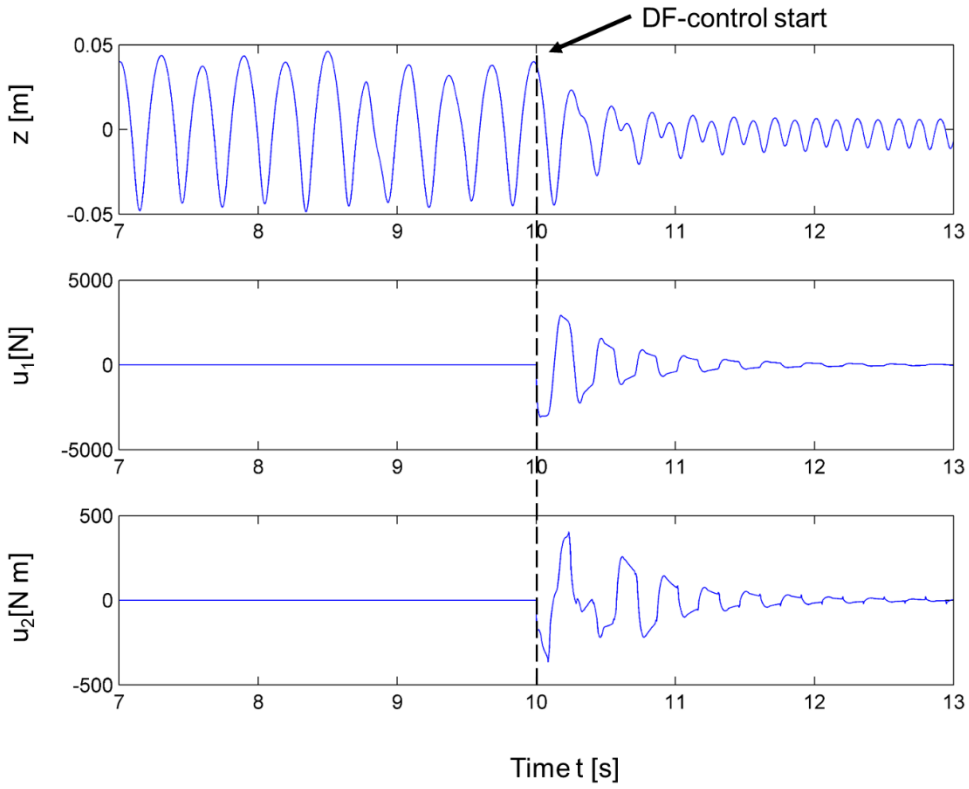

Figure 2.20 Numerical results of DF-control: (top) vertical motion z [m]; (middle) force input in the vertical equation; (bottom) torque input in the pitch equation.

At 10 seconds, the input force and moment were applied to the tractor and DF-control began. Chaotic vibration then became periodic vibration and the amplitude of vibration decreased simultaneously. These results are shown in Figure 2.21.

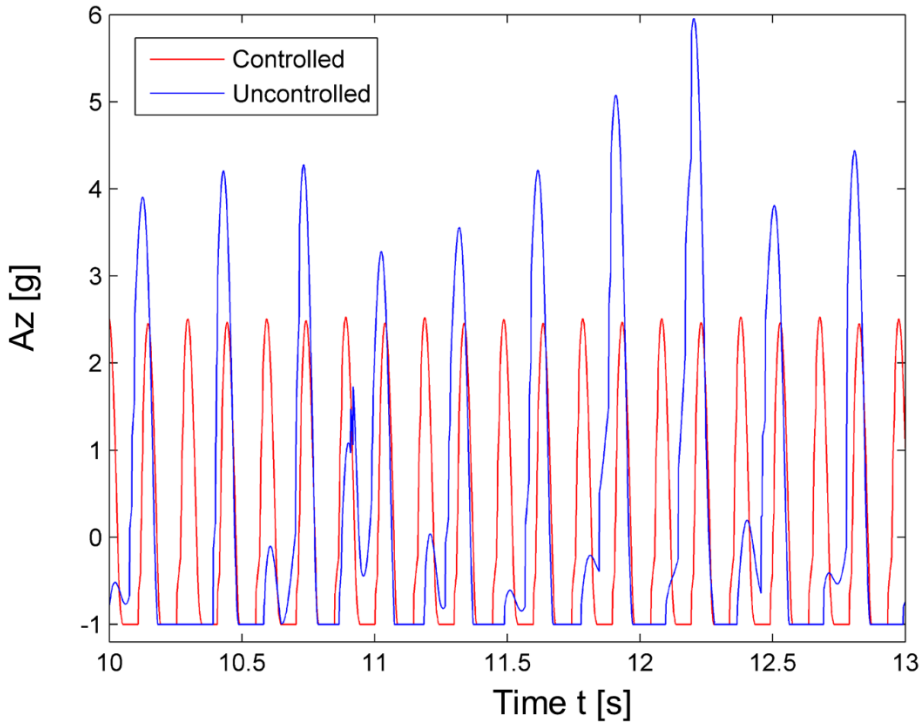

Figure 2.21 Numerical results of DF-control. Blue and red lines respectively show the uncontrolled and controlled vertical accelerations.

DF-control suppressed chaotic vibrations and reduced the amplitude of vibrations. These results indicate that DF-control suppresses the vibration level and removes chaotic behavior even though the tractor wheel lost contact with the ground and the bouncing phenomenon occurred.

2.5. Summary

In addition to the development of the bouncing tractor model, algorithms of P-control and DF control were developed to prevent an overturning accident due to the bouncing phenomenon. The obtained results indicate that P-control suppresses bouncing and DF-control removes chaotic behavior and suppresses the level of vibration. The use of the

developed algorithms is a promising approach to prevent tractor overturning accidents.

3. Steering instability induced by bouncing and sliding

3.1. Introduction

As discussed in Chapter 2, when the vertical loads on the wheels are reduced to zero, owing to road surface excitation, the wheel loses contact with the ground and jumping and hopping occur. The impact dynamics caused by bouncing are a great source of nonlinearity and dramatically deteriorate the tractor stability. In addition to this bouncing tractor dynamics, lateral sliding is another typical nonlinearity and can deteriorate the tractor stability as well. Although the vertical loads do not become zero, if the cornering forces exceed the limitation of the static friction, which is represented by the concept of the friction circle (Pacejk, 2005; Gillespie, 1992), dynamic friction occurs between the tire and the road surface, and the wheels of the tractor laterally slide. The operator cannot properly handle steering and the tractor posture dramatically deteriorates as a result of sliding.

As discussed above, the bouncing and sliding process can cause steering instability and overturning accidents. In fact, in a case study on farm accidents in Japan (Case study of farm accidents, 2013), tractor overturning occurred at steep passage slopes owing to the steering instability induced by bouncing and sliding. This bouncing and sliding combination may be a primary factor in the occurrence of overturning accidents. In addition to being a safety problem, this steering instability can also reduce the precision of the trajectory tracking used in autonomous operations (Han et al., 2019; Fang, Fan, Thuilot, Martinet, 2006).

The objective of this study was to numerically investigate the steering instability of a

tractor induced by bouncing and sliding. First, the bouncing and sliding model was developed by coupling the bouncing model (Watanabe & Sakai, 2019a) and bicycle model (Zhang & Qiu, 2004; Kayacan, Kayacan, Ramon, Saeys, 2015) based on Coulomb's classical theory of friction. Next, numerical experiments were conducted using the developed model under different operation scenarios: a turning test and operation on a passage slope. Turning test is one of typical evaluation method for vehicle performance and passage slope is a typical terrain condition where overturning accident occur. The conclusions drawn from this study are presented in the final section of this chapter.

3.2. Mathematical model

This section describes the development of the mathematical model by coupling the bouncing model and bicycle model to investigate steering instability. Three types of tire forces, namely, the vertical loads, cornering forces, and traction forces on the wheel, are coupled in the model based on Coulomb's classical theory of friction. In the modelling, it is assumed that travel velocity is constant, rolling motion is negligible, slip angle is equal in right and left tire, and C.G. point is fixed.

3.2.1. Bouncing tractor model

The two-dimensional bouncing model with two degrees of freedom, namely, the vertical motion z and pitch motion γ, was used to model the vertical loads on the wheels. Figure 3.1 (a) represents a schematic diagram of bouncing tractor model in sideview.

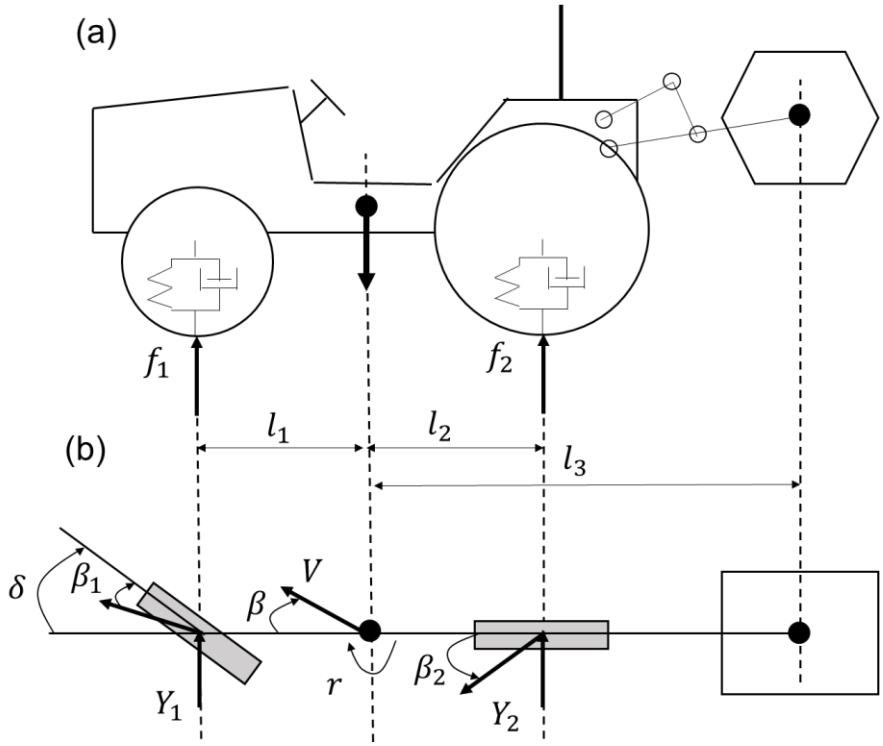

Figure 3.1 Developed mathematical model (a) Bouncing tractor model with two degrees of freedom: vertical motion *z* and pitch motion *γ*; (b) Bicycle model with two degrees of freedom: yaw rate *r* and slip angle *β*.

The model's motion equation is expressed as follows:

$$(\mathrm{M_T} + \mathrm{M_I})\ddot{z} = f_1 + f_2 - (\mathrm{M_T} + \mathrm{M_I})\mathrm{g} \tag{3.1}$$

$$\left(\mathrm{I_{yy}} + \mathrm{M_I}\mathrm{l_3^2}\right)\ddot{\gamma} = \mathrm{l_2}f_2 - \mathrm{l_1}f_1, \tag{3.2}$$

where the dot indicates differentiation with respect to time *t*.

The wheel has the characteristics of a linear spring and damper, and the vertical loads on the wheels, namely, f_1 and f_2, are expressed as follows:

$$f_i = \begin{cases} -\mathrm{k_i}(z_i - d_i) - \mathrm{c_i}(\dot{z}_i - \dot{d}_i), & \text{if the wheel is on the ground} \\ 0, & \text{if the wheel leaves the ground} \end{cases} \tag{3.3}$$

where i is an index for the wheels (i=1 or 2 corresponds to the front and rear wheel, respectively). Equation (3) expresses the bouncing or jumping of the tractor. When the wheel is in contact with the ground, the vertical loads on the wheels are equal to $-\mathrm{k_i}(z_i - d_i) - \mathrm{c_i}(\dot{z}_i - \dot{d}_i)$. When the vertical load on the wheel becomes zero and the wheel departs from the ground, the vertical loads on the wheels are set to zero. The theoretical details of the bouncing process are described in Chapter 2. The displacement of the wheels can be calculated as follows:

$$z_1 = z + \left(\mathrm{l_1} + \mathrm{l_3}\frac{\mathrm{M_I}}{\mathrm{M_T}+\mathrm{M_I}}\right)\gamma \tag{3.4}$$

$$z_2 = z - \left(\mathrm{l_2} - \mathrm{l_3}\frac{\mathrm{M_I}}{\mathrm{M_T}+\mathrm{M_I}}\right)\gamma \tag{3.5}$$

3.2.2. Bicycle model

The bicycle model was used to model the cornering force. Figure 3.1 (b) shows the schematic diagram of the bicycle model in top view. This model has two degrees of freedom: the vehicle slip angle β and yaw rate r. The bicycle model is generally used for modelling the lateral dynamics of vehicles including tractors. The equations of motion for the bicycle model are expressed as follows:

$$(\mathrm{M_T} + \mathrm{M_I})\mathrm{V}\left(\dot{\beta} + r\right) = Y_1 + Y_2 \tag{3.6}$$

$$(\mathrm{I_{zz}} + \mathrm{M_I}\mathrm{l_3^2})\dot{r} = \mathrm{l_1}Y_1 - \mathrm{l_2}Y_2, \tag{3.7}$$

The cornering forces Y_1, and Y_2 on the wheels are expressed as follows:

$$Y_1 = -\mathrm{C_{p,1}}\beta_1 = -\mathrm{C_{p,1}}(\beta + \frac{\mathrm{l_1}r}{\mathrm{V}} - \delta) \quad (3.8)$$

$$Y_2 = -\mathrm{C_{p,2}}\beta_2 = -C_{p,2}\left(\beta - \frac{\mathrm{l_2}r}{\mathrm{V}}\right), \quad (3.9)$$

In the equations, the cornering forces are linearly proportional to the slip angle of the wheel. When the tractor turns at travel velocity V, turning radius ρ, and turning angle X, the required steering angle δ and duration of steering $\mathrm{T_\delta}$ are calculated as follows:

$$\delta = \left(1 - \frac{(\mathrm{M_T}+\mathrm{M_I})(\mathrm{l_1 C_{p,1}} - \mathrm{l_2 C_{p,2}})}{2\mathrm{WB^2 C_{p,1} C_{p,2}}}\mathrm{V}^2\right)\frac{\mathrm{WB}}{\rho} \quad (3.10)$$

$$\mathrm{T_\delta} = \frac{\mathrm{X}\rho}{\mathrm{V}} \quad (3.11).$$

3.2.3. Coupling of bouncing and bicycle model

The bouncing and bicycle models were coupled based on Coulomb's classical theory of friction. Accordingly, the following inequality is satisfied when static friction occurs between the tire and the ground, and lateral sliding does not occur (Gillespie, 1992):

$$\sqrt{Y_i^2 + T_i^2} \leq \mu_\mathrm{s} f_i, \quad (3.12)$$

where μ_s is the static friction coefficient between the tire and the ground, and T_i is the traction force of the wheel. In this study, the tractor moved at constant velocity under motion and grade resistance. The traction force required for driving at constant velocity can be calculated as follows:

$$T_i = \mu_{\mathrm{r,i}} f_i + \frac{\mathrm{l_i}}{\mathrm{WB}} f_i \sin(\theta), \quad (3.13)$$

On the right side, $\mu_{r,i} f_i$ denotes the motion resistance and $\frac{l_i}{WB} f_i sin(\theta)$ denotes the grade resistance. The inequality in Equation (10) leads to the concept of a friction circle, whose schematic diagram is shown in Figure 3.2. The radius of the friction circle is $\mu_s f_i$. In Figure 3.2a, the components of the cornering force Y_i and traction force T_i are smaller than $\mu_s f_i$ ($\sqrt{Y_i^2 + T_i^2} \leq \mu_s f_i$). In this case, static friction occurs between the tire and the road and sliding does not occur. When the vertical loads on the wheel f_i decrease and the cornering force Y_i increases, as shown in Figure 3.2b, the force components exceed the limitation of static friction ($\sqrt{Y_i^2 + T_i^2} > \mu_s f_i$). In this case, dynamic friction occurs and lateral sliding ensues.

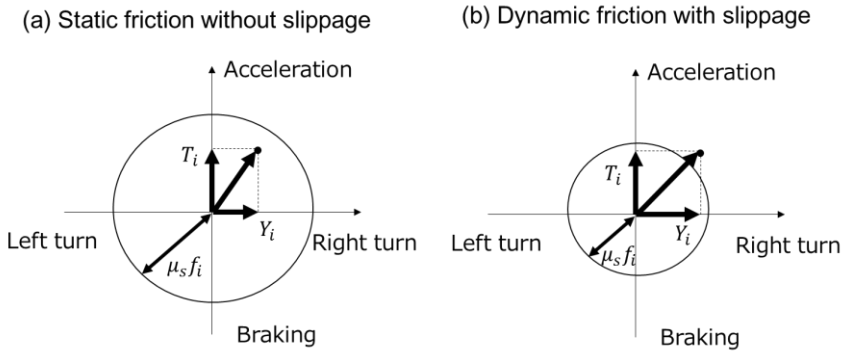

Figure 3.2 Schematic diagram of friction circle: (a) static friction without slippage; (b) dynamic friction with slippage.

The limitation of sliding is described as the maximum cornering force $Y_{max,\ i}$. The maximum cornering force can be calculated as follows:

$$Y_{max,i}(f_i) = \sqrt{\mu_s^2 f_i^2 - T_i^2} = f_i \sqrt{\mu_s^2 + \mu_{r,i}^2 + \frac{l_i^2 \sin^2\theta}{WB^2} + \frac{\mu_{r,i} l_i \sin\theta}{WB}} \quad (3.14)$$

This equation means that the maximum cornering force is a function of the vertical load on the wheel. Thus, the maximum cornering force $Y_{max,\,i}$ is not constant and varies during operations as the vertical load varies in response to the disturbance exciter under the effect of bumps or slopes. If the cornering force becomes smaller than the maximum cornering force ($Y_i < Y_{max,\,i}$), the inequality in Equation (3.10) is satisfied, and thus static friction occurs, which indicates that sliding does not occur. In contrast, if the cornering force is greater than the maximum cornering force ($Y_i > Y_{max,\,i}$), dynamic friction may occur between the tire and the ground, which indicates that sliding occurs.

According to the above discussion, we newly define the switching expression of the cornering force, as follows:

$$Y_i(t) = \begin{cases} -C_{p,i}\beta_i, & |C_{p,i}\beta_i| < Y_{max,i} \text{ (Static friction)} \\ \mathrm{sgn}(-\beta_i)|\mu_{d,i}Y_{max,i}|, & |C_{p,i}\beta_i| \geq Y_{max,i} \text{ (Dynamic friction)} \end{cases} \tag{3.15}$$

where sgn() is a sign function. When $|C_{p,i}\beta_i|$ is smaller than $Y_{i,\,max}$, the cornering force is calculated as $Y_i = -C_{p,i}\beta_i$ based on the conventional Equations (3.8) and (3.9). In contrast, when $|C_{p,i}\beta_i|$ is greater than $Y_{max,\,i}$, dynamic friction and sliding occur. In this case, the absolute value of the cornering force is $|\mu_{d,i}\ Y_{max,\,i}\ |$ and the direction of the cornering force is equal to $-\beta_i$. Based on this switching expression, the cornering force depends on the vertical load exerted on the wheel, and the vertical dynamics and lateral dynamics are coupled based on Coulomb's friction theory.

3.3. Numerical experiments

This section describes the numerical experiments conducted to investigate the

bouncing and sliding influence on the steering stability. In the numerical experiments, the developed model was numerically solved by the fourth-order Runge-Kutta method. Table 3.1 presents the parameter specification for the typical Japanese small tractor and farm field (Bukta, Sakai, Sasao, Shibusawa., 2002; Umeda & Honami, 1975; Sakai & Terao, 1987) considered in the simulation. In this study, the dynamic friction coefficient μ_d was set to 80% of the static friction coefficient μ_s (Serway, & Jewett, 2010).

Table 3.1 Parameter specification of tractor considered in numerical experiments (Bukta, Sakai, Sasao, Shibusawa, 2002; Umeda & Honami, 1975; Sakai & Terao, 1987).

Parameters	Symbol	Value	Unit
Stiffness of front wheel	k_1	200	kN m^{-1}
Stiffness of rear wheel	k_2	260	kN m^{-1}
Damping coefficient of front wheel	c_1	5500	N s m^{-1}
Damping coefficient of rear wheel	c_2	6690	N s m^{-1}
Cornering power of front wheel	$C_{p,1}$	218.54	N deg^{-1}
Cornering power of rear wheel	$C_{p,2}$	435.12	N deg^{-1}
Mass of tractor body	M_T	988	kg
Mass of implement	M_I	184	kg
Pitch moment of inertia	I_{yy}	700	kg m^2
Yaw moment of inertia	I_{zz}	700	kg m^2
Distance between centre of gravity of the tractor body and front wheel	l_1	0.68	m
Distance between centre of gravity of the tractor body and rear wheel	l_2	0.70	m

Wheelbase of the tractor	WB	1.38	m
Distance between centre of gravity of the tractor body and the centre of gravity of implement	l_3	1.24	m
Motion resistance coefficient of front wheel	$\mu_{r,1}$	0.12	-
Motion resistance coefficient of rear wheel	$\mu_{r,2}$	0.12	-

In these experiments, two different types of tractor operations, namely, a turning test and operation on a steep passage slope, were performed.

3.3.1. Turning test

The numerical turning tests were conducted to investigate the basic steering performance of the developed model, and the bouncing and sliding effect on the steering stability. The half-sine-shaped bump, which is generally used by the tractor disturbance exciter (Pershing & Yoerger, 1969; Li, Mitsuoka, Inoue, Okayasu, Hirai, 2015) was placed on the field as an obstacle. The bump is expressed as follows:

$$d(x) = \frac{d_0}{2}\left(1 - \cos\left(\frac{2\pi x}{l_b}\right)\right), \tag{3.14}$$

The bump length l_b was set to 0.5 m and the turning radius was set to 3.5 m. The tractor's travel velocity V and static friction coefficient μ_s were considered as the control parameters.

In the numerical experiments, three typical types of turning were observed: the desired turning without steering instability, turning with steering instability, and turning failure

owing to steering instability. Figure 3.3 shows these representative turning trajectories under a constant travel velocity V of 2.8 m s^{-1}.

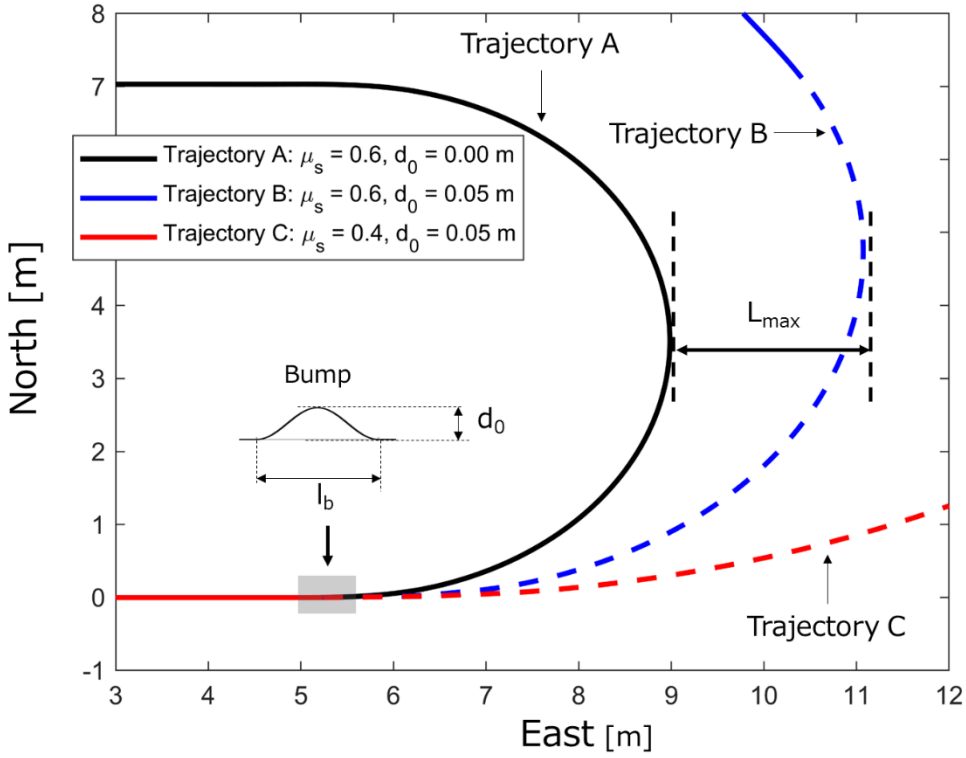

Figure 3.3 Turning trajectories of tractor in turning test; solid line and dashed line indicate stable and unstable steering, respectively; trajectory A (μ_s=0.6 and d_0=0.00 m) represents desired turning without steering instability; trajectory B (μ_s=0.6 and d_0=0.05 m) represents turning with steering instability; trajectory C (μ_s=0.4, d_0=0.05 m) represents turning failure.

In Figure 3.3, the lines are shown as a solid or dashed line indicating when the tractor steering was stable or unstable, respectively. Trajectory A represents the desired turning without steering instability. When μ_s was 0.6 and d_0 was 0.00 m, there was no bump exciter and steering instability did not occur. Thus, the maximum lateral difference from the desired trajectory L_{max} was 0 m. In contrast, bouncing and sliding gave rise to steering

instability, and the tractor trajectory deviated outward from the desired turning trajectory after the tractor moved onto the bump shown as Trajectory B in Figure 3.3.

In this case, the tractor trajectory deviated from the desired trajectory and L_{max} was 1.91 m. Contrary to the abovementioned results, the steering instability in Trajectory C was too severe for turning. In this case, it was impossible for the tractor to turn, and therefore L_{max} could not be defined.

Then, the time series of the numerical results between Trajectory A and C were compared to demonstrate the difference between stable and unstable steering. Figure 3.4 shows the vertical load on the front wheel f_1 at the top, the grip margin of the front wheel ε_1 in the middle, and the cornering force on the front wheel Y_1 at the bottom.

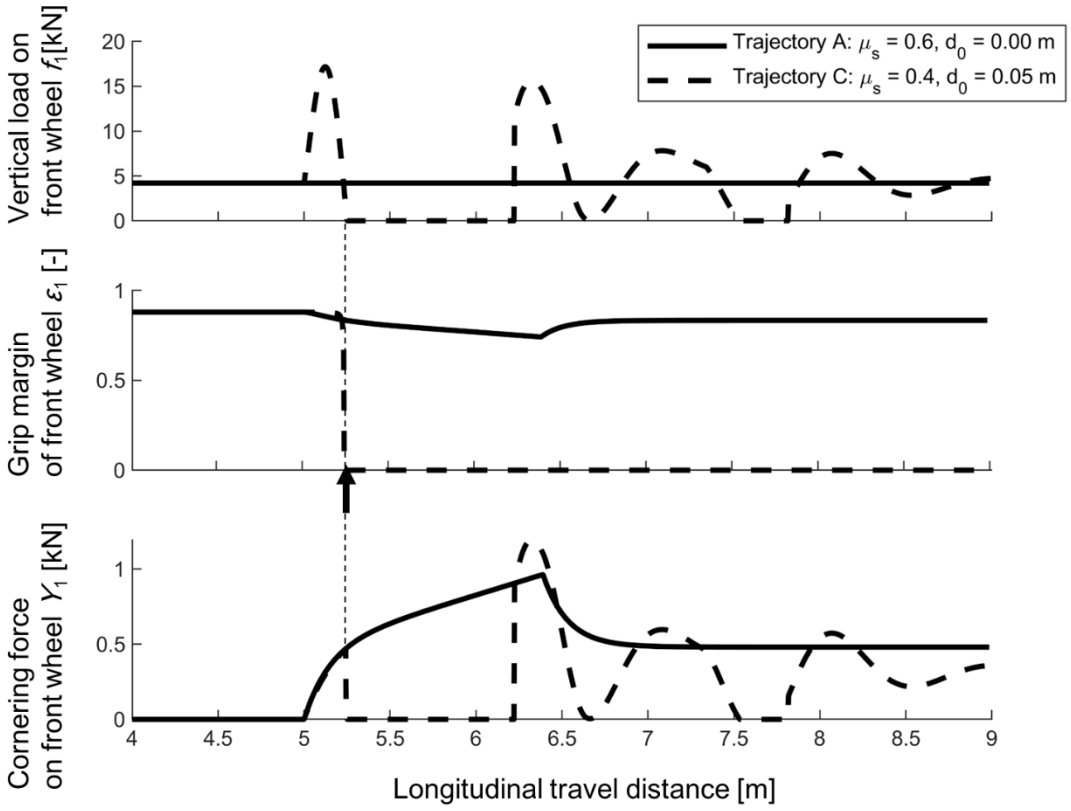

Figure 3.4 Numerical results of Trajectory A and C in numerical turning test experiment; solid line and dashed line indicate Trajectory A and C results,

respectively. Top: vertical load on front wheel f_1. Middle: grip margin of front wheel ε_1. Bottom: Cornering force on front wheel Y_1.

The grip margin ε_i is typically used to evaluate the steering stability in vehicle dynamics research (Ono, Hattori, Muragishi, Koibuchi, 2006). The grip margin ε_i is calculated as follows;

$$\varepsilon_i = 1 - \frac{\sqrt{T_i^2 + Y_i^2}}{\mu_s f_i} \tag{3.15}$$

The grip margin ε_i ranges from 0 to 1 and indicates the margin from the sliding. A smaller value of ε_i indicates that the tire is close to the limit of static friction, and lateral sliding occurs when ε_1 becomes zero. If ε_1 becomes zero, ε_1 is set to zero until the sliding ends.

For Trajectory A, the vertical load f_1 was constant because there was no road excitation. Therefore, the grip margin was relatively high and did not reach zero, which corresponds to the fact whereby steering instability did not occur. In contrast, for Trajectory C, the vertical load f_1 varied owing to the excitation. Then, as indicated by the arrow, the vertical load f_1 and grip margin ε_1 simultaneously became zero, and bouncing and sliding occurred. This process led to the reduction of the cornering force to zero and the occurrence of steering instability.

In the parametric investigation, the travel velocity V and static friction coefficient μ_s were considered as the control parameters. Figure 3.5 shows the L_{max} value in each numerical experiment.

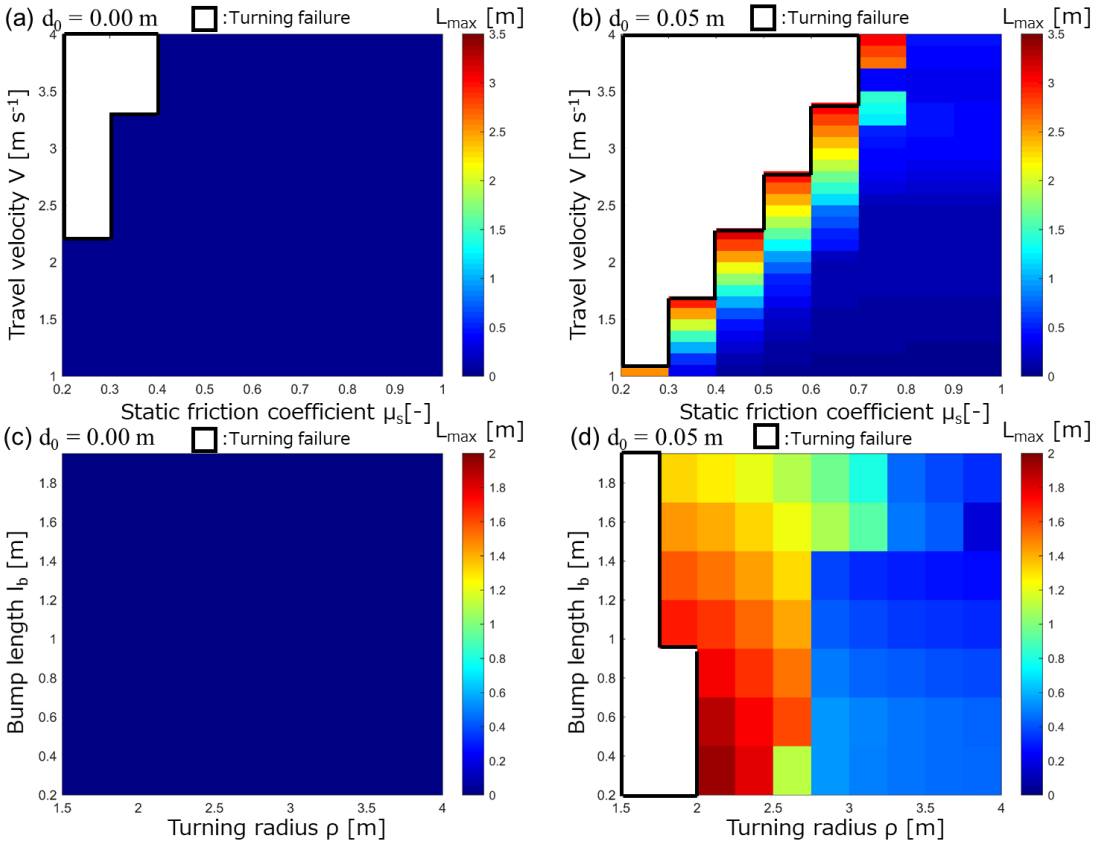

Figure 3.5 Maximum lateral difference from the desired trajectory L_{max} for different travel velocities V, friction coefficients μ_s, bump length l_b, and turning radius ρ; white blank areas represent that L_{max} could not be defined owing to the failure of the tractor to turn; (a) d_0 = 0.00 m, l_b = 0.5 m, and ρ= 3.5 m; (b) d_0 = 0.05 m, l_b = 0.5 m, and ρ= 3.5 m; (c) d_0 = 0.00 m, V = 3.0 m s^{-1}, and μ_s = 0.6; (d) d_0 = 0.05 m, V = 3.0 m s^{-1}, and μ_s = 0.6.

For the results presented in Figs. 3.5 (a) and (b), the travel velocity V and static friction coefficient μ_s were taken as control parameters while the turning radius ρ and bump length l_b were respectively fixed at 3.5 and 0.5 m. When the bump height was 0.00 m in Fig. 3.5 (a), L_{max} = 0.00 m under all combinations of V and μ_s except for combinations of a lower friction coefficient and higher travel velocity; i.e., μ_s = 0.2, V > 2.2 m s^{-1} and μ_s = 0.3, V > 3.3 m s^{-1}. In this region, the tractor could not turn and L_{max} was not defined, which is depicted as a white blank in Fig. 5. In Fig. 3.5 (b), the area within which the tractor could not turn is enlarged, and it is seen that L_{max} tended to increase overall. In particular, turning was impossible under the lowest friction coefficient of μ_s = 0.2 at a travel velocity other than V = 1.0 m s^{-1}. The steering stability improved as μ_s increased. The tractor did

not become incapable of turning, and L_{max} was relatively small when μ_s was greater than 0.7. In addition to the friction coefficient being lower, the higher travel velocity strongly reduced the steering stability at $\mu_s < 0.7$. In the results presented in Fig. 3.5 (c) and (d), the bump length l_b and turning radius ρ were taken as control parameters while the travel velocity V and static friction coefficient μ_s were respectively fixed at 3.0 m s^{-1} and 0.6. Figure 3.5 (c) shows that there was no steering instability for any combination of parameters under $d_0 = 0.00$ m. Figure 3.5 (d) shows that when the tractor traversed a bump, a region in which the tractor was not able to turn appeared and L_{max} tended to increase. Steering instability increased as the turning radius decreased. The tractor was not able to turn at $\rho < 2.0$ m. As well as the turning radius decreasing, steering became unstable at a lower bump length l_b. The abovementioned results indicate that the existence of a small bump caused bouncing and sliding, which resulted in severe steering instability, particularly under unfavourable road and driving conditions such as a higher travel velocity, and lower friction coefficient, turning radius, and bump length.

3.3.2. Operation on steep passage slope

In the case study on farm accidents conducted by the Japanese government (Case study of farm accidents, 2013), tractor overturning accidents occurred on a passage slope with steepness of 19° from a paddy field to a farm road. From the farm field, the tractor ran onto the slope at constant travel velocity. Then, the operator attempted to turn right onto the road. However, the vertical loads on the wheels decreased to zero or became sufficiently low to cause lack of stability, and bouncing and sliding occurred during the operation. Thus, this process induced steering instability, the tractor fell from the road, and overturning occurred. The details of this accident have been reported by Watanabe and Sakai (2019a). In this study, the numerical experiments for the tractor's operation on the passage slope were based on the abovementioned case. The length of slope l_s=2.0 m and angle of slope θ=19° are the same as in the accident case. In the numerical experiments, the travel velocity was 1.5 and 3.0 m s^{-1} for the low and high velocity

condition, respectively, and the static friction coefficient μ_s was 0.8 and 0.4 for the preferable and adverse road condition, respectively. Figure 3.6 shows the turning trajectories on the slope for each simulation.

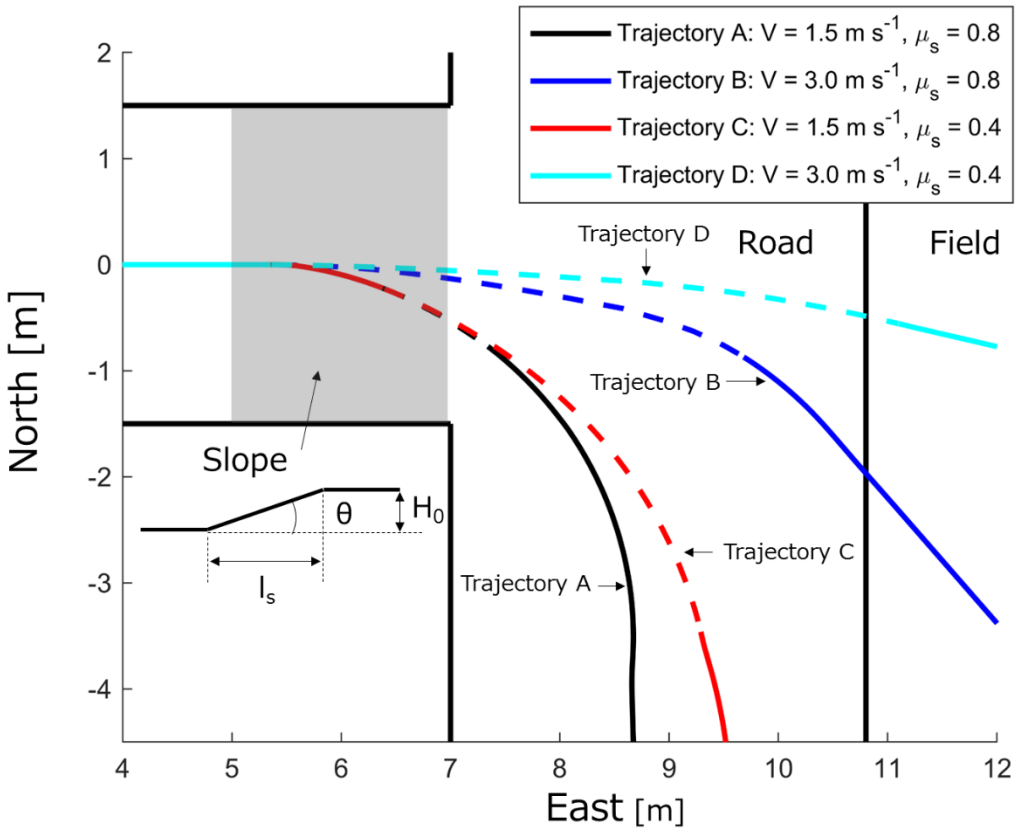

Figure 3.6 Tractor trajectories with different travel velocity and friction coefficient; solid line and dashed line indicate stable and unstable steering, respectively; Trajectory A under V=1.5 m s^{-1} and μ_s=0.8; Trajectory B under V=3.0 m s^{-1} and μ_s=0.8; Trajectory C under V=1.5 m s^{-1} and μ_s=0.4; Trajectory D under V=3.0 m s^{-1} and μ_s=0.4.

When the travel velocity V was 1.5 m s^{-1}, the turning trajectories were on the road throughout the entire simulation in Trajectories A and C, but steering instability occurred in Trajectory C. When the travel velocity was V=3.0 m s^{-1}, the tractor trajectory dramatically deviated outward and the turning radius of the trajectories became larger in

Trajectories B and D. Particularly, in Trajectory D, the steering instability continued until the tractor reached the edge of the road.

Figure 3.7 shows the comparison between the numerical results obtained for Trajectories B and D to illustrate the influence of μ_s on the steering stability. Figure 3.7 shows the vertical load on the front wheel f_1 at the top, grip margin of the front wheel ε_1 in the middle, and cornering force on the front wheel Y_1 at the bottom.

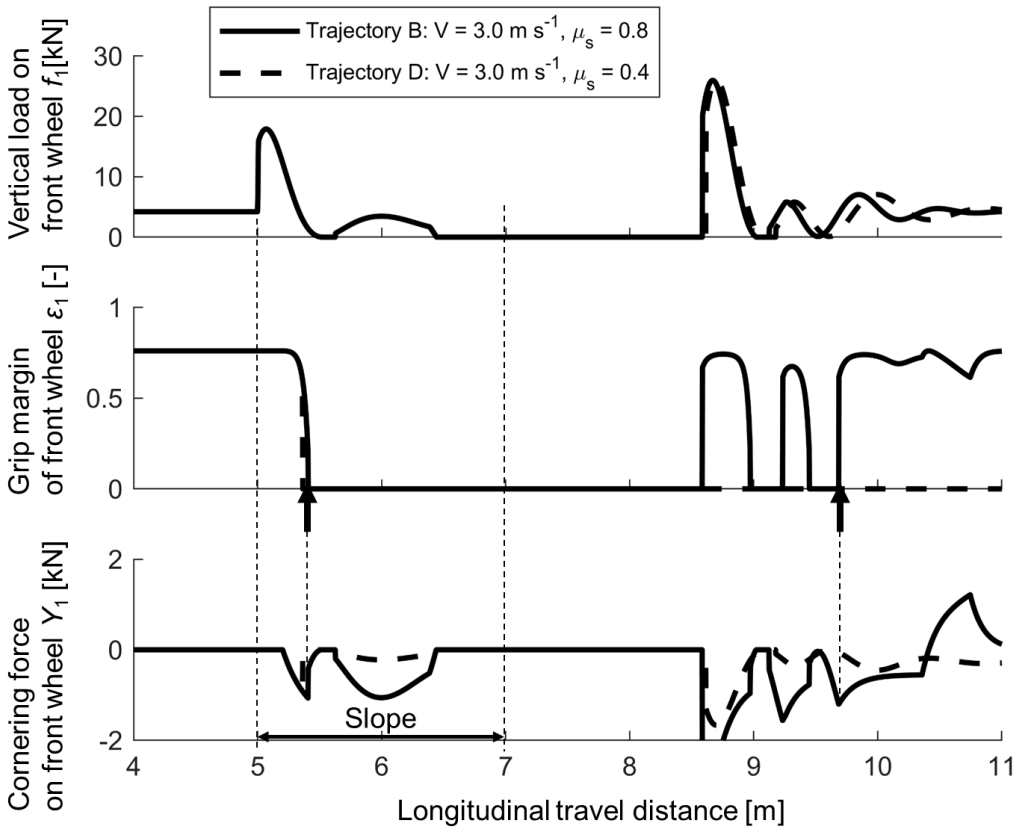

Figure 3.7 Numerical results for Trajectories B and D in numerical experiments for operation on passage slope. Top: vertical load on front wheel f_1. Middle: grip margin of front wheel ε_1. Bottom: cornering force on front wheel Y_1.

As indicated by the left arrow, the grip margin ε_1 became zero almost simultaneously in Trajectory B and D after the tractor moved onto the slope. However, the steering became

stable, as indicated by the right arrow in Trajectory B, while the steering instability continued in Trajectory D, and resulted in a severe difference of the turning trajectories between Trajectories B and D, as shown in Figure 3.6. According to the results shown in Figure 3.6 and 3.7, in case of Trajectory A, B, and C, there are longitudinal margin to the edge of the road although the steering instability occurred. Therefore, the operator may be able to avoid accident by steering. On the other hand, in case of Trajectory D, the steering instability continued to the edge of the road. Thus, it was inferred that, when steering instability occurs under low friction and high travel velocity conditions, the operator cannot properly handle the tractor and an overturning accident may occur.

In the numerical results presented in Section 3.1 and 3.2, the vertical load f_1 and grip margin μ_s decreased to zero and bouncing and sliding occurred owing to the road surface excitation caused by the bump and slope. This process reduced the cornering force Y_1 and caused steering instability. In particular, the steering stability was very vulnerable to the excitation under the unfavourable combination of terrain and driving conditions, namely, the higher travel velocity and lower friction coefficient. The results obtained in this study strongly indicate that, in Japan, this steering instability may be a possible cause of tractor overturning accidents from the viewpoint of a harsh terrain environment and higher tractor working speed.

3.4. Summary

This study numerically investigated the steering instability of a tractor using a novel dynamic tractor model. The numerical results revealed that the combination of bouncing and sliding can dramatically deteriorate the steering stability and may cause overturning accidents under unfavourable terrain and driving conditions. Although our developed

simple model shed light on a new aspect of overturning accidents, real tractor dynamic behaviour is complex because it involves rolling and a power train system. Further investigations of complex parametric combinations are therefore necessary. This task could be carried out using a virtual test drive using a driving simulator that is generally employed by the automotive industry (Yoon, Cho, Kang, Koo, Yi, 2010). In a virtual test drive, control algorithms, such as those of active steering and brake control, could be developed to avoid or prevent steering instability.

4. Power hop model

4.1. Introduction

The power hop phenomenon has been observed ever since the four-wheel-drive (4WD) tractor was introduced in the 1950s in North America. According to Wiley and Turner (2008), though power hop can occur for a two-wheel-drive (2WD) tractor in a high-pull-condition test, it is extremely rare in practical field operation. Power hop excites pitch and bounce oscillations that reduce the tractor performance and ride quality and increase damage to the tractor body, operator injury, and soil compaction. Power hop is not a forced oscillation like road lope but a self-excited oscillation that happens when the tractor delivers power to the ground. As the self-excited oscillation gradually becomes severe, the tractor tire loses contact with the ground and the tractor jumps. This impact process generates excessive vibrations and reduces steering stability, possibly resulting in fatal accidents. The mathematical model for power hop must represent these characteristic dynamics. Several mathematical models have been proposed for predicting and controlling power hop. Linear and nonlinear analytical models with two degrees of freedom, namely vertical and pitch motion, have been developed (Wiely & Turner, 2008, Flaugh, 2011). In this modelling, root locus stability analysis was conducted and sufficient and necessary conditions for stability were obtained. Only vertical tire stiffness was considered in the above analytical studies though Zoz (2007) mentioned the importance of longitudinal tire stiffness to power hop dynamics.

In power hop dynamics, nonlinear phenomena, including stick-slip oscillation, impact dynamics, and free-play in the joint, have been observed although they were not incorporated in the abovementioned conventional models. Modelling of these nonlinear

phenomenon is essential to clarify the occurrence mechanism of power hop and to prevent it. Models for each nonlinear phenomenon have been developed in different studies as follows. Longitudinal stick-slip dynamics of the tire and ground surface have been considered a possible cause of self-excited oscillation (Volfson, 1999; Sakai, et al., 1998; Sakai, Upadhyaya, Andrade-Sanches, Sviridova, 2017). Stick–slip oscillation is a typical source of self-excited oscillations and nonlinear elements in the mechanical system (Leine, Campen, Kraker, Steen, 1998; Galvanetto, 2004; Elmer, 1997). Although several stick-slip models for power hop have been developed, the stick-slip model alone is unable to represent the power hop phenomenon. Other nonlinear elements, namely the tractor jumping and free-play in the joint, are essential in formulating the power hop.

Impact dynamics generated by the jumping or bouncing of a tractor are another important aspect of power hop instability. A bouncing tractor is a typical nonlinear impact oscillator and thus has dynamics similar to those of a bouncing ball (Gilet et al., 2009, Holmes, 1982, Hubert et al., 2014, Luck and Mehta, 1993, Luo and Han, 1996). We intensively investigated the bouncing of a tractor in response to a forced road surface in previous studies (Garciano, Sakai,&Torisu,2005, Sakai, 1999, Sakai, Sasao, Shibusawa,& Bukta, 2000, Watanabe, Bauerdick, Sakai,& Bernhardt, 2018, Watanabe &Sakai, 2019a, 2019b, Watanabe & Sakai, 2020). These studies showed that nonlinear effects induced by bouncing drastically deteriorate the stability of tractor dynamics and should not be neglected in modelling.

Free-play in the joint between a tractor and implement is another nonlinear element of tractor dynamics (Collins, 1991, Bukta, Sakai, Sasao, Shibusawa, 2000, Sakai & Aihara, 1999, Sakai & Aihara, 1994). Free-play in the joint gives flexibility between the tractor and implement and strongly affects the tractor dynamics. Free-play is thus another

important factor in representing power hop.

According to the above discussion, a novel nonlinear model for power hop should include bouncing and free play in addition to stick-slip dynamics. The development of a mathematical model for power hop is essential for understanding, predicting, and control of power hop. The present paper couples these three nonlinear elements and develops a novel power hop model for time-domain simulation. The structure of the remainder of the paper is as follows. In Section 4.2, a mathematical model with three degrees of freedom—vertical, longitudinal, and pitch motion—is developed by coupling bouncing, stick–slip dynamics, and free play. In Section 4.3, the results of numerical experiments are reported for various towing, soil, and tire conditions. In the final section, concluding remarks based on the results of the numerical experiments are made.

4.2. Modelling of power hop

In this section, a novel nonlinear mathematical model for power hop is developed. Nonlinear elements, that is bouncing, stick–slip dynamics, and free-play, are modelled and coupled to describe power hop dynamics.

Figure 4.1 is a schematic diagram of the tractor model employed in this study.

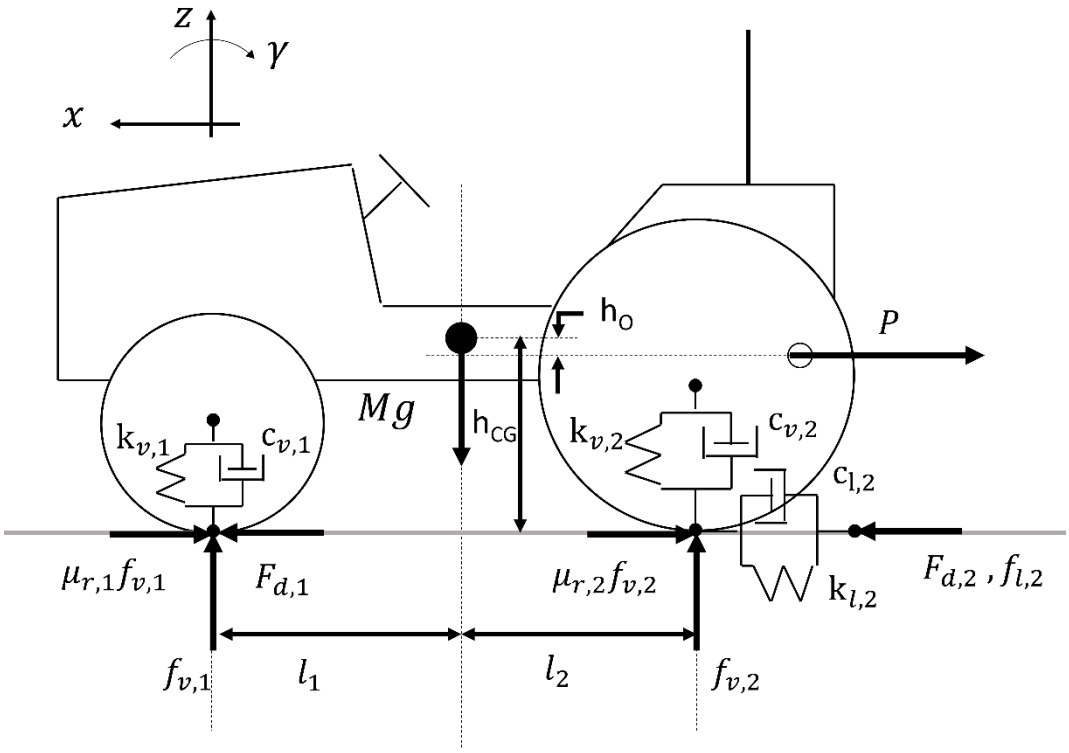

Figure 4.1 Schematic diagram of tractor power hop with three degrees of freedom, i.e., vertical, longitudinal, and pitch motion.

A two-dimensional model is employed to describe power hop. The modelling assumes that rolling and yawing motion is negligible, the draft load is applied horizontally with respect to the vehicle (i.e., there is no inclination), the vehicle operates on a flat surface, and the centre of the gravity of the tractor is fixed during operation. The model has three degrees of freedom, i.e., vertical, longitudinal, and pitch motion. The vertical and longitudinal tire characteristics are represented by a linear spring and damper. The equations of motion are

$$M\ddot{z} = f_{v,1} + f_{v,2} - Mg, \tag{4.1}$$

$$I_{xx}\ddot{\gamma} = l_1 f_{v,1} - l_2 f_{v,2} + \left(F_{d,1} + F_{d,2} - \mu_{r,1} f_{v,1} - \mu_{r,2} f_{v,2} + f_{l,2}\right) h_{CG} - h_0 P, \tag{4.2}$$

$$M\ddot{x} = F_{d,1} + F_{d,2} - \mu_{r,1} f_{v,1} - \mu_{r,2} f_{v,2} + f_{l,2} - P. \quad (4.3)$$

where z is vertical motion, γ is pitch motion, x is longitudinal motion, M is mass of the tractor, I_{yy} is pitch moment of inertia, g is gravitational acceleration, l_1 is longitudinal distance between tractor centre of gravity and front wheel axis of rotation, l_2 is longitudinal distance between tractor centre of gravity and rear wheel axis of rotation, $\mu_{r,1}$ is motion resistance coefficient on front tyres, $\mu_{r,2}$ is motion resistance coefficient on rear tyres, h_{CG} is height of centre of gravity above ground, h_o is vertical distance of centre of gravity to drawbar hitch point, $f_{v,1}$ is total vertical load on all front tyres, $f_{v,2}$ is total vertical load on all rear tyres, $f_{l,2}$ is total longitudinal load on all rear tyres, $F_{d,1}$ is total tractive force on all front tyres, and $F_{d,2}$ is total tractive force on all rear tyres, P is draft load.

4.2.1. Bouncing modelling

Tires of the tractor occasionally lose contact with the ground, and the tractor bounces or jumps. In the case of bouncing, vertical loads acting on the wheels are modelled as those of an impact oscillator. The vertical loads acting on the wheels $f_{v,1}$ and $f_{v,2}$ are expressed as

$$f_{v,i} = \begin{cases} -k_{v,i} z_i - c_{v,i} \dot{z}_i, & \text{if the wheel is in contact with the ground} \\ 0, & \text{if the wheel loses contacts with the ground} \end{cases} \quad (4.4)$$

where i is index for front and rear (i = 1 and 2 refer front and rear respectively), z_i is vertical position of the wheels, $k_{v,i}$ is total vertical stiffness at the axles, and $c_{v,i}$ is total vertical damping coefficient at the axles. This switching equation represents the bouncing of the agricultural tractor. The vertical load equals $-k_{v,i} z_i - c_{v,i} \dot{z}_i$ when the wheel is in

contact with the ground. Once the wheel loses contact with the ground, the vertical load is set to zero. The bouncing model was described in detail by Watanabe and Sakai (2019). The longitudinal force $f_{l,2}$ is similarly calculated as

$$f_{l,2} = \begin{cases} -\mathrm{k}_{l,2}x - \mathrm{c}_{l,2}\dot{x}, & \text{if the wheel is in contact with the ground} \\ 0. & \text{if the wheel loses contacts with the ground} \end{cases} \tag{4.5}$$

where $\mathrm{k}_{l,2}$ is total longitudinal stiffness at the rear axle, and $\mathrm{c}_{l,2}$ is total vertical damping coefficient at the rear axle.

4.2.2. Stick-slip modelling

When the tractive force exceeds the limit of static friction, the static friction acting between the tire and ground becomes dynamic friction, and the intermittent switching of static and dynamic friction ensues. This stick-slip oscillation is a major factor in power hop. The tractive force required for overcoming the draft load P and motion resistance $\mu_{r,i}$ $f_{v,i}$ is calculated as

$$F_{\mathrm{d,i}} = \begin{cases} \frac{P}{2} + \mu_{r,i}f_{v,i}, & |F_{\mathrm{d},i}| \le \mu f_{v,i} \text{ (Stick)} \\ \mathrm{sgn}(\mathrm{F_{d,i}}) * \mu_d f_{v,i}, & |F_{\mathrm{d},i}| > \mu f_{v,i} \text{ (Slip)} \end{cases} \tag{4.6}$$

where sgn() is sign function and μ is static friction coefficient. In modelling of the tractive force, the stick-slip dynamics are incorporated adopting Coulomb's classical friction theory; e.g., using a friction circle (Pacejka, 2005, Gillespie, 1992, Watanabe & Sakai, 2020). If $F_{\mathrm{d,i}}$ is less than $\mu f_{\mathrm{v,i}}$, which is the static friction limitation ($|F_{\mathrm{d},i}| \le \mu f_{v,i}$), stick or static friction occurs and $F_{\mathrm{d,i}}$ is set to $\frac{P}{2} + \mu_{r,i}f_{v,i}$, which is the required force for

traction with constant velocity. There is slip or dynamic friction when the driving force $F_{\mathrm{d,i}}$ exceeds the static friction limitation ($|F_{\mathrm{d,i}}| > \mu f_{v,i}$). In this case, the tractive force $F_{\mathrm{d,i}}$ is proportional to the vertical load $f_{v,i}$. This switching of static and dynamic friction modelling is typical stick-slip motion modelling.

4.2.3. Free-play modelling

There is free-play in the joint between the tractor and implement. The draft load P is thus not constant but can be modelled using a dead zone, which is typical modelling for backlash in gears (Nordin, Galic, & Gutman, 1997). The draft load P is calculated as

$$P = \begin{cases} \mathrm{P_0}, & \mathrm{x} > \mathrm{d} \\ 0, & \mathrm{x} \leq \mathrm{d} \end{cases} \tag{4.7}$$

where $\mathrm{P_0}$ is original draft load and d is joint clearance. If the longitudinal displacement of the tractor x is less than the joint clearance between the tractor and implement d, the draft load P equals zero. If the longitudinal displacement of the tractor x is greater than the clearance of the joint between the tractor and implement, the draft load P equals the original draft load $\mathrm{P_0}$.

Table 4.1 gives the tractor specifications of a typical large tractor (Collins, 1991, Flaugh, 2011) used in the numerical experiments.

Table 4.1 Parameter specifications of the tractor considered in numerical experiments (Collins, 1991, Flaugh, 2011).

Parameters	Symbol	Value	Unit
Total vertical stiffness at the front axle	$k_{v,1}$	550,000	N m^{-1}
Total vertical stiffness at the rear axle	$k_{v,2}$	600,000	N m^{-1}

Total longitudinal stiffness at the rear axle	$k_{l,2}$	646,000	N m^{-1}
Total vertical damping coefficient at the front axle	$c_{v,1}$	2350	N s m^{-1}
Total vertical damping coefficient of rear wheel	$c_{v,2}$	5000	N s m^{-1}
Total vertical damping coefficient at the rear axle	$c_{l,2}$	3278	N s m^{-1}
Tractor mass	M	4060	kg
Pitch moment of inertia	I_{yy}	6473	kg m^2
Longitudinal distance between tractor centre of gravity and front wheel axis of rotation	l_1	1.262	m
Longitudinal distance between tractor centre of gravity and rear wheel axis of rotation	l_2	1.174	m
Wheelbase of the tractor	WB	1.38	m
Height of tractor centre of gravity above the ground	h_{CG}	0.886	m
Vertical distance from tractor centre of gravity to drawbar hitch point	h_o	0.516	m
Motion resistance coefficient of front tyres	$\mu_{r,1}$	0.12	-
Motion resistance coefficient of rear tyres	$\mu_{r,2}$	0.12	-

4.3. Numerical experiments

This section reports on numerical experiments conducted for various towing, soil, and tire conditions to investigate power hop dynamics. The developed model was numerically solved adopting the fourth-order Runge–Kutta method. The time step was 0.001 s in simulations. In a parametric investigation, the original draft load P_0, joint clearance d,

traction ratio μ, ratio of static and dynamic friction coefficients R_μ, front-tire stiffness $k_{v,1}$, and rear-tire stiffness $k_{v,2}$, $k_{l,2}$ were taken as control parameters.

4.3.1. Occurrence process of power hop

Numerical experiments were conducted to demonstrate the occurrence process of power hop. The simulation time was 20 s. Transitional and steady-state power hop dynamics were investigated. In the experiments, the draft load *P* was taken as a control parameter and other parameters were fixed as d = 0.015, μ = 0.3, R_μ = 0.6, $k_{v,1}$ = 550,000, $k_{v,2}$ = 600,000, and $k_{v,3}$ = 646,000.

The original draft load P_0 was increased from 0 to 10 kN in a period of 3.0 s and then held constant at 10 kN to investigate the transitional and steady-state behaviours of the power hop dynamics. Figure 4.2 shows the transitional state power hop. In the figure, the upper graph shows the draft load *P*, the middle graph shows tractive force acting on the front tyres $F_{d,1}$, and the bottom graph shows and tractive force acting on the rear tyres $F_{d,2}$. In the graph, the static friction limitation of the front tyres $\mu f_{v,1}$ and the static friction limitation of the rear tyres $\mu f_{v,2}$ are shown as red lines.

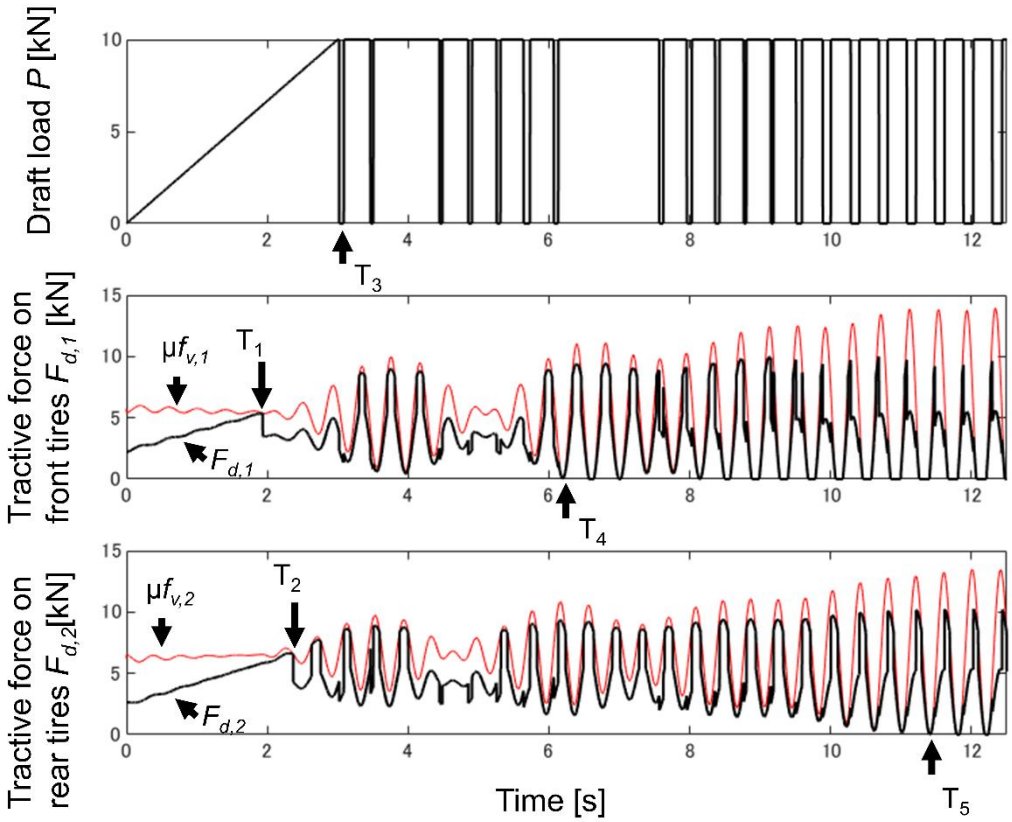

Figure 4.2 Transitional behaviour of power-hop dynamics; Top: Draft load *P* [kN]: Middle: Tractive force acting on the front wheel $F_{d,1}$ [kN] and static friction limitation of the front tyres $\mu f_{v,1}$; Bottom: Tractive force acting on the front tyres $F_{d,2}$ [kN] and static friction limitation of the front tyres $\mu f_{v,2}$.

Figure 4.2 shows that the tractive forces acting on the front and rear tyres $F_{d,1}$, $F_{d,2}$ increased as the draft load P increased. At the point T_1, $F_{d,1}$ reached the limitation of the static friction $\mu f_{v,1}$ and there was stick–slip oscillation. This oscillation leads to variation of the vertical loads $f_{v,1}$, $f_{v,2}$ and tractive forces $F_{d,1}$, $F_{d,2}$. Additionally, this variation in vertical loads and tractive forces excited stick-slip oscillation inversely. In particular, variation in the vertical load acting on the rear tyres caused the stick slip dynamics of the rear tyres at the point T_2. Figure 4.3 presents an enlargement of the tractive forces acting on the front tyres $F_{d,1}$ and the tractive force acting on the rear tyres $F_{d,2}$ to show more

clearly the abovementioned occurrence of the process of stick and slip.

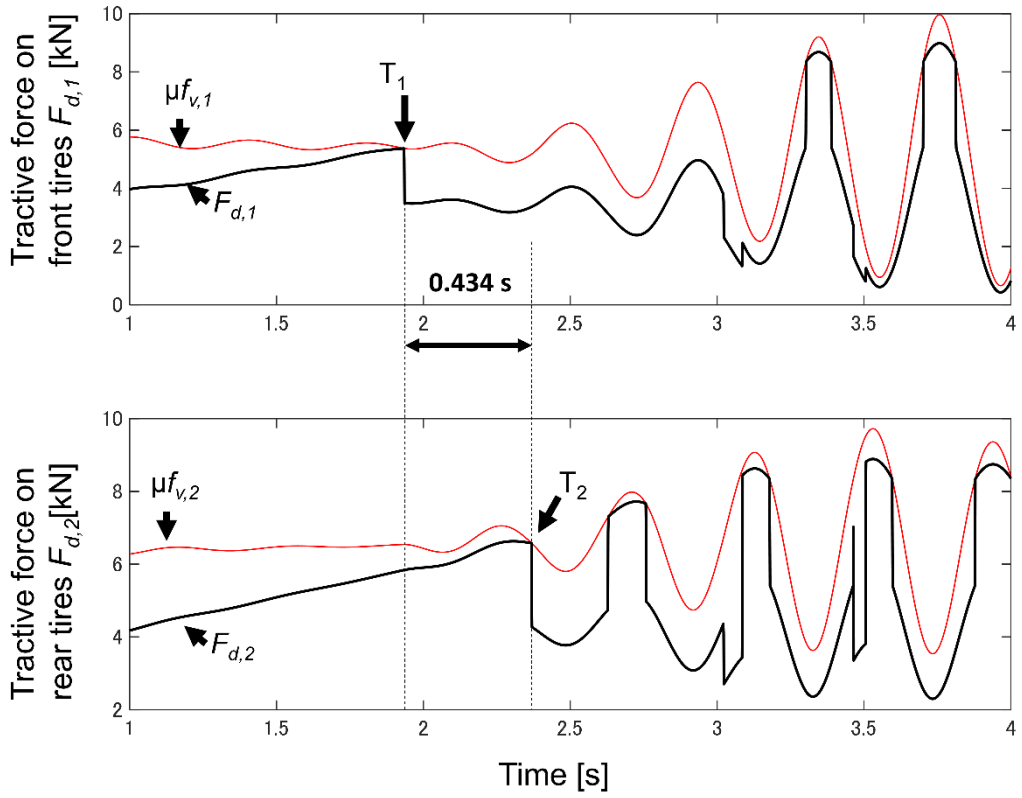

Figure 4.3 Enlargement for the points T_1 and T_2. Top: The tractive force acting on the front tyres $F_{d,1}$; Bottom: The tractive force acting on rear tyres $F_{d,2}$.

Firstly, the tractive force acting on the front tyres $F_{d,1}$ reached the static friction limitation on the front tyres $\mu f_{v,1}$. Then, the static friction limitation on the rear tyres $\mu f_{v,2}$ declined because of the oscillation and then the tractive force acting on the rear tyres $F_{d,2}$ reached the static friction on the rear tyres $\mu f_{v,2}$. The stick-slip oscillation of the front and rear tyres excited the longitudinal, pitch and vertical oscillations as shown in Fig. 4.4.

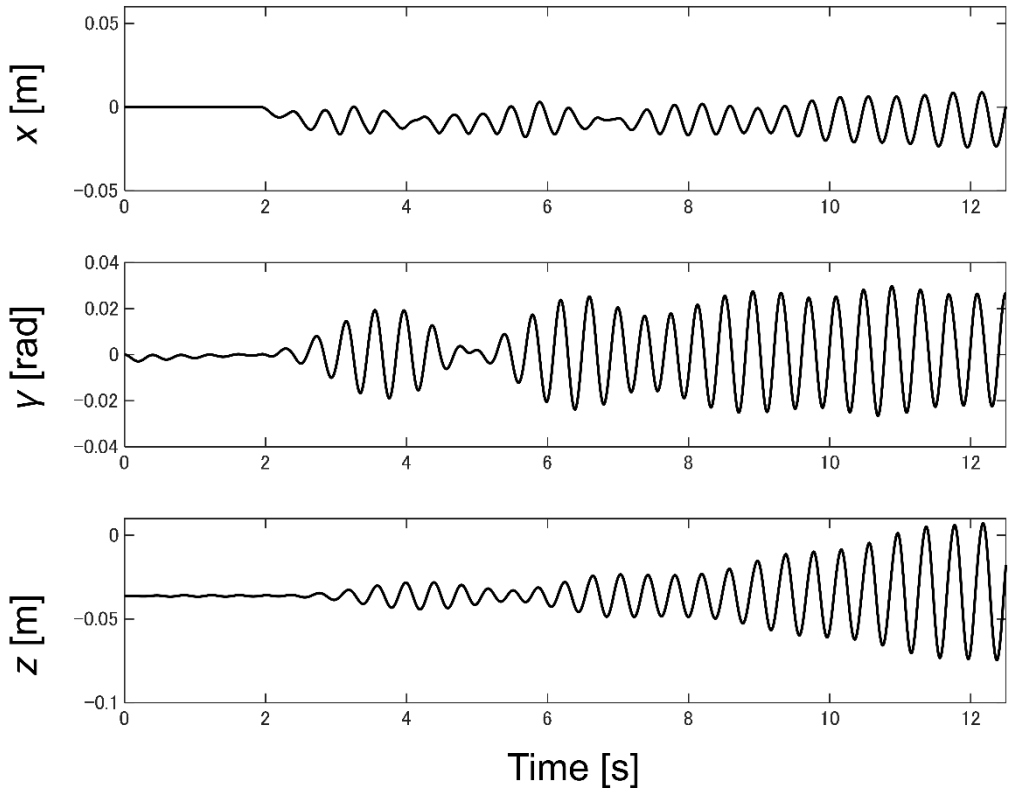

Figure 4.4 Tractor motions excited by power hop instability. Top: Longitudinal motion *x* [m]; Middle: Pitch motion γ [rad]; Bottom: Vertical motion *z* [m].

Longitudinal motion was firstly excited by the stick and slip and there was then pitch and vertical motion. When the oscillation became severe, the tractive forces reduced and there was free play at the point T_3. The draft load P became zero owing to the free play. Vertical loads acting on the front and rear wheels $f_{v,1}$, $f_{v,2}$ became zero and the front and rear wheels lost contact with the ground at points T_4 and T_5 respectively in Fig. 4.2. During bouncing, tractive forces became zero and the tractor entered a state of 100% slippage. The impact dynamics induced by free play and bouncing increased the variations in vertical loads and tractive forces. The above feedback structure is the main mechanism of the power hop phenomenon.

The steady-state behaviour of the power hop dynamics is next investigated. The

steady-state behaviour appeared after the abovementioned transient process shown in Fig. 4.5. Figure 4.5 shows the steady-state power hop under the original draft load P_0 = 10 kN.

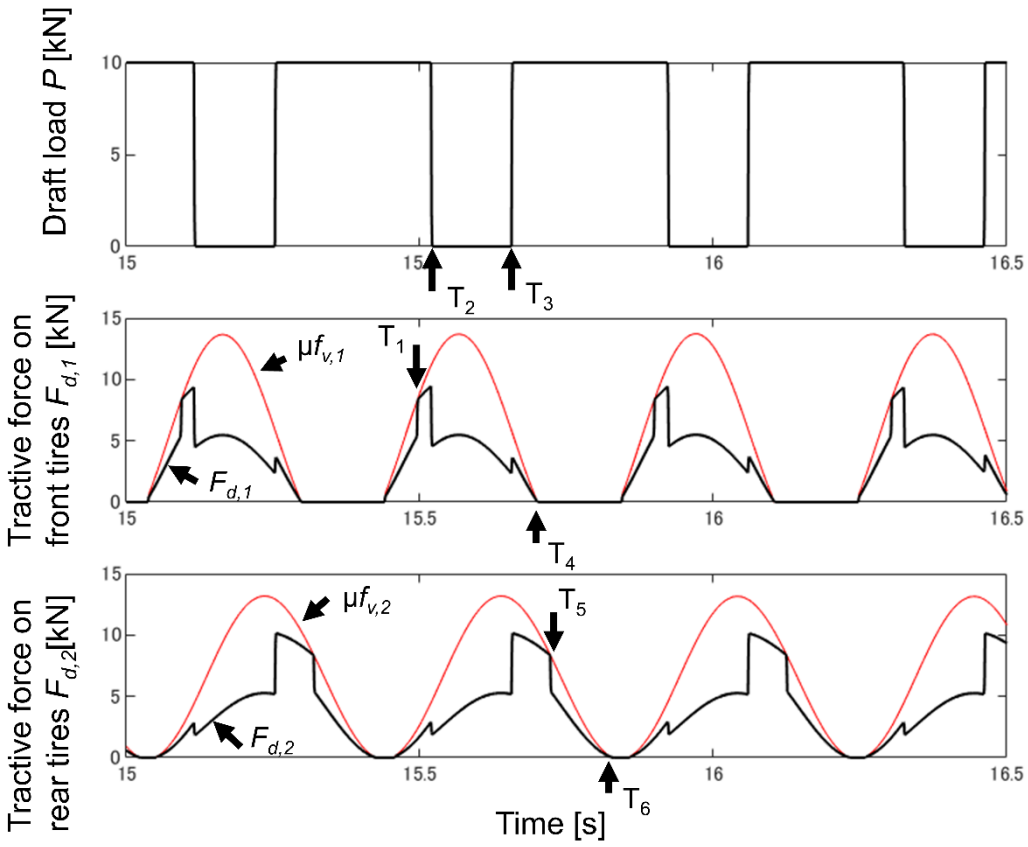

Figure 4.5 Steady-state behaviour of the power hop dynamics; Top: Draft load *P* [kN]: Middle: Tractive force acting on the front tyres $F_{d,1}$ [kN] and static friction limitation of the front tyres $\mu f_{v,1}$ [kN] as a red line; Bottom: Tractive force acting on the front tyres $F_{d,2}$ [kN] and static friction limitation of the front tyres $\mu f_{v,2}$ [kN] as a red line.

Figure 4.5 shows that when the front tyres impacted with the ground, the vertical force acting on the front tyres increased. Then, because of the increase in the vertical load, the tractive force acting on the front tyres increased, and stick-slip dynamics of the front tyres occurred at point T_1. Because of the stick slip dynamics, the tractive force was not sufficient to pull the implement and there was free play at the point T_2. The draft load *P*

was re-established at the point T_3 because of the longitudinal force generated by the tyre stiffness. The vertical load acting on the front tyres then decreased and the tyres lost contact with the ground at the point T_4. The vertical load acting on the rear tyres also decreased. The stick slip dynamics and bouncing thus occurred at points T_5 and T_6 respectively. Figure 4.5 shows that the maximum tractive forces acting on the front and rear tyres $F_{d,1}$ and $F_{d,2}$ were 8.9 and 9.6 kN respectively. These values exceed the static limit in the absence of power hop (front wheel: $5.8\ \text{kN} = \mu \text{Mg}\frac{l_2}{WB}$; rear wheel: $6.2\ \text{kN} = \mu \text{Mg}\frac{l_1}{WB}$). This repeated process is the mechanism of power hop in the steady state.

The power hop mechanism is inferred from the above numerical results as follows. First, there is sticking and slipping of the front wheel as the draft load increases and weight transfers from the front wheel to the rear wheel. The stick–slip process of the front wheel triggers variations in the vertical load and tractive force. During this variation, the vertical load acting on the rear wheel declines at a moment and there is sticking and slipping of the rear wheel. The abovementioned vibrations result in bouncing and free play, inversely generating stick–slip oscillations. This feedback effect was a main source of power hop in both experiments and is described in Figure 4.6.

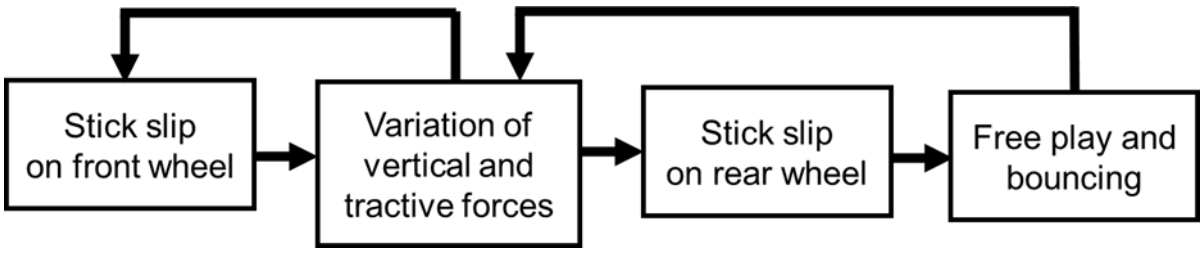

Figure 4.6 The flow chart of the obtained power hop occurrence mechanism

4.3.2. Drawbar pull conditions

The magnitude of drawbar pull is an important factor determining whether power hop happens. Power hop is generally considered to occur under conditions of a higher draft load. A parametric investigation was conducted for different conditions of the original draft load P_0 and joint clearance d. Figure 4.7 shows the maximum vertical acceleration of the tractor centre of gravity A_z in each simulation. In the parametric investigations, the simulation time was 300 s and the maximum vertical acceleration of the tractor centre of gravity A_z was taken after a transient time of 100 s.

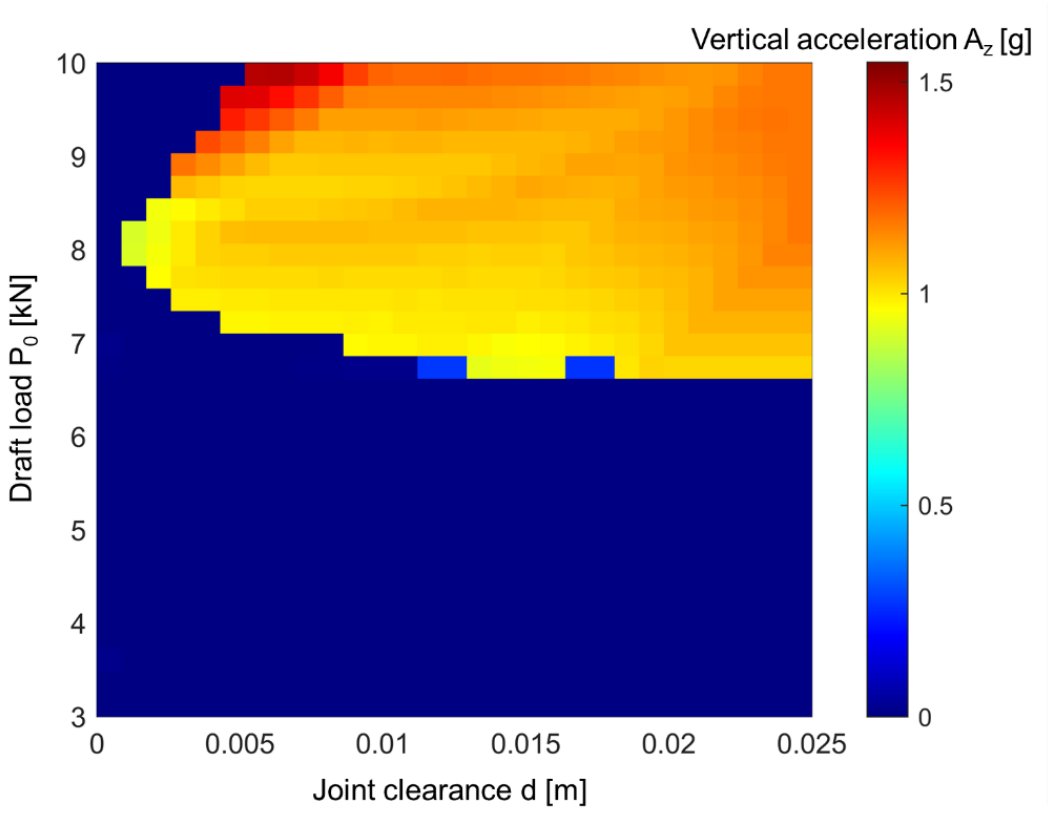

Figure 4.7 Maximum vertical acceleration of the tractor centre of gravity A_z when varying P_0 from 3 to 10 kN and d from 0 to 0.025 m.

In Figure 4.7, the abscissa is the joint clearance d and the ordinate is the original draft

load P_0. Colour shows the maximum value of A_z in each simulation. The maximum value of A_z was zero and there was no self-excited oscillation until the original draft load P_0 fell below 7 kN. If the draft load P_0 was greater than 7 kN, then self-excited vibration occurred and the maximum value of A_z increased with P_0. The maximum value of A_z generally increased with joint clearance d. However the maximum value of A_z was 1.56 g for the combination of P_0 = 10 kN and d = 0.052 m. Figure 4.8 shows time series of the vertical acceleration A_z, longitudinal acceleration A_x, and draft load P for an original draft load P_0 of 9 kN and joint clearance of 0.005 m.

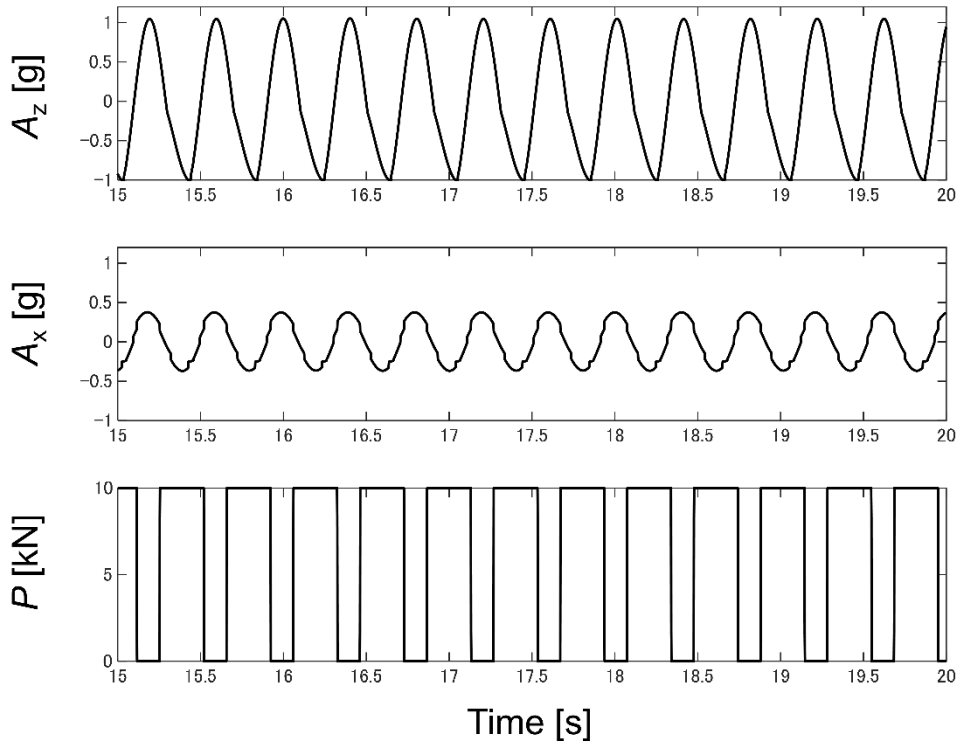

Figure 4.8 Time series of the vertical acceleration of the tractor centre of gravity A_z longitudinal acceleration of the tractor centre of gravity A_x, and draft load P for an original draft load P_0 of 9 kN and joint clearance of 0.005 m.

Figure 4.8 shows that there were initially stick–slip dynamics, longitudinal oscillation,

and free play. Vertical oscillation then became severe and the tractor hopped. In the numerical experiments of Figure 4.7, self-excited vibrations were observed for a higher draft load and larger joint clearance. A higher draft load contributed to the occurrence of stick–slip dynamics. Larger joint clearance increased the severity of the impact between the tractor and implement. Such combinations of a higher draft load and larger joint clearance are considered to have resulted in power hop in the simulations.

4.3.3. Soil conditions

Soil conditions strongly affect power hop. Experimental research has shown that power hop tends to occur under drier soil conditions. Power hop rarely occurs under wet soil conditions. The coefficients of static and dynamic friction acting between a tire and soil vary among different soil conditions. The coefficient of dynamic friction is generally lower than the coefficient of static friction. In the numerical experiments, the static friction coefficient μ and the ratio of static and dynamic friction coefficients $R_\mu = \frac{\mu}{\mu_d}$ were taken as control parameters. Figure 4.9 shows the results of numerical experiments.

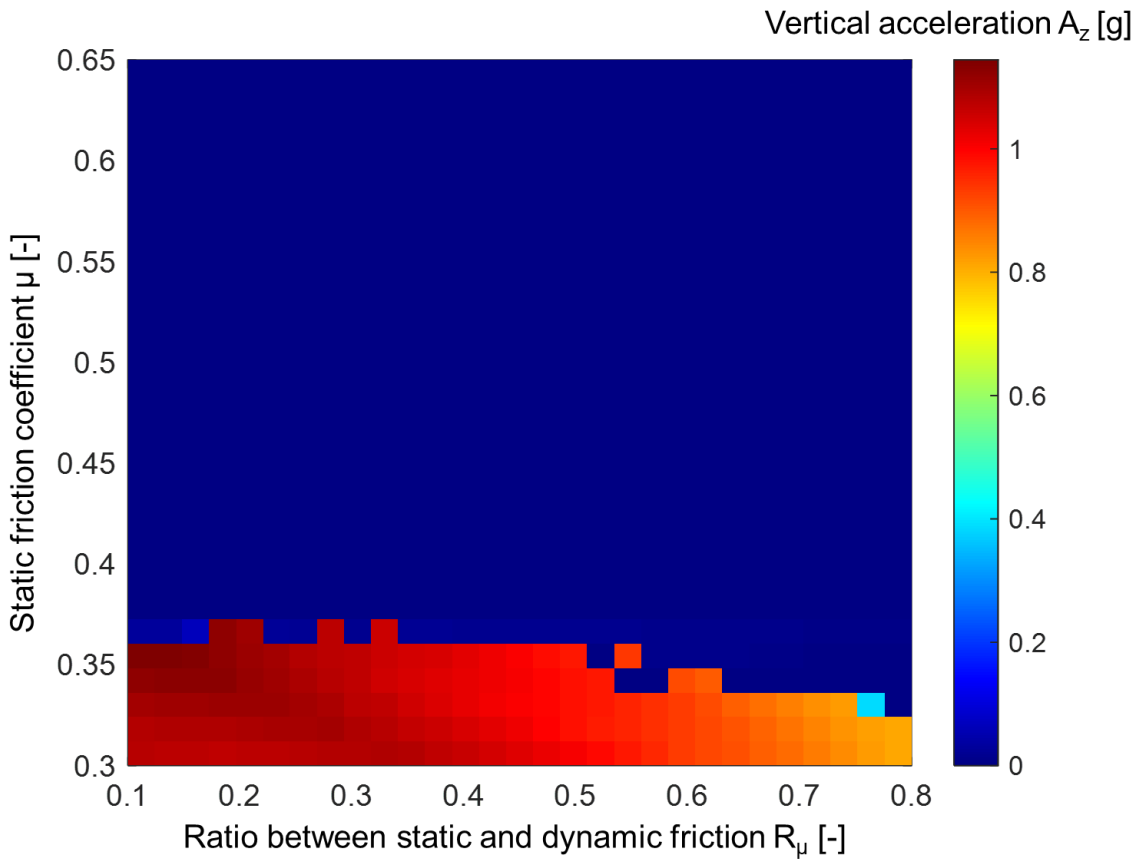

Figure 4.9 Maximum vertical acceleration of the tractor centre of gravity A_z for μ varying from 0.3 to 0.65 and R_μ from 0.1 to 0.8.

In Figure 4.9, the abscissa is the ratio of coefficients of static and dynamic friction R_μ and the ordinate is the coefficient of static friction μ. There was no self-excited vibration in the region where the static friction coefficient was greater than 0.37. In the region where the static friction coefficient was less than 0.37, there was self-excited vibration and the maximum value of A_z was larger. As R_μ decreased, the maximum value of A_z became larger in the region where the static friction coefficient was less than 0.37.

In the above experiment, power hop tended to occur for the smaller static friction coefficient μ and smaller ratio between the static and dynamic friction coefficients R_μ. A smaller static friction coefficient corresponds to drier soil conditions (Umeda, Takeda,

Matsui, Tanaka, 1981) and a smaller ratio between the static and dynamic friction coefficients strengthens stick-slip vibrations in general mechanical systems (Nakano, 2006). In this regard, the developed model can generally predict the power hop occurrence.

4.3.4. Tire conditions

Wiley & Turner (2006) showed that the tire inflation pressure plays an important role in the control of power hop. They concluded that it is desirable for avoiding power hop to increase the inflation pressure of the front tires and reduce the inflation pressure of the rear tires. Tire stiffness is generally proportional to the tire inflation pressure. This “front stiff and rear soft” method prevented the occurrence of power hop in their field experiments. Parametric investigations were thus conducted in the present study, taking the stiffness of the front and rear tires as control parameters. We assumed that the vertical stiffness and longitudinal stiffness of the rear tire were the same in the numerical experiments. Figure 4.10 shows the results of the numerical experiments.

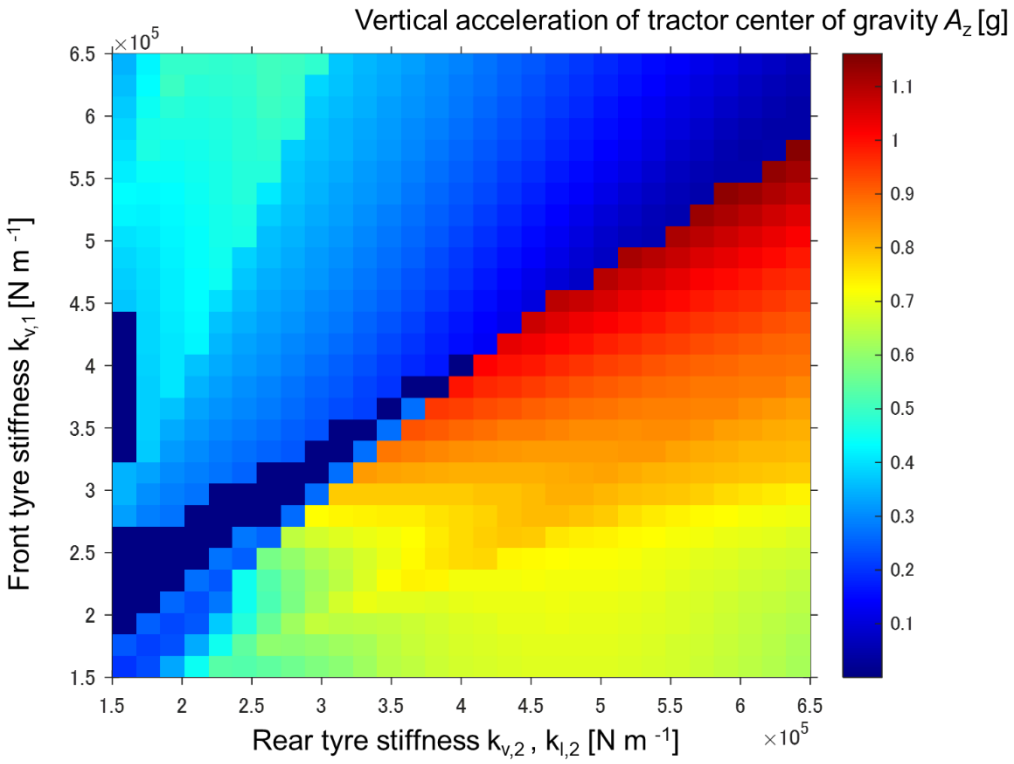

Figure 4.10 Maximum vertical acceleration of the tractor centre of gravity A_z for $k_{v,1}$ varying from 150,000 N m^{-1} to 650,000 N m^{-1} and $k_{v,2}$ and $k_{l,2}$ varying from 150,000 N m^{-1} to 650,000 N m^{-1}.

In Figure 4.10, the abscissa is the rear-tire stiffness $k_{v,2}$ and $k_{l,2}$ and the ordinate is the front-tire stiffness $k_{v,1}$. The maximum value of A_z increased with the front- and rear-tire stiffness. However, if the front tire stiffness increased and exceeded a threshold, the maximum value of A_z became drastically small. As an example, when the rear tire stiffness was 550,000 N m^{-1}, the maximum value of A_z became small if the front tire stiffness exceeded 500,000 N m^{-1}. The results obtained indicate that the developed model supports the validity of the "front stiff and rear soft" approach for specific tyre stiffness conditions.

In the above numerical experiments, the developed model predicted the occurrence of power hop under conditions of a higher draft load and drier soil. The numerical results

agree with empirical knowledge of the occurrence of power hop. The results also revealed that a more severe impact in the joint and a larger difference between static friction and dynamic friction increase the severity of power hop. In a parametric investigation of tire stiffness, the control method of "front stiff and rear soft" tire stiffness proposed by Wiley & Turner (2005) was validated. The developed model can therefore predict the occurrence of power hop appropriately for various towing, soil, and tire conditions.

4.3.5. Power hop for a 2WD tractor

The above investigations assumed a 4WD tractor because power hop generally becomes a problem for 4WD tractors. According to Wiley & Turner (2008), power hop can occur for a 2WD tractor only in a high drawbar pull test and it rarely occurs in real farm operations. Parametric investigation with a 2WD tractor was conducted to validate the developed power hop model. In the 2 WD tractor modelling, the driving force acting on the front tyres $F_{\mathrm{d},1}$ was set to zero and the driving force acting on the rear tyres was set as follows.

$$F_{\mathrm{d},2} = \begin{cases} P + \mu_{r,1} f_{v,1} + \mu_{r,2} f_{v,2}, & |F_{\mathrm{d},2}| \le \mu f_{v,2} \text{ (Stick)} \\ \mathrm{sgn}(F_{\mathrm{d},2}) * \mu_d f_{v,2}, & |F_{\mathrm{d},2}| > \mu f_{v,i} \text{ (Slip)} \end{cases} \tag{4.8}$$

In the parametric investigation of the 2WD tractor, the original draft load P_0 and the static friction coefficient μ were taken as typical parameters of the drawbar and soil conditions. The original draught load P_0 was varied from 0 to 30 kN and the static friction coefficient μ was varied from 0.3 to 0.9. Figure 4.11 shows the results of the parametric investigation of the 2WD tractor.

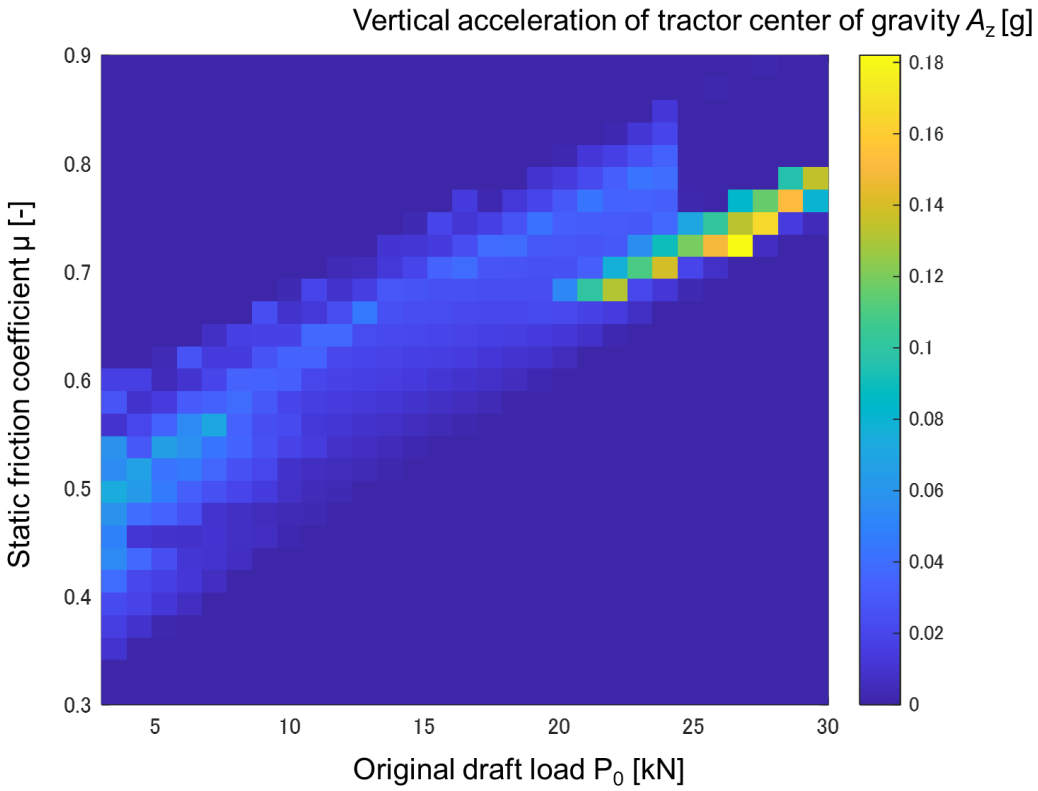

Figure 4.11 Maximum vertical acceleration of the tractor centre of gravity A_z for μ varying from 0.3 to 0.9 and P_0 from 0 to 30 kN.

In Figure 4.11, the magnitude of the maximum A_z is smaller than that in the 4WD tractor results, and power hop rarely occurred in the lower drawbar pull conditions ($P_0 < 10$ kN). In extremely high draft load conditions ($P_0 > 20$ kN), power hop oscillations were observed for higher static friction coefficients. The obtained results are consistent with conventional test results and in this regard the developed model is validated not only for the 4WD tractor but also for the 2WD tractor.

4.3.6. Bifurcation diagram of the power hop dynamics

The qualitative structure of nonlinear dynamics, such as the stability of the periodic orbit, can change as control parameters are varied (Strogatz, 2015). This qualitative change is called bifurcation. The bifurcation diagram is widely used to visualize the

structure of the bifurcation of dynamics. In addition to plotting a bifurcation diagram, phase-space and frequency-domain analyses were conducted to clarify the bifurcation. Figure 4.12 shows the bifurcation diagram of the power hop dynamics. In this study, the bifurcation diagram of the developed power hop model was obtained by plotting peaks of the vertical acceleration of the tractor centre of gravity A_z with regard to the original draft load P_0 varying from 5.0 to 13.0 kN. In the simulation, the simulation time was 300 s and the peaks of the vertical motion z were taken after a transient time of 100 s.

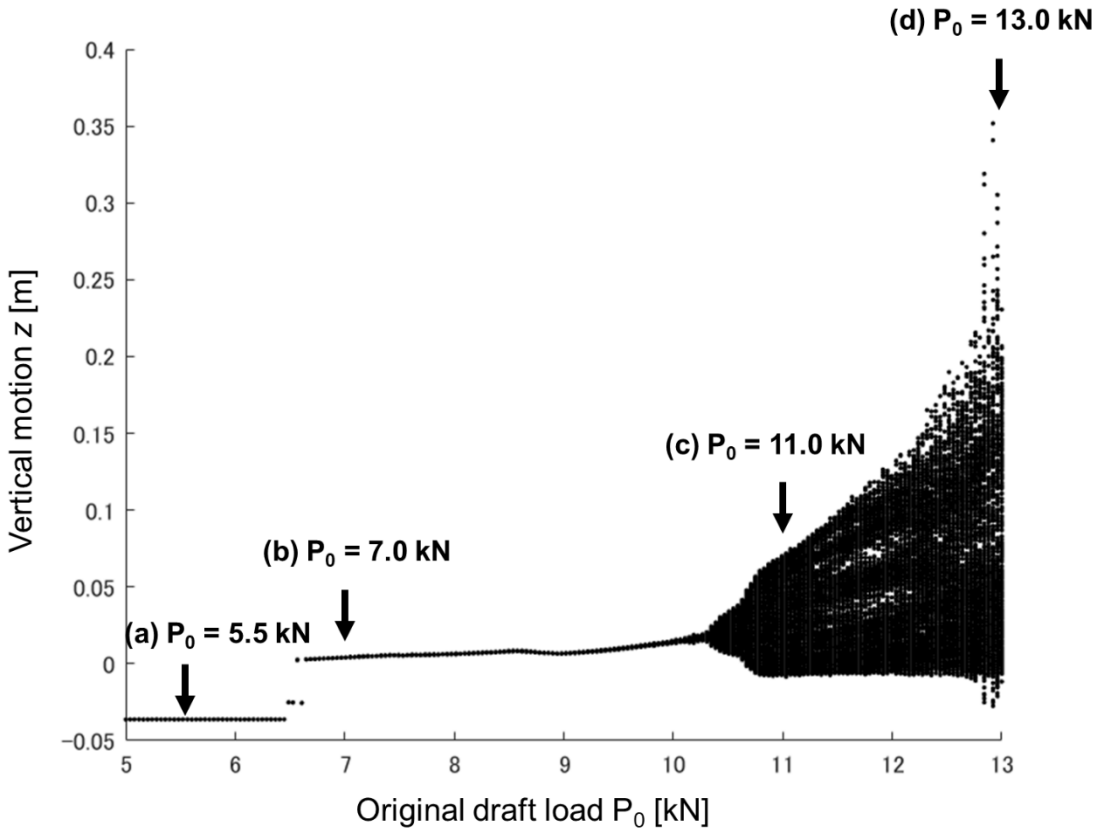

Figure 4.12 Bifurcation diagram of the power hop model plotting the vertical motion *z* against the original draft load P_0.

Figure 4.13a, b, c, and d shows the phase-space trajectory at (a) P_0 = 5.5 kN, (b) P_0 = 7.0

kN, (c) P_0 = 11.0 kN, and (d) P_0 = 13.0 kN respectively. In the figure, phase spaces are spanned by vertical motion *z*, vertical velocity $\dot{z}$, and pitch γ.

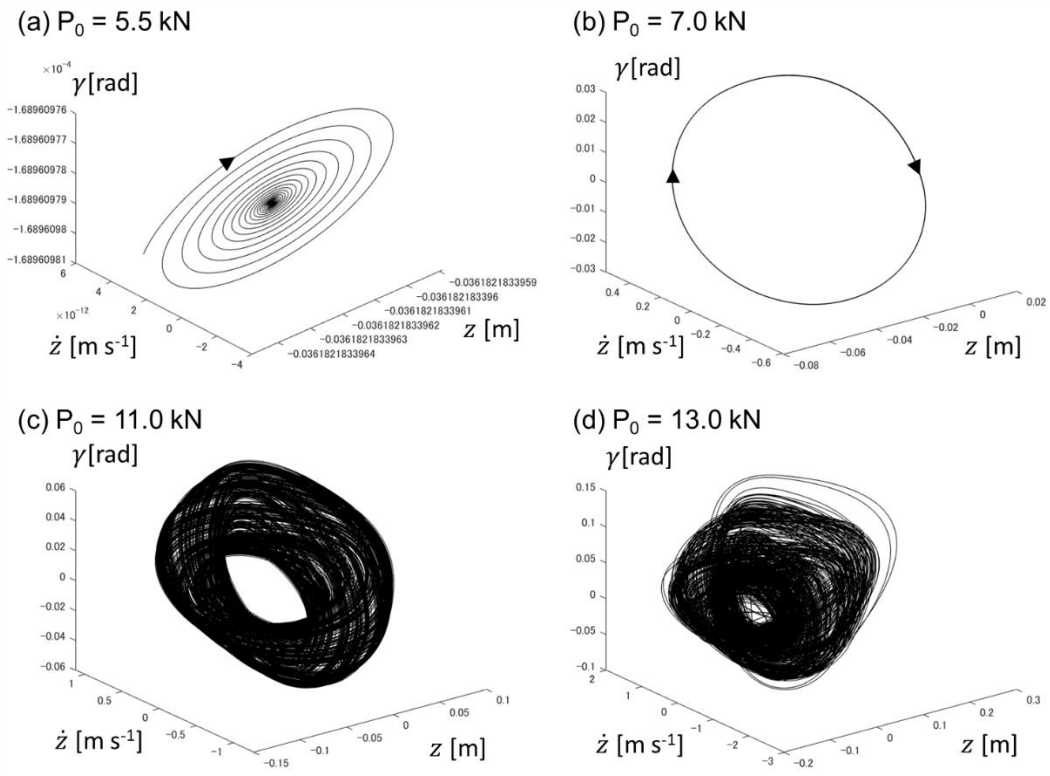

Figure 4.13 Phase space spanned by vertical motion *z*, vertical velocity $\dot{z}$, and pitch γ : (a) P_0 = 5.5 kN; (b) P_0 = 7.0 kN; (c) P_0 = 11.0 kN; (d) P_0 = 13.0 kN.

Until P_0 reached 6.49 kN, self-excited oscillations did not occur and there was a point attractor. Figure 4.13a shows a point attractor at P_0 = 5.5 kN. After P_0 exceeded 6.49 kN, bifurcation occurred and a self-excited oscillation commenced. Figure 4.13b shows a limit cycle at P_0 = 7.0 kN. The limit cycle is a typical periodic oscillation in nonlinear self-excited oscillations. As P_0 increased, the oscillation became severe and complicated. Figure 4.13c and d shows a torus at P_0 = 11.0 kN and chaos at P_0 = 13.0 kN respectively.

Figure 4.14a b, c, and d shows the Fourier spectrum of the point attractor at P_0 = 5.5 kN, the limit cycle at P_0 = 7.0 kN, the torus at P_0 = 11.0 kN, and chaos at P_0 = 13.0 kN respectively.

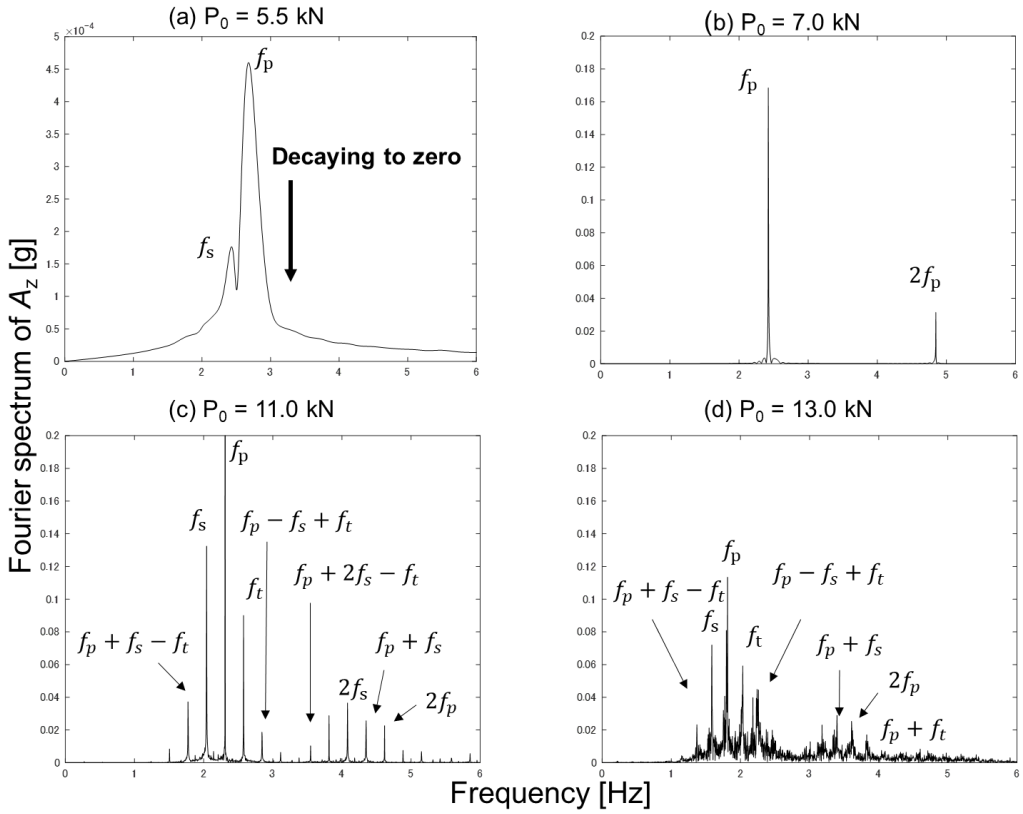

Figure 4.14 Fourier spectrum of the vertical acceleration of the tractor centre of gravity A_z. Top: Limit cycle at P_0 = 5.5 kN; Middle: Torus at P_0 = 7.0 kN; Bottom: Chaos at P_0 = 11.0 kN.

The results of the point attractor presented in Figure 4.14a have two peaks, one at f_p = 2.67 Hz and one at f_s = 2.42 Hz, which correspond to the natural frequencies of vertical motion and pitch motion. Owing to damping, the trajectory settled on the point attractor after free oscillation. In the limit cycle of Fig. 4.14b, the primary frequency is f_p = 2.42 Hz and there are super-harmonics at $2f_p$ = 4.84 Hz and $3f_p$ = 7.26 Hz. In the torus of Fig.

4.14c, there is a primary frequency f_p = 2.31 Hz, secondary frequency f_s = 2.04 Hz, and tertiary frequency f_t = 2.57 Hz. In addition to these frequencies, there are linear coupling frequencies $f_p + f_s - f_t$ = 1.77 Hz, $f_p - f_s + f_t$ = 2.84 Hz, $f_p + 2f_s - f_t$ =3.54 Hz, and $f_p + f_s$ = 4.34 Hz as well as super-harmonics $2f_s$ = 4.08 Hz and $2f_p$ = 4.62 Hz. These multiple peaks in the frequency domain typically indicate quasi-periodic vibrations on the torus. In the chaos of Fig. 4.14d, there is the primary frequency f_p = 1.82 Hz, secondary frequency f_s = 1.59 Hz, and tertiary frequency f_t = 2.03 Hz. In addition to these frequencies, there are linear coupling frequencies $f_p + f_s - f_t$ = 1.37 Hz, $f_p - f_s + f_t$ = 2.26 Hz, $f_p + f_s$ = 3.40, and $f_p + f_t$ = 3.82 Hz as well as super-harmonics $2f_s$ = 4.08 Hz and $2f_p$ = 3.60 Hz. In addition to the abovementioned frequencies, the noise level was high in the Fourier spectrum of the chaos though there is no stochastic term in the developed model. This is a typical characteristic of chaotic vibrations.

According to the above analysis, the stability of the power hop dynamics changed from a point attractor, to a limit cycle, torus, and chaos depending on the original draft load P_0.

4.4. Summary

A power hop model was developed by coupling three typical nonlinear elements, namely vertical bouncing, longitudinal stick-slip dynamics, and free-play in the joint between a tractor and implement. The developed model revealed the occurrence process of power hop in transitional and steady-state dynamics. The results of simulations with the model indicate that the feedback structure is the main cause of power hop. In a parametric investigation, the novel model was successfully used to predict the occurrence of power hop under conditions similar to those of field experiments. In a

bifurcation diagram, the stability of the power hop dynamics changed from a point attractor to a limit cycle, torus, and chaos. The developed model can thus be used as a platform for controlling the occurrence of power hop.

5. Road profile generation for a tractor driving simulator

5.1. Introduction

Agricultural tractors are subjected to excessive vibrations generated by the road roughness or profile, resulting in damage to machinery and dynamic disturbances. Unfavorable road conditions are a major factor reducing operational performance and increasing the overturning opportunity. Assessment indicators for road roughness have been developed; e.g., the International Roughness Index and PSD. In particular, the PSD has been used as a road roughness standard by the International Organization for Standardization (ISO).

Much effort has been made to model and generate a road profile as a vertical disturbance for vehicle dynamic simulations. Conventionally, a road profile on a single wheel path has been modeled based on the PSD for vehicle simulation in a two-dimensional plane. However, in a real field, the left and right tracks are not identical and road profiles along the two (left and right) wheel paths thus need to be constructed by combining the PSD and coherence function. These road profiles are adopted in simulation using a three-dimensional space model.

In contrast with previous chapters 2, 3, and 4, this chapter reports on numerical experiments conducted using the tractor driving simulator in three-dimensional space to investigate overturning scenarios in more detail. This chapter develops a road profile generation algorithm for the tractor driving simulator based on PSD and coherence analyses. The chapter is structured as follows. Section 5.2 conducts power spectrum and coherence analyses of surveyed road profile data. Sections 5.2 and 5.3 develop

algorithms for road profile generation. The final section summarizes conclusions drawn from the results of the chapter.

5.2. Analysis of the surveyed road profile

This section analyzes surveyed road profiles adopting PSD and coherence analyses. The surveyed road profile of the Tokyo University of Agriculture and Technology is used as analysis data (Inaba, 1999). Figure 5.1 shows the surveyed road profile and surveying method. The surveyed road is 2.5 m in width and 75 m in length as shown in Figure 5.1b. Five road profiles were surveyed adopting a transit with a resolution of 0.5 m. Road profiles are labelled as shown in Figure 5.1b.

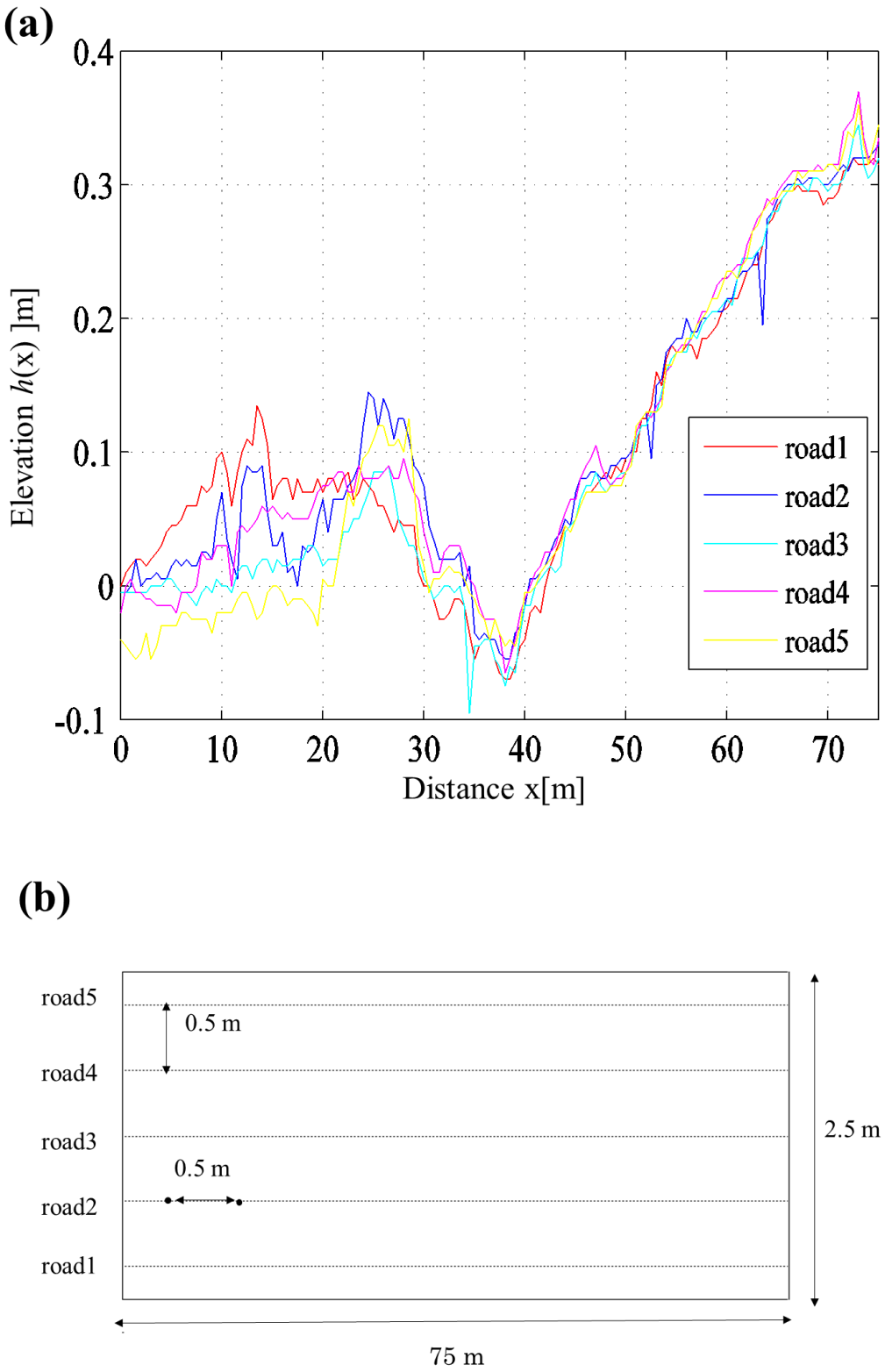

Figure 5.1 (a) Real road data from surveying and (b) the surveying method.

5.2.1. Power spectrum density analysis

This section analyzes the surveyed road profiles using the Power Spectrum Density (PSD). The PSD is generally used to investigate signal characteristics in the frequency domain. The PSD is generally defined as the Fourier transform (FT) of the autocorrelation function (Hino, 2010):

$$P(f) = \int_{-\infty}^{\infty} C(\tau) e^{-j2\pi f\tau} df. \tag{5.1}$$

This definition is also known as the Wiener–Khinchin theorem.

The ISO standard of road roughness is first presented and then analysis is conducted. Road roughness has been standardized by the ISO and its PSD is defined as (Ohmiya, 1990)

$$P(f) = P(f_0)\left(\frac{f}{f_0}\right)^{-W}, \tag{5.2}$$

where f_0 = 1/2π c/m, W = 2, f is the spatial frequency [c/m], and $P(f_0)$ [10^{-6} m^2c/m] is the PSD when f is f_0. In this modeling by the ISO, the PSD of the rough roughness is expressed as red or random-walk noise. In the ISO standard, the road roughness is divided into Classes A to H depending on the value of $P(f_0)$. Class A is the least rough surface while Class H is the roughest surface. Classes A, D, and E respectively correspond to a highway road, unpaved road, and poor unpaved road (Yamakawa, 1976).

Figure 5.2 shows the PSDs of road profiles and their average.

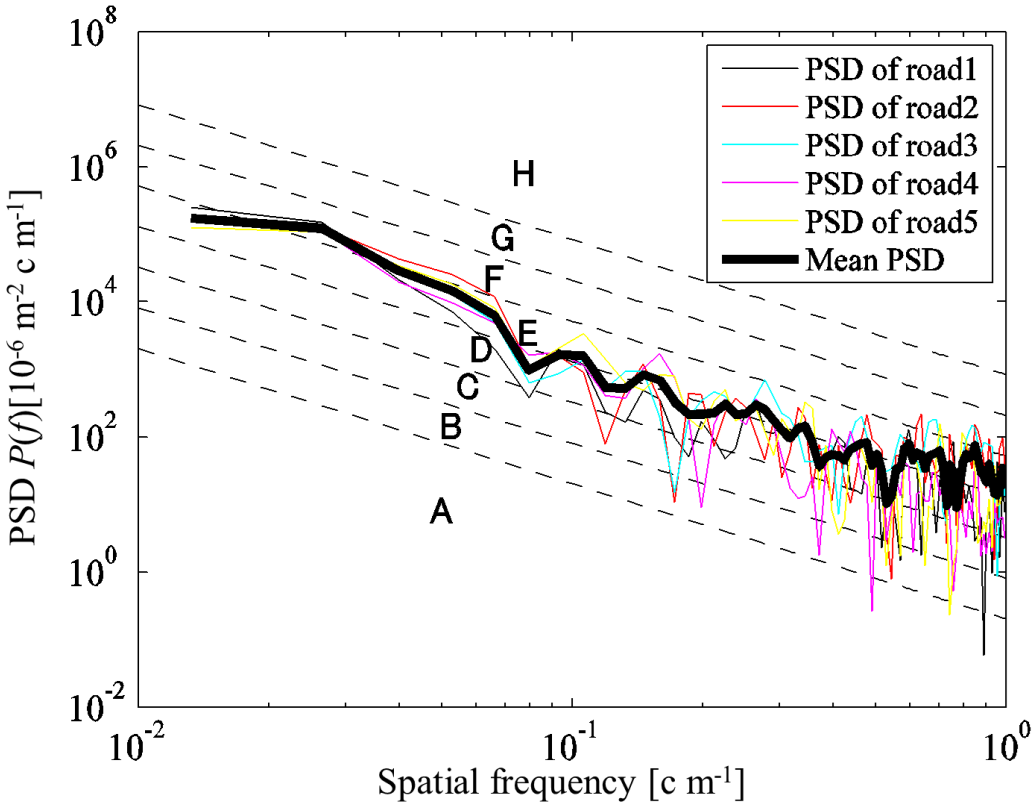

Figure 5.2 PSDs of real road data.

The PSDs of road profiles are inversely proportional to the spatial frequency. The PSD corresponds ranges from Class E to Class F when the spatial frequency is less than 10^{-1} c m^{-1} and from Class C to Class E when the spatial frequency is greater than 10^{-1} c m^{-1}. In Figure 5.2, the shapes and values of the PSD are mostly the same for the five road profiles. The value of W, which is the inclination of the PSD, is 2.05, which is close to the ISO's standard of W = 2.

5.2.2. Coherence analysis

This section investigates the surveyed road profiles adopting coherence analysis. A coherence function is generally used to investigate correlation between two signals in the frequency domain. The coherence function is defined as

$$r^2(f) = \frac{|P_{xy}(f)|^2}{P_{xx}(f)P_{yy}(f)}, \tag{5.3}$$

where $P_{xx}(f)$ is the PSD of $x(t)$, $P_{yy}(f)$ is the PSD of $y(t)$, and $P_{xy}(f)$ is the cross-spectrum density of x(t) and y(t). The range of the coherence function is $0 \leqq r^2(f) \leqq 1$ and the correlation between signals is proportional to the coherence function.

Coherence functions are calculated for the combinations of road 1 and road 3, road 2 and road 4, road 3 and road 5, road 1 and road 4, and road 2 and road 5 because tractor tread typically ranges from 1.0 to 1.5 m. Figure 5.3 shows all coherences and their average.

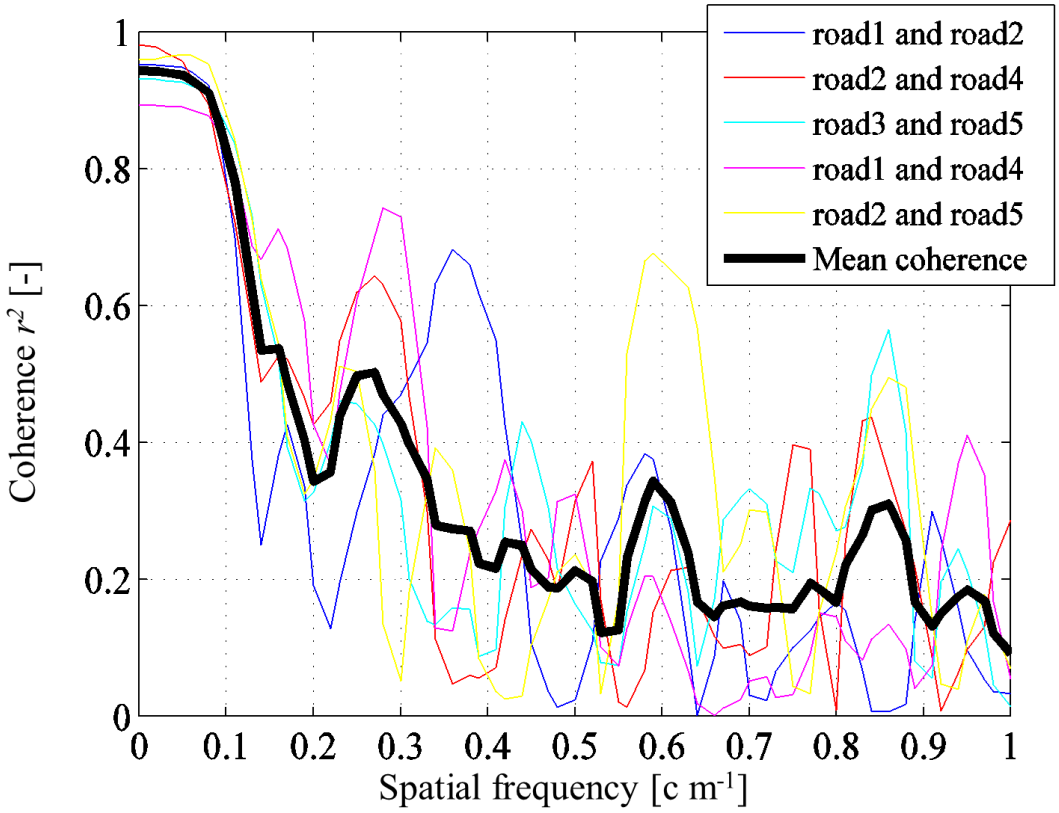

Figure 5.3 Coherence of surveyed data and the mean coherence.

In Figure 5.3, the average coherence is greater than 0.8 when the spatial frequency is less

than 0.1 c m^{-1}. Meanwhile, coherence rapidly decreases when the spatial frequency exceeds 0.1 c m^{-1}. The obtained results indicate high correlation between left and right tracks in the low-frequency band (f < 0.1 c m^{-1}) while correlation is drastically lost in the high-frequency band (f > 0.1 c m^{-1}).

5.3. Algorithms for generating the road profile

5.3.1. Fourier Transform surrogate method

Algorithms are developed for generating the road profile using the Fourier Transform (FT) surrogate method and Auto Regressive (AR) method. The algorithm of the FT surrogate method is first developed.

The FT surrogate method is generally adopted in nonlinear time series analysis (Theiler et al., 1992). Applying this method to road generation, road profiles that have the same PSD but different shapes can be indefinitely generated. When generating a road using the FT surrogate method, the road elevation h(x) at a distance x is defined as

$$h(x) = \sum_{n=1}^{\infty} 2\sqrt{P(f_n)f_r}\cos(2\pi f_n x + \theta_n), \tag{5.4}$$

where $P(f_n)$ is the PSD, f_r is the fundamental frequency, and θ_n is a random uniform phase whose range is $-\pi < \theta_n < \pi$. The random road profile is generated using the ISO's standard PSD expressed by (5.2). The abovementioned algorithm can generate a road profile on a single wheel path.

Driving simulation in three-dimensional space requires left and right tracks for the road profile input. Coherence modeling is required to generate road profiles on two wheel paths. Coherence function models, such as the isotropic model (Usui, 1990), two-

dimensional filtered Poisson model (Xiang Wei Zhang, 1986), and exponential parametric model (Bogsjö, 2008), have been developed.

This paper develops a more concise way to generate road profiles. According to surveyed data, left and right tracks have PSDs that are mostly the same and the coherence is greater than 0.8 in the low-frequency band where $f < 0.1$ cm^{-1}. The following is a description of the algorithm developed using these characteristics.

1) $P(f_0)$ is set the same for left and right tracks in equation (5.4).
2) θ_n is set the same for left and right tracks in equation (5.4) when the spatial frequency f is less than 0.1 cm^{-1}.

As a result of the above process, the PSDs of left and right tracks become the same and the coherence becomes 1.0 in the low-frequency band ($f < 0.1$ cm^{-1}). The above process is called the extended FT surrogate method.

5.3.2. Autoregressive model

Autoregressive (AR) modeling is adopted in linear time series analysis. The mth-order AR model is expressed as

$$x_n = \sum_{j=1}^{m} a_j x_{n-j} + \varepsilon_n, \tag{5.5}$$

where a_j is the AR coefficient while ε_n is white noise having a mean of zero and variance σ^2. Theoretically, the PSD of the AR model is derived as (Akaike, 1969)

$$P(f) = \frac{\sigma^2}{\left|1-\sum_{j=1}^{m} a_j e^{-2\pi f i j}\right|^2}. \tag{5.6}$$

The order of the AR model and AR coefficient are needed for the generation of the road profile. The AR model was estimated from the surveyed road profile shown in Figure 5.1. The order of the AR model m was estimated using Akaike's information criterion; m = 1 for all road profiles. AR coefficients were estimated using the Yule–Walker equation. Table 5.1 gives the estimated AR coefficients.

Table 5.1 AR coefficients of respective roads

Road profile	AR coefficient a_1
road1	0.98
road2	0.97
road3	0.98
road4	0.98
road5	0.98

The order of the AR model m is 1 and AR coefficients a_1 are nearly 1. The road profile can therefore be modeled using a random walk. Obtained results are equivalent to red noise modeling in the ISO standard.

Based on the above results, a first-order AR model is used in this study:

$$h_n = a_1 h_{n-1} + \varepsilon_n, \tag{5.7}$$

where h_n is the road elevation [m], $a_1 = 0.98$, and ε_n is white noise having a mean of zero and variance satisfying

$$\sigma^2 = P(f)\left|1 - a_1 e^{-2\pi f j}\right|^2. \tag{5.8}$$

5.4. Generation of the road profile

5.4.1. Road profile generation for a single wheel path

A road profile for a single wheel path is generated in this section. Figure 5.4 shows road profiles and their PSD-based FT surrogate and AR model for $P(f_0) = 256 \times 10^{-6}\,\mathrm{m^2c\,m^{-1}}$.

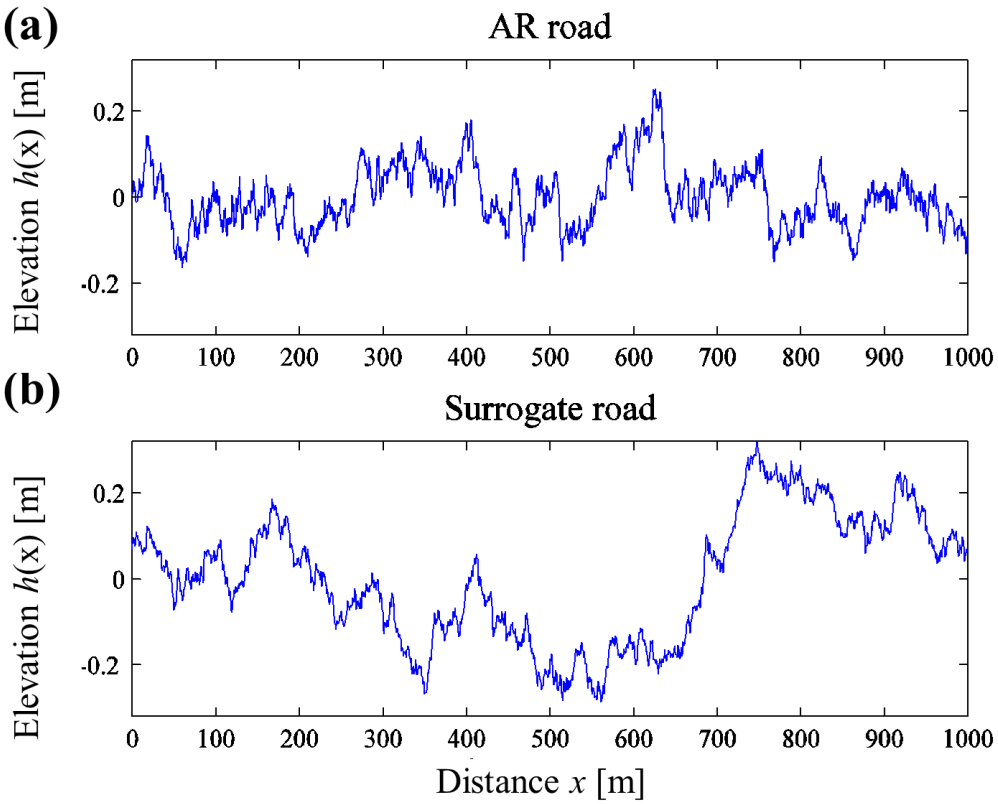

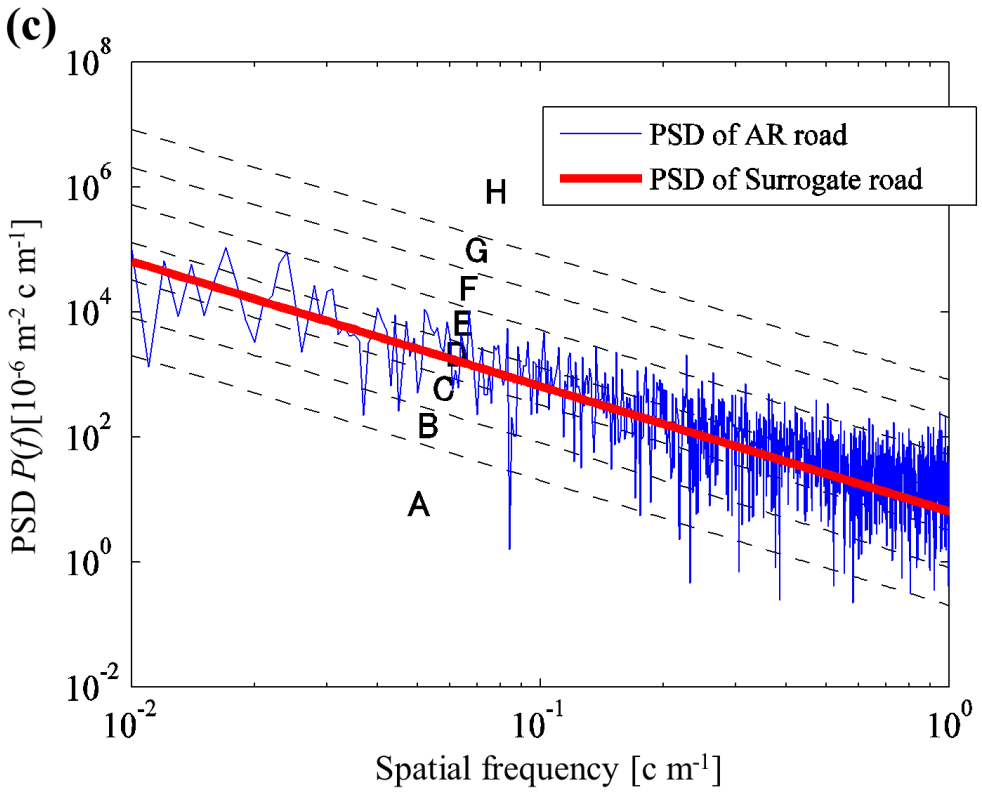

Figure 5.4 (a) AR road, (b) surrogate road, and (c) PSDs of the AR road and surrogate road.

Both algorithms can generate the random road profile. The PSD of the FT surrogate road profile corresponds to $P(f_0)$ of 256×10^{-6} m^2cm^{-1} while the PSD of the AR road is scattered around $P(f_0) = 256 \times 10^{-6}$ m^2 cm^{-1}. W takes values of 2.00 and 1.79 for the FT surrogate road and AR road, respectively.

5.4.2. Road profile generation for two-wheel paths

Road profiles for two-wheel paths (left and right) are generated in this section. Figure 5 shows the road profiles generated using the extended FT surrogate method. Figure 5.5a, b, and c respectively shows the right road profile $h_R(x)$ [m], left road profile $h_L(x)$ [m], and difference between right and left road profiles $\Delta h(x) = h_R - h_L$[m].

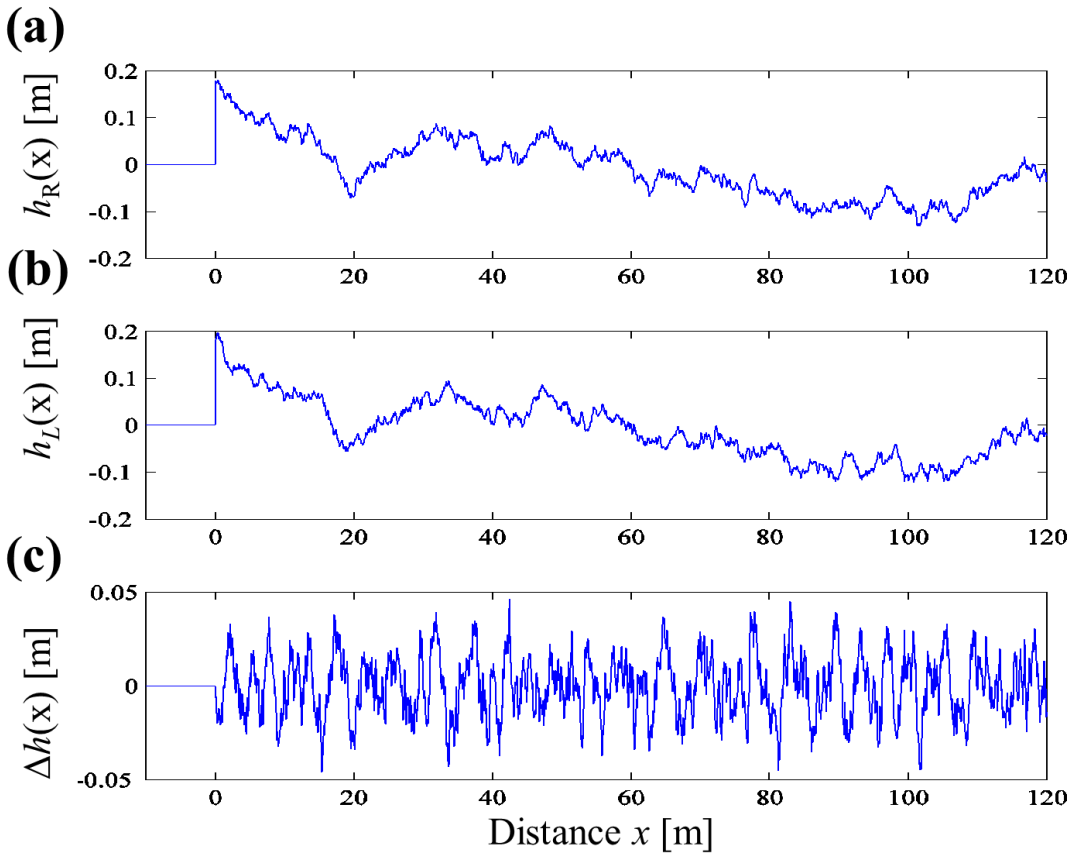

Figure 5.5 (a) Right surrogate road, (b) left surrogate road, and (c) difference between right and left surrogate roads.

Random road profiles maintain correlation in the low-frequency band with the difference ranging from 0.05 to −0.05 m. The average of 100 coherence functions is calculated to validate correlation between left and right. Figure 5.6a shows five representative coherences and the mean of 100 coherences. Figure 5.6b shows the mean coherence of the extended FT surrogate road and coherence of the surveyed road.

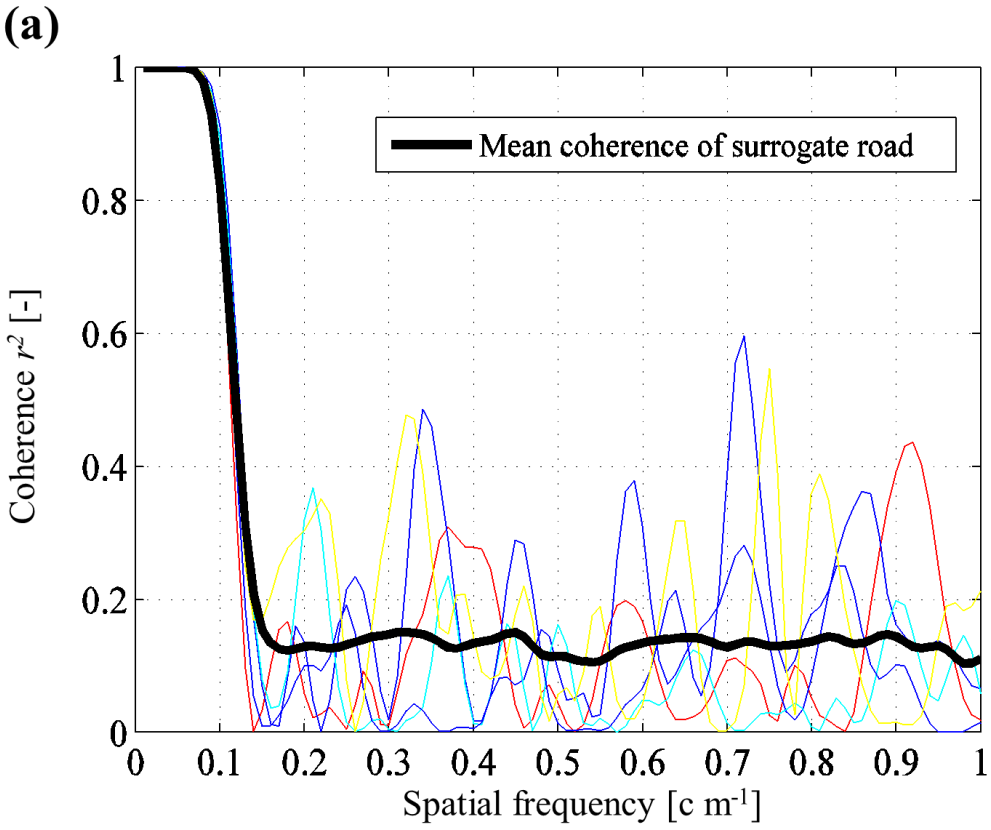
(a)
Mean coherence of surrogate road
Coherence r^2 [-]
Spatial frequency [c m^{-1}]
0
0.2
0.4
0.6
0.8
1
0.1
0.3
0.5
0.7
0.9

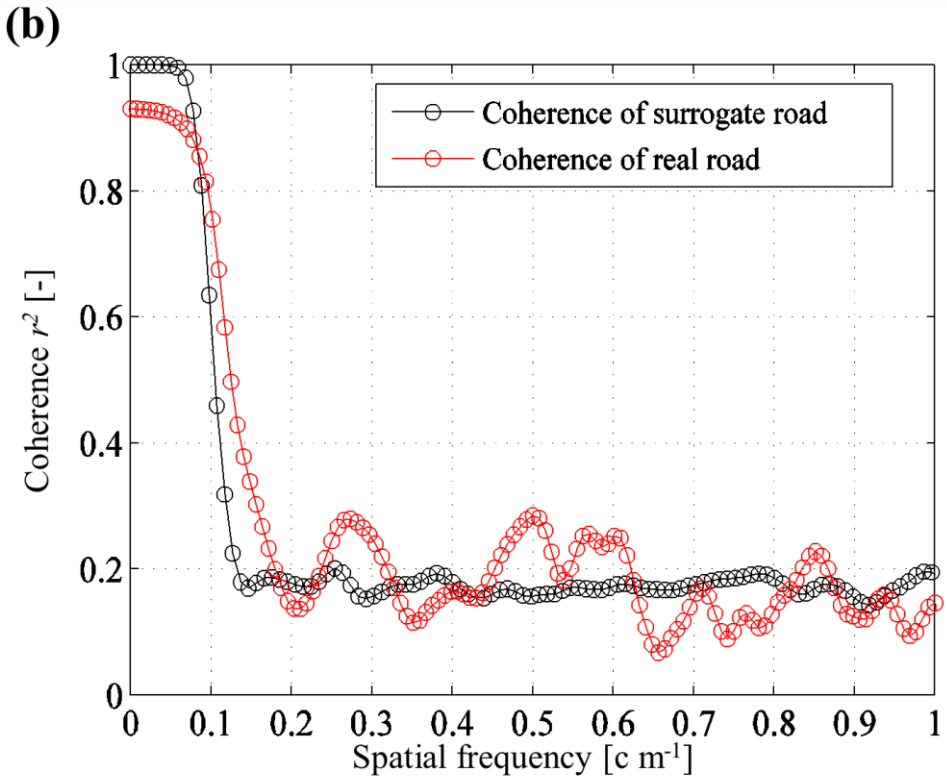
(b)
Coherence of surrogate road
Coherence of real road
Coherence r^2 [-]
Spatial frequency [c m^{-1}]
0
0.2
0.4
0.6
0.8
1
0.1
0.3
0.5
0.7
0.9

Figure 5.6 (a) Coherence of 100 pairs of the surrogate road and (b) mean coherence of 100 pairs of the surrogate road and coherence of the real road

Coherences of surrogate and surveyed roads similarly attenuate as the spatial frequency increases. The developed algorithm thus realizes high correlation in the low-frequency band ($f < 0.1$ cm^{-1}).

5.4.3. Gap elimination using a one-sided Hanning window

The tractor enters the generated road profile from a flat surface in the tractor driving simulator. Occasionally, the road surface gap in the boundary region is observed using the FT surrogate method described in Figure 5.7a. If the gap is relatively large, numerical errors, such as those relating to overturning and excessive vibration, occur in the initial part of the simulation. In this section, a newly developed one-sided Hanning window is introduced to eliminate the gap. A one-sided Hanning window is defined as

$$w(n) = 0.5\left(1 - cos\left(\frac{2\pi n}{N}\right)\right) \quad \text{if } \left(0 \le n \le \frac{N}{2}\right)$$
$$= 1 \qquad \text{if } \left(\frac{N}{2} \le n \le N\right). \quad (5.9)$$

Figure 5.7b and c shows the one-sided Hanning window and the road profiles after eliminating the gap.

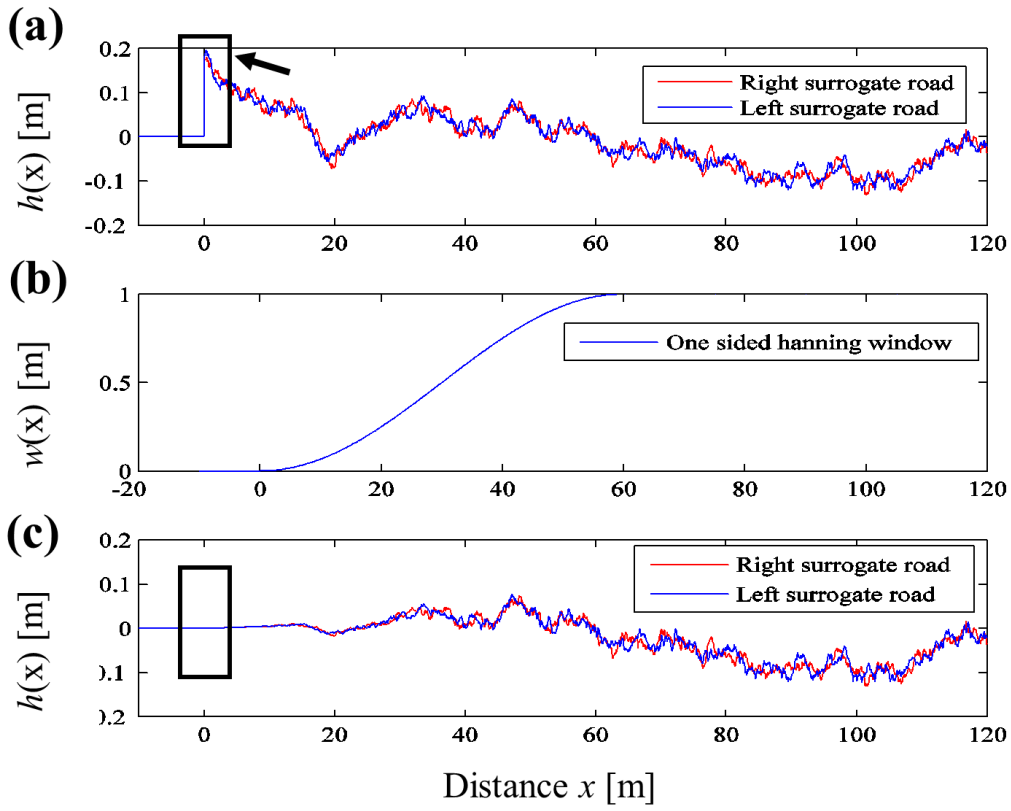

Figure 5.7 (a) Road before removing the discontinuous part, (b) one-sided Hanning window, and (c) road after removing the discontinuous part.

The gap is successfully removed using the one-sided Hanning window.

5.5. Summary

Algorithms for road profile generation were developed as a component technology of the tractor driving simulator. Surveyed road profiles were investigated by combining PSD and coherence analyses. The FT surrogate method and AR method were developed for generating a road profile on a single wheel path using the ISO's standard. Road profiles on two (left and right) wheel paths were generated using the extended FT surrogate method. In addition to the road profile generation algorithms, a one-sided Hanning window was developed to remove the road surface gap in the boundary region. The

developed algorithms can be used for the road surface in the tractor driving simulator.

6. Development of a tractor driving simulator

6.1. Introduction

Previous sections developed nonlinear dynamics models of agricultural tractors to identify tractor overturning scenarios. As well as the dynamic tractor models, road profile generation algorithms were developed by combining PSD and coherence analyses. Although the abovementioned investigations are highly useful in clarifying typical overturning scenarios, it is especially difficult to elucidate complex real accident cases of an agricultural tractor in various terrain environments because real physical behaviors involve multibody physics and are affected by many factors and control parameters.

It is not feasible, however, to conduct a tractor overturning experiment in a farm field with manual operation because of the high risk of injury and high cost. Conducting computer simulations using a driving simulator is thus a promising way to identify overturning processes and scenarios. Owing to cutting-edge advances in computing capability, computer graphics, and computational technology, driving simulators for automobiles have been used in many types of research, including vehicle system design, active control development, autonomous driving, and human factor studies (Tango & Botta, 2013; Underwood, Crundall, Chapman, 2011). Driving simulators provide a virtual test drive platform and allow researchers to duplicate a real driving situation more safely and inexpensively. Numerical experiments conducted using driving simulators offer higher fidelity and a more rapid speed of experiment compared with a physical field driving experiment. In addition to these advantages of driving simulators, the use of a driving simulator makes it easier to comprehend the physical meaning than when conducting a purely physical experiment. The above nature of a driving simulator is

beneficial not only to automobile safety but also to agricultural tractor safety.

The agricultural tractor has mechanisms and devices different from those of automobiles. As an example, the tractor brake system has left and right brakes that work independently, which is beneficial to turning in agricultural fields. The tractor throttle lever can be controlled to be constantly open for various farm operations. These characteristics of tractor systems must be included in the tractor driving simulator. In contrast with the case for automobiles, few studies have been conducted on the development of a driving simulator for an agricultural tractor. Karimi et al. (2008) applied a tractor driving simulator to straight-line driving guidance, Gonzalez et al. (2017) used a tractor driving simulator for training to avoid occupational injuries, and Lleras et al. (2016) developed a tractor driving simulator for stability testing. However, the tractor driving simulator is still in an early stage of development compared with its automotive counterpart and further investigation is necessary.

The present chapter develops a tractor driving simulator with a motion platform for reproducing tractor overturning scenarios within a virtual test drive platform. In previous chapters, we identified several tractor overturning scenarios based on the nonlinear dynamic modeling of agricultural tractors and generated road profile generations by combining PSD and coherence analyses. In the present work, a tractor driving simulator was developed using the commercial automotive driving simulator CarSim® (Mechanical Simulation Cooperation, MI, US). The characteristic tractor mechanism was implemented in the driving simulator using the MATLAB®/Simulink® (Mathworks, MA, US) platform.

This chapter is structured as follows. Section 6.2 presents configurations for the tractor driving simulator to demonstrate how to set the tractor driving simulator

parameters. Section 6.3 carries out validation tests of driving simulator configurations to confirm simulator settings. A gear shift operation test and minimum radius turning test are conducted. Section 6.4 develops a motion system for the tractor driving simulator to emulate the tractor overturning behavior physically. The motion system is offered by Solution, Inc., Tokyo, Japan.

6.2. Configuration of the tractor driving simulator

Tractor model configurations were set to conduct numerical simulations. In the CarSim® system, the vehicle configurations can be set in the vehicle assembly library. CarSim® was originally developed for the simulation of automobiles, such as sedans, hatchbacks, and sport utility vehicles. The CarSim® system is therefore designed generally for automobile characteristics. It is thus necessary to adjust the CarSim® system to represent farm tractor characteristics. The powertrain, steering, and brake systems are configured in this section. The vehicle configuration is based on a typical small tractor generally used in Japanese agriculture (Inaba, 1999). Table 1 gives the vehicle specifications used for the driving simulator.

Table 6.1 Specifications for a small tractor designed to operate in a paddy field

Parameter	Value	Unit
Mass of the tractor body	988	kg
Mass of the implement	184	kg
Pitch moment of inertia	700	kgm^{-2}
Distance between the center of gravity of the tractor body and front wheel	0.64	m

Distance between the center of gravity of the tractor body and rear wheel	0.70	m
Wheelbase of the tractor	1.34	m
Distance between the center of gravity of the tractor body and the center of gravity of the implement	1.24	m
Engine power (diesel engine for a small tractor)	30	kW
Steering gear ratio	13.5	–
Front tread	0.96	m
Rear tread	1.035	m
Driving type	RWD	–

These specifications are set in the CarSim® sprung mass screen shown in Figure 6.1.

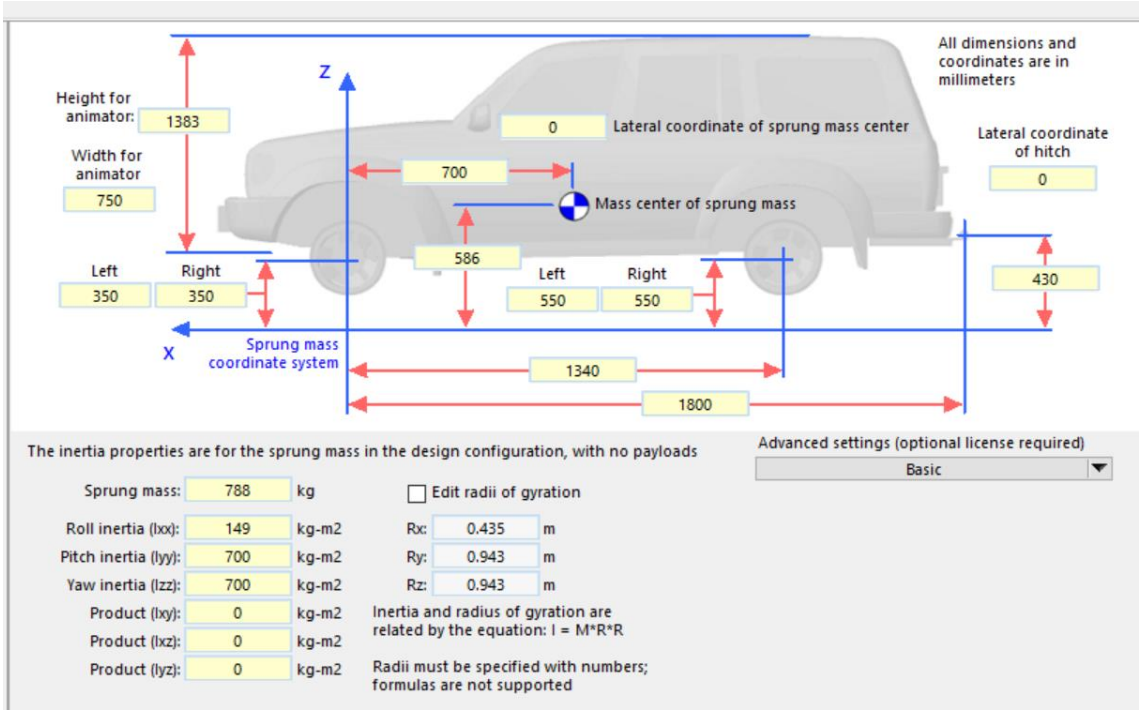

Figure 6.1 CarSim® sprung mass screen for setting the tractor dimensions, mass, and moment of inertia.

6.2.1. Powertrain system

In CarSim®, powertrain characteristics, such as the engine power, transmission, and differential, are set on the power train system screen. In the software, the powertrain system comprises the engine, clutch or torque converter, transmission, transfer case (only for a 4WD vehicle), and differential. Figure 6.2 shows the power flow in the CarSim® powertrain system.

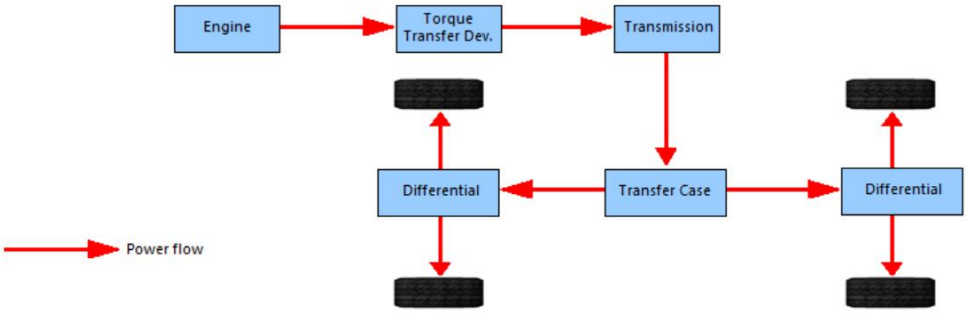

Figure 6.2 Schematic diagram of power flow in the CarSim® powertrain system from engine to wheel.

First, drive power is generated in the engine. Through a torque transfer device, the engine power is transferred from the engine to the transmission, transfer case, differential, and each wheel. The throttle input is connected directly to the engine to generate power. In CarSim®, several engine models, such as gasoline and diesel engines, can be selected.

In Japan, small tractors driven by rear wheels are generally used in paddy fields. In this paper, the driving type and engine type are respectively set to rear wheel drive (RWD) and a small diesel engine. Engine characteristics are based on a 30-kW diesel engine for a small agricultural tractor determined by JISB8018 (JISB8018, 1989). Figure 6.3 shows the adopted engine characteristics.

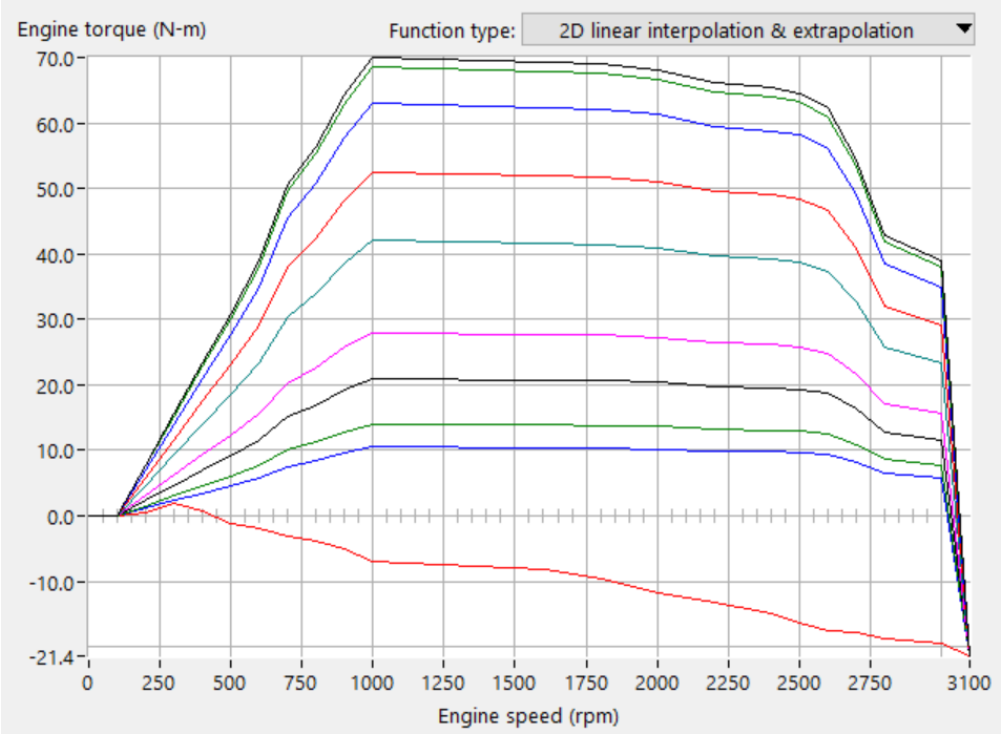

Figure 6.3 Engine characteristics of a small agricultural tractor (JISB8018, 1989).

Figure 6.3 shows that the engine torque increases with the engine speed until an engine speed of 1000 rpm. This torque rise is a typical feature of a diesel engine used for an agricultural tractor. Owing to this characteristic, the tractor can operate even when the engine rotation suddenly decreases because of a sudden operational burden.

Figure 6.4 shows the 4WD and RWD powertrain system flow in CarSim® after the engine generates power and this power is transferred.

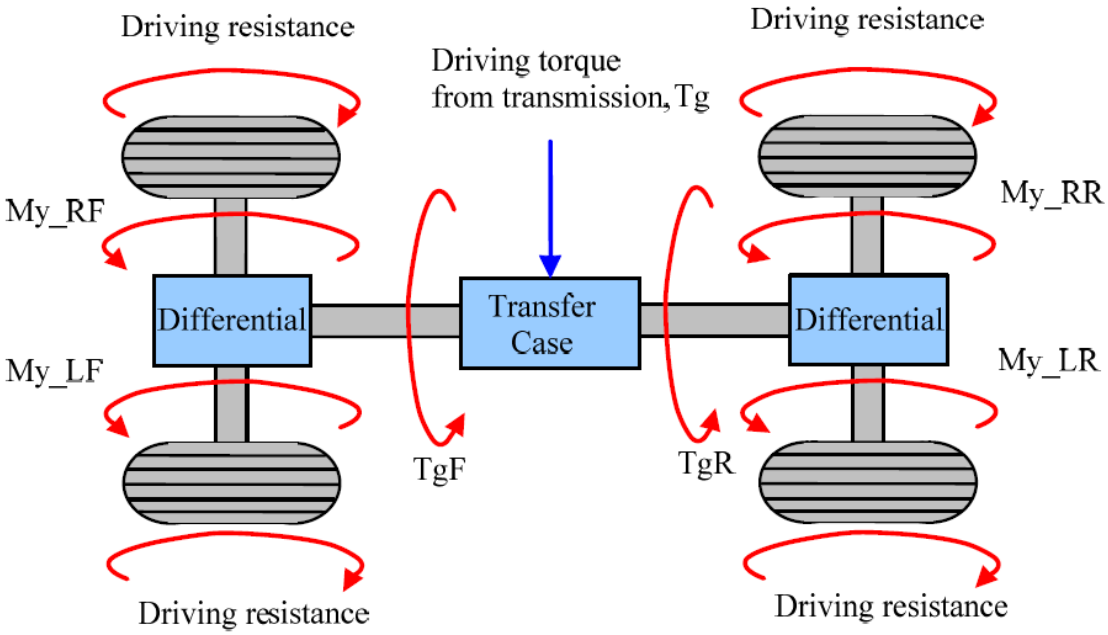

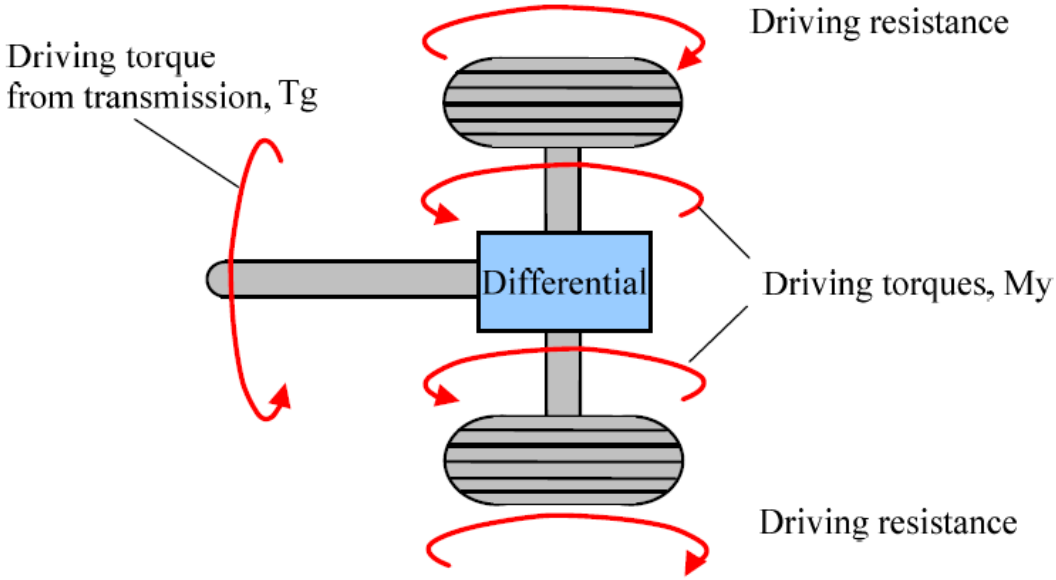

Figure 6.4 4WD and RWD powertrain systems in CarSim ®.

Travel of the agricultural tractor is extremely slow compared with that of automobiles. It is thus necessary to remodel the transmission gear ratio. The gear ratio in the powertrain system was determined so that first, second, third, fourth, fifth, and sixth speeds correspond to 0.05, 0.5, 1.0. 2.0, 3.0, and 4.0 m s^{-1} respectively. Figure 6.5 shows transmission gear ratios for the RWD tractor.

Up to 18 gears

6 Forward gears

	Gear Ratio	Inertia	Efficiencies Driving	Efficiencies Coasting
R:	-850	0.034	0.9	0.9
N:		0.034		
1:	850	0.037	0.92	0.92
2:	85	0.034	0.92	0.92
3:	42	0.042	0.95	0.95
4:	21	0.04	1	1
5:	14	0.04	1	1
6:	10.5	0.04	1	1

Figure 6.5 Gear transmission ratios for the RWD tractor; first, second, third, fourth, fifth, and sixth speeds correspond to 0.05, 0.5, 1.0. 2.0, 3.0, and 4.0 m s^{-1} respectively.

6.2.2. Steering system

In Carsim®, there are two options for the steering system, namely a rack & pinion system and a recirculating ball system. In this study, a rack & pinion system is chosen for steering because generally available automobiles and tractors are equipped with this mechanism. A front steering system is employed as this is the tractor steering system generally available. The steering ratio, which refers to the ratio between the steering wheel angle and the road wheel angle, is determined by measurement of a real tractor in the laboratory. In the laboratory experiment, the operator turned the steering wheel through a maximum angle of 360 degrees and the road wheel angle was measured as 26.7 degrees. The steering gear ratio was thus determined as 13.5. In setting the steering system, the steering ratio was indirectly determined by the C factor, which is the translation of the rack per revolution of the pinion gear. After trial-and-error adjustment, the C factor was determined as being 65 mm per revolution.

6.2.3. Brake system

In general, tractors are only equipped with a rear brake system while automobiles are normally equipped with front and rear brake systems. Additionally, agricultural tractors have independent left and right brake systems to conduct farm operations, which is not normal for automobiles. These brake characteristics are set in the CarSim® brake setting screen. Figure 6.6 shows the screen for setting the brake systems.

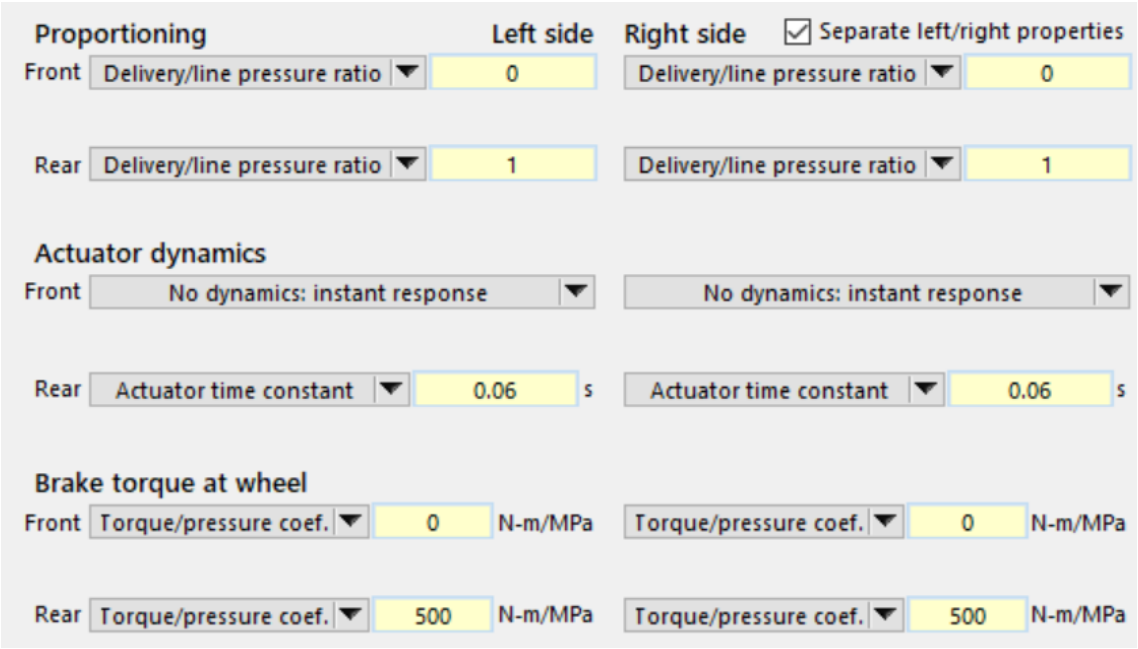

Figure 6.6 Screen for setting the brake systems in CarSim®.

The front proportioning and brake torque are set to zero to make the front brake system ineffective and thus realize a sole rear brake system. In this setting, the left and right brake systems can be set independently. A one-sided brake system can thus be realized during operation by changing the rear proportioning and brake torque to zero on one side. The torque of the rear left and right brakes is set to 500 N m.

6.2.4. Suspension and axle system

Front and rear suspension system parameters can be set in CarSim®. In the suspension system configuration, the axle type and spring and damper characteristics can be set. Figure 6.7 shows the axle type setting and suspension stiffness and damping characteristics. In this study, a solid axle is chosen for the agricultural tractor model. In the suspension settings, the spring rate is set to 200 N/mm and the damping coefficient is set to 55 kN/m. Unsprung masses of front and rear wheels are set to 100 kg.

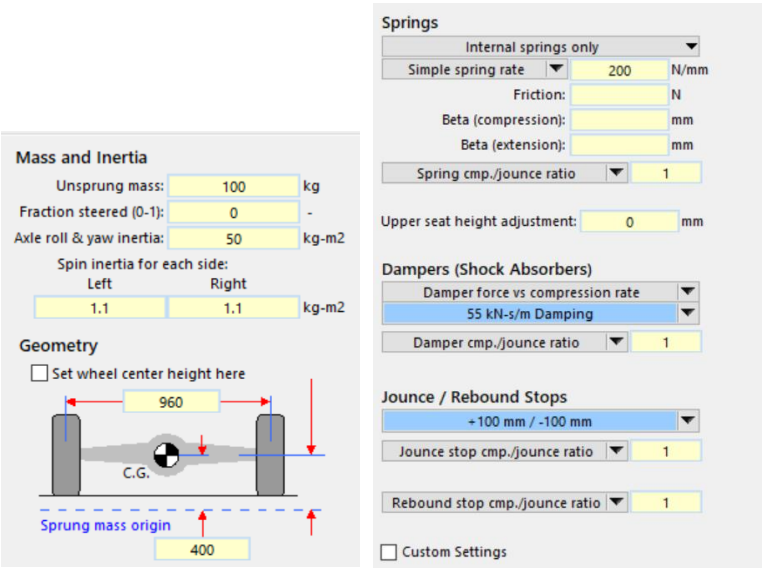

Figure 6.7 Axle and suspension system setting.

6.3. Validation test of configurations of the tractor driving simulator

This section validates the above tractor configuration by reporting numerical simulations. A gear shift operation test was first conducted to validate the powertrain system. A minimum radius turning test was then carried out to validate the steering and brake systems.

6.3.1. Gear shift operation test

The gear shift test was conducted for validation of the powertrain system configuration to achieve a desirable operational tractor speed. The tractor drove along a flat road surface while shifting from first to sixth gear. Figure 6.8 shows the numerical results of the gear shift test. The top panel shows the operational velocity of the tractor for each gear shift, the middle panel shows the engine rotational speed, and the bottom

panel shows the gear position.

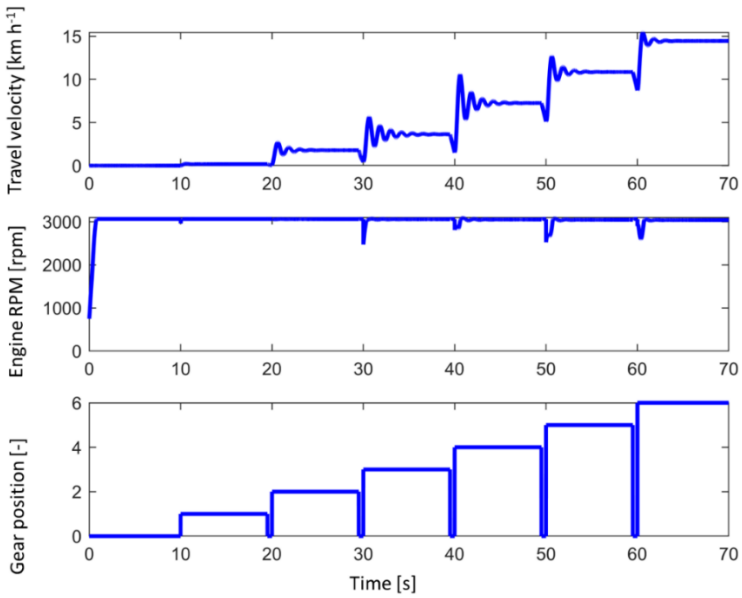

Figure 6.8 Numerical results of the gear shift test: (top) travel velocity of the tractor [km h^{-1}]; (middle) engine speed [rpm]; (bottom) gear position [–].

In the numerical experiments, the engine rotational speed increased to 3000 rpm as the simulation progressed. During the simulation, the operator changed gear from first to sixth. In the first gear position, the travel velocity of the tractor was 0.05 m s^{-1}. This speed corresponds to towing operations in agricultural fields. As the gear position increased, the travel velocity of the tractor increased from 0.05 to 4.0 m s^{-1}. A higher travel velocity corresponds to traveling along a farm road. The engine rotation decreased rapidly to 3000 rpm at the moment of gear change.

6.3.2. Minimum radius turning test

A minimum radius turning test was conducted to validate the tractor steering system. In the general tractor specification test, the minimum turning radius is measured adopting one-side-braking turning. Adopting a measurement standard of the tractor minimum

turning radius (JISD6708, 1976), the gear position was set to second (0.5 m s^{-1}) in the numerical experiments. In the turning, the right brake was ineffective, and a left turn was made with a minimum turning radius. Figure 6.9 shows the numerical results of the minimum radius turning test. The top panel shows the steering wheel angle, left road wheel angle, and right road wheel angle, the middle panel shows the left and right cornering forces acting on the front wheel, and the bottom panel shows the left and right cornering forces acting on the rear wheel.

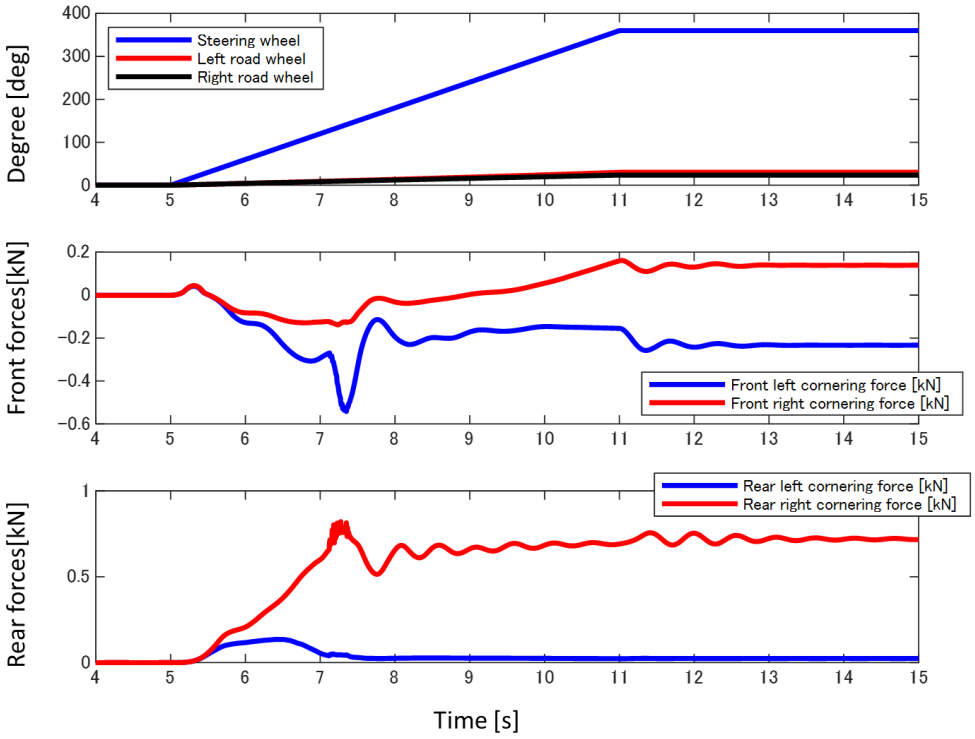

Figure 6.9 Numerical result of the minimum radius turning test with left-braking: (top) steering wheel angle and front road wheel angle [deg]; (middle) front left and right cornering forces [kN]; (bottom) rear left and right cornering forces [kN].

The maximum steering wheel angle was 360 degrees according to a measurement of the real tractor. Thus, in the turning test, the steering wheel angle was ramped from 0 to 360

degrees. As the steering wheel angle increased to 360 degrees, the road wheel angle increased to 26.7 degrees. The cornering force acting on the front wheel increased as the road and steering wheel angles increased. Meanwhile, the cornering force acting on the rear left wheel was zero while the cornering force acting on the rear right wheel increased. This means the rear left brake system worked and made the cornering force acting on the rear left wheel zero. In this turning test, the minimum turning radius was 2.9187 m, which is a typical value for the minimum turning radius of a tractor. The above two numerical simulations demonstrated that the configurated powertrain and steering system worked appropriately for a tractor driving simulator.

6.3.3. Validation of the suspension system

In the CarSim® vehicle configuration, vehicle models generally have axial suspension for front and rear wheels. However, most tractors used in agriculture are not equipped with axial suspensions although several front-suspension tractors and full-suspension tractors have been developed. This section investigates the effect of the CarSim® suspension system on tractor dynamics by reporting a bump driving test. In the numerical experiment, the tractor drove in third gear over a 0.035-m bump. Figure 6.10 shows the road surface used in the numerical experiment.

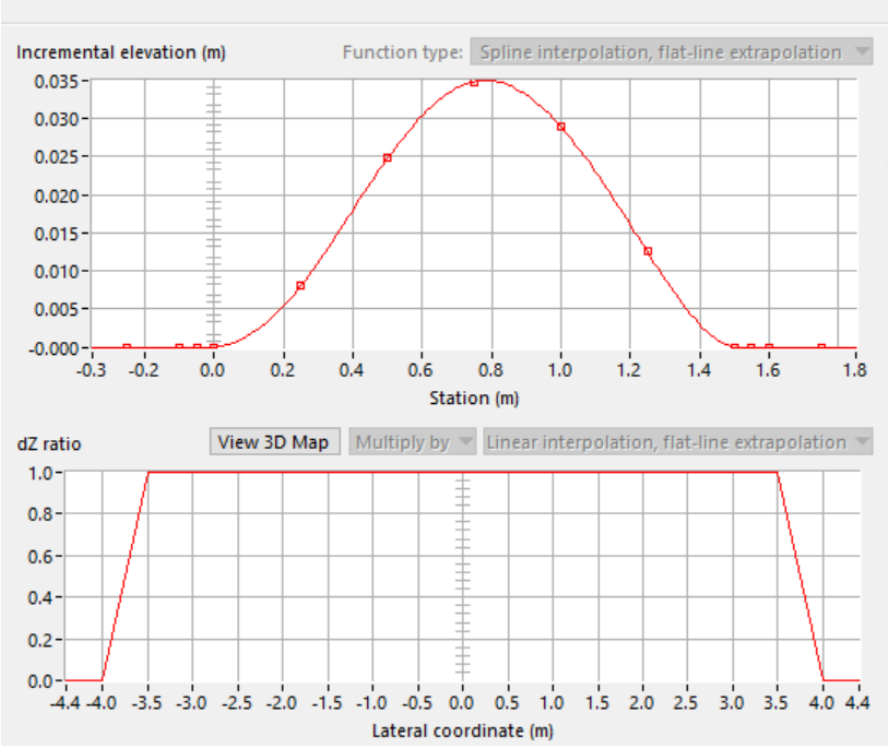

Figure 6.10 Road surface having a 0.035-m bump used in validation of the suspension system.

If a tractor is not equipped with an axial suspension system, the tractor body and rear axial are rigidly connected. Thus, there is no difference between the body position and rear axial position if the tractor drives over a bump. In the CarSim® system, however, the tractor model is equipped with an axial suspension system and there should thus be a difference between the body position and rear axial position in the bump driving test. Figure 6.11 shows the difference between the tractor body position and rear axle position.

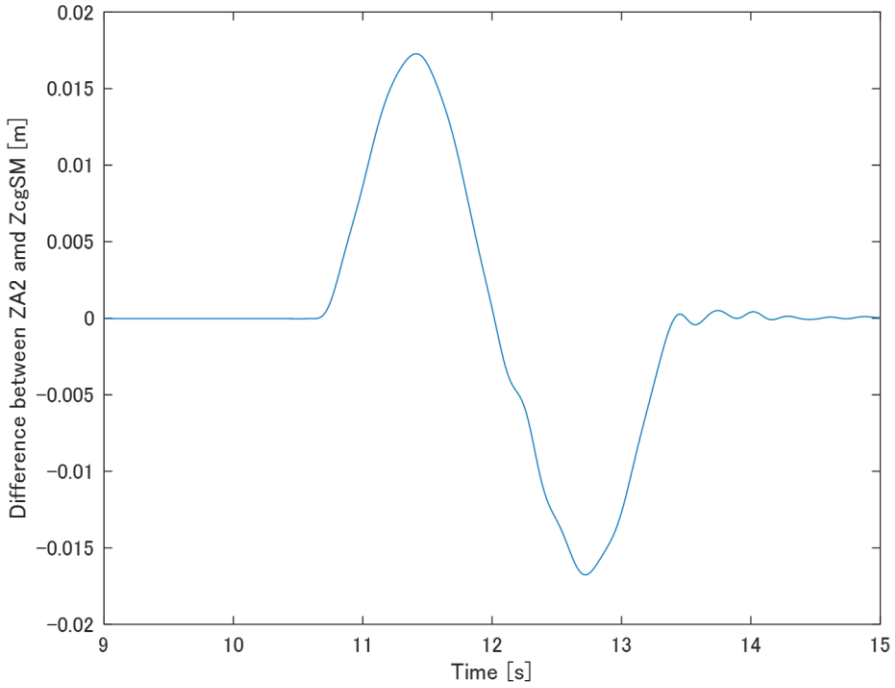

Figure 6.11 Difference between the tractor body position and rear axial position.

Figure 6.11 shows that the difference between the tractor body position and rear axial position was not zero. The maximum difference is ±0.017 m.

6.4. Development of a motion system for a tractor driving simulator

6.4.1. Outline of the tractor driving simulator with a motion system

This section presents the development of a tractor driving simulator. The tractor driving simulator was developed using CarSim® DS, MATLAB® & Simulink®, and a Logitech® G27. We used the CarSim® driving simulator as a computational platform in this investigation. CarSim® is a commercial driving simulator that was developed by Mechanical Simulation Cooperation. The CarSim® vehicle assembly has various types

of validated automotive models, including sedan, hatchback, sport utility vehicle, and truck models. In addition to these automotive models, CarSim® has a farm tractor model (Kim, et al., 2016; Watanabe & Sakai, 2019). CarSim® has a computationally efficient mathematical model based on multibody physics with more than 100 degrees of freedom. CarSim® software includes an interface for other software packages, such as MATLAB® and Simulink ®.

Vehicle parameters, such as dimensions, mass, the moment of inertia, parameters of the powertrain system, brake system, and steering system, tire characteristics, and compliance characteristics can be determined. Road conditions and driver models can be set. Road parameters, such as the shape of the road, friction coefficient, and road excitation, can be configured. Driver model parameters, such as the travel velocity, steering wheel angle, and gear shift control, can be set. In addition to there being a driver model, an operator can handle the steering wheel, operational pedals, and gear shifter manually using the Logitech G27. Using the MATLAB®/Simulink ® interface, CarSim® DS is connected to the Logitech® G27, which is joystick hardware comprising a steering wheel, accelerator, brake, and clutch pedals, and gear shifter.

Figure 6.12 is a schematic diagram of the configuration of the developed tractor driving simulator.

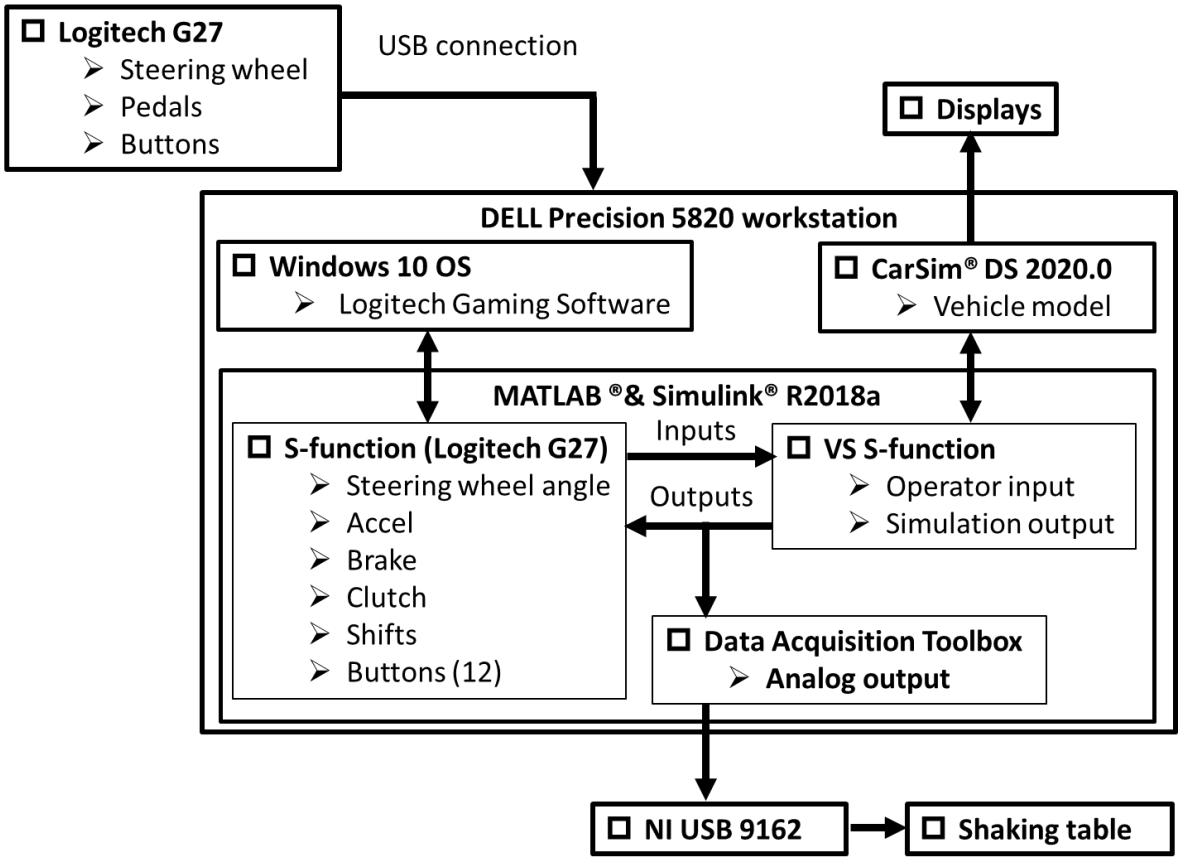

Figure 6.12 Schematic diagram of the configuration of the developed tractor driving simulator.

The Logitech® G27 is connected to a workstation computer through a USB connection. Tractor operators handle tractor models using the steering wheel, operational pedals, and button controls. CarSim® DS is connected to the MATALB® & Simulink® interface by a VS S-function, and the operational inputs are transferred to CarSim® DS. The numerical computation of the vehicle simulation is conducted in the vehicle model of CarSim® DS. Simulation outputs are transferred to the Logitech® G27 as force feedback that represents the reaction steering force. In addition to the Logitech® G27, outputs are transferred to the motion system through the MATLAB® & Simulink® data acquisition toolbox and D/A converter by the National Instrument®.

6.4.2. Simulink model of the developed system

Figure 6.13 shows the Simulink® model used in the development of the tractor driving simulator.

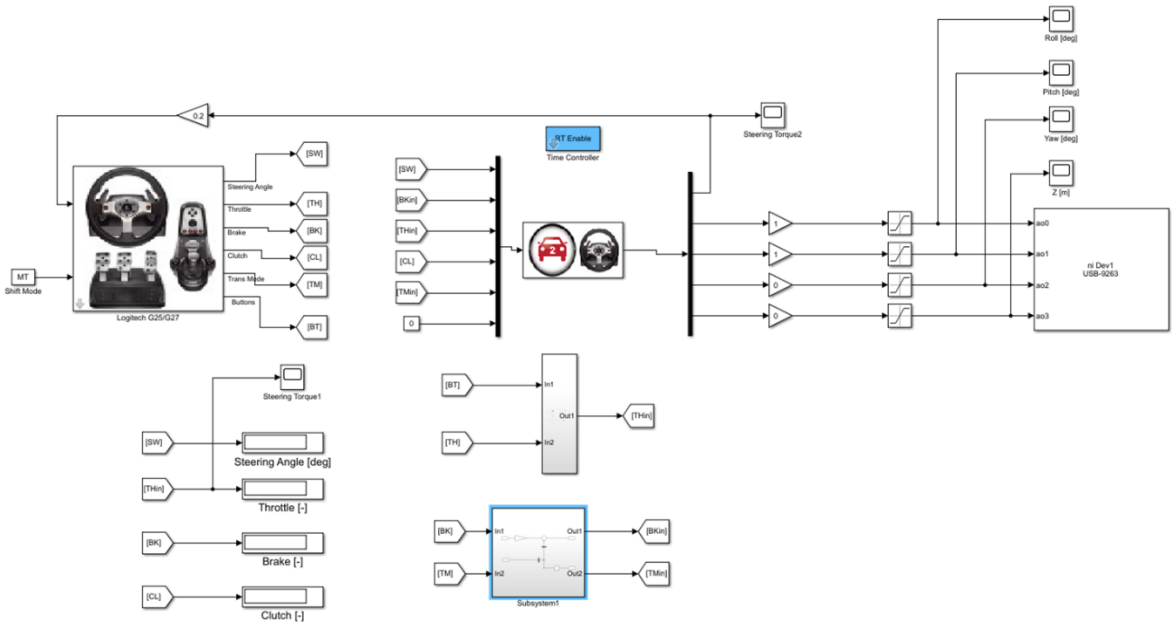

Figure 6.13 Simulink® model used in the tractor driving simulator.

In the Simulink® model, the tractor characteristic mechanisms (i.e., the throttle lever control and left and right brake systems) are developed. The operator can change the accelerator model by pushing the right paddle button shown in Figure 6.13. In normal acceleration mode, the foot accelerator is activated and the operator accelerates the vehicle using the foot accelerator. In lever accelerator mode, the throttle openness is varied from 0 to 1.0 in increments of 0.2 by pushing the left paddle button. The operator can change the brake mode by pushing left and right brake buttons. If the operator pushes the left or right brake button once, then the left or right brake is disabled. If the operator pushes the brake button twice, then the left and or right brake is enabled again. An independent brake system was developed using this mechanism.

6.4.3. Developed tractor driving simulator with a motion system

The tractor driving simulator was developed using the abovementioned configuration. In the development, a motion system offered by Solution Inc, Tokyo, Japan, was used as a driving platform. The tractor seat, Logitech® G27 racing wheel & pedals, and other jig items supporting the system were set on the motion system. Figure 6.14 shows a photograph of the developed tractor driving simulator with a motion system.

Figure 6.14 Developed tractor driving simulator with a motion system setup.

Various driving simulations can be carried out in various terrain environments using the developed tractor driving simulator with a motion system.

6.5. Summary

A tractor driving simulator with a motion system was newly developed for the reproduction of overturning accidents within a virtual test drive platform. A tractor

characteristic mechanism was implemented in the configuration of CarSim®. Numerical experiments involving a gear shift operation test and minimum radius turning test were conducted to validate the driving simulator configuration. In addition to the driving simulation system, a driving simulator with a motion system was developed using CarSim®, MATLAB® & Simulink®, a Logitech® G27, and a motion system offered by Solution Inc. The developed motion system was validated in a laboratory experiment and can be applied in numerical experiments to reproduce tractor overturning scenarios.

7. Numerical experiments conducted using the developed tractor driving simulator

7.1. Introduction

In chapter 6, the tractor driving simulator with a motion system was developed for a virtual test drive. This chapter conducts numerical experiments using the developed tractor driving simulator with a motion system to identify tractor overturning scenarios. Driving simulators are generally used in the automobile industry for research and development purposes. This virtual test drive is a standard methodology for automobile manufacturers to make their products (Yoon, Cho, Kang, Koo, & Yi, 2010). Furthermore, the virtual test drive is applied to develop advanced driver assistance systems and autonomous driving as well as conventional products. The developed tractor driving simulator can be used for a virtual test drive of a tractor the same as that for an automobile.

In this work, using the developed driving simulator, overturning scenarios were reproduced based on a real accident case reported in Japan. The chapter is structured as follows. First, the tractor model in the driving simulator was validated in field experiments of a bump test and double-lane-change test. Numerical experiments were then carried out to reproduce a tractor overturning accident within virtual test drive platform.

7.2. Field-experiment validation of the tractor driving simulator

This section reports on the validation of the developed tractor driving simulator in

field experiments. The developed CarSim® tractor model was validated by comparing results of the CarSim® tractor model and field experiments. Bump tests were first conducted to validate the vertical dynamics of the tractor model. A double-lane-change test was then conducted to validate the lateral dynamics of the tractor model. The double lane change was designed based on ISO 3888-2 (ISO 3888-2, 2011).

7.2.1. Experimental instruments

This section presents experimental instruments used in the validation test. An Iseiki TH22K tractor was used in the field experiments. An AS10-B three-axis acceleration transducer (KYOWA, Tokyo, Japan) was used to measure acceleration. Figure 7.1 shows the three-axis acceleration transducer.

Figure 7.1 Three-axis acceleration transducer (KYOWA AS-10TB).

The acceleration transducer was set on a tractor seat and connected to a Panasonic CF-20 Toughbook placed on the tractor bonnet. Figure 7.2 is a schematic diagram of the experimental instruments on the tractor.

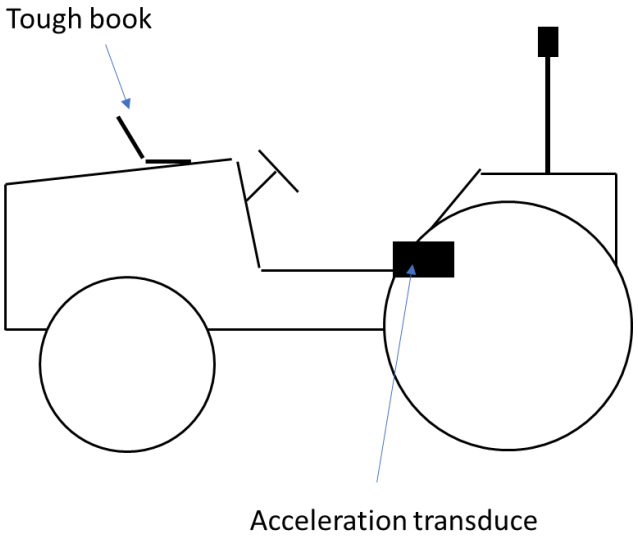

Figure 7.2 Schematic diagram of the measurement system.

Vertical, longitudinal, and lateral accelerations (A_z, A_x, A_y) were collected using the developed experimental system. The sampling period was set to 50 s and the sampling frequency to 200 Hz (which means the sampling interval was 0.005 s).

7.2.2. Bump test validation

This section reports on bump tests conducted to validate the vertical dynamics of the tractor model in the driving simulator. Figure 7.3 is a schematic diagram of the tractor bump tests.

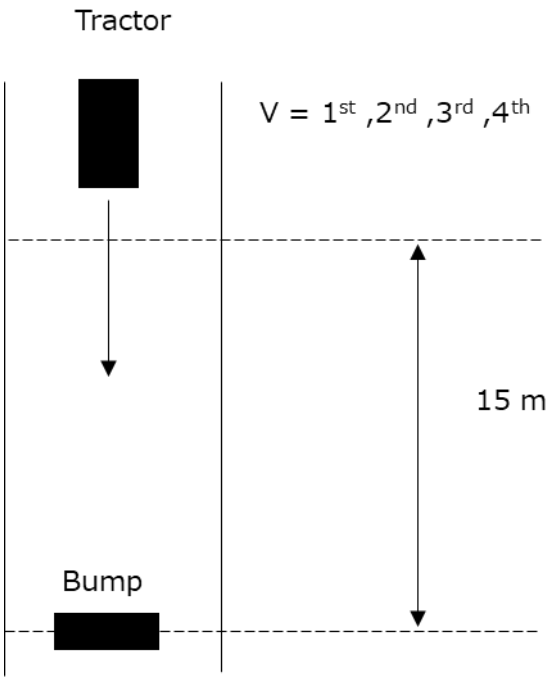

Figure 7.3 Schematic diagram of bump tests.

In the tests, the tractor drove along a farm road at the Tokyo University of Agriculture and Technology and passed over a 0.05-m bump. The tractor traveled in first, second, third, and fourth gears. The travel velocity was measured manually in each test. Table 7.1 gives the average travel velocity of the agricultural tractor for each gear position.

Table 7.1 Average travel velocity of the agricultural tractor for each gear position

Gear position	Travel velocity (m s^{-1})
First	1.44
Second	1.82
Third	2.46
Fourth	3.62

Three repeated tests were conducted for each gear position. A total of 12 tests were thus

conducted. Figure 7.4 shows typical results of the vertical acceleration (fourth gear, N = 1).

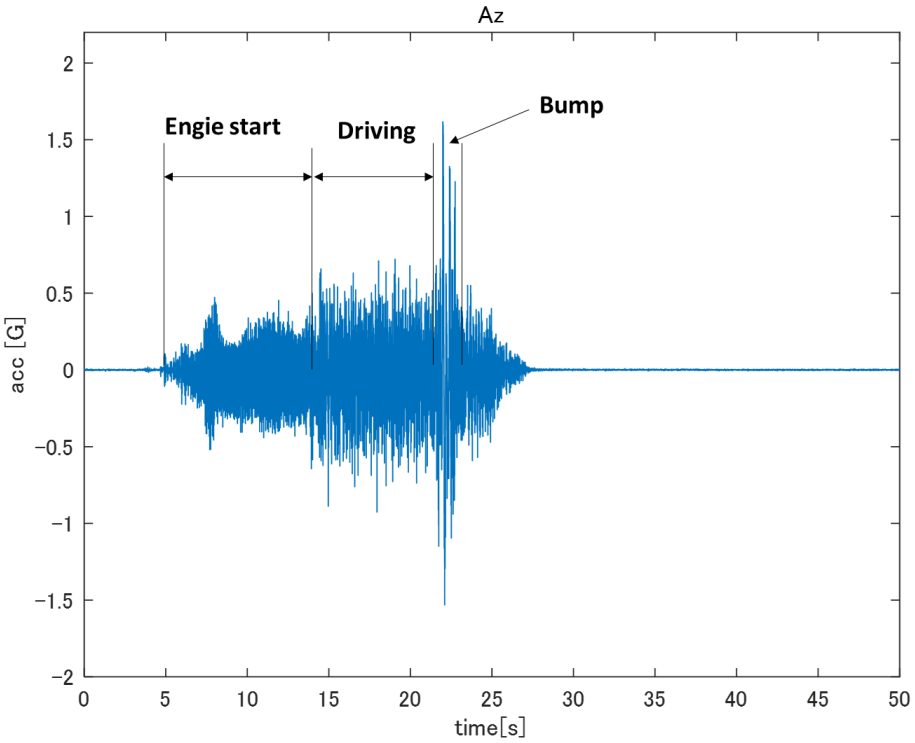

Figure 7.4 Experimental results of a bump test (fourth gear, N = 1).

At 5.0 s, the tractor engine was turned on and engine vibration began. The tractor began to drive at 14.2 s and there was vibration excited by tire lugs. At 21.5 s, the tractor rode over the bump and bump excitation occurred. As described above, the vertical acceleration comprised three phases, namely engine vibration, tire lug vibration, and bump excitation vibration. Thus, data analysis should be conducted on each phase separately. In this chapter, bump excitation vibration is analyzed for validation of the tractor model because engine and lug vibrations are beyond the scope of the validation. Engine and lug vibration data analysis is presented in the Appendix. Figure 7.5 shows

bump excitation vibrations in each test.

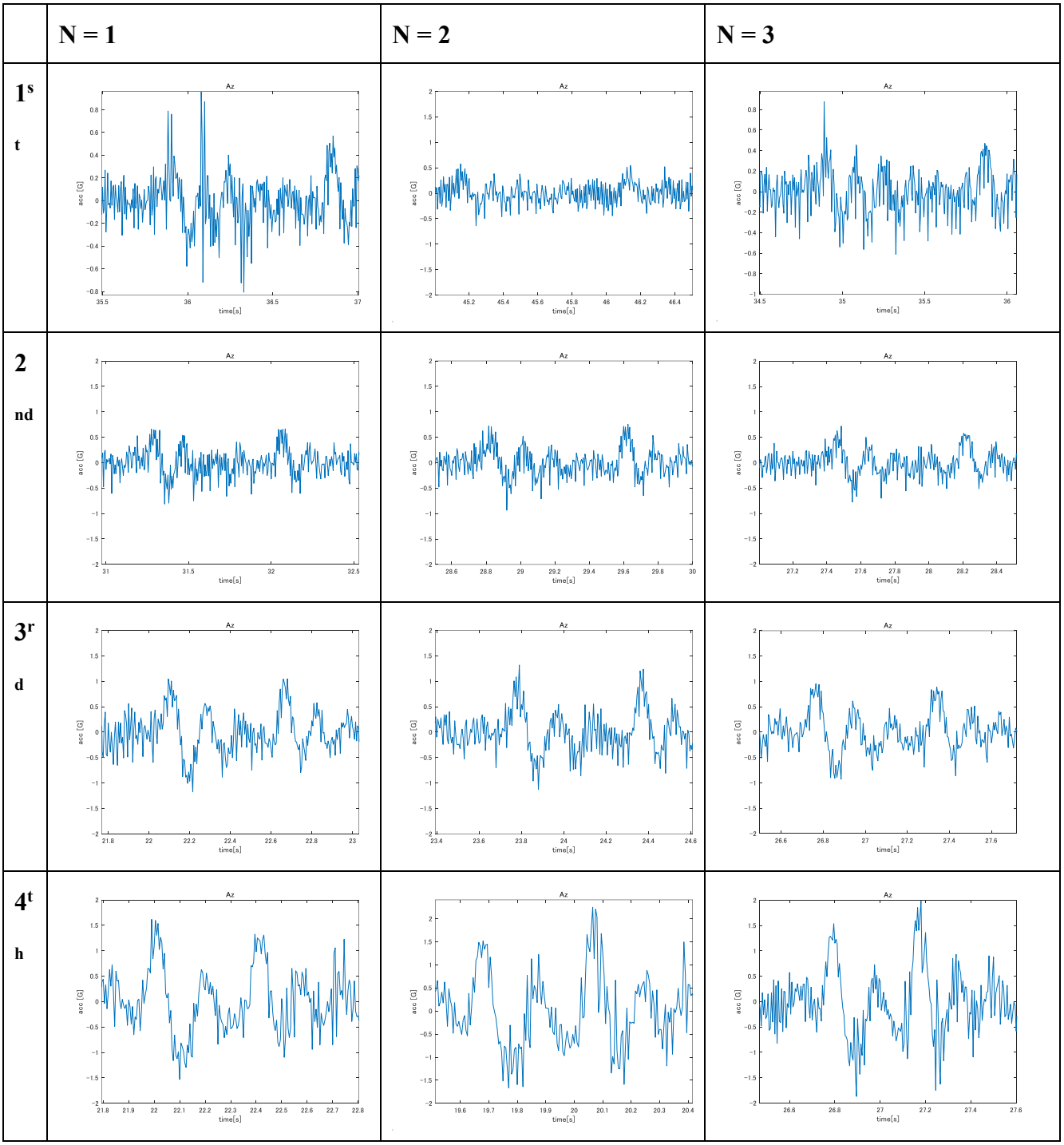

Figure 7.5 Vertical acceleration of the bump excitation vibration in each test.

Figure 7.6 shows the Fourier spectrum of vertical acceleration in each test.

	N = 1	N = 2	N = 3
1st	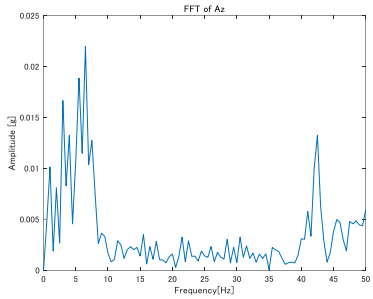	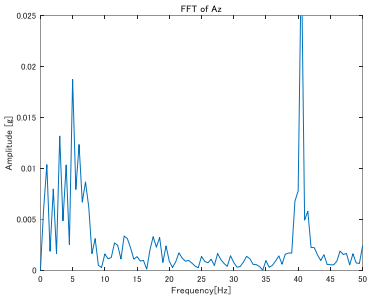	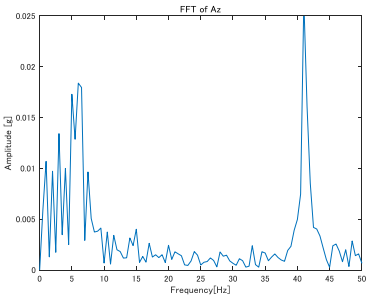
2nd	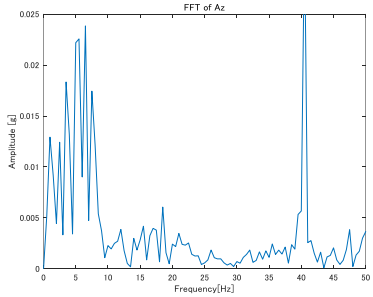	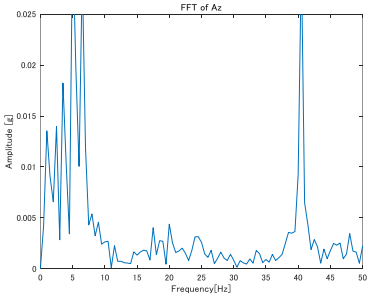	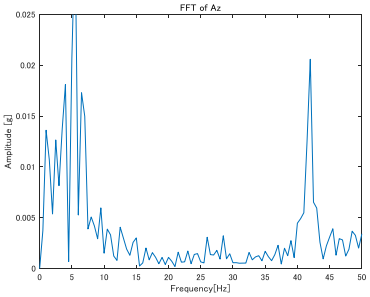
3rd	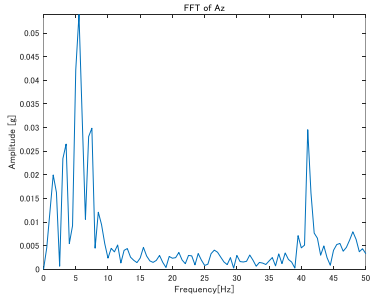	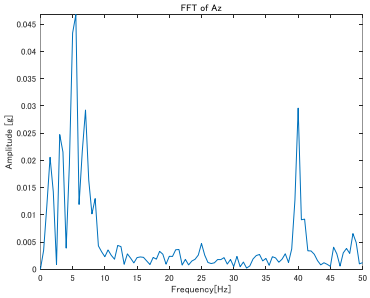	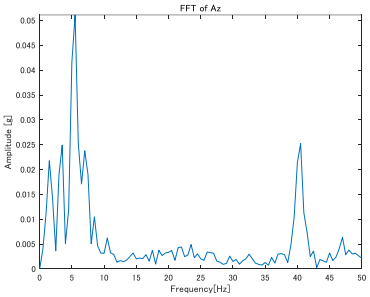
4th	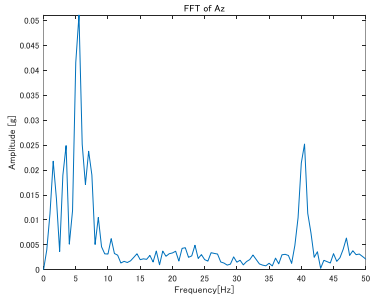	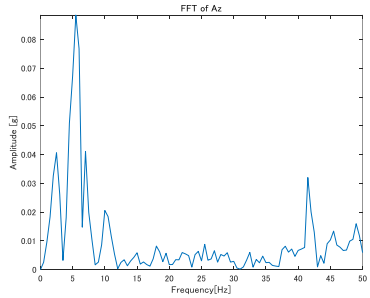	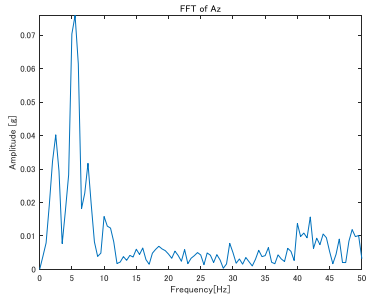

Figure 7.6 Fourier spectrum of vertical acceleration in each test.

Figure 7.7 shows a typical example of the time series and Fourier spectrum of vertical

acceleration (fourth gear, N = 3).

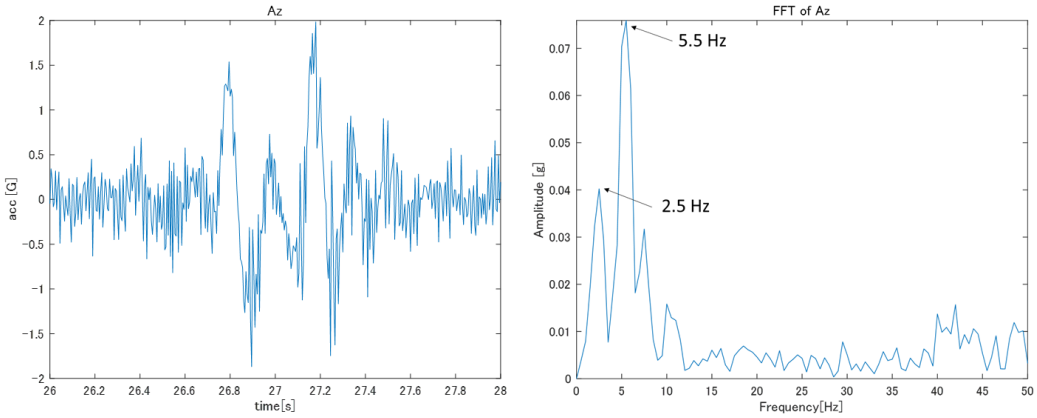

Figure 7.7 Time series and Fourier spectrum of vertical acceleration in the fourth gear, N = 3 experiment.

The experimental data presented in Figure 7.5 show that tractor vibrations were generated when the front wheel and rear wheel encountered the bump. This generation of vibrations became increasingly evident as the travel velocity of the tractor increased. The Fourier spectrum in Figure 7.6 shows that there was an evident engine rotational frequency around 40 Hz when the travel velocity was low, such as when the tractor was in first or second gear. As the travel velocity increased, a low-frequency spectrum below 10 Hz became distinct. This low-frequency spectrum came from the natural frequency of the tractor and the bump excitation frequency which was calculated from V/WB. The Fourier spectrum in Figure 7.7 shows that there was a clear natural frequency of 5.5 Hz and bump excitation frequency of 2.5 Hz.

The MATLAB bouncing tractor model (detailed in Chapter 2), CarSim® tractor model (detailed in Chapter 6), and bump test results are next compared to validate the CarSim® tractor model. In the comparison, a typical experimental result (fourth gear, N

= 3) is used. To make a clear comparison, a 10-Hz lowpass filter is applied to the experimental values. Figure 7.8 compares the models and experimental values.

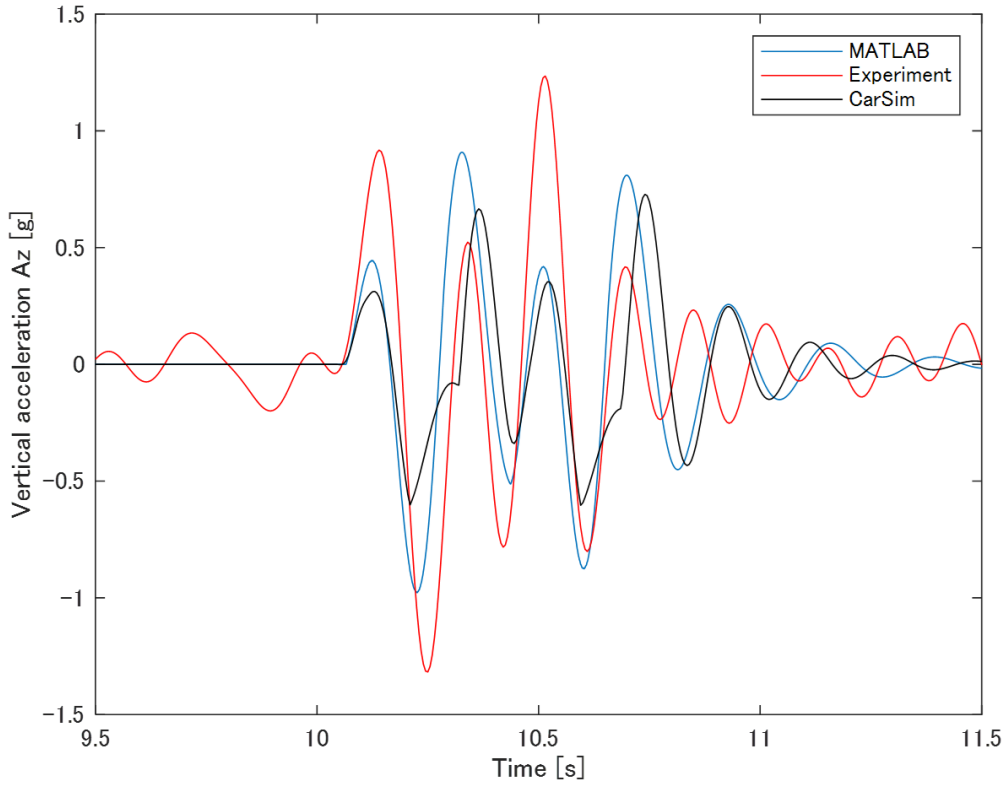

Figure 7.8 Comparison of the MATLAB® bouncing tractor model, CarSim® tractor model, and experimental results (fourth gear, N = 3).

In the comparison, the shapes of time series are similar to each other though damping characteristics are different slightly.

7.2.3. Double-lane-change test validation

This section reports on double-lane-change tests conducted to validate the lateral dynamics of the CarSim® tractor model. The double-lane-change test was based on ISO3888-2, which stipulates a standard for automotive double-lane-change tests. However, the travel velocity of agricultural tractors is generally much lower than that of

normal automobiles. Thus, a 1/2 scaling was applied to the double-lane-change standard. Figure 7.9 is a schematic diagram of the double-lane-change test for agricultural tractors.

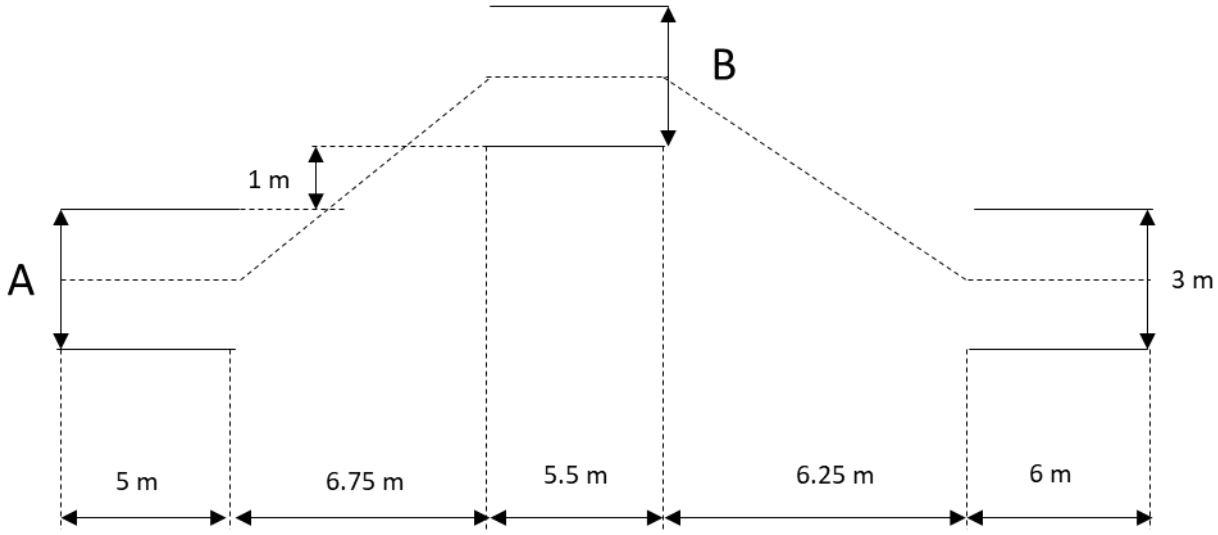

Figure 7.9 Schematic diagram of the proposed double-lane-change test for agricultural tractors.

Figure 7.10 shows raw data of the lateral acceleration (fourth gear, N = 3) and data filtered using a 0.5-Hz lowpass filter.

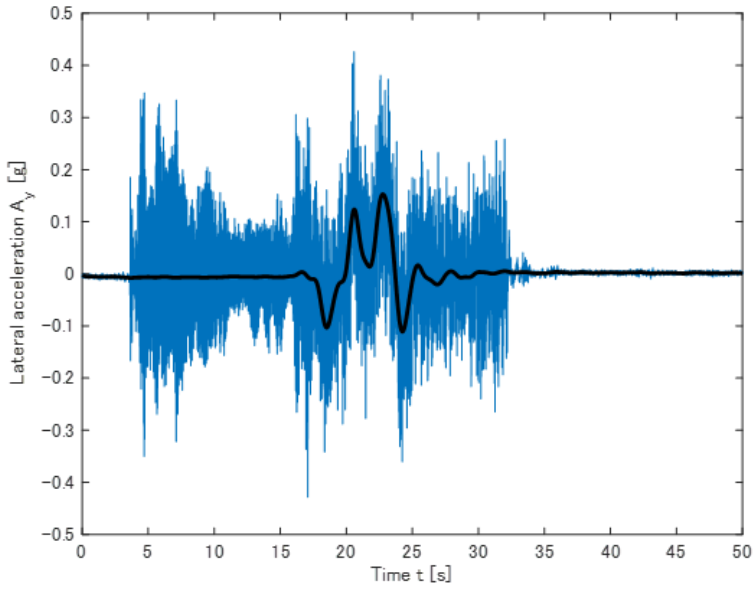

Figure 7.10 Raw data and 0.5-Hz lowpass filter data of lateral acceleration (fourth gear, N = 3).

Lateral motion of the tractor was clearly observed using the 0.5-Hz lowpass filter. Figure 7.11 shows all experimental data of the double-lane-change tests.

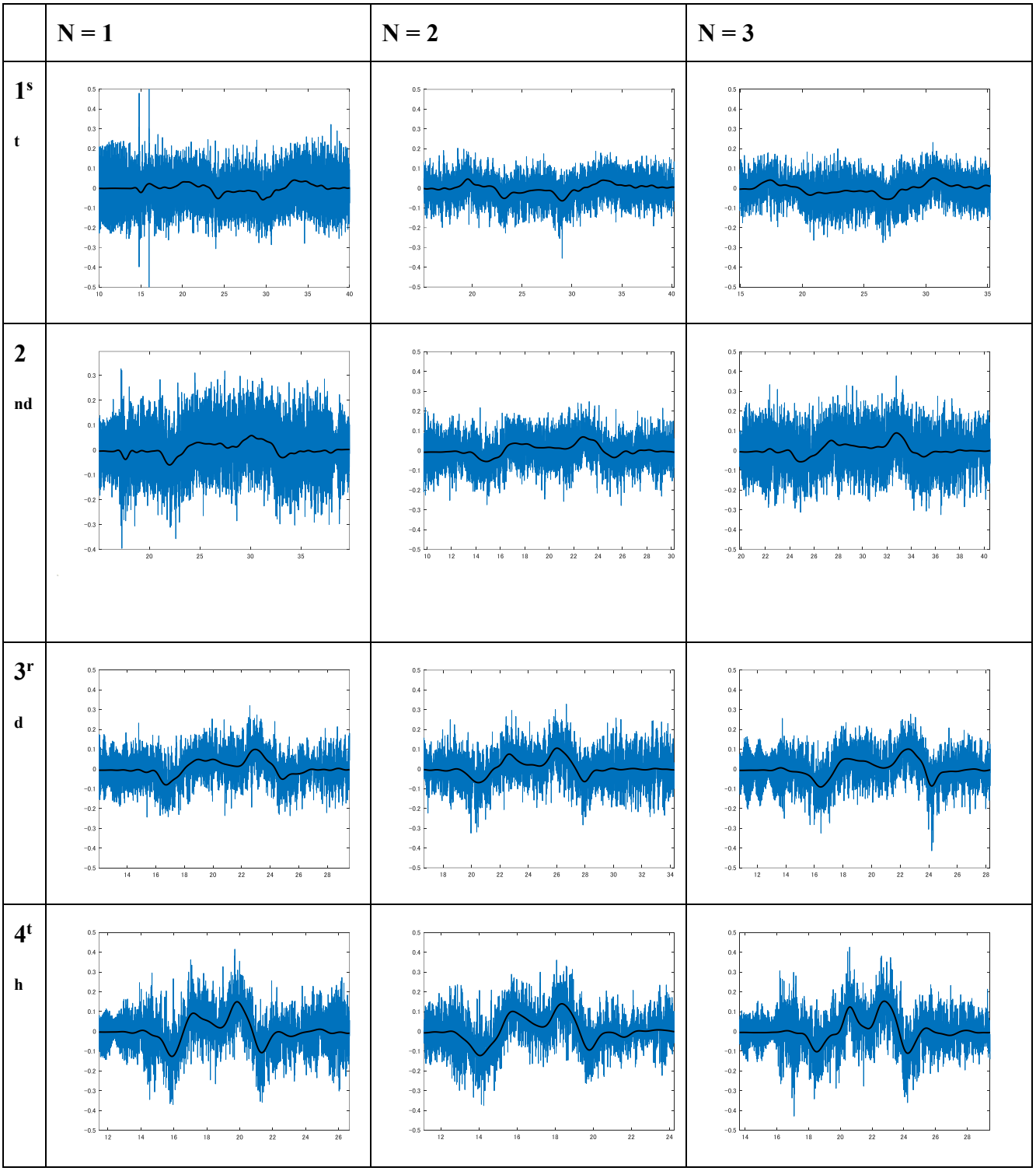

Figure 7.11 Lateral acceleration in double-lane-change tests.

An increase in the travel velocity increased the maximum lateral acceleration and thus

the tractor cornering forces. The MATLAB bicycle model (detailed in Chapter 3), CarSim® tractor model, and the experimental values are compared as for the bump test. The comparison, shown in Figure 7.12, is made for the experimental results of the fourth gear and N = 3.

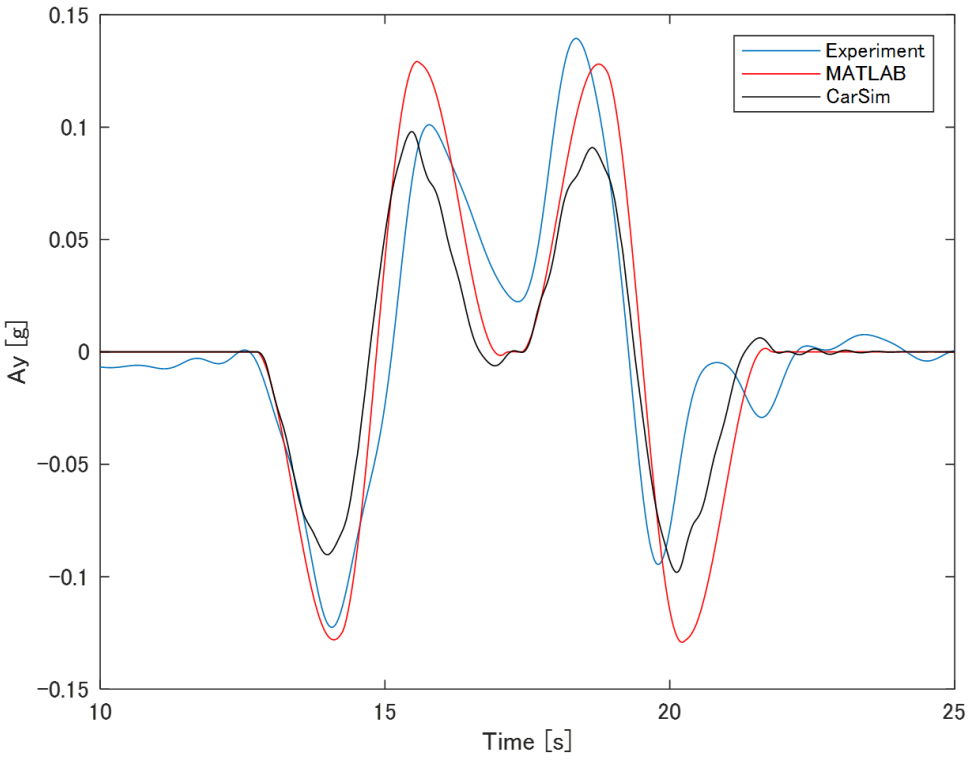

Figure 7.12 Comparison of the lateral acceleration among the MATLAB® bicycle model, CarSim® tractor model, and experiment (fourth gear, N = 3).

The shapes and magnitudes of the curves in Figure 7.12 are similar. The results of the bump test and double-lane-change test reveal that the CarSim® tractor model is generally capable of reproducing the experimental results. Additionally, CarSim® model results are generally similar to the results of the MATLAB® bouncing and bicycle models, which indicates that the MATLAB® model results obtained in the present paper can be applied

to the tractor driving simulator. The CarSim® model can therefore be used as a computational platform in the tractor driving simulator.

7.3. Nonlinear dynamics in the tractor driving simulator

This section presents nonlinear dynamics in the developed tractor driving simulator. The previous chapter obtained characteristic nonlinear dynamics of agricultural tractors, such as bouncing, sliding, and power hop, by developing nonlinear mathematical models.

7.3.1. Bouncing in the tractor driving simulator

As detailed in Chapter 2, impact dynamics generated by the bouncing tractor are a typical nonlinear phenomenon in tractor dynamics. This subsection presents bouncing tractor dynamics in the CarSim® driving simulator. A sinusoidal function is used to represent the road surface:

$$d(x) = \mathrm{d}_0(1 - \cos(2\pi \mathrm{f}_s x)), \tag{7.1}$$

where d_o is set to 0.025 and f_s is set to 1. This section presents numerical simulations of the nonlinear dynamics of a tractor on the sinusoidal road surface. The travel velocity of the tractor was set to 3.0 m/s. Figure 7.13 shows the front and rear vertical loads.

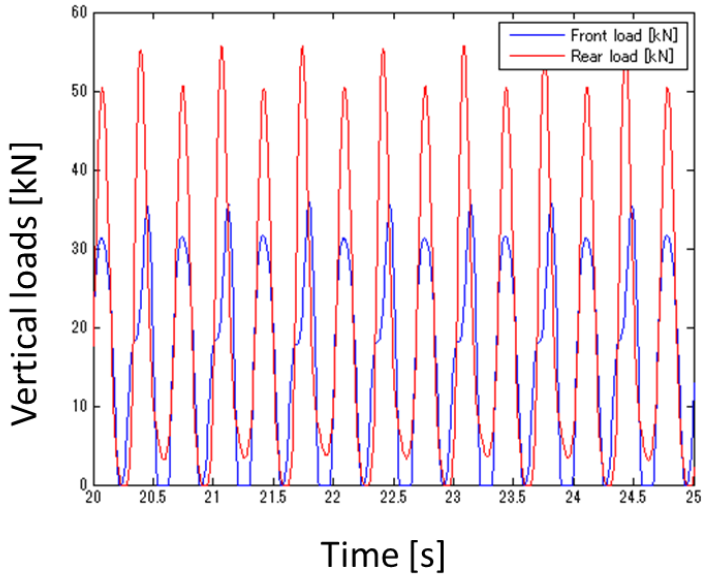

Figure 7.13 Time series of vertical loads acting on the wheels. Blue and red lines show the front and rear vertical loads, respectively.

The front and rear vertical loads became zero, which means the tractor tire lost contact with the ground and the tractor jumped. Figure 7.14 shows the time series of the vertical acceleration A_z and the Fourier spectrum of A_z.

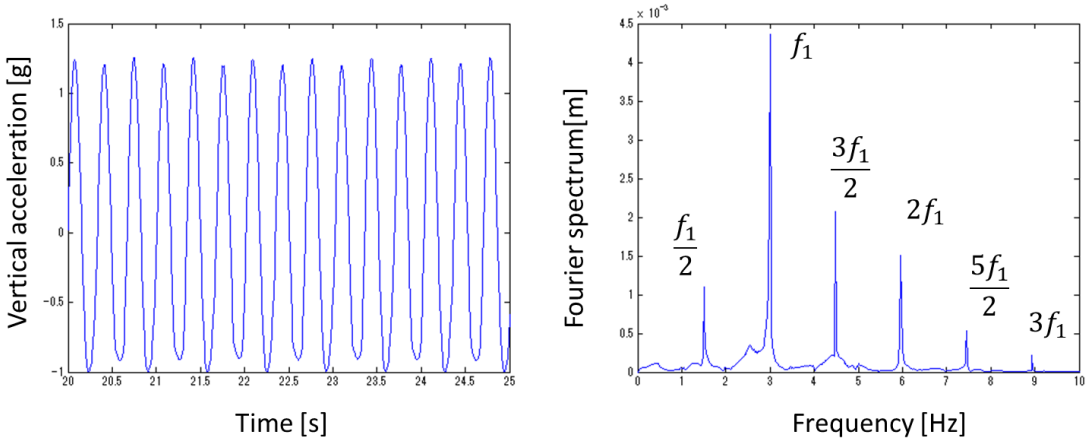

Figure 7.14 (Left) Time series of the vertical acceleration A_z and (right) Fourier spectrum of the vertical displacement.

The maximum and minimum values of the vertical acceleration were 1.23g and –1.0g. This means the tractor experienced free fall. A forcing frequency f_1 = 3.0 Hz appeared in the Fourier spectrum. In addition to the forcing frequency, the subharmonic $f_1/2$, super-harmonics $2f_1$ and $3f_1$, and ultra-subharmonics $3f_1/2$ and $5f_1/2$ appeared. These frequencies are typical of nonlinear dynamics. Figure 7.15 shows the trajectory in the phase plane of the vertical displacement and velocity.

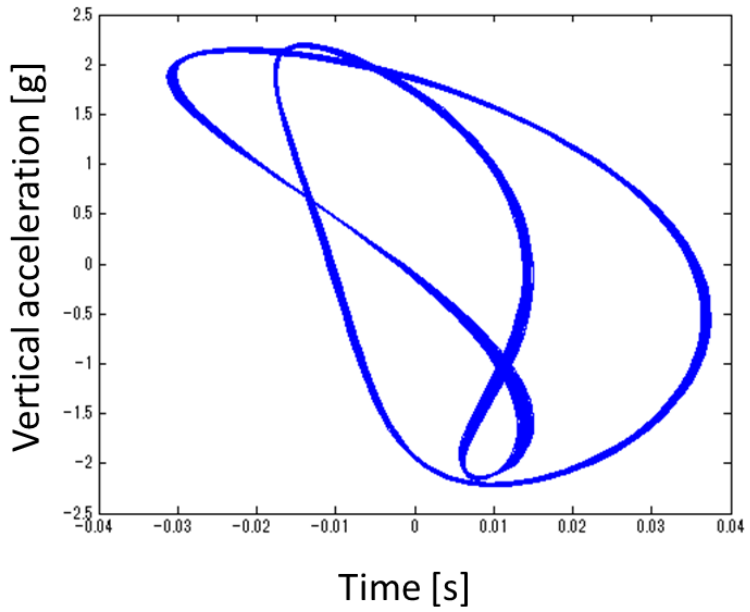

Figure 7.15 Numerical trajectory in the phase plane of the vertical displacement and velocity.

The trajectory shows complicated nonlinear motion, which cannot occur in linear dynamics. In this study, the nonlinear dynamics of a bouncing tractor were investigated using a driving simulator. The results indicate that bouncing or jumping occurs when tractor vibration is excited by a sinusoidal road surface. These impact dynamics generate

subharmonics, ultra-subharmonics, and super-harmonics, which are typical characteristics of a nonlinear dynamical system. The numerical results reveal that CarSim® reproduces the characteristic nonlinear dynamics of an agricultural tractor and provides a platform for investigating tractor dynamics.

7.3.2. Power hop in the tractor driving simulator

This section reports on numerical experiments conducted to investigate nonlinear tractor dynamics and identify overturning scenarios using the developed tractor driving simulator. First, the power hop phenomenon was demonstrated in the tractor driving simulator as a typical example of tractor nonlinear dynamics. The tractor driving simulator was then applied to real cases of overturning accidents and to identify overturning scenarios.

Power hop is a well-known dynamic instability of a tractor. Self-excited oscillation occurs when a tractor is operated in or on an agricultural field, slope, or road. This power hop reduces the operational performance and safety and increases machine damage and soil compaction. Power hop is a combination of nonlinear dynamics, namely bouncing and stick-slip dynamics. It is therefore important to demonstrate the occurrence process of power hop in the tractor driving simulator for its application to the investigation of overturning. In the numerical experiments, the gear was set to fourth and the inclination of the slope was varied from 0 to 14 degrees. Figure 7.16 shows the maximum vertical acceleration A_z in each experiment.

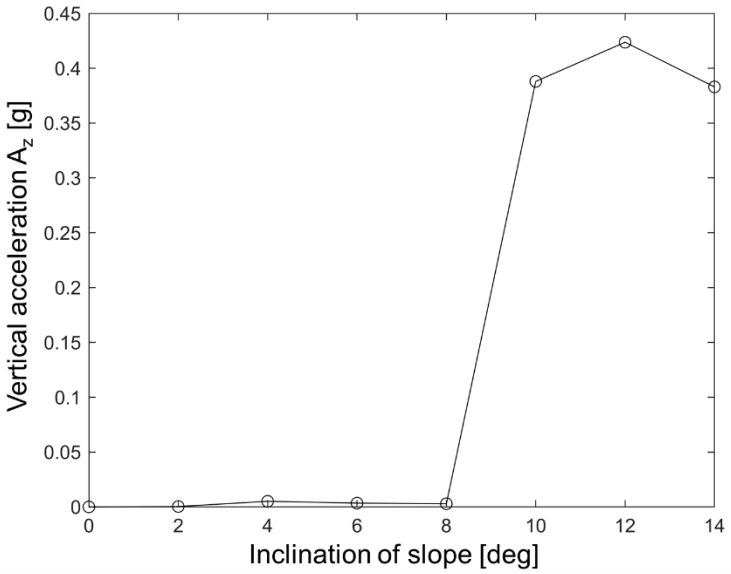

Figure 7.16 Maximum vertical acceleration of the tractor in each numerical simulation.

When the inclination of the slope was greater than 10 degrees, there were self-excited oscillations and the maximum value of A_z increased. Figure 7.17 shows the time series of the vertical acceleration, longitudinal acceleration, and vertical loads acting on the front and rear wheels for an inclination of 10 degrees.

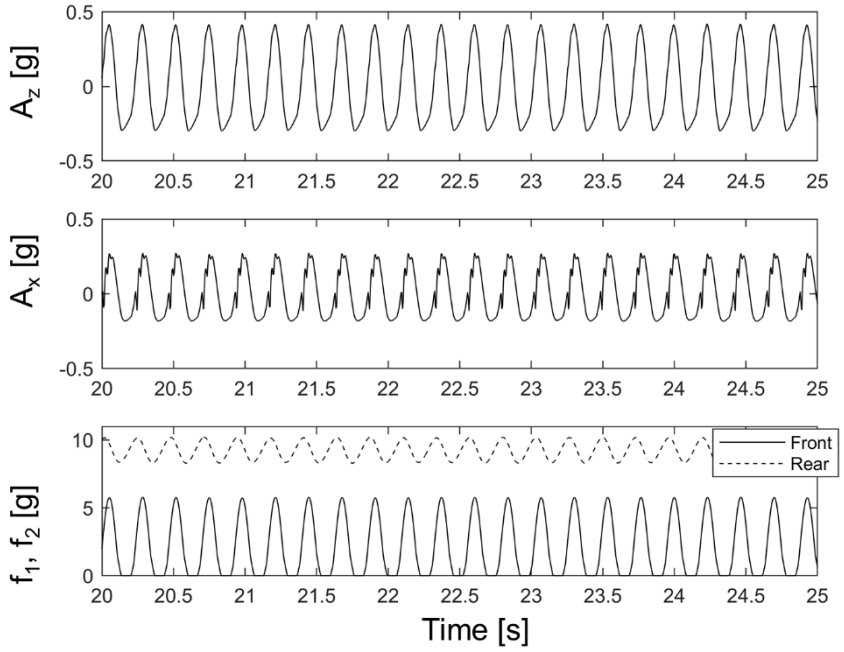

Figure 7.17 Numerical results (slope inclination of 10 degrees): (top) time series of the vertical acceleration; (middle) longitudinal acceleration; (bottom) vertical loads acting on the front and rear wheels.

Figure 7.17 shows self-excited oscillations. The front wheel of the tractor periodically lost contact with the ground. The above numerical results indicate that the nonlinear power hop phenomenon can be reproduced in the tractor driving simulator.

7.4. Reproducing overturning scenarios using the developed tractor driving simulator

7.4.1. Overturning accident on a steep passage slope

In Japan, the most arable land comprises small and narrow paddy fields used to cultivate rice and has many steep slopes, inclined side paths, and rough roads. Case studies conducted by the Japanese government have revealed that tractor overturning frequently happens in these potentially dangerous environments. This section reports on

numerical experiments pertinent to reported cases that were conducted to reproduce tractor overturning accidents on the virtual test drive platform. One representative accident topography is a steep passage slope between a farm field and road. The survey found that the tractor overturned on a passage slope of 19 degrees. The accident topography and process were detailed by Watanabe & Sakai (2019, 2020). The tractor entered the slope in a higher gear. The axial load then decreased low enough to cause steering instability and the overturning accident.

In the present study, numerical experiments were carried out to reproduce the abovementioned accident case using the developed tractor driving simulator. The slope was 2.0 in length, 0.7 in height, and 19 degrees in inclination as for the accident case. The gear was set into fourth and the coefficient of friction between the wheel and ground was set at 0.75, 0.50, and 0.25 for the preferable, mid-range, and adverse road conditions. Figure 7.18 shows the trajectories simulated under different road conditions.

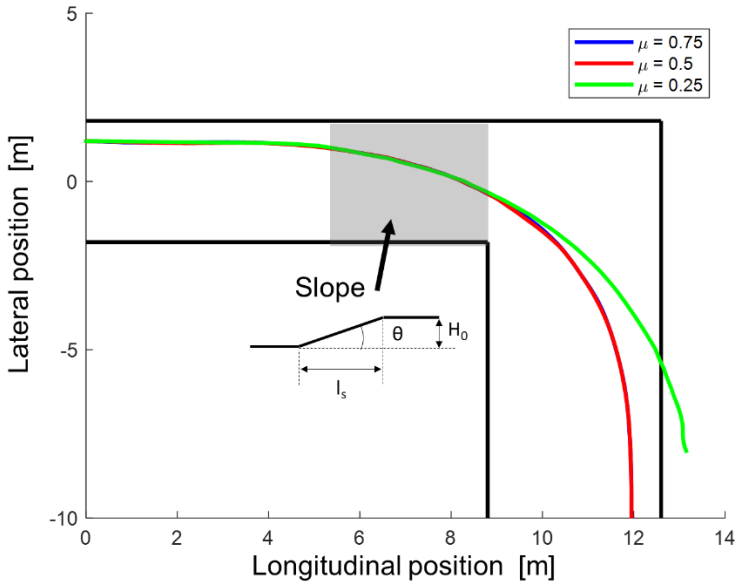

Figure 7.18 Numerical simulation results of the accident on the passage slope.

When the road condition was preferable or mid-range (μ = 0.75 or 0.50), the tractor was able to turn right on the road. Meanwhile, the tractor was not able to turn and the travel trajectory was off the road when the road condition was adverse (μ = 0.25). In this case, the tractor overturned and the simulation was interrupted. Figure 7.19 compares the time series of vertical loads and cornering forces acting on the front wheel between preferable and adverse conditions.

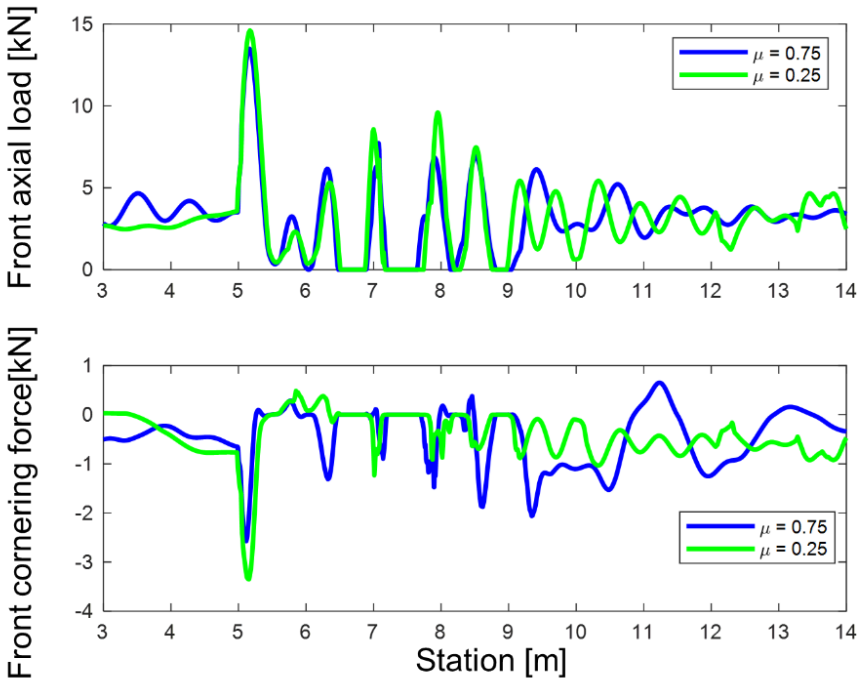

Figure 7.19 (Top) Front axial load [kN] and (bottom) front cornering force [kN].

In Figure 7.19, the top panel shows the axial load acting on the front wheel and the bottom panel shows the cornering force acting on the front wheel. When the tractor ran into the

slope, the axial loads increased. Simultaneously, the cornering forces were increased in an effort to turn right. If the axial loads decreased to zero, the cornering forces also became zero because the wheel lost contact with the ground. At the point depicted by an arrow, there was sliding in the adverse condition. The cornering force in the adverse condition thus became low compared with that in the preferable condition. The abovementioned steering instability meant that the cornering force was not sufficient to turn, resulting in the overturning accident. Figure 7.20 shows snapshots of the overturning process.

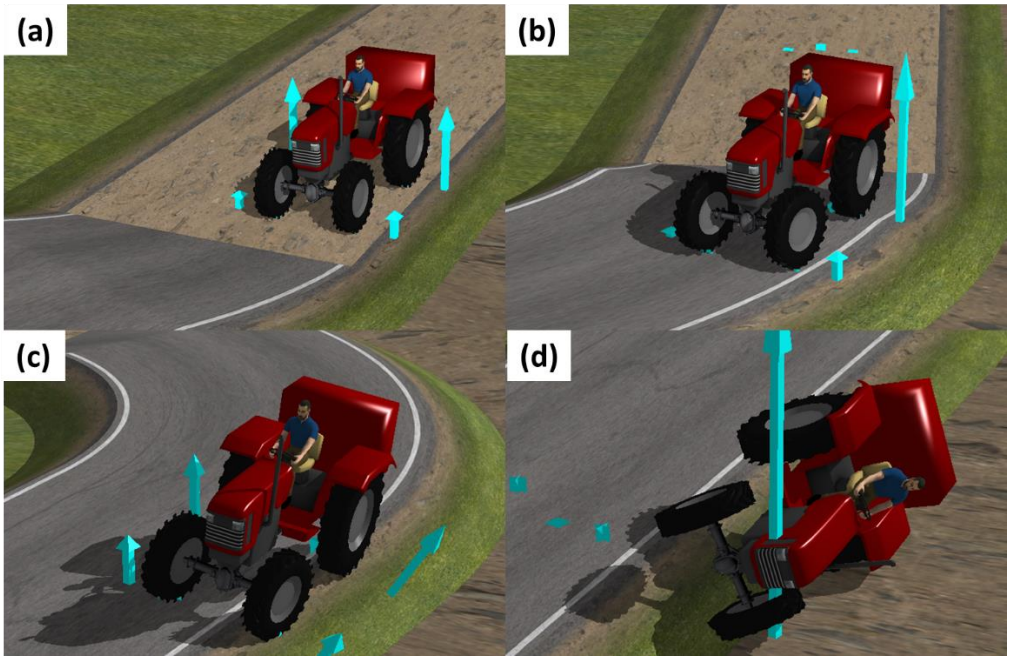

Figure 7.20 Overturning process of the tractor on a passage slope.

Figure 7.21 shows the motion system behavior during the overturing of the tractor.

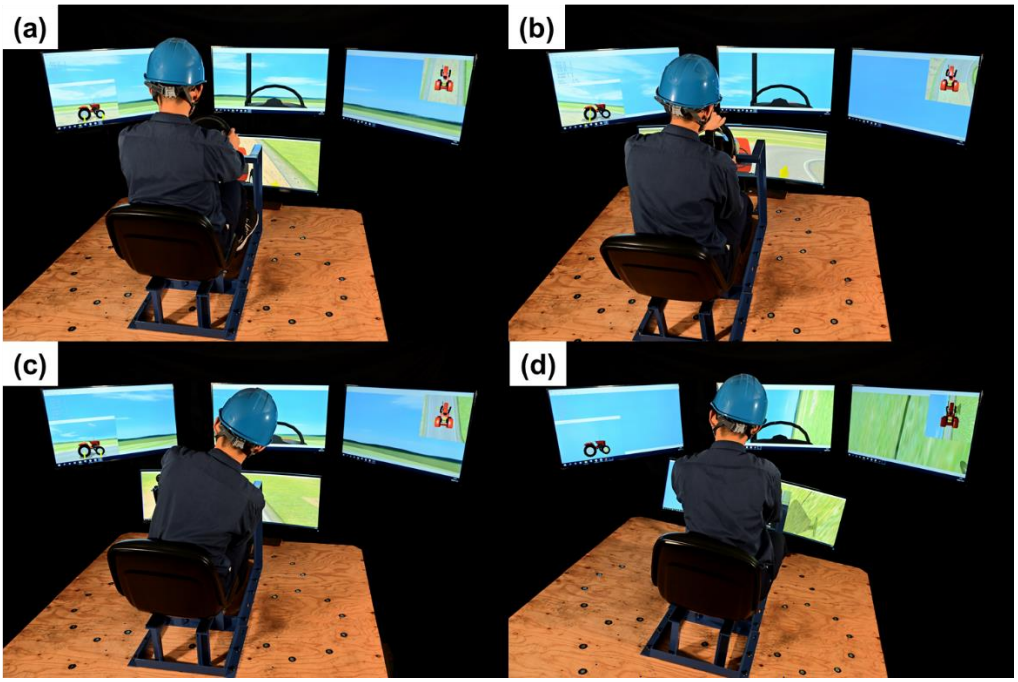

Figure 7.21 Motion system behavior during the tractor overturing simulation.

7.4.2. Overturning accident on a steep slope in rain

According to the governmental survey, overturning on a slope in rainy conditions is another typical accident scenario. A tractor entered a steep slope having an inclination of 23.5 degrees and height of 7.0 m in light rain. The tractor was able to drive up to the middle of the slope. However, the tractor slid just before completing its operation and then rolled over and fell down the slope. Numerical experiments were conducted in the same conditions recorded for the reported accident case. The gear was set into fourth and the coefficient of friction between the wheel and ground was set at 0.75, 0.50, and 0.25 for preferable, mid-range, and adverse road conditions. Figure 7.22 shows the simulated trajectories under the various road conditions.

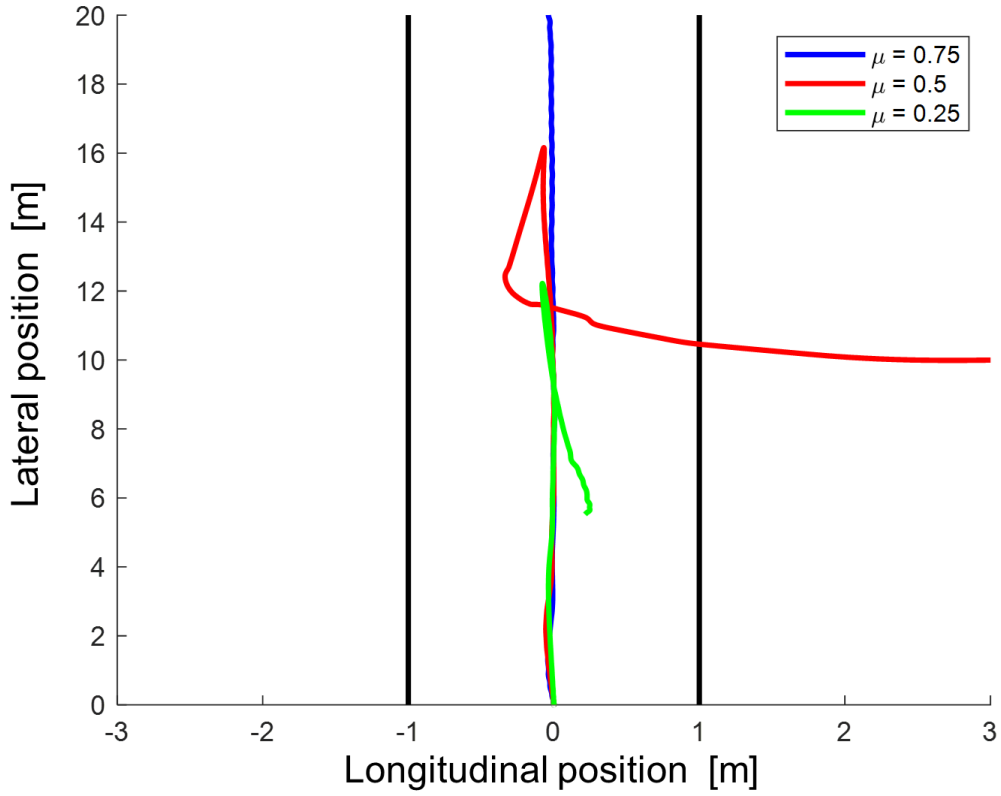

Figure 7.22 Numerical simulation results of the accident on a steep slope.

When the road condition was preferable (μ = 0.75), the tractor was able to drive upslope and there was no overturning. Meanwhile, when the road condition was mid-range or unpreferable (μ = 0.50, 0.25), the tractor slid and was not able to drive up the slope. The tractor made no progress at all up the slope when the friction coefficient μ = 0.25. In this case, the operator gave up driving and overturning thus did not occur. However, when the road condition was mid-range, the tractor was able to drive up to the middle of the slope. The tractor then slid and its orientation deteriorated. The travel trajectory of the tractor was off the slope and the tractor then rolled over and fell down the slope. Figure 7.23 shows snapshots of the overturning process.

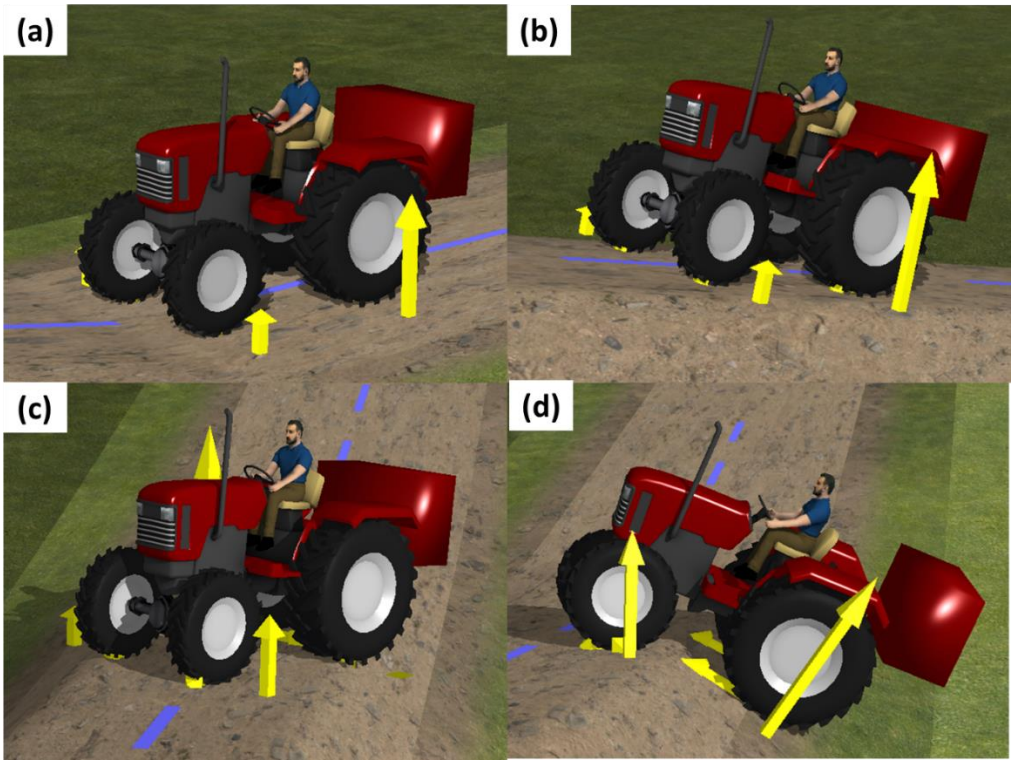

Figure 7.23 Process of the tractor overturning on a steep slope.

7.5. Summary

The developed tractor driving simulator was applied to reproduce overturning scenarios based on accident cases reported by the Japanese government. The numerical results indicate that the developed tractor driving simulator works well as a virtual test drive platform for safety research. Using the developed driving simulator, further studies, such as those on accident-avoidance control and anomaly detection during operation, will be conducted to improve tractor operational safety. Additionally, the developed simulator can be used to develop autonomous tractor driving, which is another important topic in this field.

8. Conclusion

8.1. Perspective

The major motivation of the present study was to investigate the nonlinear dynamics of an agricultural tractor for the prevention of overturning accidents. Tractor overturning has been a leading cause of farmer fatalities around the world since farm mechanization began. In addition to the safety issue, tractor overturning is a major obstruction for the development of autonomous driving. Autonomous driving and farm operations would be stopped if tractor accidents, such as overturning, occur. Tractor overturning is thus also an important research topic from the perspective of autonomous driving.

The agricultural tractor that is designed for off-road use and farm operations has a mechanical structure that is totally different from that of other vehicles such as normal automobiles. As an example, the tractor is generally not equipped with suspension and the front axle pivots at the center of the axle while the automobile is equipped with independent suspensions. The center of gravity of the tractor is higher than that of the automobile so as to maintain clearance between the tractor and ground for farm operations. Additionally, the length of the wheelbase of the tractor is short so that the turning radius is minimized at the headland of a farm field.

Owing to its abovementioned characteristics, the tractor lacks static and dynamic stability when being driven. This instability leads to nonlinear dynamics, such as bouncing, sliding, and power hop, which do not occur for automobiles and can lead to fatal accidents in which the tractor overturns. This thesis numerically investigated nonlinear dynamics through dynamic vehicle modeling and tractor driving simulation to clarify the mechanism of tractor overturning.

8.2. Summary

Several general conclusions are drawn from the results of the study as follows.

1) Development and analysis of nonlinear dynamic models for the agricultural tractor. Chapters 2, 3, and 4 investigated typical nonlinear phenomena in tractor operation by developing and analyzing nonlinear dynamic models. Chapter 2 investigated impact dynamics generated by a bouncing or jumping tractor. A bouncing tractor model was developed as a nonlinear forced oscillator based on bouncing ball dynamics. Several numerical experiments were conducted to investigate nonlinear characteristics of the developed model. The developed bouncing tractor model demonstrated typical nonlinear characteristics, such as a discontinuous frequency response, subharmonics, and super-harmonics. Parametric investigations on a steep passage slope were conducted using a model developed on the basis of a real accident case. The numerical results indicated that the abovementioned nonlinear characteristics cause overturning accidents on a steep passage slope.

Chapter 3 numerically investigated the steering instability induced by bouncing and sliding. A lateral sliding model was developed based on friction circle theory and was coupled with the bouncing tractor model. Turning tests were carried out to investigate the basic performance of the developed model. According to the numerical results, the combination of bouncing and sliding drastically deteriorated the steering stability of the tractor. In parametric investigations on the steep passage slope, bouncing and sliding caused steering instability, resulting in an overturning accident.

Chapter 4 developed a novel power hop model by coupling three nonlinearities, namely bouncing, stick–slip dynamics, and free play in the joint. The newly developed

model demonstrated the steady-state and transitional power hop occurrence in numerical experiments. The obtained results revealed that the feedback structure in the model is a main source of power hop. In parametric investigations, the developed model predicted the occurrence of power hop properly under the conditions of the field experiments.

2) Development of component technology for a tractor driving simulator. Chapters 5, 6, and 7 developed component technology for a tractor driving simulator. Chapter 5 developed algorithms for generating a road profile in constructing the terrain environment in the tractor driving simulator. First, a road profile on a single-wheel path was generated adopting the Fourier Transform surrogate method and AR model. Next, road profiles along two (left and right) wheel paths were developed adopting the extended Fourier Transform surrogate method and coherence analysis.

Chapter 6 developed a tractor driving simulator with a motion system and set the configuration using the general commercial driving simulator CarSim®. Vehicle systems, such as the sprung mass, power train, brake, steering, suspension, and tire, were configured to represent the characteristics of agricultural tractors. In addition to the configuration in CarSim®, a motion system offered by Solution Inc., Tokyo, Japan, was used with a Logitech G27 and MATLAB®/Simulink® interface. The steering wheel, operational pedals, and gear shifter were developed using Logitech G27 devices.

Chapter 7 conducted numerical experiments using the developed tractor driving simulator. First, the CarSim® tractor model and field experiment data were compared to validate the developed tractor driving simulator. Nonlinear dynamics of the driving simulator, such as the bouncing tractor and power hop phenomenon, were then presented. Using the developed tractor driving simulator, overturning scenarios were identified in numerical experiments.

8.3. Further investigations

The present thesis demonstrated that potential nonlinearities of agricultural tractor dynamics can lead to abnormal behaviors and cause fatal overturning accidents. A tractor driving simulator was developed using the results of nonlinear dynamic modeling. Typical overturning scenarios were identified in numerical experiments. Although the present study revealed the effects of nonlinear dynamics on tractor overturning, further investigations are needed as follows:

1) Developing a prediction algorithm for nonlinear dynamic behavior. According to the results of the numerical experiments, nonlinear dynamics, such as bouncing and sliding, can cause abnormal behaviors of tractors and overturning accidents. If vertical axial loads reduce to zero, the wheels lose contact with the ground and bouncing or jumping occurs. In addition to the impact dynamics caused by bouncing, lateral sliding occurs when the combination of the cornering force and traction force exceeds the limit of static friction, which is described by a friction circle. As mentioned above, the vertical, lateral, and longitudinal wheel forces play a decisive role in determining the dynamic behaviors of a tractor.

The measurement of wheel forces is difficult compared with the measurement of other vehicle variables, such as acceleration and the angular rate. It is therefore important to estimate the wheel force in predicting abnormal behaviors and possible overturning accidents. Machine learning techniques, such as linear and multivariate regression, are promising for the estimation of tractor wheel forces. However, general machine learning techniques do not assume strong nonlinear elements, such as bouncing and sliding, in tractor dynamics and should be modified to adapt to the nonlinear dynamics of

agricultural tractors. The use of a deep neural network and nonlinear Kalman filter are possible machine learning approaches of estimating the wheel forces. Using the estimated wheel forces, the grip margin, which is a typical steering stability indicator, can be estimated and dangerous behaviors predicted.

2) Developing a control system to avoid overturning accidents. A primary goal of the present research project is to prevent tractor overturning accidents instead of only protecting the operator during accidents. A vehicle dynamics control system must be developed to achieve this goal. Vehicle control systems have been developed and investigated in automotive engineering; e.g., the anti-lock braking system, traction control system, and electronic stability control. In the abovementioned systems, the control algorithm is generally designed based on linear vehicle dynamic systems. Nonlinear control must therefore be implemented in the tractor dynamic system to prevent overturning accidents. Possible nonlinear control methods are open-plus-closed-loop control, DF-control and sliding model control. In the present thesis, DF-control and P-control were applied to the bouncing tractor model in the numerical simulation. However, the developed control must be validated in a field experiment, such as that involving a real tractor or a scale model.

References

Abubakar, M. S. A., Ahmad, D., & Akande, F. B. (2010). A review of farm tractor overturning accidents and safety. Pertanika J Sci Technol, 18, 377-385.

Ahmadi, I. (2011). Dynamics of tractor lateral overturn on slopes under the influence of position disturbances (model development). Journal of Terramechanics, 48(5), 339-346.

Ahmed, O. B., & Goupillon, J. F. (1997). Predicting the ride vibration of an agricultural tractor. Journal of Terramechanics, 34(1), 1-11.

Andren, P. (2006). Power spectral density approximations of longitudinal road profiles. International Journal of Vehicle Design, 40(1-3), 2-14.

Aoyagi, Y., Matsui, M., Morio, D., Tamura, T., Uchikawa, Y., Kimura, T. (2016). Study on tractor behavior based on accident topography. Journal of the Japanese Society of Agricultural Machinery and Food Engineers, 78 (6), pp. 529-535.

Aoyagi, Y., & Matsui, M.,Driving Force Control for Suppression of Tractor's Dynamic Pitching Angle, 2019 International Joint Conference on JSAM and SASJ, and CIGR VI Technical Symposium joining FWFNWG and FSWG Workshops 2019.

Ayers, P., Khorsandi, F., Wang, X., & Araujo, G. (2018). ROPS designs to protect operators during agricultural tractor rollovers. Journal of terramechanics, 75, 49-55.

Baker, V., & Guzzomi, A. L. (2013). A model and comparison of 4-wheel-drive fixed-chassis tractor rollover during Phase I. Biosystems Engineering, 116(2), 179-189.

Bogsjö, K. (2008). Coherence of road roughness in left and right wheel-path. *Vehicle System Dynamics*, *46*(S1), 599-609.

Bukta, A. J., Sakai, K., Sasao, A., & Shibusawa, S. (2002). Free play as a source of nonlinearity in tractor-implement systems during transport. Transactions of the ASAE, 45(3), 503-508.

CDC Agricultural safety (2018, April, 12). Retrieved from http://www.cdc.gov/niosh/topics/aginjury/default.html

Captain, K. M., Boghani, A. B., & Wormley, D. N. (1979). Analytical tire models for dynamic vehicle simulation. Vehicle System Dynamics, 8(1), 1-32.

Case study of farm accidents in Japan II (in Japanese). (2013, March) Retrieved from http://www.maff.go.jp/j/seisan/sien/sizai/s_kikaika/anzen/23taimen.html#houkoku2

Chisholm, C. J. (1979a). A mathematical model of tractor overturning and impact behaviour. Journal of Agricultural Engineering Research, 24(4), 375-394.

Chisholm, C. J. (1979b). Experimental validation of a tractor overturning simulation. Journal of Agricultural Engineering Research, 24(4), 395-415.

Claar, P. W., Sheth, P. N., Buchele, W. F., & Marley, S. J. (1982). Simulated tractor chassis suspension system. Transactions of the ASAE, 25(3), 590-0594.

Collins, T. S. (1991). Loads in tractor linkages when transporting rear-mounted implements: Development of modelling and measurement techniques. Journal of agricultural engineering research, 49, 165-188.

Crolla, D. A., Horton, D. N. L., & Stayner, R. M. (1990). Effect of tyre modelling on tractor ride vibration predictions. Journal of Agricultural Engineering Research, 47, 55-77.

Davis, D. C., & Rehkugler, G. E. (1974a). Agricultural Wheel-Tractor Overturns-Part II: Mathematical Model Verification by Scale-Model Study. Transactions of the ASAE, 17(3), 484-0488.

Davis, D. C., & Rehkugler, G. E. (1974b). Agricultural wheel-tractor overturns part I: Mathematical model. Transactions of the ASAE, 17(3), 477-0483.

Elmer, F. J. (1997). Nonlinear dynamics of dry friction. *Journal of Physics A: Mathematical and General*, *30*(17), 6057.

Die Sozialversicherung für Landwirtschaft, Forsten und Gartenbau: Tödliche Arbeits- und Wegeunfälle (SVLFG),http://www.svlfg.de/11-wir/wir042_daten_zahlen/wir042_01_uv-noch-grafiken_unterordner/wir042_01_02_toedliche_au-noch-grafiken/index.html, Nov, 8, 2017.

Fang, H., Fan, R., Thuilot, B., & Martinet, P. (2006). Trajectory tracking control of farm vehicles in presence of sliding. Robotics and Autonomous Systems, 54(10), 828-839.

Flaugh, A. B. (2011). Studies on power hop using a nonlinear model of an agricultural tractor.

Franceschetti, B., Lenain, R., & Rondelli, V. (2014). Comparison between a rollover tractor dynamic model and actual lateral tests. Biosystems engineering, 127, 79-91.

Galvanetto, U. (2004). Sliding bifurcations in the dynamics of mechanical systems with dry friction—remarks for engineers and applied scientists. *Journal of Sound and Vibration*, *276*(1-2), 121-139.

Garciano, L. O., Sakai, K., & Torisu, R. (2005). Experimentally obtained bifurcation phenomenon in chaotic tractor vibrating in time and frequency domain. International Journal of Bifurcation and Chaos, 15(01), 225-231.

Garciano, L., Torisu, R., Takeda, J. I., & Sakai, K. (2002). Random, quasi-periodic and chaotic vibrations of farm tractors. Journal of the Japanese Society of Agricultural Machinery, 64(1), 91-99.

Gilet, T., Vandewalle, N., & Dorbolo, S. (2009). Completely inelastic ball. Physical Review E, 79(5), 055201.

Gillespie, T. D. (1992). Fundamentals of vehicle dynamics. Warrendale, PA: Society of automotive engineers, (Chapter 10, pp364).

Goering, C. E., & Buchele, W. F. (1967). Computer Simulation of an Unsprung Vehicle, Part I and Part II.Transactions of the ASAE, 10(2), 272.

Gonzalez, D. O., Martin-Gorriz, B., Berrocal, I. I., Morales, A. M., Salcedo, G. A., & Hernandez, B. M. (2017). Development and assessment of a tractor driving simulator with immersive virtual reality for training to avoid occupational hazards. Computers and Electronics in Agriculture, 143, 111-118.

Gunston, T. P., Rebelle, J., & Griffin, M. J. (2004). A comparison of two methods of simulating seat suspension dynamic performance. Journal of Sound and Vibration, 278(1-2), 117-134.

Guzzomi, A. L. (2012). A revised kineto-static model for Phase I tractor rollover. Biosystems engineering, 113(1), 65-75.

Guzzomi, A. L., Rondelli, V., Guarnieri, A., Molari, G., & Molari, P. G. (2009). Available energy during the rollover of narrow-track wheeled agricultural tractors. Biosystems engineering, 104(3), 318-323.

Han, X., Kim, H. J., Jeon, C. W., Moon, H. C., Kim, J. H., & Yi, S. Y. (2019). Application of a 3D tractor-driving simulator for slip estimation-based path-tracking control of auto-guided tillage operation. Biosystems engineering, 178, 70-85.

Hansson, P. A. (1995). Optimization of agricultural tractor cab suspension using the evolution method. Computers and Electronics in Agriculture, 12(1), 35-49.

Hansson, P. A. (1996). Rear axle suspensions with controlled damping on agricultural tractors. Computers and Electronics in Agriculture, 15(2), 123-147.

Hansson, P. A. (2002). Working space requirement for an agricultural tractor axle suspension. Biosystems Engineering, 81(1), 57-71.

Hesami, R., & McManus, K. J. (2009, January). Signal processing approach to road roughness analysis and measurement. In *TENCON 2009-2009 IEEE Region 10 Conference* (pp. 1-6). IEEE.

Holmes, P. J. (1982). The dynamics of repeated impacts with a sinusoidally vibrating table. Journal of Sound and Vibration, 84(2), 173-189.

Homori, H., Sakai, K., Sasao, A., & Shibusawa, S. (2003). 2D dynamics simulator for impact oscillators analysis of tractor-implement system. Journal of the Japanese Society of Agricultural Machinery, 65(1), 85-90.

Hubert, M., Ludewig, F., Dorbolo, S., & Vandewalle, N. (2014). Bouncing dynamics

of a spring. Physica D: Nonlinear Phenomena, 272, 1-7.

ISO (1995). Mechanical vibration—Road surface profiles—Reporting of measured data. ISO 8608: 1995.

ISO (2011). Passenger cars — Test track for a severe lane-change manoeuvre — Part 2: Obstacle avoidance. ISO 3888-2:2011.

Itoh, H., Oida, A., & Yamazaki, M. (1999). Numerical simulation of a 4WD–4WS tractor turning in a rice field. Journal of Terramechanics, 36(2), 91-115.

Jarašūniene, A., & Jakubauskas, G. (2007). Improvement of road safety using passive and active intelligent vehicle safety systems. Transport, 22(4), 284-289.

JISB 8018 (1989). Test Method of Performance of Small Size Diesel Engines for Land Use (in Japanese). Retrieved from https://kikakurui.com/b8/B8018-1989-01.html

JISD 6708 (1976). Testing Method for Turning Circle and Turning Space of Agricultural Tractors (in Japanese). Retrieved from https://kikakurui.com/d6/D6708-1976-01.html

Karimi, D., Mann, D. D., & Ehsani, R. (2008). Modeling of straight-line driving with a guidance aid for a tractor-driving simulator. Applied Engineering in Agriculture, 24(4), 403-408.

Karkee, M., & Steward, B. L. (2010a). Study of the open and closed loop characteristics of a tractor and a single axle towed implement system. Journal of Terramechanics, 47(6), 379-393.

Karkee, M., & Steward, B. L. (2010b). Local and global sensitivity analysis of a tractor and single axle grain cart dynamic system model. Biosystems engineering, 106(4), 352-366.

Karkee, M., & Steward, B. L. (2011). Parameter estimation and validation of a tractor and single axle towed implement dynamic system model. Computers and electronics in agriculture, 77(2), 135-146.

Kayacan, E., Kayacan, E., Ramon, H., & Saeys, W. (2014). Nonlinear modeling and identification of an autonomous tractor–trailer system. Computers and Electronics in Agriculture, 106, 1-10.

Kayacan, E., Kayacan, E., Ramon, H., & Saeys, W. (2015). Towards agrobots: Identification of the yaw dynamics and trajectory tracking of an autonomous tractor. Computers and Electronics in Agriculture, 115, 78-87.

Khorsandi, F., Ayers, P. D., & Truster, T. J. (2017). Developing and evaluating a finite element model for predicting the two-posts rollover protective structure nonlinear behaviour using SAE J2194 static test. Biosystems Engineering, 156, 96-107.

Kim, K. U., & Rehkugler, G. E. (1987). A review of tractor dynamics and stability.

Transactions of the ASAE, 30(3), 615-0623.

Kimura, K., Chino, A., Arita, H., & Seto, T. (1991). Arrangement of lot form on paddy field in a steep sloping area for safer tractor passageway. Transactions of the Japanese Society of Irrigation, Drainage and Reclamation Engineering, 155, 77-84.

Langley, J. D., Clarke, J., Marshall, S. W., Cryer, P. C., & Alsop, J. (1997). Tractor fatalities and injury on New Zealand farms. Journal of Agricultural Safety and Health, 3(3), 145.

Larson, D. L., Smith, D. W., & Liljedahl, J. B. (1976). The dynamics of three-dimensional tractor motion. Transactions of the ASAE.

Leine, R. I., Van Campen, D. H., De Kraker, A., & Van Den Steen, L. (1998). Stick-slip vibrations induced by alternate friction models. *Nonlinear dynamics*, *16*(1), 41-54.

Li, Z., Mitsuoka, M., Inoue, E., Okayasu, T., & Hirai, Y. (2015). Development of stability indicators for dynamic Phase I overturn of conventional farm tractors with front axle pivot. Biosystems Engineering, 134, 55-67.

Li, Z., Mitsuoka, M., Inoue, E., Okayasu, T., Hirai, Y., & Zhu, Z. (2016). Parameter sensitivity for tractor lateral stability against Phase I overturn on random road surfaces. Biosystems Engineering, 150, 10-23.

Lin, J. (2012). Identification of road surface power spectrum density based on a new cubic spline weight neural network. *Energy Procedia*, *17*, 534-539.

Liu, B., & Koc, A. B. (2013). SafeDriving: A mobile application for tractor rollover detection and emergency reporting. Computers and electronics in agriculture, 98, 117-120.

Liu, J., & Ayers, P. (1999). Off-road vehicle rollover and field testing of stability index. Journal of Agricultural Safety and Health, 5(1), 59.

Liu, J., & Ayers, P. D. (1998). Application of a tractor stability index for protective structure deployment. Journal of Agricultural Safety and Health, 4(5), 171.

Liu, X., Wang, H., Shan, Y., & He, T. (2015). Construction of road roughness in left and right wheel paths based on PSD and coherence function. Mechanical Systems and Signal Processing, 60, 668-677.

Lleras, N. O., Brennan, S., Murphy, D., Klena, M. J., Garvey, P. M., & Sommer Iii, H. J. (2016). Development of an open-source tractor driving simulator for tractor stability tests. Journal of Agricultural Safety and Health, 22(4), 227-246.

Luck, J. M., & Mehta, A. (1993). Bouncing ball with a finite restitution: chattering, locking, and chaos. Physical Review E, 48(5), 3988.

Luo, A. C., & Han, R. P. (1996). The dynamics of a bouncing ball with a sinusoidally vibrating table revisited. *Nonlinear Dynamics*, *10*(1), 1-18.

Mashadi, B., & Nasrolahi, H. (2009). Automatic control of a modified tractor to work on steep side slopes. Journal of Terramechanics, 46(6), 299-311.

Matsui, M., Aoyagi, Y., Morio, D., Tamura, T., Uchikawa, Y., Kimura, T. (2017). Study on tractor behavior based on accident topography: swing mechanism modeling of front axle and influence of mass center position on anteroposterior fall. Journal of the Japanese Society of Agricultural Machinery and Food Engineers, 79(1), 59-65.

Matthews, J., & Talamo, J. D. C. (1965). Ride comfort for tractor operators: III. Investigation of tractor dynamics by analogue computer simulation. Journal of Agricultural Engineering Research, 10(2), 93-108.

Mitchell, B. W., Zachariah, G. L., & Liljedahl, J. B. (1972). Prediction and control of tractor stability to prevent rearward overturning. Transactions of the ASAE, 15(5), 838-844.

Moon, F. C., Moon, F., 1987. Chaotic vibrations: an introduction for applied scientists and engineers. Wiley Online Library.

Moon, F. C., Shaw, S. W., 1983. Chaotic vibrations of a beam with nonlinear boundary conditions. International Journal of non-linear Mechanics 18 (6), 465-477.

Nakano, K. (2006). Two dimensionless parameters controlling the occurrence of stick-slip motion in a 1-DOF system with Coulomb friction. Tribology Letters, 24(2), 91-98.

Nguyen, N. V., Harada, Y., Takimoto, H., & Shimomoto, K. (2020). Measurement of static lateral stability angle and roll moment of inertia for agricultural tractors with attached implements. Journal of Agricultural Safety and Health, 26(1), 15-29.

Noguchi, N., Reid, J. F., Zhang, Q., Will, J. D., & Ishii, K. (1998). Development of robot tractor based on RTK-GPS and gyroscope. In 2001 ASAE Annual Meeting (p. 1). American Society of Agricultural and Biological Engineers.

Nordin, M., Galic', J., & Gutman, P. O. (1997). New models for backlash and gear play. *International journal of adaptive control and signal processing*, *11*(1), 49-63.

Ohmiya, K. (1990). Studies on roughness of meadow. Memoirs of the Faculty of Agriculture, Hokkaido University, 17(2), 151-209.

Ono, E., Hattori, Y., Muragishi, Y., & Koibuchi, K. (2006). Vehicle dynamics integrated control for four-wheel-distributed steering and four-wheel-distributed traction/braking systems. vehicle system dynamics, 44(2), 139-151.

Pacejka, H. (2005). Tire and vehicle dynamics (3rd ed.). Elsevier. (Chapter 1, pp5)

Pershing, R. L., & Yoerger, R. R. (1969). Simulation of tractors for transient response. Transactions of the ASAE, 12(5), 715-719.

Prasad, N., Tewari, V. K., & Yadav, R. (1995). Tractor ride vibration—A review.

Journal of Terramechanics, 32(4), 205-219.

Previati, G., Gobbi, M., & Mastinu, G. (2007). Farm tractor models for research and development purposes. Vehicle System Dynamics, 45(1), 37-60.

Previati, G., Gobbi, M., & Mastinu, G. (2014). Mathematical models for farm tractor rollover prediction. International Journal of Vehicle Design, 64(2-4), 280-303.

Pyragas, K. (1992). Continuous control of chaos by self-controlling feedback. Physics letters A, 170(6), 421-428.

Qin, J., Zhu, Z., Ji, H., Zhu, Z., Li, Z., Du, Y., ... & Mao, E. (2019). Simulation of active steering control for the prevention of tractor dynamic rollover on random road surfaces. Biosystems Engineering, 185, 135-149.

Raney, J. P., Liljedahl, J. B., & Cohen, R. (1961). The dynamic behavior of farm tractors. Transactions of the ASAE, 4 (2), 215-221

Rehkugler, G. E. (1980). Simulation of articulated steer four-wheel drive agricultural tractor motion and overturns. Transactions of the ASAE, 23(1), 2-0008.

Report on fatal farm accidents (2019 January 28). Report on fatal farm accidents that happened in 2017 (in Japanese) .Retrieved from: http://www.maff.go.jp/j/press/seisan/sizai/190128.html.

Report on fatal farm accidents that happened in 2016 (in Japanese). (2018, February, 13). Retrieved from http://www.maff.go.jp/j/press/seisan/sizai/180213.html

Report on fatal farming accidents that happened in 2014, http://www.maff.go.jp/j/press/seisan/sien/pdf/160428-01.pdf, Nov. 8, 2017.

Report on industrial fatality (in Japanese), Ministry of Health, Labour and Welfare. Retrieved from https://www.mhlw.go.jp/bunya/roudoukijun/anzeneisei11/rousai-hassei/index.html

Report on traffic accidents (in Japanese), National Policy Agency. Retrieved from https://www.npa.go.jp/publications/statistics/koutsuu/index_jiko.html

Reynolds, S. J., & Groves, W. (2000). Effectiveness of roll-over protective structures in reducing farm tractor fatalities. American Journal of Preventive Medicine, 18(4), 63-69.

Sakai, K. (1999). Theoretical analysis of nonlinear dynamics and chaos in bouncing tractor. Journal of the Japanese Society of Agricultural Machinery, 61(6), 65-71.

Sakai, K., & Aihara, K. (1994). Nonlinear vibrations in an agricultural implement system. International Journal of Bifurcation and Chaos, 4(02), 465-470.

Sakai, K., & Aihara, K. (1999). Bifurcation structure of vibrations in an agricultural tractor-vibrating subsoiler system. International Journal of Bifurcation and Chaos, 9(10), 2091-2098.

Sakai, K., & Terao, H. (1987). The Study on the Vibratory Soil Cutting of Vibrating

Subsoiler (Part 4). Journal of the Japanese Society of Agricultural Machinery, 49(1-2), 71-79.

Sakai, K., A. Sasao, and S. Shibusawa. 1999. Nonlinear dynamics of bouncing and power hop. ASAE Paper No. 991066. St. Joseph, Mich.: ASAE.

Sakai, K., Sasao, A., Shibusawa, S., & Bukta, A. (2000). Experimental analysis of nonlinear dynamics and chaos in bouncing tractor. Journal of the Japanese Society of Agricultural Machinery, 62(4), 63-70.

Sakai, K., Upadhyaya, S. K., Andrade-Sanchez, P., & Sviridova, N. V. (2017). Chaos emerging in soil failure patterns observed during tillage: Normalized deterministic nonlinear prediction (NDNP) and its application. *Chaos: An Interdisciplinary Journal of Nonlinear Science*, *27*(3), 033115.

Sayers, M. W. (1990). Profiles of roughness. Transportation Research Record, (1260), 106-111.

Sayers, M. W. (1995). On the calculation of international roughness index from longitudinal road profile. Transportation Research Record, (1501), 1-12

Serway, R. A., & Jewett, J. W. (2010). Physics for scientists and engineers with modern physics. Cengage learning, (Chapter 5, pp132).

Shibata, Y., & Sakai, J. (1979). Dynamic Characteristics of Tractors with Rotary-tillers Mounted (II). Journal of the Japanese Society of Agricultural Machinery, 41(1), 37-42.

Šmerda, T., & Čupera, J. (2010). Tire inflation and its influence on drawbar characteristics and performance–Energetic indicators of a tractor set. Journal of Terramechanics, 47(6), 395-400.

Smith, D. W. (1984). The influence of drawbar position on tractor rearward stability. ASAE Paper 84-1560, ASAE, St. Joseph, MI.

Smith, D. W., & Liljedahl, J. B. (1972). Simulation of rearward overturning of farm tractors. Transactions of the ASAE, 15(5), 818-821.

Smith, D. W., & Yoerger, R. R. (1975). Variations in the forward motion of farm tractors. Transactions of the ASAE, 18(3), 401-0403.

Smith, D. W., Perumpral, J. V., & Liljedahl, J. B. (1974). The kinematics of tractor sideways overturning. Transactions of the ASAE, 17(1), 1-3.

Söhne, Walter; Schwanghart, Helmut: Stand und Entwicklung von Prüfmethoden bei Schlepperumsturzschutzvorrichtungen. In: Grundlagen der Landtechnik 28 (5), 2013.

Stayner, R. M., Collins, T. S., & Lines, J. A. (1984). Tractor ride vibration simulation as an aid to design. Journal of agricultural engineering research, 29(4), 345-355.

Strogatz, S. H., 2014. Nonlinear dynamics and chaos: with applications to physics, biology, chemistry, and engineering. Hachette UK.

Sun, C., Nakashima, H., Shimizu, H., Miyasaka, J., & Ohdoi, K. (2019). Physics engine application to overturning dynamics analysis on banks and uniform slopes for an agricultural tractor with a rollover protective structure. Biosystems Engineering, 185, 150-160.

Sun, L. (2001). Developing spectrum-based models for international roughness index and present serviceability index. Journal of transportation engineering, 127(6), 463-470.

Takai, R., BARAWID Jr, O., Ishii, K., & Noguchi, N. (2010). Development of crawler-type robot tractor based on GPS and IMU. IFAC Proceedings Volumes, 43(26), 151-156.

Taylor, R. K., Bashford, L. L., & Schrock, M. D. (2000). Methods for measuring vertical tire stiffness. Transactions of the ASAE, 43(6), 1415.

Umeda, S., & Honami, N. (1975). Studies on the steering characteristics of tractor (I). Journal of the Japanese Society of Agricultural Machinery, 37(2), 149-155.

Umeda, S., Takeda, S., Matsui, K., & Tanaka, T. Farm power machinery, Tokyo, Japan (1981)

Usui, S., Tani, K., Shirai N., Horiguchi, E. (1990). A two-dimensional statistical model of uneven road surface. Transactions of the JSME C series，56（526），1408-1413.

Vidoni, R., Bietresato, M., Gasparetto, A., & Mazzetto, F. (2015). Evaluation and stability comparison of different vehicle configurations for robotic agricultural operations on side-slopes. Biosystems Engineering, 129, 197-211.

Volfson, B. P. (1999). Comparison of two simulation models of tire-surface interaction. In Proc. 13th Intl. Conf. of the ISTVS, 311-318.

Volfson, B. P., & Estrin, M. (1983). The slip-stick phenomenon in vehicle ride simulation. Computers in Engineering 1983, 1, 229-235.

Watanabe, M. & Sakai, K. (2017). Algorithm of Generating Road for Tractor Driving Simulator. Journal of the Japanese Society of Agricultural Machinery and Food Engineers.*79*(2), 149-157.

Watanabe, M., & Sakai, K. (2019a). Impact dynamics model for a nonlinear bouncing tractor during inclined passage. *Biosystems engineering*, *182*, 84-94.

Watanabe, M., & Sakai, K. (2019b). Numerical Analysis of Tractor Accidents using Driving Simulator for Autonomous Driving Tractor. In *Proceedings of the 5th International Conference on Mechatronics and Robotics Engineering* (pp. 65-68).

Watanabe, M., & Sakai, K. (2020). Numerical analysis of steering instability in an agricultural tractor induced by bouncing and sliding. *biosystems engineering*, *192*, 108-116.

Watanabe, M., Bauerdick, J., Sakai, K., & Bernhardt, H. (2018). Comparison of jumping process between small-sized and large-sized tractors. In 38. GIL-Jahrestagung: Digitale Marktplätze und Plattformen, 247-250.

Watanabe, M., Sakai, K. (2017). Algorithm of generating road for tractor driving simulator. Journal of the Japanese Society of Agricultural Machinery and Food Engineers, 79(2), 149-157.

Wiley, J. C., & Turner, R. J. (2008). *Power hop instability of tractors*. American Society of Agricultural and Biological Engineers.

Wismer, R. D., & Luth, H. J. (1974). Off-road traction prediction for wheeled vehicles. Transactions of the ASAE, 17(1), 8-0010.

Xiang, W., & Nakagiri, S. (1986). A model and spectrum analysis of uneven road surface by means of tow-dimensional filtered Poisson process. Transactions of the JSME A series, 52(477), 1411-1416.

Yamakawa S. (1976). Road for vehicle test. Journal of Society of Automotive Engineers of Japan, 30(8), 656-661.

Yang, L., & Noguchi, N. (2012). Human detection for a robot tractor using omni-directional stereo vision. Computers and Electronics in Agriculture, 89, 116-125.

Yisa M. G., & Terao H. (1999). Scale-model analysis of a tractor-trailer system on slope. In Proc. 13th Intl. Conf. of the ISTVS, 557-564.

Yisa, M. G., & Terao, H. (1995). Dynamics of Tractor-implement Combinations on Slopes (Part I): State-of-the-art Review. Memoirs of the Faculty of Agriculture, Hokkaido University, 66(2), 240-262.

Yisa, M. G., Terao, H., Noguchi, N., & Kubota, M. (1998). Stability criteria for tractor-implement operation on slopes. Journal of Terramechanics, 35(1), 1-19.

Yoon, J., Cho, W., Kang, J., Koo, B., & Yi, K. (2010). Design and evaluation of a unified chassis control system for rollover prevention and vehicle stability improvement on a virtual test track. Control Engineering Practice, 18(6), 585-597.

Zhang, Q., & Qiu, H. (2004). A dynamic path search algorithm for tractor automatic navigation. Transactions of the ASAE, 47(2), 639.

Zhang, C., & Noguchi, N. (2017). Development of a multi-robot tractor system for

agriculture field work. Computers and Electronics in Agriculture, 142, 79-90.

Zheng, E., Fan, Y., Zhu, R., Zhu, Y., & Xian, J. (2016). Prediction of the vibration characteristics for wheeled tractor with suspended driver seat including air spring and MR damper. Journal of Mechanical Science and Technology, 30(9), 4143-4156.

Zoz, F. M. 2007. The cause of power hop. ASABE Paper No. 071110. St. Joseph, Mich.: ASABE. Available at: asae.frymulti.com/request.asp?search=1&JID=5&AID=22913&CID=min2007&v=&i=&T=1.

eSafety – Making Europe's roads safer for everyone, eSafety support. Brussels, 2001, p. 2–10.

A. Appendix: Results of tractor field experiments

A.1 Bump test results

As mentioned in chapter 7, vertical acceleration data in bump tests have three phases corresponding to engine vibrations, lug vibrations, and bump excitation vibrations. In chapter 7, bump excitation vibrations were analyzed to validate the CarSim® tractor model. In this chapter, engine vibrations and lug vibrations are analyzed. Figure A.1 and A.2 respectively show the vertical acceleration time series and Fourier spectrum during engine vibrations while Figure A.3 and A.4 respectively shows the vertical acceleration time series and Fourier spectrum of the vertical acceleration during lug vibrations.

Figure A.2 shows a single dominant frequency of 42.0 Hz in the spectrum. This frequency is considered to be excited by engine rotation. In Figure A.4, there are several dominant frequencies, such as frequencies lower than 10.0 Hz, at ~42.0 Hz, and a frequency band from 10.0 to 35.0 Hz. Frequency lower than 10.0 Hz represents the natural frequency of the tractor, while frequency at ~42.0 Hz represents the engine rotation. The frequency band from 10.0 to 35.0 Hz is the result of tire lug vibration, which is analyzed in Appendix 2.

	N = 1	N = 2	N = 3
1st	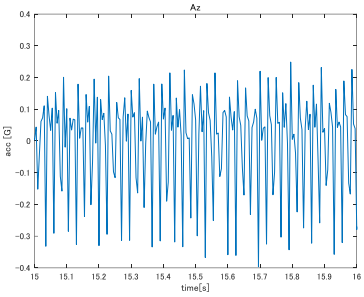	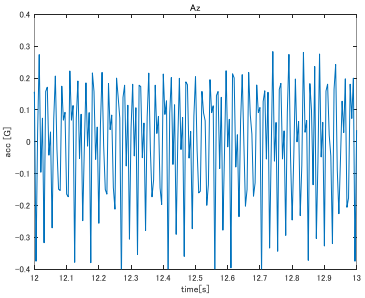	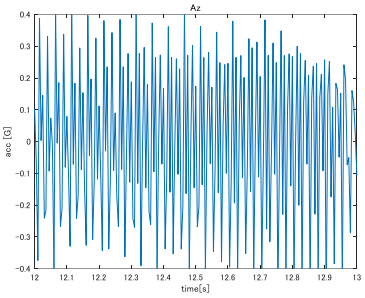
2nd	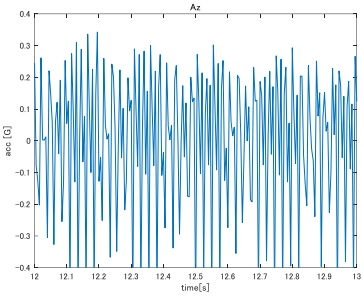	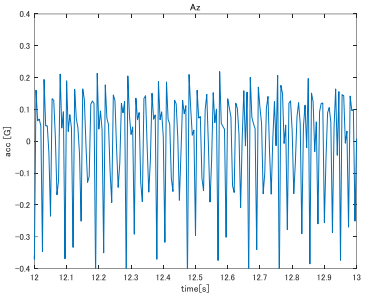	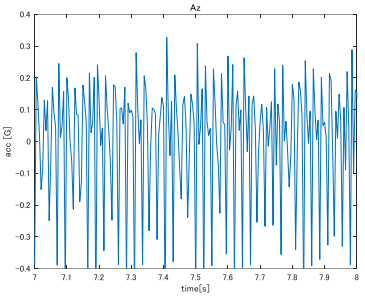
3rd	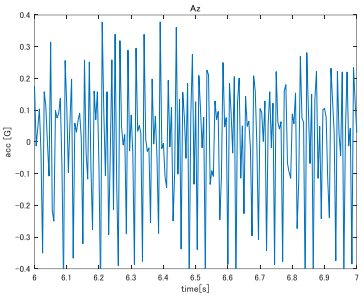	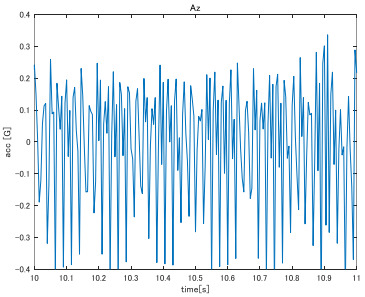	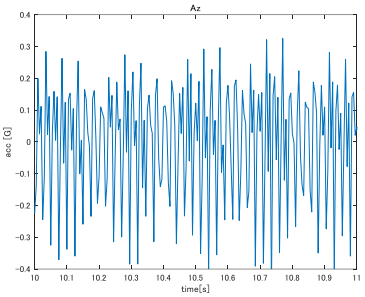
4th	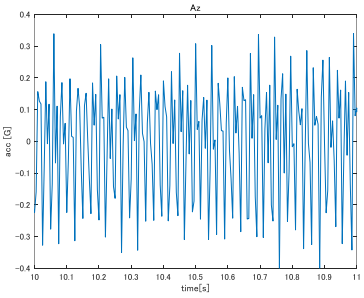	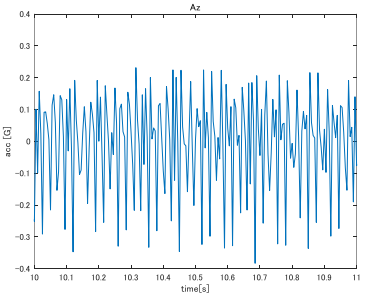	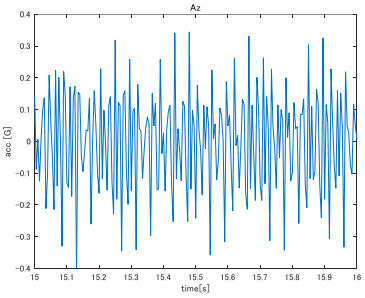

Figure A.1 Vertical acceleration of engine vibrations.

	N = 1	N = 2	N = 3
1st	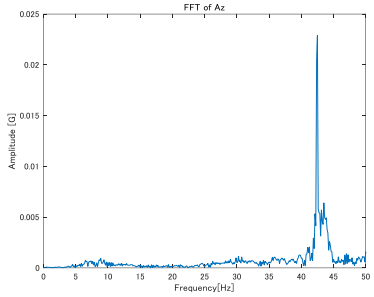	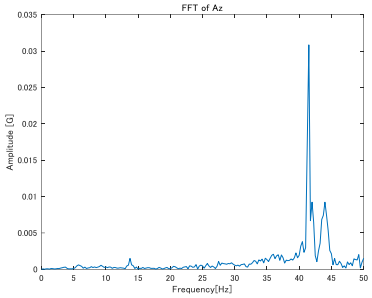	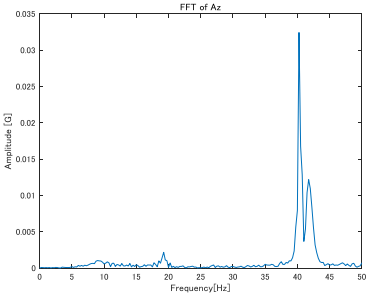
2nd	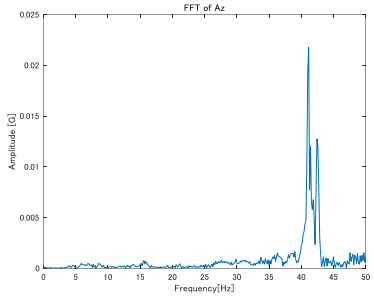	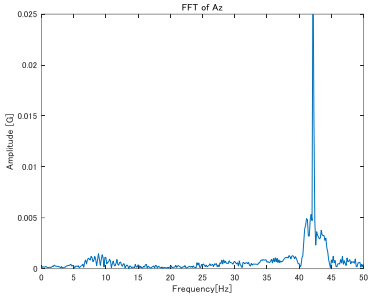	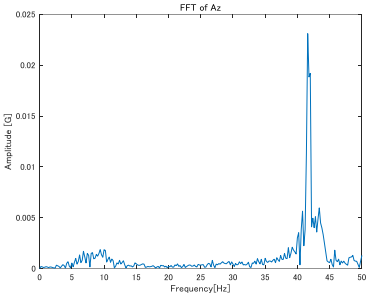
3rd	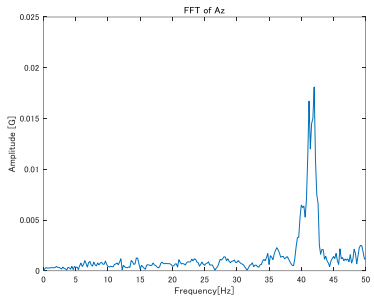	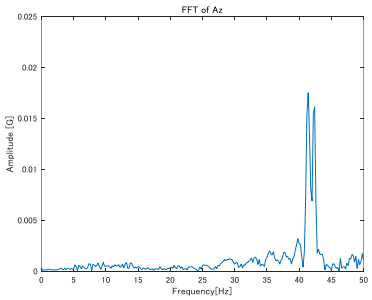	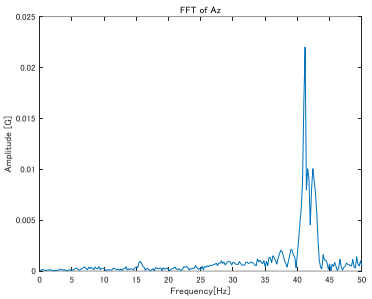
4th	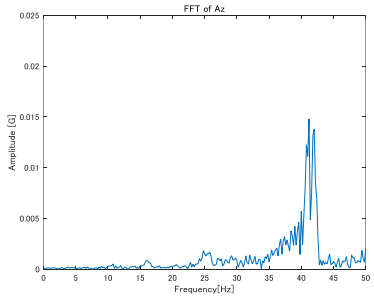	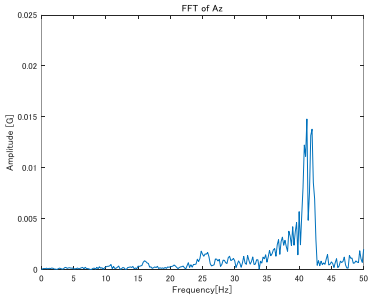	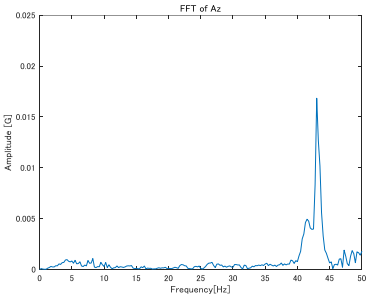

Figure A.2 Fourier spectrum of vertical acceleration during engine vibrations.

	N = 1	N = 2	N = 3
1st	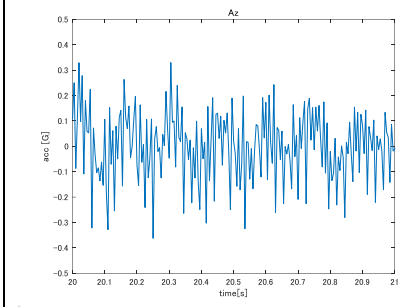	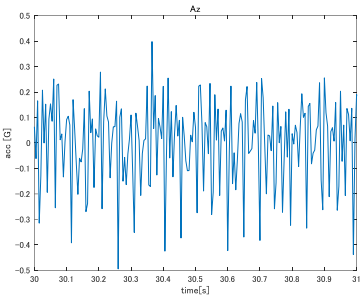	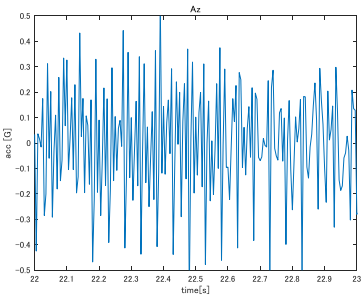
2nd	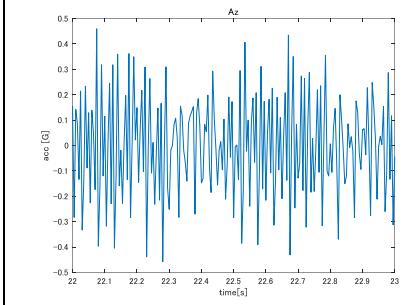	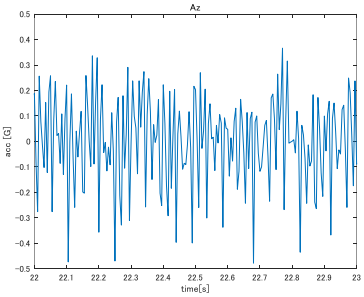	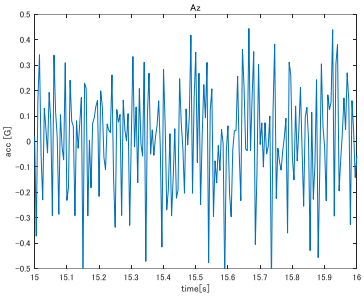
3rd	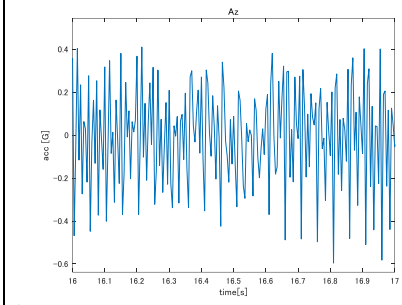	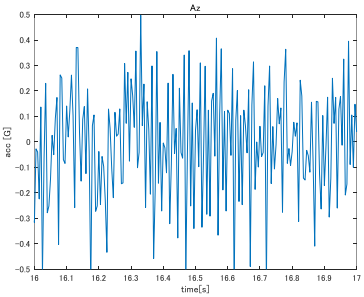	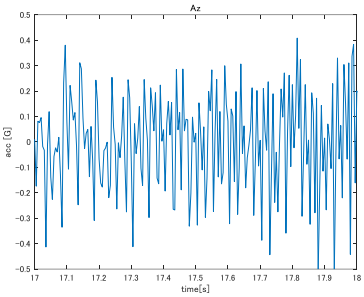
4th	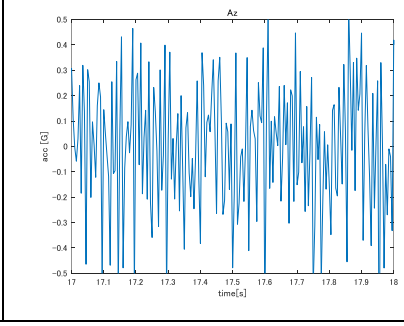	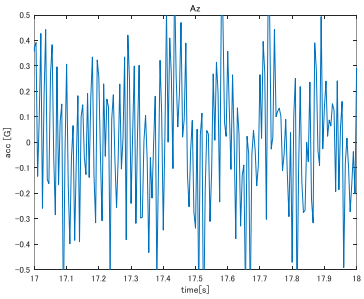	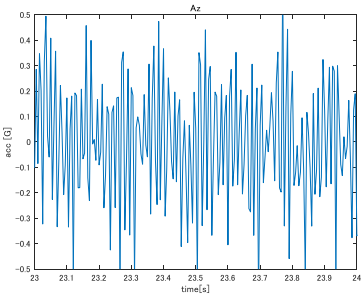

Figure A.3 Time series of vertical acceleration during engine vibrations.

	N = 1	N = 2	N = 3
1st	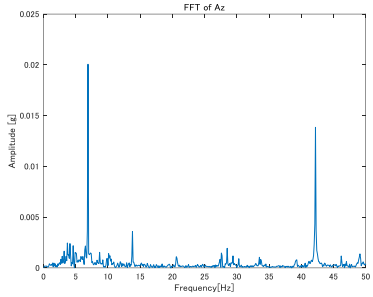	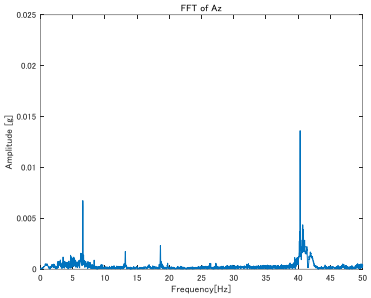	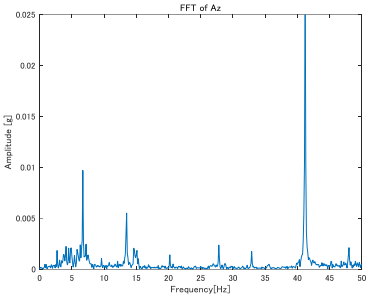
2nd	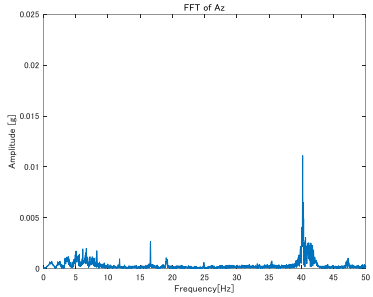	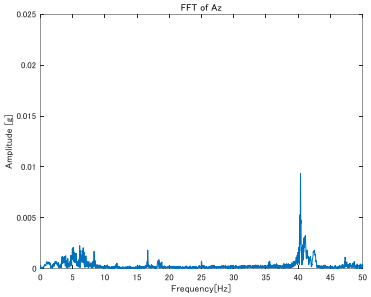	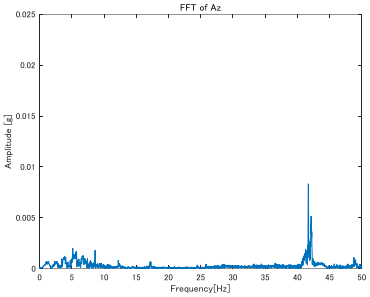
3rd	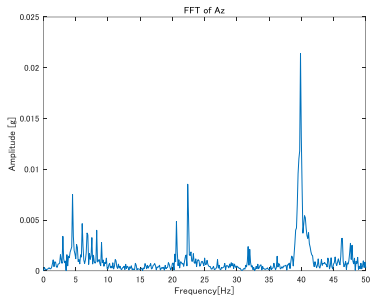	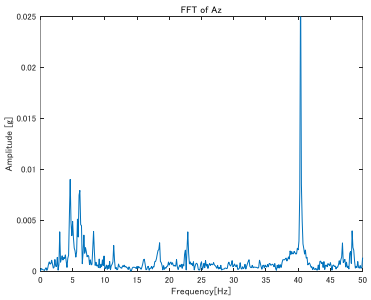	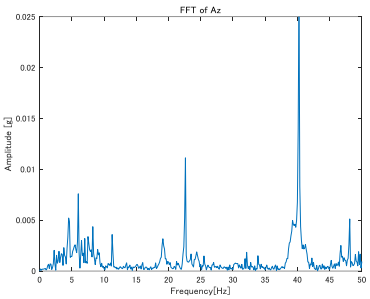
4th	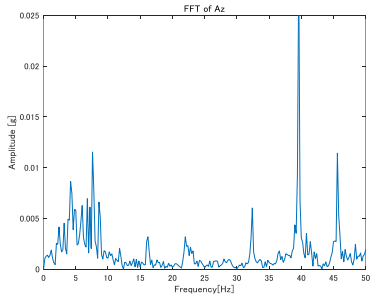	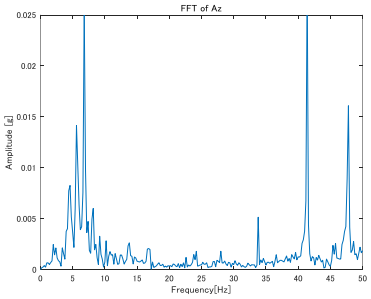	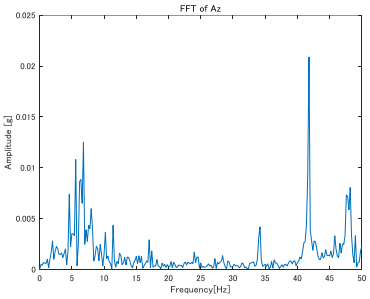

Figure A.4 Fourier spectrum of vertical acceleration during lug vibrations.

A.2 Frequency analysis of the tire lug

The frequency band from 10.0 to 35.0 Hz was observed in section A.1. This frequency band was varied in the experiment and depended upon the travel velocity of the tractor. Table A.1 gives the average travel velocity and the frequency band in the experiment.

Table A.1 Average travel velocity and frequency band in the experiment

Travel velocity V [m s^{-1}]	Frequency band [Hz]
1.44	13.4
1.82	16.9
2.46	22.2
3.62	32.9

The values in Table A.1 are plotted in Figure A.5.

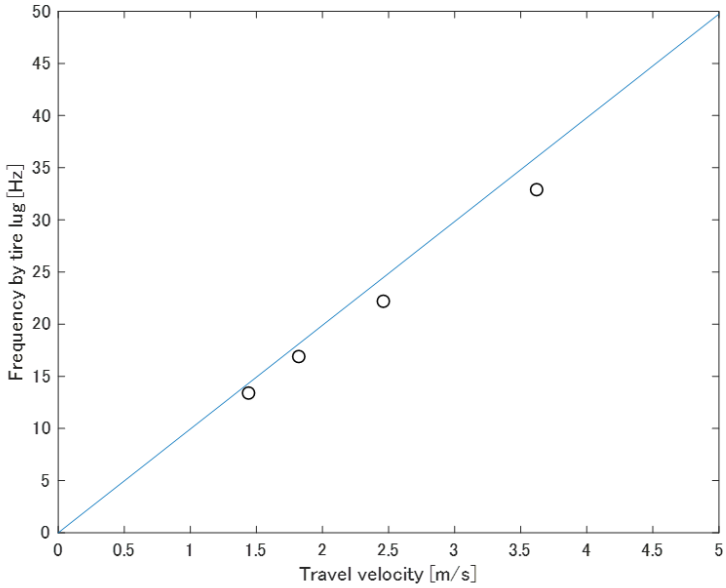

Figure A.5 Frequency of tire lug vibration vs travel velocity of the tractor.

According to Figure A.5, the tire lug frequency is linearly proportional to the travel velocity of the tractor. Theoretically, the relationship between the travel velocity of the tractor V and the tire lug frequency F_{lug} is described as

$$F_{lug} = \frac{N}{D\pi} * V, \tag{A.1}$$

where N is lug number of the tire and D is the tire diameter. According to laboratory measurement, N = 30 and D = 0.96 m, and N/(Dπ) = 9.9472 is thus acquired. Linear regression on bump test data gives a regression coefficient of 9.1147. This result strongly indicates that the frequency band from 10.0 to 35.0 Hz is excited by tire lug vibrations.